Exploring new frontiers of carbon dioxide electrolysis at industrially relevant conditions

Giron Rodriguez, Carlos Andres

Publication date:
2023

Document Version
Publisher's PDF, also known as Version of record

DTU

DTU Physics
Department of Physics

Exploring new frontiers of carbon dioxide electrolysis at industrially relevant conditions

Carlos Andres Giron Rodriguez

Ph.D. thesis

Supervisor: Prof. Brian Seger
Co-supervisor: Prof. Ib Chorkendorff

Department of Physics
Section of Surface Physics and Catalysis
Technical University of Denmark (DTU)

Kongens Lyngby, Denmark
January 2023

Preface

The following thesis is submitted as partial fulfillment of the Ph.D. degree in physics at the Technical University of Denmark (DTU). The work was conducted at the Section for Surface Physics and Catalysis (Surfcat) at DTU Physics, under the supervision of Prof. Brian Seger and Prof. Ib Chorkendorff, between February 2020 and January 2023. The project was funded by the European Union's Horizon 2020 research and innovation program under grant 851441 (SelectCO2), and the Villum Fonden (grant 9455 through the VILLUM center for the science of sustainable fuels and chemicals). Most of the results presented here were based on my personal work but were not possible without the constant contributions of my colleagues and other project partners. The specific contribution of their work to this thesis was stated in the respective sections and chapters of this document.

Carlos Andres Giron Rodriguez
Technical University of Denmark
January 2023

Abstract

Electrochemical CO_2 reduction (CO_2R) driven by renewable energies has emerged as a promising solution to mitigate greenhouse gas emissions and produce carbon–neutral energy-dense chemicals. In recent years, developments in electrocatalysts for CO_2R have resulted in materials with enhanced selectivity toward hydrocarbons and alcohols. Nevertheless, mass transport issues can limit the testing of these materials in traditional electrolyzer configurations, which may be detrimental since parameters such as selectivity and activity strongly depend on reaction rates and microenvironments. Therefore, operations at high current densities should be encouraged to increase production rates while demonstrating their technical and economic feasibility.

Although intensive efforts are being made to increase the efficiency of CO_2 electrolyzers through catalyst development, process intensification, and system design, it is challenging to achieve high selectivity towards a specific product, reaction rates, and long-term stability. This is primarily due to catalyst deactivation, salt precipitation, GDE flooding, inadequate water management, and a lack of components designed specifically for CO_2R applications. To enhance performance, research has been undertaken to develop highly efficient and stable CO_2R electrocatalysts; however, other engineering factors must also be considered, such as reactor configuration, electrode structure, reaction conditions (temperature, pressure, pH), and electrolyte selection.

Throughout this thesis, I propose different strategies for addressing the most relevant challenges of operating CO_2 electrolyzers at industrially relevant conditions using gas-fed reactors. I have attempted to improve catalytic activity, selectivity, and stability by analyzing the effect of operating conditions (through the design and construction of a reaction setup), electrolyzer components (e.g., ion-exchange membranes), and electrocatalysts. As a first step, I investigated the effects of different reaction components on the overall performance of gas-fed reactors. My subsequent work focused on understanding how the operating temperature affected catalyst activity, water management, and product distribution over Cu-based GDEs using a zero-gap cell. This study aimed to investigate the effect of temperature on the kinetics and transport of CO_2R, demonstrating its potential to enhance its catalytic performance and emphasizing the importance of appropriate heating during these experiments.

Moreover, I focused on electrocatalysts using tandem catalysts following a two-step electrolysis procedure. This work compared the sputtering with nanoparticulate approaches, the effects of metal loading, and electrode composition ratios during electrode preparation. Additionally, a "CO-selective" catalyst layer was added to examine how it affects the selectivity of C_{2+} products. This electrode type showed promising results evaluated during its testing, characterization, and product quantification using a simple preparation method.

Further, I investigated the role of the anion-exchange membrane by testing a new gen-

eration of membranes designed explicitly for CO_2 electrolysis. In this study, RG-AEM membranes were synthesized with different functionalized head groups. The relationship between their mechanical properties and CO_2R performance has been examined through properties like the ion exchange capacity, water uptake, and thickness. Results showed that AEMs with heterocyclic groups exhibited competitive mechanical, thermal, and chemical properties compared to current commercial membranes and provided stable long-term CO_2R operation under industrial conditions.

Finally, I investigated various other strategies, including adding recycling lines to boost the CO_2 conversion, manipulating the backpressure to control CO_2 surface coverage, or adding ionomers to the catalyst layer to enhance gas and ionic transport, some of which have shown promising results in CO_2R applications. Ultimately, the described alternatives were combined, demonstrating their benefits for a stable and selective long-term operation (>200 hours). Through this research, I have proposed alternatives to address existing CO_2R challenges, proposing potential solutions that can be easily scaled up in the industry and showing additional research opportunities in this field.

Resumé

Elektrokemisk CO_2 reduktion drevet af grøn energi har udviklet sig til et lovende alternativ i kampen mod udledning af drivhusgas og til at producere karbon-neutrale kemikalier. Nylige fremskridt inden for elektrokatalyse har ledt til materialer med bedre selektivitet mod kulstofforbindelser – herunder alkoholer. Desværre er test af disse materialer i traditionelle elektrolyse konfigurationer begrænset af lav strøm grundet masseoverførsels begrænsninger, hvilket har store konsekvenser for den målte selektivitet og aktivitet. Ved at teste ved højere strømtæthed kan produktionshastigheden forbedres, samtidig med at katalysatorerne kan testes ved betingelser, der er relevante for industrien. Introduktionen af GDE's har ledt til udviklingen af nye reaktordesign, hvilket har forbedret den overordnede ydeevne og energieffektivitet. På trods af den omfattende indsats for at opskalere og udvikle katalysatorer, reaktordesign og overordnede systemer, så er der stadig mange begrænsninger forbundet med CO_2 elektrolyse. Den ønskede selektivitet, produktionshastighed og stabilitet kan endnu ikke opnås, og det skyldes især nedbrydning er selve katalysatoren, uønskede sidereaktioner, og et fænomen kaldes "flooding", hvor vand trænger ind i GDE'en. Det er desuden svært at finde elektrolyse komponenter specifikt designet til at håndtere CO_2 reduktion.

Meget forskning går ind i at udvikle effektive and stabile elektrokatalysatorer for CO_2 reduktion. Det er dog lige så vigtigt at undersøge de andre faktorer, som spiller ind på ydeevnen af CO_2 elektrolyse. Eksempler på dette er reaktor konfiguration, struktur af elektroden, reaktionsbetingelser som temperatur, tryk, pH og lign., samt valg af elektrolyt. Alle disse faktorer har indflydelse på kinetik og masseoverførsels begrænsninger. I denne afhandling kommer jeg med forskellige forslag til hvordan man kan takle de mest relevante udfordringer forbundet med CO_2 elektrolyse under industri-relevante forhold. Jeg har forsøgt at forbedre selektivitet, aktivitet og stabilitet af reaktionen ved at undersøge effekten af førnævnte reaktionsbetingelser (tryk, temperatur og pH), samt komponenter af designet såsom membranen og katalysatoren. Til at starte med undersøgte jeg hvordan de forskellige komponenter af elektrolysedesignet havde indflydelse på ydeevnen af en gas-fed reaktor. Derefter undersøgte jeg indflydelsen af temperatur på aktivitet, vandforvaltning og produktdistribution på en Cu-baseret GDE i en zero-gap reaktor. Og til sidst lavede jeg et systematisk studie af temperaturens indflydelse på reaktionskinetik og massetransport, hvilke viste vigtigheden af opvarmning under disse eksperimenter.

Udover overstående, så havde jeg stort fokus på elektrokatalyse ved brug af et tandem katalyse system, hvor der indgår 2 katalysatorer og 2 elektrokemiske steps. I dette arbejde bliver ydeevnen af tynde film sammenlignet med ydeevnen af nanopartikler. Her har kompositionen af katalysatoren og elektroden stor betydning. Tilførsel af den "CO - selektive" katalysator viste lovende resultater i forhold til de analyserede produkter, især C_2+ produkter, og kunne forberedes ved en simpel teknik.

Herudover testede jeg en ny generation af anion exchange membranes, der er specifik

designet til CO_2 reduktion. De forskellige RG-AEM membraner var syntetiseret med forskellige iongrupper. Forholdet mellem deres mekaniske egenskaber og deres ydeevne for CO_2 reduktion blev undersøgt på baggrund af deres ionbytningsevne, vandkapacitet og tykkelse. Resultatet var at AEM's med heterocykliske grupper viste bedre mekaniske, termiske og kemiske egenskaber i forhold til de membraner vi har på markedet nu. De nye membraner gav mulighed for længere test med mere stabil CO_2 reduktion.

Til sidst afprøvede jeg en mængde af andre strategier såsom at implementerer CO_2 genanvendelse for at forbedre konverteringen af CO_2 gas. Jeg prøvede derudover af kontrollere hvor meget CO_2 vi kunne gå til at sidde på katalysator overfladen ved af manipulerer gastrykket, samt tilføje iongrupper til katalysatoren for at forbedre gas og ion transport. Sidstnævnte har tidligere vist lovende resultater. De mange alternativer og forbedringer til CO_2 elektrolyse blev kombineret og deres effekt blev demonstreret i et $>$200 timer langt eksperiment. Gennem min forskning er jeg derfor kommet med alternativer, som adresserer de eksisterende udfordringer CO_2 elektrolyse har, og de løsninger jeg er kommet med kan både videreudvikles på et forskning niveau eller skaleres op til mere industrielt relevante størrelser.

Acknowledgements

This journey would not have been possible without the contributions, support, and collaboration of my family, friends, and colleagues.

I am deeply grateful to my supervisors, Prof. Brian Seger and Prof. Ib Chorkendorff, for allowing me to pursue this Ph.D. project and for their ongoing guidance, support, and encouragement. Special thanks to my primary supervisor, Brian, for his immense trust in me and my fellow CO_2 reduction group members, which made it a privilege to work under his guidance. Also, for all the advice, tips, and discussions he has shared with me, both scientific and non-scientific - these will remain with me for the rest of my professional and personal life.

My most profound appreciation and thanks to all the members of the SelectCO2 project for the exciting discussions and fantastic collaboration. I particularly thank Dr. Erdem Irtem from TU Delft for his scientific input and continual support throughout this project, and Dr. Terry Wilson and Prof. John Varcoe from the University of Surrey for providing me with their excellent membranes and expertise in the field, as well as patience in helping me filling in all my chemistry gaps. Furthermore, I want to thank Prof. Feng Jiao and his research group at the University of Delaware for their support and warm welcome during my external stay in the US.

My sincere appreciation goes to Johanna, Dhananjai, and Barbara (the "fantastic four") for helping me fall in love with electrochemistry and always inspiring me. They became my small family in Germany. To Rade for his advice, support, and sincere kindness. Also, to my friend Carlos who has been an amazing support here in Denmark. Thank you all for always being there for me.

I want to thank SurfCat and Cattheory at DTU for providing a pleasant working environment. Many thanks to our floor managers, Brian Peter Knudsen, Jakob Ejler Sorensen, and Patrick Strom-Hansen, as well as to Birgit Bohn and Jacqueline McAnulty for their assistance and collaboration when needed and for keeping the labs running for us. It was a pleasure working with all the CO_2 reduction group members here at DTU. My gratitude to former members Dr. Ming Ma, Dr. Ezra Clark, and Dr. Gaston Larrazabal for helping me during my first Ph.D. year and introducing me to the world of electrochemical CO_2 reduction. I want to thank Dr.Katja Li (honorary member of the CO_2 group), Degenhart Hochfiltzer, Francesco Longhin, Dr.Wanyu Deng, and Dr.Quicheng Xu for their support and collaboration. I am deeply grateful to Bjort Oladottir and Clara Brunn for all their scientific and non-scientific contribution, friendship, and being wonderful human beings; Yu Qiao, who started the Ph.D. with me and has been a great officemate and colleague throughout this time.

Among everyone, though, I want to express my sincere appreciation to three people in the CO_2 group who helped me a lot during this Ph.D. First, thanks to Dr.Sahil Garg for being a fantastic colleague to collaborate with and for his significant bits of advice, thoughtfulness,

and friendship. Tugce Yilmaz, for being my friend and rock during this journey, for listening to me and encouraging me during the hard times. To Dr.Asger Moss for being the best partner-in-crime anyone could ask for. His friendship and input/contribution during my Ph.D. were enormous, and I'm grateful for it.

Finally, I want to dedicate this thesis to all my family, who have a special place in my heart. In particular, I would like to thank my sister, who has consistently helped me throughout my life, and my parents, who have always been supportive and motivated me to have big dreams. I couldn't have done it without them; there are simply the best parents. Love you unconditionally.

List of Publications

Paper I
Influence of headgroups in ETFE-based radiation-grafted anion exchange membranes for CO_2 electrolysis
Carlos A. Giron Rodriguez, Bjørt Oladottir Joensen, Asger B. Moss, Gaston Larrazabal, Daniel K. Whelligan, Brian Seger, John R. Varcoe, and Terry Wilson.
ACS Sustainable Chemistry and Engineering, 2023. *in appendix*

Paper II
Insights into zero-gap CO_2 electrolyzer at elevated temperatures
Carlos A. Giron Rodriguez, Asger Barkholt Moss, Sahil Garg, Wanyu Deng, Ib Chorkendorff, and Brian Seger.
In preparation, 2023. *in appendix*

Paper III
How membrane characteristics influence the performance of CO_2 and CO electrolysis
Sahil Garg, Carlos A. Giron Rodriguez Thomas E. Rufford, John R. Varcoe, and Brian Seger.
Energy and Environmental Science, 2022, 15, 4440

Paper IV
In operando investigations of oscillatory water and carbonate effects in MEA-based CO_2 electrolysis devices
Asger B. Moss*, Sahil Garg*, Marta Mirolo Carlos A. Giron Rodriguez, Roosa Ilvonen, Ib Chorkendorff, Jakub Drnec, and Brian Seger.
Accepted in Joule, 2023. * These authors contributed equally

Paper V
Radiation-grafted anion-exchange membranes for CO_2E: an unexpected effect of using a lower excess of N-methylpiperidine in their fabrication
Terry Wilson, Carlos A. Giron Rodriguez, Qiucheng Xu, Jordan Frow, Ravi Kumar, Ihtasham Salam, Arun P. Periasamy, Mohammed Mamlouk, Hungyen Lin, Brian Seger, Daniel K. Whelligan, and John R. Varcoe.
In preparation, 2023

Paper VI
Mechanistics insights into aldehyde production from electrochemical CO_2 reduction on CuAg alloys via operando X-ray measurements.
Yu Qiao, Georg Kastlunger, Ryan C. Davis, Carlos A. Giron Rodriguez, Wanyu Deng, Peter Benedek, Daniel Lee, Thomas F. Jaramillo, Ib Chorkendorff, and Brian Seger
Submitted, 2023.

Contents

List of Tables

Nomenclature

Latin Symbols

A	Geometric Area	cm^2
C	Capacitance	F
c	Concentration	M
D	Diffusion	$cm^2 \cdot s^{-1}$
E	Potential	V
E_0	Standard Potential	V
E_A	Activation Energy	J
E_{cell}	Cell Potential	V
F	Faradaic Constant	96485 $A \cdot s \cdot mol^{-1}$
FE	Faradaic Efficiency	%
G	Gibbs Free energy	$KJ \cdot mol^{-1}$
H	Enthalpy	$KJ \cdot mol^{-1}$
I	Current	A
IEC	Ion-Echange capacity	$mmol \cdot g^{-1}$
J	Flux	$m^{-2} \cdot Kg \cdot s^{-2}$
j	Current Density	$mA \cdot cm^{-2}$
L	Electrode distance	cm
M	Molar Mass	$g \cdot mol^1$
m	Mass Loading	mg
n	Mol number	mol
n_i	Molar gas flow	$mol \cdot s^{-1}$
p	Pressure	bar
Q	Charge	$A \cdot s$
q	Heat	W
r	Reaction Rate	s^{-1}
R	Ideal Constant Gas	8.314 $J \cdot mol^{-1} K^{-1}$
R_i	Resistance	Ω
RH	Relative Humidity	%
T	Temperature	K
T_i	Thickness	cm
t	Time	s
TPS	Through-plane swelling	%
V	Volume	L
V_t	Volumetric flow	$mL \cdot min^{-1}$
w	Membrane width	cm

WU	Water Uptake	%
z	Number of electrons	-

Greek Symbols

η	Overpotential	V
σ	Ionic Conductivity	mS
α	Charge Transfer Coefficient	-
μ	Ion Mobility	$m^2 \cdot V^{-1} \cdot s^{-1}$
λ	Hydration Number	-
ϕ	Work function spectrometer	eV
v	Scan rate	$mV \cdot s^{-1}$

Subscript

a	Anode
c	Cathode
dry	Dry
hyd	Hydrated
i	Specific Product, Component
M	Membrane
O	Oxidation
r	Resistance
R	Reduction
CO_2	Carbon Dioxide
2+	Products >2 carbons

Abbreviations

AcO-	Acetate
AEM	Anion exchange membrane
BPM	Bipolar membrane
BPR	Backpressure regulator
CA	Chronoampetiometry
CE	Counter Electrode
CEM	Cation exchange membrane
CL	Catalyst Layer
CO_2E	CO_2 Electrolysis
CO_2R	CO_2 Reduction
CO_2RR	CO_2 Reduction Reaction

CP	Chronopotentiometry
cp	Carbon Paper
CV	Cyclic Voltammetry
DAD	Diode-Array Detector
DFT	Density Functional Theory
E-cell	Electrochemical cell
EDX	Energy-Dispersive X-ray Spectroscopy
EE	Energy Efficiency
EIS	Electrochemical Impedance Spectroscopy
EtOH	Ethanol
FC	Flow Cell
FID	Flame Ionization Detector
GC	Gas Chromatography
GDE	Gas-Diffusion Electrode
GDL	Gas-Diffusion Layer
HER	Hydrogen Evolution Reaction
HPLC	High Performance Liquid Chromatography
IHP	Inner Helmholtz Plane
LSV	Linear Sweep Voltammetry
MEA	Membrane Electrode Assembly
MFC	Mass Flow Controler
MPL	Microporous Layer
MPS	Macroporous Substrate
NP	Nanoparticles
OCV	Open Circuit Voltage
OER	Oxygen Evolution Reaction
OHP	Outer Helmholtz plane
PrOH	n-propanol
PTFE	Polytetrafluoroethylene
PVD	Physical Vapor Deposition
QA	Quaternary amine
RE	Reference Electrode
RG	Radiation-Grafted
RHE	Reversible Hydrogen Electrode
RID	Refractive Index Detector
RT	Room Temperature
SEM	Scanning Electron Microscopy
TCD	Thermal Conductivity Detector
WE	Working Electrode
XPS	X-ray Photoelectron Spectroscopy

Chapter 1

Introduction

1.1 Motivation

The escalating effects of global warming are causing concern in today's world. Anthropogenic activities, such as fossil fuel combustion, deforestation, and industrialization, have contributed significantly to this issue by releasing high levels of greenhouse gases (GHGs) into the atmosphere. In the last decade, around 37 Gton of carbon dioxide (CO_2) has been released from using fossil fuels [1], leading to a rise in average temperatures of 1.1°C since pre-industrial times (Figure 1.1). In the absence of immediate actions to reduce GHGs, another 1.5°C increase by 2100 is anticipated, with catastrophic effects on the environment and ecosystems[2]. The Paris Climate Accord was thus established in December 2015 with the participation of 195 countries and the UNFCCC aiming to keep global temperatures by achieving net zero emissions by 2050 through decarbonization, or carbon sequestration [3, 4].

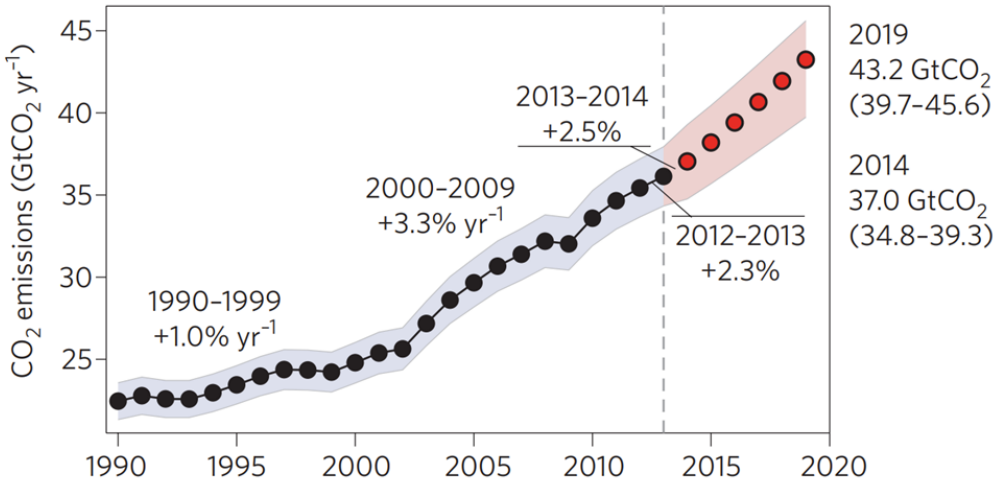

Figure 1.1: CO_2 emissions from fossil fuel combustion and industrial production over the last few decades (a; black dots); and projected emissions for future years (red dots), based on historical CO_2 emissions data. Image reprinted from Reference [5].

Combining these strategies with carbon capture and recycling systems could provide sustainable carbon sources, store renewable energy, and turn CO_2 into added-value products [6]. Thus, there are several ways to convert CO_2, including biological, thermochemical, photochemical, and electrochemical [7]. Each approach for CO_2 conversion has its economic benefits and must be considered in the portfolio of solutions for reducing atmospheric CO_2 concentrations and reaching climate change

goals. Furthermore, these CO_2 utilization technologies have a very ambitious goal: to disrupt a 5 trillion dollar market by supplying fuels and chemicals at lower prices than petrochemical production can offer while ensuring a low environmental impact operation [8]. Although this might sound ambitious, a sustainable economy that utilizes carbon is becoming more apparent as governments' support for carbon pricing mechanisms increases and new technologies become available to convert carbon into energy. Therefore, beginning with less conservative markets and developing technology/infrastructure faster is imperative.

The electrochemical conversion of CO_2 into commodities and fuels can be scaled up under milder conditions with high selectivity. Due to their similarity to commercial hydrogen electrolyzers, their operation, and logistics can leverage existing infrastructure, accelerating their implementation and adapting this technology into this application [9]. Through increased research and development, CO_2 electrolysis using renewable power could be a cost-effective and sustainable way to produce stable chemical products and store energy, thereby reducing GHGs and closing the carbon cycle [10].

1.2 Electrochemical CO_2 reduction (CO_2R)

As mentioned before, CO_2R driven by renewable energies is an alternative to mitigate CO_2 emissions by converting them into added-value products and decarbonizing the chemical industry. In addition, the electrochemical CO_2 reduction offers several advantages, including combining water splitting with an analogous electrocatalytic process, the ability to synthesize products that are difficult to prepare using conventional thermal processes, and the operation at ambient conditions [11].

A CO_2 electrolyzer is a device that uses electricity to convert CO_2 into reduced carbon-containing products. An externally applied voltage with a sufficient potential (E) is required to transfer electrons from the anode to the cathode, which reduces CO_2 (Eq. 1.2.1) into hydrocarbons and oxygenates, and ions (OH^- or protons, depending on reaction environment). Through the electrolyte, ions are transported across an ion-exchange membrane (IEM) to the anode, where they are consumed through water oxidation, where oxygen evolution reaction (OER) and electron generation occur (Eq. 1.2.2), resulting in a redox reaction (reduction-oxidation).

CO_2 Reduction Reaction (CO_2RR):

$$\mathrm{xCO_2 + yH_2O + ze^- \longrightarrow product + zOH^-} \tag{1.2.1}$$

Oxygen Evolution Reaction (OER):

$$\mathrm{4\,OH^- \longrightarrow O_2 + 2\,H_2O + 4\,e^-} \tag{1.2.2}$$

The CO_2RR can proceed through a proton-coupled electron transfer reaction pathway to produce various C_1 products such as carbon monoxide, methane, and formate, C_2 products as ethylene, ethanol, and acetate, or even C_3 products such as n-propanol (Table 1.1). In addition, other compounds as traces have been reported, including glyoxal, hydroxyacetone, ethylene glycol, acetaldehyde, propionaldehyde, methanol, or acetone, accounting for around 16 different products coming from this mechanism [12]. Additionally, if electrochemical CO_2 reduction is carried out in an aqueous solution, the hydrogen evolution reaction (HER) may occur as a competitive reaction. Table 1.1 exhibits the most common half-reactions and the thermodynamic potentials for multiple CO_2RR under alkaline conditions.

Table 1.1: Common cathodic CO_2R and hydrogen evolution reaction (HER), products in aqueous and alkaline solution, their standard potentials using reversible hydrogen electrode (V vs. RHE) at 1 atm and 298 K. Data Adapted from Reference [11].

Cathodic Reactions	**E^0 (V vs. RHE)**	**z**
CO_2 (g) + $2H_2O$ (l) + $2e^- \rightarrow CO(g) + 2OH^-$	-0.10	2
CO_2 (g) + $5H_2O$ (l) + $6e^- \rightarrow CH_3OH$ (l) + $6OH^-$	0.03	6
CO_2 (g) + $2H_2O$ (l) + $2e^- \rightarrow HCOO^-(aq) + 2OH^-$	-0.12	2
CO_2 (g) + $6H_2O$ (l) + $8e^- \rightarrow CH_4$ (g) + $8OH^-$	0.17	8
CO_2 (g) + $5H_2O$ (l) + $8e^- \rightarrow CH_3OO^-(aq) + 7OH^-$	0.11	8
CO_2 (g) + $9H_2O$ (l) + $12e^- \rightarrow C_2H_5OH$ (l) + $12OH^-$	0.09	12
CO_2 (g) + $8H_2O$ (l) + $12e^- \rightarrow C_2H_4$(g) + $12OH^-$	0.08	12
CO_2 (g) + $13H_2O$ (l) + $18e^- \rightarrow C_3H_7OH$ (g) + $18OH^-$	0.10	18
$2H_2O$ (l) + $2e^- \rightarrow H_2$ (g) + $2OH^-$	0.0	2

1.3 Fundamentals and relevant metrics for CO_2R

The role of potential

The work described in this thesis is conducted through electrochemical reactions (excluding unwanted carbonate reactions, as discussed in Chapter 2), where electricity is used as a driving force to overcome the activation energy required to achieve the desired reaction. During the standard operation, the thermodynamic potential indicates at which applied redox potential should ideally occur. However, the potential to initiate a reaction is typically higher due to inefficiencies in the reactor design, reaction mechanisms, and activation barriers (cell potential) [11]. Therefore, the thermodynamic potential (E^0) determines the minimum driving force and the total amount of charge transferred during the reaction. The cell potential is related to the Gibbs free energy of the system (ΔG) since it measures the difference in the chemical potential.

$$G^0 = -z \cdot F \cdot E^0 \tag{1.3.1}$$

At thermodynamic potential, the reaction is reversible, where both forward and reverse reactions occur at the same reaction rate. By applying a potential, the electron energy levels change accordingly. A reduction reaction occurs if the electron's energy level at the electrode is higher than the unoccupied molecular orbital in the reactant. Alternatively, electrons can be transferred to the electrode from molecules whose electron energy level is lower than the occupied molecular orbital, resulting in an oxidation reaction. Therefore, the applied potential determines what reactions can take place. For most reactions, kinetic limitations require increasing the driving force to reach measurable reaction rates (overpotentials). A catalyst will lower this overpotential by catalyzing the electrochemical reaction at the surface of the electrode with a considerable reaction rate. Nevertheless, overpotentials are not solely caused by kinetic limitations, as high reaction rates can result in the depletion of reactants, causing mass transport limitations (e.g., low diffusion). As both mechanisms affect the reaction mechanism and performance, it is vital to consider their effects when operating CO_2R at high current densities.

Metrics for CO_2R

Recent advances have been made in developing nanostructured metals, and metal oxide electrocatalysts for converting CO_2 into fuels and feedstocks [13, 14, 15]. The catalytic performance of such materials is evaluated using the most relevant metrics for CO_2R catalysts, such as Faradaic Efficiency (FE), overpotentials (η), partial current density (j_i), and Energy Efficiency (EE).

Faradaic Efficiency (FE): the FE correlates the selectivity towards a specific product during the CO_2R process and is expressed as the ratio between the charge needed to generate the concerned product (Q_A) and the total charge (Q).

$$FE_i = \frac{Q_A}{Q} = \frac{z \cdot n \cdot F}{Q} \tag{1.3.2}$$

Overpotential (η): it is defined as the difference between the overall thermodynamic potential (E^0) and the applied potential for the reaction (E). During electrolysis, the CO_2R and OER show significant cathodic overpotential (η_c) and anodic overpotential (η_a), respectively. The sum of such overpotentials may, however, be less than the overall overpotential (η) due to several resistances associated with resistance losses in the device, namely the ohmic losses resulting from ion conductivity in the electrolyte, the membrane, and other resistances associated with electrical resistances in cells and between reaction components [16].

$$\eta = E - E^0 \tag{1.3.3}$$

$$\eta = \eta_c + \eta_a + \eta_M + \eta_R + \eta_O \tag{1.3.4}$$

Partial current density (j_i): it measures the activity towards a particular reaction, serving as a crucial indicator for the reaction rate on a specific electrocatalyst towards a product. While it can be normalized to different areas (geometric area, electrochemically active surface area (ECSA), or specific surface area), I only show j_i normalized to the geometric area in this thesis.

$$j_i = \frac{I}{A} \cdot FE_i \tag{1.3.5}$$

Energy efficiency (EE): is the ratio of the energy used to produce a specific product to the net energy input (E_{cell}), and has been implemented to correlate the net energy consumption of a specific product. Generally, studies do not use this metric measurement, as they do not consider the anodic potential or the effects of the electrolyzer components/design.

$$EE_i = \frac{E^0 \cdot FE_i}{E^0 + E_{cell}} \tag{1.3.6}$$

Tafel Slope: a calculation of the Tafel slope (derived from the Butler-Volmer equation) provides information about the change in reaction mechanisms caused by catalyst surface morphology or reaction conditions. Through this method, it is possible to identify the rate-determining steps and elementary steps of the reaction mechanism [17].

1.4 Electrocatalysts for CO_2R

Nanostructured metallic electrocatalysis has become a viable option for CO_2R [11]. These materials offer the possibility of stabilizing reaction intermediates and improving the catalysis by increasing the active surface area, modifying the surface morphology, or altering electronic structure [18, 19]. Moreover, they are relatively low-cost and environmentally friendly. This has led to increased research into how these materials can be utilized as effective catalysts for CO_2RR.

Dabbling this field, in 1985, Hori and co-workers presented a study that evaluates multiple polycrystalline metal electrodes for CO_2R. During this series of experiments, electrolysis was conducted at constant current density ($5\ mA \cdot cm^{-2}$) on CO_2-saturated 0.5 M $KHCO_3$, followed by the gaseous and liquid product measurements [20]. This resulted in a major classification of metal catalysis (divided into four main groups), which has been extended in recent research based on its selectivity towards a major product (Figure 1.2).

In accordance, metals such as Hg, Pb, Bi, Sn, or In prefer to bind the *OCHO intermediate, producing formic acid/formate. In contrast, metals such as Au, Ag,

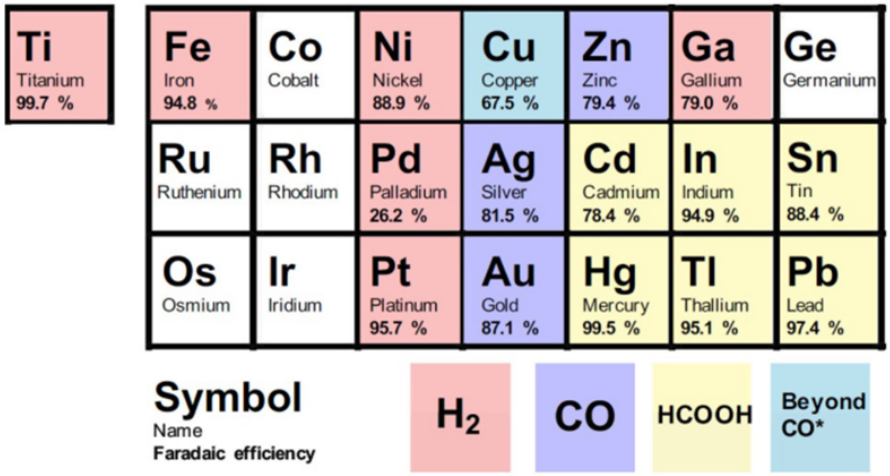

Figure 1.2: Major product classification groups of metal catalysts for CO_2 electroreduction based on Hori's experiments, represented in a cropped periodic table with colors and major product Faradaic Efficiency (selectivity towards H_2 (red), $HCOO^-$ (yellow), CO (blue), and beyond CO* (cyan)). Image reprinted from reference [21].

Zn, and Ga strongly bind *CO intermediate and favor CO production. Even though research has been carried out extensively on new catalysts, most of the work has focused on using Cu as an electrocatalyst for CO_2R. This is because it is the only monometallic with negative adsorption energy for CO and positive adsorption energy for H, reducing CO_2 into low-chain hydrocarbons and alcohols [22]. Finally, Pt, Ni, Fe, or Ti produces H_2, favoring the H* binding over CO_2 intermediates, tuning the HER selectivity over CO_2RR [21, 11].

In this thesis, I focused on CO-selective catalysts and Cu-based electrocatalysts. A more detailed description of these metals will follow:

CO-selective catalysts: Ag nanoparticles have proven to be an effective metal for selective CO production. Currently, the use of alternative Ag morphologies (corals or spheres) and different reaction conditions have enhanced its activity at high current densities by stabilizing the rate-determining intermediate (e.g., >90% at 1 $A \cdot cm^{-2}$) [23]. In my thesis, I used Ag to study the effects of the membrane's chemistry and the introduction of a recycling line due to its simplicity compared to Cu-based electrodes. Additionally, Au nanoparticles (<10 nm) have also been used in fundamental studies, as they provided high electrochemical surface areas even at low loadings [24]. In the high current density regime, they also proved stable selectivity, achieving j_{CO}=540 $mA \cdot cm^{-2}$ with FE_{CO}=92% [25, 26]. In contrast to monometallic catalysts, single-metal-site catalysts and molecular complexes have demonstrated their competitiveness at neutral pH, providing lower onset potential versus SHE. by using Fe^{3+} dispersed in pyrrolic-N sites [27] Ni single sites embedded in MOFs, or as Ni–N–Cs [28]. Molecular Co phthalocyanine and Fe porphyrin have also shown similar onset potentials, making them promising electrocatalysts despite

not reaching the required high current densities for CO_2R [29]. Furthermore, Zn has also proven selective towards CO and alcohols when combined with Cu due to the synergy between the two metals [30].

Cu-electrocatalyst: As mentioned before, Cu is the only monometallic that can reduce CO_2 into C_{2+} products. Nanostructured-based Cu electrocatalysts have displayed better catalytic performance than bulk materials/flat faces materials [11]. However, large overpotentials in Cu electrocatalysts result in unsatisfactory efficiency and limited product selectivity.

Recently, researchers have proposed various strategies to address this issue through the formation of grain boundaries [31], vacancy steering [32], dopant modification [33], alloying with other metals (tuning the d-band position) [34], improvements in the surface morphology to expose the preferred crystalline facets (e.g, nanowires, nanocubes, etc.) [35], the manipulation of the oxidation state [36], or the electrolyte design [37]. In terms of crystalline facets, theoretical studies suggest that Cu(100) surfaces are more active than Cu(111) and Cu(211) surfaces in terms of CO dimerization [38]. Cu(100) has achieved the lowest reported overpotential for pure Cu catalyst, reaching a j_{C2H4} of 391 $mA \cdot cm^{-2}$ and a Faradaic Efficiency of 67% at -0.72V vs. RHE [39]. At higher current densities, there is little difference in the performance of catalysts based on Cu(100) surface and Cu thin films or nanoporous morphologies of Cu. This implies that other strategies for catalyst modifications are needed to boost the intrinsic activity of Cu at industrially relevant conditions [40]. Further state-of-the-art will be discussed in Section 1.10.

1.5 Proposed reaction mechanism for CO_2R

While the electrochemical pathway for CO_2 reduction towards specific C_2+ is still being debated, there is a general consensus about the adsorption, catalytic, and desorption steps for CO_2R. As a first step, CO_2 is mass transferred from the gas phase to the bulk electrolyte (1), then transported to the cathode/electrolyte interface (2), where the CO_2 is absorbed in the cathode surface (3). Then, through electron transfer reactions, adsorbed CO_2 species are dissociated into intermediates like COOH*, CO*, CHO*, and COH*, which then are converted into carbon-derived products, and further desorbed from the electrode surface (6) [11, 16].

Thermodynamics and kinetics models, along with DFT calculations, are widely used to predict the reaction mechanisms for CO_2R, including the rate-determining step (RDS) and intermediate precursors for specific products over Cu surfaces. The DTU Cattheory group and SelectCO2 members have proposed a common predicted mechanism that agrees with experiments in the experimental DTU CO_2 group (Figure 1.3) [41]. From electrochemical CO_2 reduction to CO, the adsorbed CO (*CO) has been detected as a common intermediate before the final rate-limiting

step towards multicarbon products or methane. Through simulations of activation energies via the nudged elastic band (NEB) method under constant potential at alkaline conditions, it has been found *CO dimerization (C-C coupling) is the most likely RDS [11, 42], as the initial CO protonation is unfavored. Another possible explanation for CO_2 activity towards C_2+ products results from the polarization of *OCCO intermediates [43].

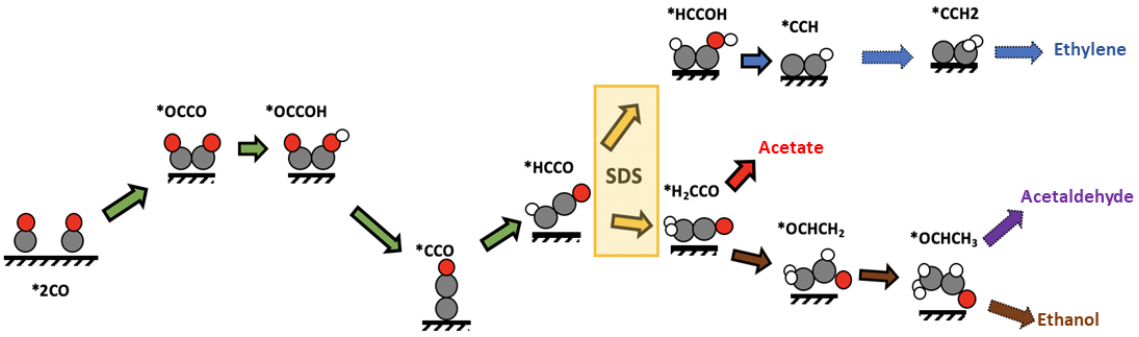

Figure 1.3: Scheme of the reaction mechanisms towards C_2-products after CO formation (assuming CO-CO coupling the RDS). The Green arrows represent common steps towards all products. Yellow arrows symbolize the determining step (SDS) between ethylene, acetate, acetaldehyde, and ethanol. Arrows colored differently represent the path to the product of the respective color. Courtesy image from DTU CatTheory and reprinted from SelectCO2 Deliverable D7.5 [41].

Two significant pathways toward C_{2+} products have been identified as a function of the applied potential. When overpotentials are low, the ketene (H_2CCO) intermediate dominates, leading to higher selectivity toward oxygenated products (e.g., ethanol). In contrast, the HCCOH pathway prevails at higher overpotentials, switching selectivity towards ethylene due to a high barrier, preventing the central carbon protonation, and creating the thermodynamically most stable *OHCCH intermediate [41]. A detailed study has shown that ethanol and acetaldehyde are produced via desorption rather than protonation of adsorbed *$OCHCH_3$. Hence, its selectivity is enhanced by low overpotentials and improved mass transport. Ethylene is favored at higher overpotentials due to the stronger stabilization of the oxygen protonation of *HCCO intermediate. The acetate pathway relies on the nucleophilic attacks on desorbed *H_2CCO, promoted at low overpotentials, roughness, and high pH [41, 11]. These findings have been supported by experimental estimation of Butler-Volmer transfer coefficients or isotope studies for multiple reaction mechanisms [17, 44].

1.6 Reaction conditions

Electrolyte effects: an essential requirement of inert electrolytes commonly used in CO_2R processes is that they dissociate rapidly into cations and anions and are

highly conductive. However, the effect of the electrolyte ions on CO_2R is far more complex than a simple charge carrier relationship, as it influences the local reaction environment, CO_2 mass transport, and acid/base equilibria [45].

-Cation effects: metal cations are essential in steering reaction activity and product distribution. Koper's group has demonstrated that CO_2R cannot occur without metal cations [46]. It is known that electrostatic interactions between adsorbed species with dipole moments and cations placed in the outer Helmholtz plane (OHP) enhance CO_2R through an electric field effect. Further, cation hydration and stabilization of the negatively charged intermediate can affect the reaction mechanism selectivity [47, 48]. The identity of the metal cation also influences the performance, as Murata and Hori observed a higher selectivity for C_{2+} products with larger cations using a series of electrolytes with ionic size increasing, following the trend: $Cs^+ > K^+ > Na^+ > Li^+$ [49].

-Anion effects: anionic species in the electrolyte can also influence CO_2R due to their buffering effects and specific adsorption at the cathode surface. Bell's group proved that the composition and concentration of anions have no significant effects on the formation of hydrocarbons and alcohols but rather a significant influence on the formation of CH_4 and HER, which are pH dependent [50].

-pH effects: CO_2 phase stability in aqueous solutions is influenced significantly by pH, as demonstrated by the Pourbaix diagram. As for selectivity, low pH shifts to the competing hydrogen evolution reaction (HER) [43], as pH affects protons' availability, enhancing HER over CO_2RR (since specific pathways are pH-independent). At alkaline conditions, HER's equilibrium potential shifts to a more negative value, reducing its activity, favoring C_2+ products [11]. However, operating at high pH may promote the formation of carbonates, which deplete local CO_2 concentrations and thereby limit the CO_2 mass transport.

Operation conditions

- Pressure effects: an increase in CO_2 partial pressure has shown to enhance the CO_2R total current and mass transfer to electrode surfaces due to the CO_2-solvent solubility relationship (Henry's law) [51]. In addition, pressure can directly modulate the surface coverage of the CO_2, and key intermediates at the surface [52]. However, an increase in the operating pressure elevates the complexity and construction costs of the electrolyzer, so optimizing the pressure must consider during the CO_2R [53]. On the other hand, high-pressure CO_2R operation also requires balancing the pressure in the anode and cathode chambers. A pressure imbalance can deform the membrane and alter water management, resulting in electrode flooding [54] and limiting its application. A study of this parameter's effects on CO_2 electrolysis is presented in Chapter 7.

-Temperature effects: increasing the operation temperature alters CO_2E in various ways, affecting multiple operational parameters. There are currently few studies focusing on understanding its effect on CO_2R, despite the necessity of operating it under such conditions due to resistive heating and its benefits for increasing activity at lower overpotentials at industrially relevant conditions. Nevertheless, the task is not straightforward, as temperature affects kinetics, mass transport, and hydrodynamic properties, including mass transfer (solubility, diffusion rate), reaction pathways, viscosity, electrical conductivity, and membrane conductivity [55]. As part of my Ph.D, I conducted a systematic investigation to understand its influence, and I described these effects exhaustively in Chapter 4.

1.7 Component integration and electrolyzer design

CO_2 electrolyzers consist of a cathode, anode, and an ion exchange membrane (IEM). Gas diffusion electrodes (GDEs) are commonly used for CO_2 cathodes for high current densities (GDE: a gas diffusion layer and a catalyst layer). The gas diffusion layer (GDL) consists of a macroporous layer (MPS) and a microporous layer (MPL, usually carbon-based coated with hydrophobic PTFE), allowing CO_2 diffusion to the surface and controlling the mass transfer of species to and from the catalyst layer (CL) [56]. The CL consists of heterogeneous metals, molecular complexes, or single-metal atom-doped carbons coated on the GDL. For the anode, IrO_x on GDEs, Ni, NiFe, or Platanized-Ti are highly effective and preferred materials for oxidation at low overpotentials under different reaction conditions [57]. In between the electrodes, there is an ion-exchange membrane (IEM) made of a polymer sheet that transfers ions and inhibits the product crossover. Membranes for CO_2R can be categorized into three category types on their ionic permeability: cation-exchange membranes (CEM), anion-exchange membranes (AEM), and bipolar membranes (BPM).

The configuration of the electrolyzer considerably influences the overall efficiency of the CO_2R process [16]. Electrochemical reactors for CO_2 can be classified as batch or semi-batch cells (H-cell) and continuous flow cells (Figure 1.4). The primary difference between these architectures is a roughly 3-order magnitude reduction in the CO_2 diffusion pathway to the catalyst's surface: from 50 µm in H-cell to nm scale using GDLs [58].

H-cells are often used in laboratory CO_2R studies due to their low cost and simplicity; however, they are not suitable for treating large volumes of gas and scaling-up operation due to the low solubility of CO_2 in aqueous media (33 mM), limiting their operation at low current densities regime ($<35\ mA \cdot cm^{-2}$) [59]. Gas-fed reactors can facilitate this transition by providing an interface between the inbound CO_2 and the reaction environment, reaching operation at high current densities.

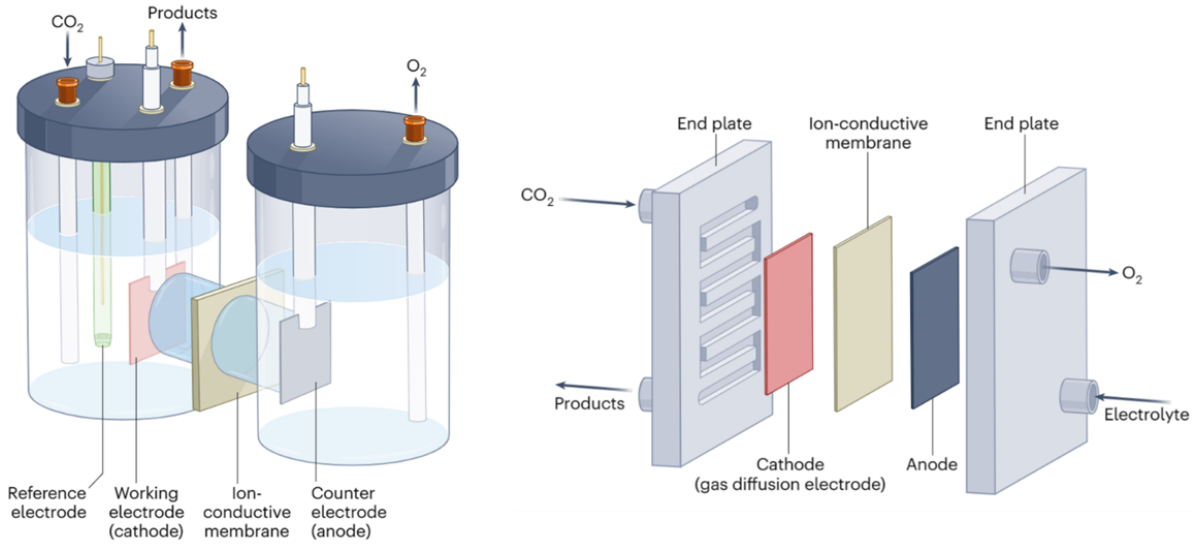

Figure 1.4: Schematic illustration of the basic configuration of an electrochemical cell for CO_2 reduction experiments. a). three-electrode H-type batch cell, and b). Gas-diffusion-electrode-based flow cell.

Flow cells for this application are inspired by water-splitting electrolyzers. There are three types of electrochemical flow cells that apply to CO_2R: gas, solid (SOEC), and liquid phase. Gas-fed electrolyzers or membrane electrode assemblies (MEA) operate efficiently due to their zero-gap design with gas-diffusion electrodes (GDEs) [60]. The cathodic compartment receives humidified CO_2, while the anodic compartment is filled with a flowing electrolyte (usually carbonate-based salt), which provides the necessary conductivity and cations for electrolysis. Electrical contact in MEAs can be established using a conducting plate, and flow fields, featuring either circular or serpentine designs can achieve effective reactant transport within the system [61]. Several studies have demonstrated improved partial current density, higher stability, and enhanced selectivity for C_1-C_3 products using this cell configuration [62, 63, 64, 65].

Liquid phase electrolyzers are widely employed in CO_2R. It features a liquid electrolyte between the GDL and IEM. As opposed to the gas phase electrolyzer, this type of reactor allows for the flow of catholyte, the placement of reference electrodes (RE), the absence of humidified CO_2, or the possibility of operating at high pressures [59, 62]. Depending on the desired outcome, both electrolyzer designs have multiple benefits, such as lower cell resistances in MEAs or easier liquid product collection/detection in liquid-phase electrolyzers (catholyte flow cells). However, each design has its drawbacks, including product crossover, water management problems, contamination sensitivity, carbonate salt precipitation, and GDE flooding [40, 66]. Chapter 2 will address the current limitations of CO_2 electrolysis in more detail and some proposed strategies to overcome them.

1.8 The prospects for CO_2R commercialization

The commercialization of CO_2 electrolysis has been studied through techno-economic studies in recent years. The Jiao group evaluated the economic feasibility of various carbon dioxide (CO_2) reduction products for large-scale chemical production, assessing a current density between 200 and 400 $mA \cdot cm^{-2}$ as the threshold for its operation [67]. Gaseous products like CO and formic acid are more profitable but have smaller market potential and higher storage/transport costs. In contrast, liquids such as ethanol and n-propanol may generate greater future profits than light hydrocarbons, based on the existing energy market, but require higher overpotentials. Furthermore, electricity and separation costs must be reduced for higher-order alcohols to become economically viable [68]. Through further research on electrocatalysts, C_2-C_3 alcohols produced from CO_2R could enable renewable energy sources to penetrate the transportation sector while reducing GHG emissions.

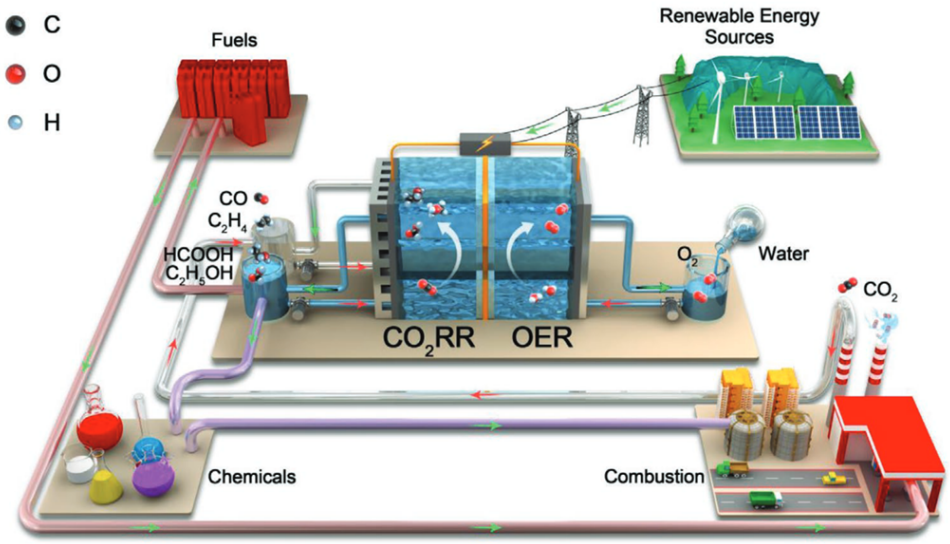

Figure 1.5: Scheme of the commercialization prospect for CO_2 electroreduction. Image reprinted from reference [69].

1.9 Why must electrochemical CO_2 reduction be assessed at commercially relevant conditions?

For its commercialization, future devices must demonstrate stable long-term operation (> 20000 hours) at substantial current densities (> 200 $mA \cdot cm^{-2}$) [58, 70]. Currently, studies are primarily conducted on the fundamental scale, which aims to find the optimal catalyst; however, it is unknown how representative these results are when examining at industrially relevant conditions, and ordinarily, such trends do not translate in a reciprocal manner [16, 69].

Various experiments, transport phenomena, and DFT modeling have demonstrated how local reactions may vary with the current density. This significantly impacts a catalyst's surface reactions when applied to industrial conditions since its activity depends on its surrounding environment as much as its physical inherent catalyst properties [11]. For example, when operating at low current densities, CO_2 is rapidly depleted by a combination of diffusion restrictions and buffer capacity imposed by the bulk electrolyte, favoring HER over CO_2R [40]. Conversely, at higher current densities (>100 mA $\cdot$ cm^{-2}), the local pH (lower buffer capacity) will increase rapidly, enhancing the activity of CO_2R and reducing the overpotential for C_2+ products. However, it is essential to consider that performing at such conditions could affect mass transport and decrease local CO_2 concentration due to side reactions associated with CO_2 acid-base equilibrium [58].

1.10 Current-state-of-the art for CO_2 electrolysis

The field of CO_2 electrolysis has advanced significantly over the past decade. CO selectivity has been enhanced using Ag NPs, which have a high intrinsic selectivity (FE_{CO} typically >90%) and are relatively inexpensive compared with Au NPs or single-atom catalysts. The current state-of-the-art was achieved by introducing GDEs in the MEA approach, which reached a j_{CO} of 1 A $\cdot$ cm^{-2} (90% FE_{CO}) at 1 bar CO_2 and 65°C in 0.1 M CsOH [23]. Similarly, substantial improvements in formic acid production have been achieved over the past decade through Sn or Pb catalysts attaining current densities up to 450 mA $\cdot$ cm^{-2} (selectivities around 97% over Pb [71], and 90% with Sn [72]).

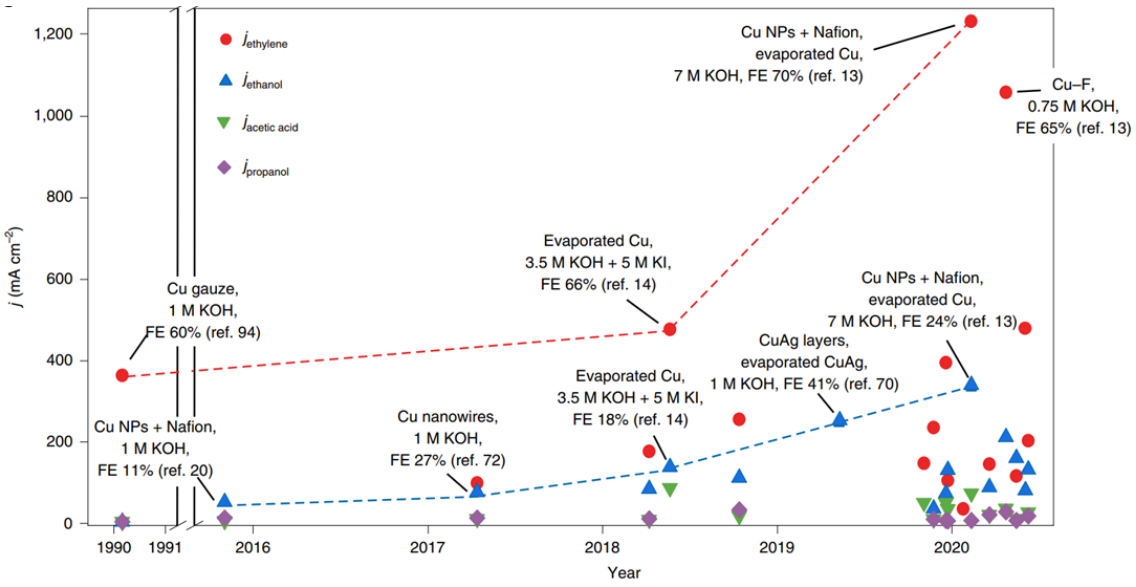

Figure 1.6: Metrics and progress in partial current densities for various electrochemical CO_2 reduction products over years. Image reprinted from reference [40].

Ethylene production has been improved through reactor and catalyst engineering. Currently, partial current densities are above $1A \cdot cm^{-2}$, and selectivity is above 60% at ambient conditions over Cu, exceeding the threshold for techno-economic analysis to consider the system profitable [63]. Similarly, present-day ethanol production can reach $337mA \cdot cm^{-2}$ at 24% FE_{EtOH} when using Cu nanoparticles in the presence of a Nafion binder [63]. Nevertheless, acetic acid and n-propanol have not witnessed the same improvements and continue to be produced with low selectivity, with partial current densities below 100 $mA \cdot cm^{-2}$ for acetic acid [73] and around 30 $mA \cdot cm^{-2}$ for n-propanol [74].

1.11 Overview and perspectives on CO_2 electrolysis

There is great potential for CO_2E to address current energy and climate problems while closing the carbon cycle. Using renewable electricity to drive single-step production processes, various liquid and gaseous fuels can be created from CO_2 in a decentralized system. Research has made impressive advances in developing efficient electrocatalysts for CO_2 conversion. However, further developments are needed from reactor components and process design perspectives to meet the performance goals for commercializing the CO_2 electrolyzer. Regarding the reactor, flow cell types for CO_2 electrolysis provide a promising alternative for practical applications.

Achieving efficient CO_2R should overcome limitations with design factors and catalyst materials, focusing on reducing cell potentials, boosting selectivity, and production rates. Similarly, it is crucial to examine operational parameters such as pH, temperature, pressure, and gas/liquid flow rates and to understand the structure–property relationship of electrode/electrolyte or membranes for CO_2R to tune the CO_2 conversion towards a desirable product.

Lastly, future developments should address complications specific to large-scale applications, such as excessive resistive heating from high amperage, integrating renewable power sources, or operating with low-purity and large quantities of CO_2 feed. Energy efficiency still needs to be improved for industrial operations to reduce operational costs and reach economic feasibility [67].

1.12 Thesis outline

In this thesis, I proposed multiple strategies to overcome some challenges in CO_2 electrolysis operating at industrially relevant conditions, improving the selectivity, activity (partial current density), and stability towards C_{2+} products.

In Chapter 2, I will summarize the current challenges in CO_2 electrolysis and suggest some strategies to address them. Chapter 3 outlines the experimental setup and methods used in this thesis project, including some preliminary results from the

selection of reaction components. Chapter 4 examines the effects of temperature on CO_2 electrolysis using zero-gap cells, including its impact on cathode activity, mass transport, product distribution, and the influence of the heating method. Detailed results of Chapter 4 and further studies on this topic can be found in the attached manuscript in the Appendix. Chapter 5 focuses on implementing tandem electrocatalysts prepared layer-by-layer in GDEs to improve C_{2+} selectivity, exploring the composition ratio, mass loading in the catalyst layer, and the role of the CO-selective layer in the overall performance.

Chapter 6 describes the synthesis, characterization, and testing of a new generation of AEMs for CO_2 electrolysis and investigates the membrane properties' influence on overall performance. Results from Chapter 6 have been published in a paper found in the Appendix of this work. Chapter 7 outlines additional strategies to enhance system stability, such as using a recycling loop, manipulating the back-pressure, and the effects of using ionomers for CO_2 electrolysis. Finally, Chapter 8 presents the general discussions and overall conclusions. This thesis also includes, at the end of each chapter (Chapters 4-8), a stability test, as it is one of the metrics I used to determine the viability of the strategy and also includes a small section where I describe my contribution to the chapter, together with the others from colleagues and partners.

Chapter 2

Challenges and strategies in CO_2 electrolysis at high current densities

2.1 Chapter Overview

As described in Chapter 1, CO_2 electrolysis is a feasible option to produce valuable chemicals and fuels, close the carbon cycle, and create a decentralized system. However, the process requires high current densities for scalability and high production rates, as well as a robust system for reducing operational and separation costs. Consequently, gas-fed CO_2 reactors are the most popular design for high current density operations because of their ability to overcome mass transfer limitations. Figure 2.1 shows a schematic of a gas-fed CO_2 electrolyzer with its components.

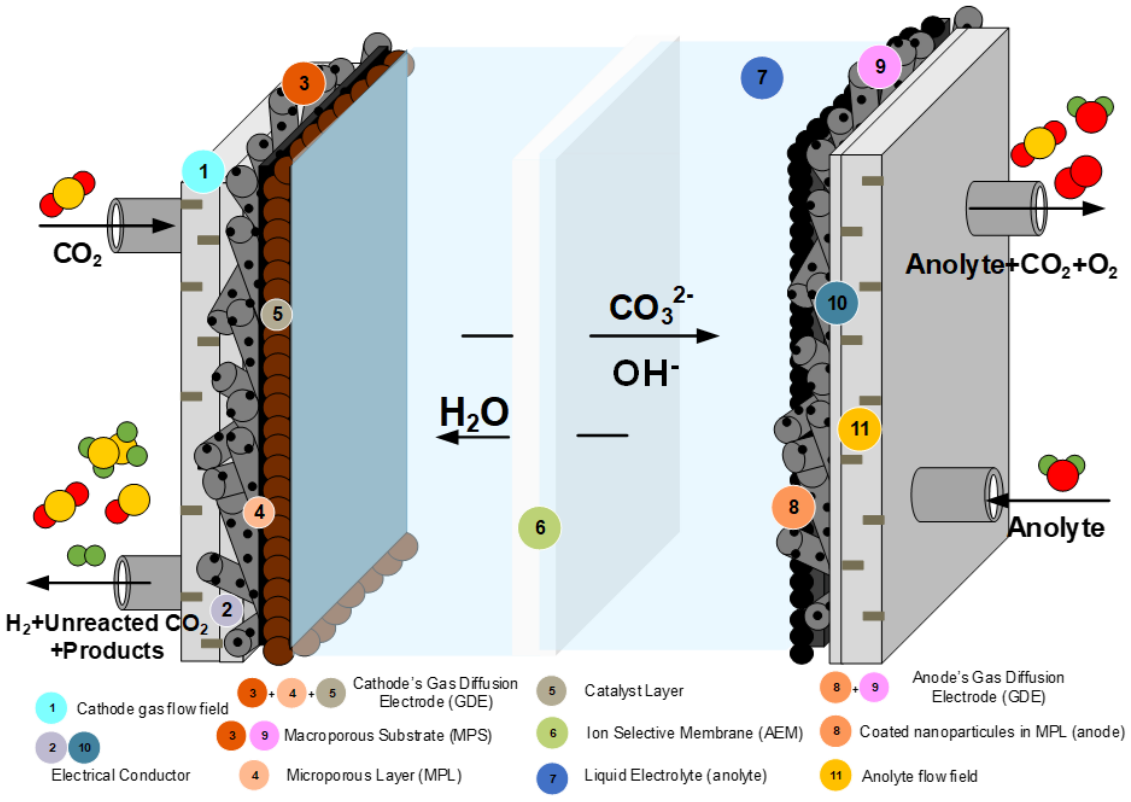

Figure 2.1: Scheme of a gas-fed CO_2R electrolyzer with all main components.

A comprehensive understanding of the role and effect of each reactor element is crucial to ensure reliable system operation since the performance of these systems is not entirely determined by the catalyst itself, but rather by several other factors that affect catalysis and are influenced by the electrolyzer components [75]. The aim of this section is to provide an overview of the major challenges of gas-fed CO_2 electrolyzers at industrially relevant conditions regarding the catalyst and the reactor components.

2.2 Current challenges in CO_2 electrolysis

Can GDLs and IEM from water electrolysis be translated to electrochemical CO_2 reduction applications?

a. Gas diffusion layers (GDLs): GDLs are widely used in the fuel cell, water electrolyzers, and chlor-alkali industries, providing a viable foundation for their use in CO_2 electrolysis [76]. However, GDLs designed for this application are not currently marketed, and those currently available may not be optimized for this purpose [77]. Additionally, there has been little evidence of long-term GDL performance without degradation or activity loss for carbon-based GDLs, nor have the effects of GDL properties on CO_2E (thickness, porosity, gas permeability, and hydrophobicity) been studied or modeled [40].

b. Anion exchange membranes and water management: the properties of commercially available and experimental AEMs have been reported in the context of fuel-cell and water electrolyzer conditions, but no well-defined metrics are currently established for CO_2R [78]. State-of-the-art in this field commonly use imidazolium groups or QA that tend to degrade at high-temperature operations and alkaline conditions, resulting in IEC losses and low durability [79]. Moreover, CO_2E operation has been restricted by a lack of ion-selective membranes with optimal mechanical and chemical properties, product crossover, and high interfacial and ohmic losses [80].

Low selectivity and catalyst poisoning

Rapid advances have been made in the electrochemical reduction of CO_2 over the past few decades. However, low selectivity and efficiency towards C_{2+} species remain challenging, owing to undesired H_2O reduction or high C-C coupling activation barriers [11, 75]. In the current CO_2R scenario, electrochemical systems have low activity, selectivity for desirable products, and insufficient durability due to poisoning by intermediates, byproducts, or impurities (experiments in this field have only been reported in hours-scale time) [81, 82]. Developing practical systems requires a significant increase in conversion rates and efficiency, which can be achieved by discovering and designing robust electrocatalysts, electrolytes and optimizing electrochemical reactors.

GDE Flooding

In CO_2 electrolysis, GDL failure due to flooding is a common problem caused by excessive water transport and cation migration to the cathode GDE, increasing its wettability and thus favoring HER [83]. Flooding may also be accelerated by pressure imbalance, enhanced loss of GDL hydrophobicity, or MPS degradation. Figure 2.2 shows an example of an operation in which my GDE flooded, and some pictures illustrate this mechanism.

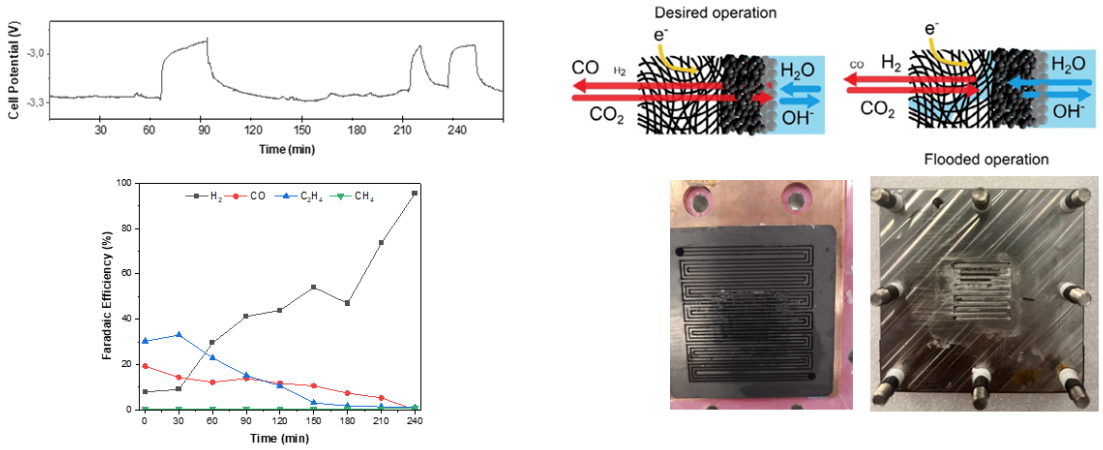

Figure 2.2: Example of a flooded experiment during my Ph.D., and schematic representation of flooded operation and salt precipitation in the flow field. Illustration of the flooding mechanism is adapted from Reference [84].

Carbonate salt formation

The formation of carbonate salts (from the electrolyte) is a problem that affects the CO_2E long-term durability and industrial applicability. CO_2 reacts with hydroxide ions, which leads to a high local concentration of carbonate and is further exacerbated by cationic species crossing from the anolyte (Eq. 2.1.2 and 2.2.2). This leads to the precipitation of carbonate salts throughout the gas diffusion electrode (GDE) and flow fields, reducing its activity and thus impeding the CO_2 diffusion through the substrate (mass-transport limitations) [85]. In a work related to this topic, I worked with my colleagues Dr.Asger Moss and Dr.Sahil Garg, investigating the phenomenon using in-operando techniques in CO_2 electrolysis at MEA configuration [86].

$$CO_2 + OH^- \longrightarrow HCO_3^- \ (pKa = 7.8) \tag{2.2.1}$$

$$HCO_3^- + OH^- \longrightarrow {CO_3}^{2-} + H_2O \ (pKa = 10.3) \tag{2.2.2}$$

Low stability and lack of long-term measurements

Most studies on CO_2R have mainly focused on enhancing the catalyst activity and

selectivity. Nonetheless, research on stability has not been given adequate attention, an essential requirement for the commercial application of CO_2RR devices [87]. State-of-the-art is around 4000 h from CO_2R to CO, far from the most optimistic predictions for CO_2R commercialization [88].

Product crossover

Product crossover through the AEM is more evident at high current densities (>100 $mA \cdot cm^{-2}$). In MEAs, for example, ethanol may be transported across the membrane due to electroosmotic drag and diffusion, leading up to 75% of the ethanol produced at the cathode passing through the AEM, which is then further oxidized at the anode, limiting the recoverable yield [89]. In general, negatively charged products (e.g., $HCOO^-$ or acetate) can cross the AEM, while the oxygenated products (e.g., acetone, ethanol, and n-propanol) may evaporate through the GDE into CO_2R off-gas, due to their volatility [90]. Multiple crossover mechanisms, especially in MEA systems, make liquid product quantification difficult and will increase separation costs when scaling up [91].

High cell overpotentials

Low energy efficiency is currently a major issue in CO_2 zero-gap electrolysis. The overpotential gap between cathodic and anodic reactions, and ohmic resistances make it difficult to achieve high current densities at low cell potentials [92]. The operational cell potential is a key performance indicator, as it will directly affect the CO_2R efficiency. Commercial units must be able to maintain current densities (> 200 $mA \cdot cm^{-2}$) while operating at E_{cell} of -3.0 V or less [77]. Unfortunately, most experiments at ambient conditions haven't fully met such requirements.

Low CO_2R utilization and single-pass conversion

Despite the high selectivity towards CO_2R-derived products, the operation is limited by a low CO_2R utilization and one-pass conversion, usually not exceeding 10% [93]. Additionally, when carbonate is the dominant charge carrier through the AEM, CO_2R conversion efficiency is limited to 50%. This low efficiency requires energy-demanding gas separation for CO_2R retrieval, making the operation too expensive (Jeng and Jiao estimated that 23% of the total operating cost would correspond to separate the mixture of gases from CO_2RR, assuming just 10% conversion [94]). Moving beyond this conversion limit is critical to progress in this area. Different strategies exist to overcome the low CO_2R conversion in current cell devices [95]. For example, the Stinton group proposed using a permeable CO_2R regeneration layer (PCRL), which provides an alkaline environment at the catalyst surface and enables local CO_2R regeneration. The approach has been shown to be efficient with 85% single pass conversion, a lower CO_2 crossover, and comparable cell potentials

compared to those obtained with MEAs [96]. In our group, we have proposed the creation of a recycling line after the electrochemical cell, following similar approaches used in industrial processes like biodiesel and some light-hydrocarbon production.

2.3 Strategies for CO_2R electrolysis at industrially relevant conditions

Various solutions could be implemented to overcome the abovementioned challenges, including optimizing operating parameters, developing selective electrocatalysts, and designing new reaction systems. In the following section, I propose strategies for addressing each current challenge in the reaction system.

Current Challenge: Low current density and high-cell overpotentials

Strategy I: Selecting the proper cell configuration, anode, GDL, and electrolyte

Among the different types of continuous CO_2 electrolyzers under development, vapor-fed electrolyzers are the most promising for large-scale CO_2R processes since this configuration feeds humidified CO_2 directly into the electrolyzer. Thus, I chose the MEA configuration because it also offered reduced interfacial and ohmic losses at lower cell potentials (except when I studied tandem catalysts, for which I implemented flow cells due to their advantages in liquid collections). Alternatively, studying the anode catalyst for CO_2R is also crucial since current materials are expensive, unstable, and affect the overall cell potential [92]. Despite not being a primary goal of my thesis, I have conducted preliminary experiments to examine how different anodes, GDLs, electrolyte concentrations, and CO_2 feeding rate affect the CO_2E. The results of such studies will be primarily used to guide the selection of the different reaction elements to be used in this thesis rather than for optimizing them (Appendix A.1.3).

Current Challenge: Low selectivity and activity toward C_{2+} products

Strategy II: Use of Tandem Catalysts

Using a tandem approach in CO_2R can help break linear scaling relationships (LSR), since Cu's overpotential and selectivity for the formation of C_{2+} products are limited by a trade-off between high CO production rates and high CO-CO coupling rates, which are determined by the LSR between the activation energy and intermediate binding energies. [97]. As described in Chapter 1, dimerization of adsorbed CO or coupling with its hydrogenated derivatives (e.g., *CHO) constitute critical steps toward C_{2+} products, so optimization of all key intermediates' binding strength over a single reactive site is challenging. Combining Cu with another CO-selective

(e.g., Zn, Ag, or Au) co-catalyst provides more segregated active sites, increases the CO coverage (key intermediate), and decreases CO_2RR overpotential by decoupling individual steps with a multi-component catalyst design [98].

The working principle of such a tandem catalyst consists of conducting the CO_2R on two different segregated active sites: CO_2 electroreduction is first converted to CO on CO-selective sites, followed by cascade dimerization and hydrogenation of CO on C_{2+} products on Cu-selective sites [99]. As reported in the literature, tandem catalysts, such as CuAg, CuZnO, Ag-Cu nanodimers, and mixed Cu nanoparticles with CO-selective catalysts (Au, Ag, ZnO, and Ni-N-C), show greater partial current density and Faradaic Efficiency (1-4 times greater) than bare Cu electrodes or alloys [100]. Wang et al. reported improved ethylene formation on CuO_x deposited on single-atom Ni-N-doped carbon, varying the CO concentration with different CO and CO_2R mixtures as reactants [101]. The Jaramillo group reported the formation of oxygenates at low overpotentials (enhancement of ethanol and n-propanol formation) on Au clusters deposited on Cu, and its modeling suggested the increase of the CO flux near-by the Cu surface [102].

A more straightforward approach for tandem catalysts involves preparing electrodes with two independent layers coated in the CL to improve local CO concentration and mass transfer. She et al. synthesized catalysts with two distinct layers (Ag, Au, or Ni-N-C with Cu), achieving a higher C_{2+} Faradaic Efficiency of 85% at 250 $mA \cdot cm^{-2}$ in tandem $Cu_{0.6}Ag_{0.4}$ compared to bare-Cu [98]. Other studies using ZnO as a CO-selective layer has proven an enhanced CO utilization, leading to Faradaic Efficiency and partial current density by 1.2-3.4 times compared to Cu electrodes and 1.3-1.8 times higher than mixed electrodes in the same catalyst layer [97].

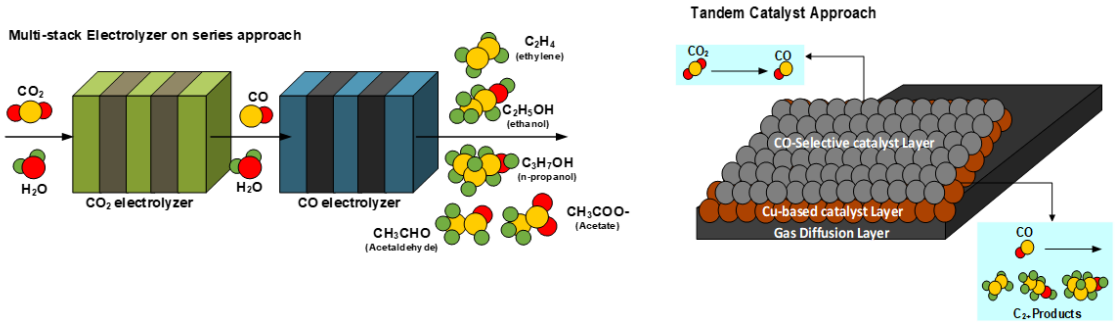

Figure 2.3: Strategy to enhance the selectivity towards C_{2+} products from CO_2RE. a). Two step multistack electrolyzer (CO_2R to CO) and (CO to C_{2+} products) in series. b). Synthesis of tandem catalysts by layer-by-layer approach following the multi-stack configuration.

To properly fabricated such tandem catalysis, the CO-selective site must be adjacent to the Cu active site, which requires deliberate synthesis of tandem catalysts to control CO_2/CO diffusion and CO* surface coverage. Using "layer-by-layer" tandem

electrodes with two CLs over GDL provides two-sequential pathways, controlling the gas transport and acting as an analog to two reactor systems in cascade [98]. In this method, the top layer acts as a CO-supplier, where CO_2R is reduced to CO. In contrast, the bottom layer serves as a C_{2+} active site, where CO intermediates diffuse and are further reduced to form C_{2+} products since the value of CO self-diffusion coefficient in porous electrodes is higher than in aqueous electrolytes [100].

In Chapter 5, I explored the tandem catalysts through the layer-by-layer approach (using Ag, Au, or Zn as co-catalysts) to maximize the CO utilization and partial current densities of C_{2+} products compared to Cu-bare catalysts. A preliminary study examined fabrication methods, mass loading, and catalyst layers. Moreover, tandem electrodes were synthesized by varying their composition ratios and mass loading to understand the principle of tandem electrodes and the role of the CO-selective catalyst. I synthesized my electrodes using this method, as it involves the simple fabrication of two distinct catalyst layers coated on a substrate without requiring a complex chemical synthesis, making them easier to fabricate and manufacture at an industrial scale. Additionally, this tandem approach makes it easier to decouple the co-catalyst effect, owing to the increased CO local flux and independent active sites for the different CO_2RR [97].

Current Challenge: Limited stability, high overpotentials, and product crossover

Strategy III: Tuning the reaction conditions through temperature and pressure

Temperature

Although temperature plays a significant role in the catalytic environment and performance, most studies of CO_2R have been conducted at room temperature. In large-scale systems, operating CO_2R electrolyzers at room temperature may prove counterproductive since higher temperatures might be needed to overcome the overpotentials and resistance losses or handling high-temperature CO_2 emissions that can result from industrial operations (e.g., thermocatalytic processes). Temperature studies can also provide information about electrochemical steps in CO_2R and identify the optimal conditions for enhancing activity and selectivity.

Even though temperature affects the intrinsic behavior of CO_2R (higher activity at low cell potentials), few researchers have focused on performing experiments under elevated temperatures due to the complex interactions between different factors and temperature, which have, thus far, prevented any distinct trends for CO_2R. Initially, temperature affects CO_2R solubility, and diffusion coefficients, influencing mass transport [16]. Furthermore, it alters the reaction environment, equilibrium potentials, and intermediate adsorption equilibria, varying charge transfer, and

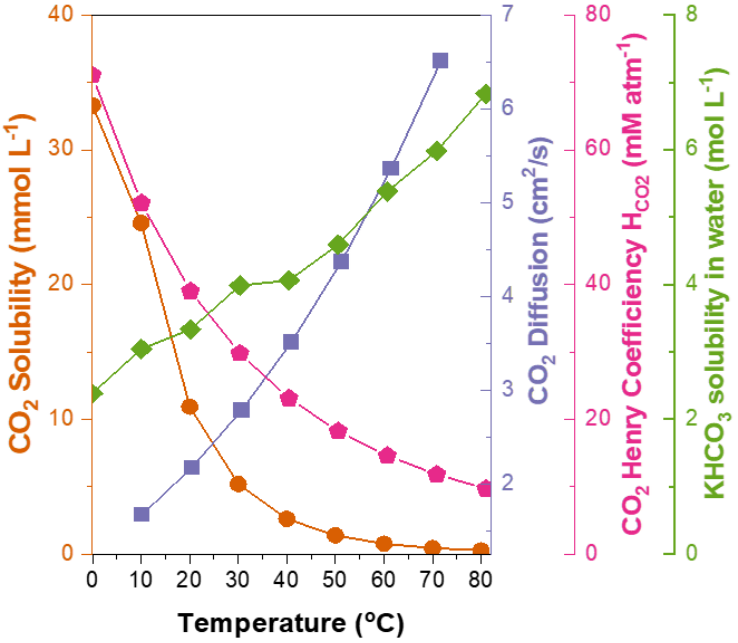

Figure 2.4: Transport and kinetics factor's temperature dependency on CO_2RR (CO_2R solubility, CO_2R diffusion, salt solubility, and Henry's constant).

homogeneous reaction rates [103]. Moreover, it enhances ionic and membrane conductivity by lowering ohmic and mass-transport overpotentials and modifying water transport or product crossover by enhancing evaporation and electroosmotic drag mechanisms [104]. Figure 2.4 shows the influence of temperature in some transport parameters for CO_2R, proving its trade-off during the operation.

In Chapter 4, I presented the study of the effect of temperature on CO_2 electrolysis in Cu-based GDEs in MEA-cells. According to the experimental results, operating at elevated temperatures improved activity and selectivity towards CO_2-derived products, lowered product crossover, and enhanced stability by suppressing hydrogen evolution (HER). Moreover, I discussed the importance of stable-AEMs for this operation and the role of the heating methods in defining different selectivity trends. As part of this investigation, a robust system for monitoring and controlling all system components has been developed, in addition to guidelines for reproducible electrocatalytic temperature measurements.

Pressure

The operating pressure plays a unique role in CO_2R as its effects are threefold: the capillary effect on electrode flooding, improved contact between the electrolyzer components, and an increase in the CO_2 concentration at the gas phase (CO_2 surface coverage) [11]. I evaluated the pressure effects in Chapter 7 by manipulating the electrolyzer's back pressure. The back pressure was varied from 0-1000 mbar to control CO_2R coverage on the electrode surface, minimize flooding, and control product selectivity. Further, I integrated the effects of partial pressure and tem-

perature, as those two could enhance CO_2R transport to the surface and enhance electrode stability.

Current Challenge: Insufficient water management in CO_2 electrolysis

Strategy IV: Design of anion-exchange membranes suitable for CO_2 electrolyzers

The choice of IEM dictates the reaction environments and defines the ion-driven force across the system [80]. Based on the charge and distribution of fixed ionic groups, membranes can be classified as cation exchange membranes (CEMs), anion exchange membranes (AEMs), or bipolar membranes (BPMs). The primary charge carrier for CEMs are H^+ or alkali cations, while AEMs predominantly conducts OH^- or carbonate ions (HCO_3^- and CO_3^{2-}). BPMs combine an anion exchange layer (AEL) and cation exchange layers (CEL), jointed to an interfacial catalyst layer (CL). They can operate in reverse and forward bias, depending on the membrane orientation. Under reverse bias operation, the CEL faces the cathode, and ions are formed via water dissociation, driving the H^+ transport to the cathode and the OH^- to the anode. In forward bias, the AEL faces the cathode, and the ions are transported toward the recombination interface [105] (Figure 2.5).

In CO_2E, the membrane might affect the catalytic selectivity if the catalyst is directly in contact with it (MEA configuration), as membranes play a unique role in ion/water transport, modifying the local environment, especially in terms of water management, which affects pH and mass transfer properties on CO_2R. [92]. The water net flux across the membrane is governed mainly by diffusion, hydraulic permeation (or back-convection), and electroosmotic drag [106]. These mechanisms are influenced by the cathode's water consumption and anionic species' hydration shells, so membranes for CO_2R applications should be optimized for proper water management [80].

Parameters like the water uptake (WU) or the hydration number (λ) are linked to water transport and can modulate product crossover, water content, and ion mobility [107]. The ion exchange capacity (IEC) is a valuable metric for assessing membrane performance and correlates with ionic conductivity. Although a higher value is preferable, too many cationic groups in the polymeric backbone can increase the WU, causing swelling and decreasing charge carriers' concentration, thereby reducing overall conductivity [108]. Generally, AEMs for CO_2R reduction should have a high IEC, ionic conductivity, moderate WU, high mechanical strength, low gas permeability, and good stability in alkaline media[78]. A growing interest has been oriented on membranes with stable backbones and functionalized groups to improve their transport properties and stability for CO_2 electrolyzers.

The mechanical and chemical properties of AEMs are known to be influenced by ionomer chemistry (cationic groups and polymeric backbone). Using stable polymer

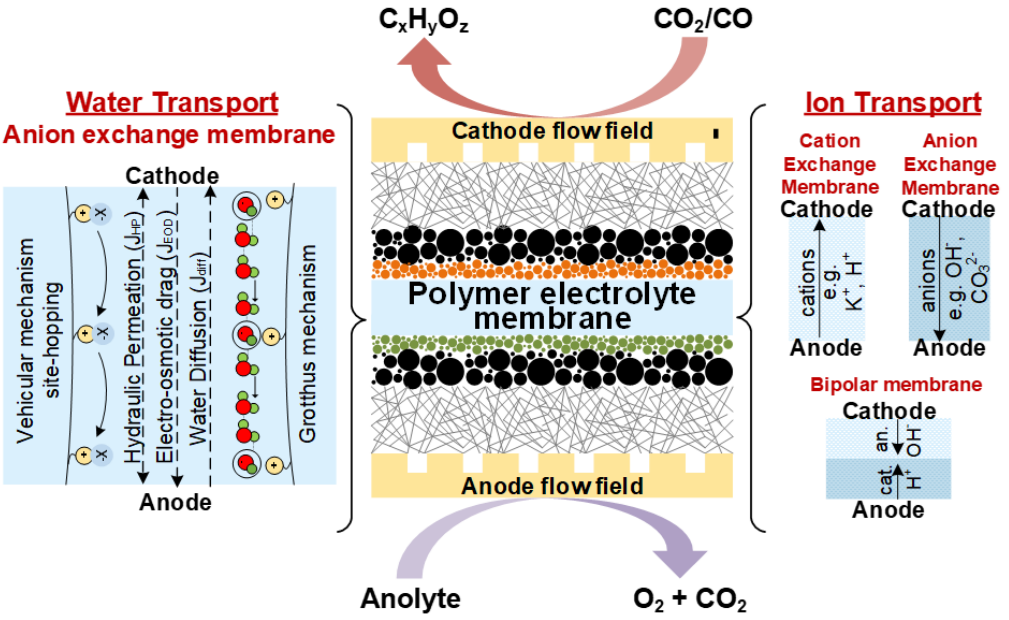

Figure 2.5: Schematic of a typical (a) zero-gap for CO_2 electrolysis, including all the water and ionic transport mechanisms in an anion-exchange membrane (AEM). Image adapted from our published paper: [80].

backbones (e.g., aromatic groups), the AEM's stability is dictated by its cationic group, meaning that different ionic groups will affect the chemical stability and ionic conductivity [79]. For example, membranes functionalized with trimethylamine (TMA) groups have shown improved thermo-chemical stability for water and CO_2R electrolyzers, partly due to the absence of longer subgroups, which might suppress the degradation through the Hoffmann mechanism [108]. Conversely, AEMs based on imidazolium-functional groups have high OH^- conductivity, and IEC [109]. In addition, cycloaliphatic QAs (e.g., N-methylpiperidinium) have been identified as alkali-stable, attributed to the minimum ring strain and conformation restrictions imposed by the cyclic structure [110].

Developing new AEMs should overcome current operational challenges and match the requirements for CO_2R electrolyzers under industrially-relevant conditions. Such fabrication should focus on decreasing the AEM ohmic losses and improving chemical and mechanical stability. The ratio of carbonate/hydroxyl transfer and cation permeation to the cathode are also functions of the AEM structure, so optimizing the membrane design can also favor the hydroxyl transfer and mitigate cationic build-up, and salt precipitation at the cathode [78]. In a collaboration with the University of Surrey, we have proposed a new generation of radiation-grafted AEMs with heterocyclic QA-headgroups that may be suitable for CO_2R due to their unique ionomeric structure, enhanced transport, and mechanical properties [111].

Chapters 3 and 6 describe in detail the fabrication and testing of these AEMs for CO_2R applications by co-grafting vinylbenzyl chloride (VBC) monomer onto

electron-beam activated ethylene-co-tetrafluoroethylene (ETFE) polymer films and amination with triethylamine (TMA), N-methylpyrrolidine (MPY), or N-methyl piperidine (MPIP). These covalently-bonded VBC-grafted films with tailored cationic groups are expected to provide improved chemical stability, ionic transport, high ion-exchange capacities, moderate water uptake, high ionic conductivity, reduced product crossover, and stability in alkaline conditions.

Current Challenge: Poor gas transport and accelerated flooding

Strategy V: Use of ionomers for CO_2R electrolysis

The use of ionomers in CO_2R has been proposed to immobilize the catalyst and control the reaction microenvironment. As these ionomers are confined to the catalyst layer, interfacial interactions between these species and the electrocatalysts are expected [112]. The primary objective of ionomers for CO_2R is to provide a structure with different hydrophobic/hydrophilic domains to enhance the gas and ion transport over the catalyst surface [63]. The presence of hydrophobic functionalities is expected to enhance gas transport, while the hydrophilic domains should improve ionic conductivity, chemical stability, and water transport within the system, preventing excessive water permeation in the GDE [113].

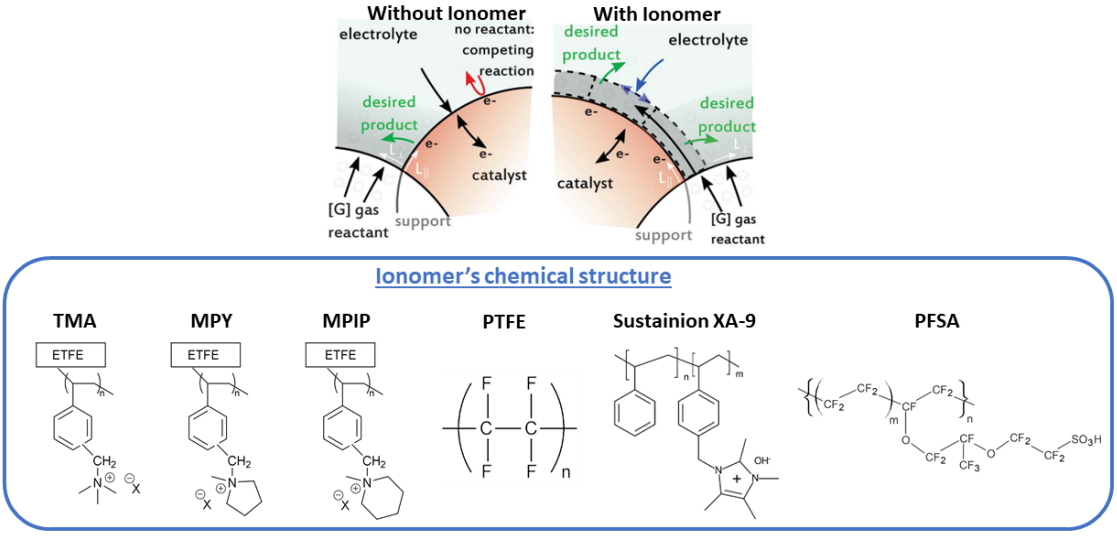

Figure 2.6: Schematic Representation of the effect of adding ionomers in the CL for CO_2R electrolysis and all the different chemistries used in this thesis work following such approach. Image adapted from Reference [63].

The role of ionomers in CO_2R has typically been empirical and contradictory [110]. Therefore, it is crucial to systematically understand how adding ionomer layers on the electrocatalyst impacts the selectivity and activity of CO_2R. The effect of ionomer chemistry on structure-property relationships will be revealed by understanding its role in gas and ion transport at the electrode-electrolyte interface

and tailoring the reaction microenvironment. The Bell and Stinton groups have taken advantage of the effects of ionomers on local microenvironments to enhance C_{2+} product selectivity and CO_2R activity, setting the state-of-the-art on this field through this approach [113, 63].

As part of Chapter 7, investigations of CO_2R over Cu-GDEs coated with different ionomers are presented with an assessment of the structure-property relationship of the ionomer films. I investigated how different anion-exchange ionomers (AEIs) and cationic-exchange ionomers (CEIs) might influence the overall performance through effects on loading, product distribution, and modifying the local reaction environment, leading to a stable CO_2R operation (>50 hours).

Current Challenge: Low CO_2R utilization and single-pass conversion

Strategy VI: Introduction of recycling line

As mentioned before, using a recycling line in the reaction system could improve the CO_2R conversion rate compared to one-pass operation by the selective consumption of unreacted CO_2. Modeling this scenario showed that the loop's inclusion in the CO_2R conversion process outperformed the single-pass operation. The recycling loop is expected to operate at lower overpotentials, thereby recycling the produced CO and other products, which can then be further reduced towards ethanol, thereby overcoming possible overpotential limitations CO_2R towards C_{2+} products. However, the experimental implementation of the recycling line might be limited by GDEs flooding, catalyst deactivation, and selectivity towards in-side reactions such as HER or carbonate formation.

The results of the recycling loop are discussed in Chapter 7, including single-pass studies, the influence of the reflux ratio, and the effects of recycling on product selectivity. The CO_2 conversion in the experiments can generally be expressed as follows:

$$X_{CO2} = \frac{n_{CO2,in} - n_{CO2,out}}{n_{CO2,in}} \tag{2.3.1}$$

Where n($CO_{2,in}$) is the molar flow of the inlet CO_2, n($CO_{2,out}$) is the outlet flow of the unreacted CO_2, n(CO_{out}) is the molar flow rate of CO in the gas effluent measured by the flowmeter and GC, and X_{CO2} is the CO_2 conversion. To estimate CO_2 conversion more accurately, this equation should include all generated products and account for carbonate species during neutralization reactions.

2.4 Aim of this thesis

In this thesis, I explore strategies for addressing common challenges in CO_2 electrolysis at industrially relevant conditions, especially those related to the cathode and AEMs. The data reported in this study follow established metrics in this field and are presented in terms of Faradaic Efficiency, cell potential, current density, and stability. At the end of the thesis, I will briefly describe the energy efficiency parameter and compare it to recent studies since it was not the goal of my work to break the current state of the art regarding activity and selectivity.

For all experimental details, I have included the chemical purity, the synthesis methods, pretreatment and preconditioning procedures, and electrochemical operating conditions as they influence the catalyst's performance. In addition, by using commercial MEA cells for zero-gap experiments, I could have consistency between experiments and comparability across different laboratories (especially working on an EU project), which could benefit the translation of knowledge gained.

With commercial CO_2R electrolyzers requiring a high lifespan to be economically viable, it is tough to determine whether my suggested approaches are genuinely stable by operating short-term. Thus, I conducted multiple stability tests for at least 10 hours (or more, if possible) to detect any issues that may arise during the operation of the device and to gain a better understanding of its stability, including either one strategy (Chapter 4-7) or multiple strategies (Chapter 7-8).

Chapter 3

Experimental Methods

3.1 Chapter Overview

This chapter describes sample preparation, experimental setups, electrochemical methods, characterization techniques, and data analysis methods used in this thesis. Some of these methods are standard and have been previously described in more detail in the literature. Therefore, I will provide an overview of such techniques and describe the reason for performing such measurements and the information I obtained from each method.

3.2 Electrochemical Cells

As stated in Chapter 2, most of the experimental results for this thesis were conducted in zero-gap MEA CO_2 electrolyzers (Chapters 4- 7). However, a catholyte flow cell was also used in some experiments in Chapter 5. In the following section, I will explain the basis of two- and three-compartment cells.

3.2.1 Electrochemical two-electrode cells (zero-gap MEA)

Electrochemistry is a branch that studies chemical reactions involving electron and charge transfer. Its application requires at least an electrochemical cell with two electrodes: a cathode (where the reduction reactions take place) and an anode (where the oxidation occurs) connected to a power source (potentiostat). The electrons move through an external circuit that connects both electrodes, and the ions are conducted through the electrolyte. The electrode on which the reaction of interest occurs is the working electrode (WE), while the other electrode is the counter electrode (CE).

Zero-gap CO_2 electrolyzers are standard two-electrode cells consisting of both anodic and cathodic compartments, including flow plates, current collectors, gaskets, and electrodes (as shown in Chapter 2). The cathode is fixed directly with the membrane, forming the membrane-electrode assembly structure (MEA). This approach improved the operation at higher current densities with low cell resistances. However, it can only control the WE electrode potential due to the absence of RE, measuring just the cell potentials [114].

For this configuration, I have implemented two different designs (but with the same

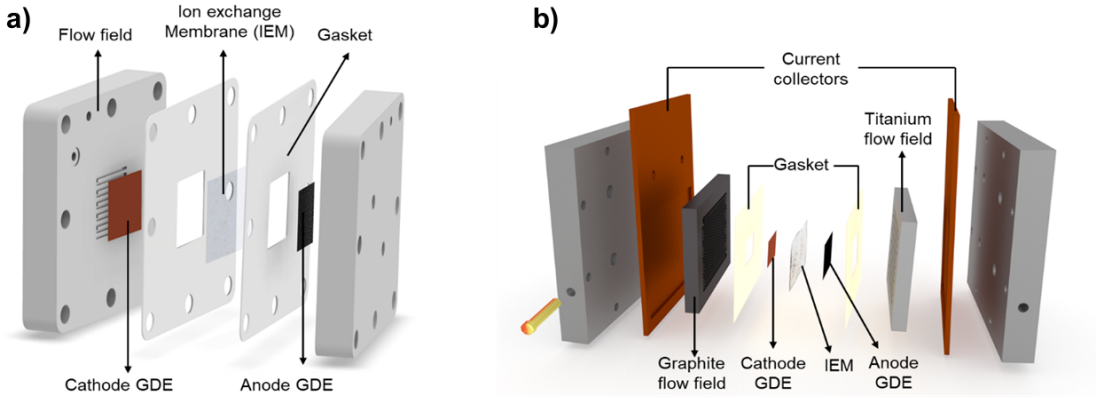

Figure 3.1: Illustration of the common MEA-type cells used in this thesis work a). Commercial MEA-electrolyzer and b). Modified CO_2 electrolyzer in MEA redesigned here at DTU.

operation principle). The first is a standardized commercial cell reactor, inspired by the Dioxide Materials zero-gap electrochemical cell, with minor modifications in the flow fields (Figure 3.1a). The work presented in this thesis used this type of commercial MEA cell (unless otherwise specified). Nevertheless, preliminary studies of the recycling loop were conducted using a second type of MEA cell inspired by the liquid-gas fuel cell from Scribner Associates. This electrolyzer is equipped with copper current collectors, titanium and graphite flow fields for the anode and the cathode (Figure 3.1b).

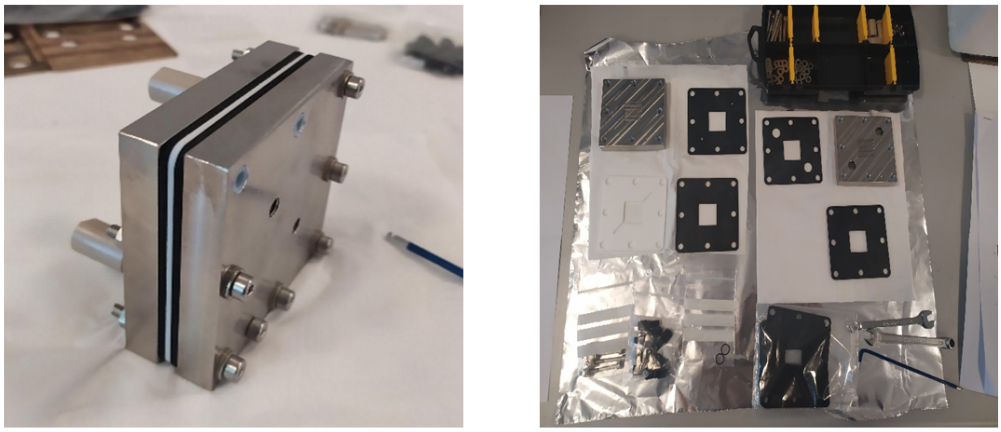

Figure 3.2: Images of the assembled cell and all the required cell components

Cell assembly

The assembly of MEA cells for my experiments consisted of loading a fresh membrane (area: 7.4 cm^2) inserted between a cathode (area: 2.25 cm^2) and anode (area: 4 cm^2). PTFE gaskets further sandwiched the MEA device, which helped prevent electrolyte leakage and also prevented potential short-circuiting. The system was mechanically pressed, using cell bolts fastened with a torque of 3 $N \cdot m$ to guarantee sufficient compression. Furthermore, CO_2 feed in the cathode compartment must

be humidified to avoid AEM dehydration. Also, electrodes were prepared as GDEs, as it facilitates the CO_2 transport to the CL with low mass-transfer resistances.

3.2.2 Electrochemical three-electrode setup (catholyte flow-cells)

In a three-electrode setup, it is possible to quantify the WE's potential using a reference electrode (RE) to measure the potential between both electrodes. A reference electrode (RE) is an electrode where a well-known electrochemical occurs at a stable potential and is used to compare the WE potential. At this configuration, the potential is measured between the WE and RE, while the current is drawn between the WE and the CE. For my experiments, Ag/AgCl was used as RE (making the further conversion to the RHE scale). Figure 3.3 shows a scheme of two-and three cell compartments.

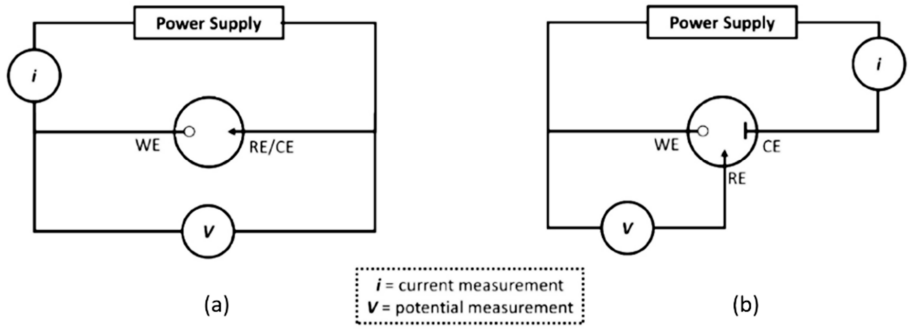

Figure 3.3: Scheme of electrochemical cells with a).two-electrode, and b). three-electrode configuration. Image adapted from Reference [115]

My experiments using CO_2 electrolyzers in flow cells approach were conducted using different electrochemical cells. First, the described in Figure 3.1a was adapted by adding a catholyte flow channel between the flow field and the IEM. I designed and adopted the flow channel with the help of Dr.Asger Moss and Dr.Erdem Irtem from TU Delft, optimizing the liquid/gas transport in the system, avoiding excessive liquid penetration through the GDE and gas percolation through the catholyte. The other implemented cell is referred as the "Teflon flow cell," a design adopted from the Burdyny/Smith group at TU Delft (partners from my EU project) and slightly modified by Dr. Ming Ma at DTU (Figure 3.4) [116]. This cell design was implemented in some Chapter 5 experiments, benefiting from the facilitated liquid product collection.

Comparison between different cells and approaches has been previously conducted to evaluate those effects in the CO_2E performance (Appendix A.3). It isn't my intention with those experiments to establish which configuration is better, as both possess different advantages and disadvantages, but rather to show the trends obtained regarding cell potential, stability, and product selectivity.

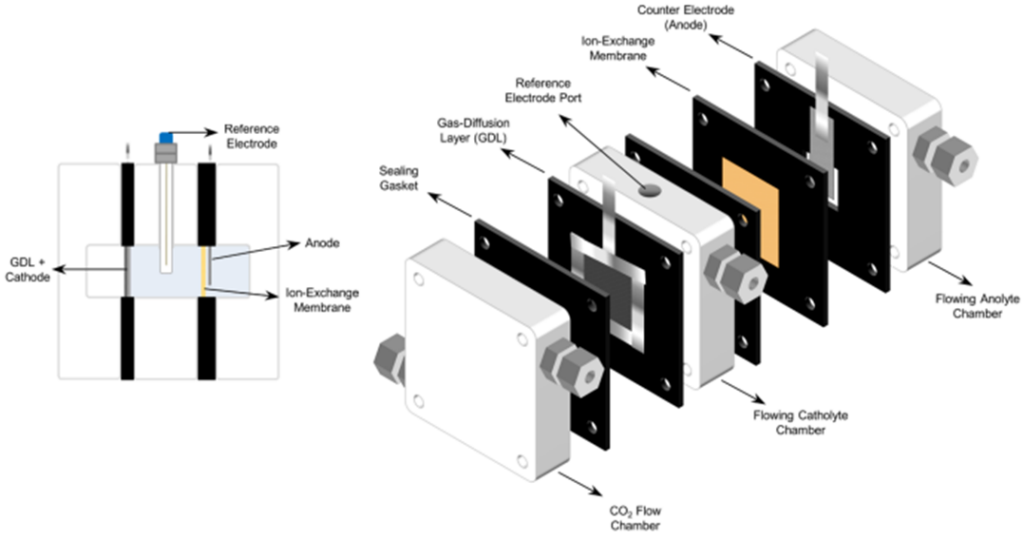

Figure 3.4: Illustration of the flow cell with catholyte. a). Side profile, and b). schematic representation of all individual cell components. Image adapted from Reference [116]

3.3 Electrode Preparation

3.3.1 Preparation of Cu-GDEs

I considered two approaches for electrode synthesis: a 2D-thin film and a 3D-nanoparticulate layer. Appendix A describes the materials and chemicals needed for electrode and membrane preparation.

Metal sputtering in commercial GDLs

2D structures (prepared by physical vapor deposition (PVD) methods like sputtering) improve the activity and selectivity by maintaining a uniform local reaction environment because the catalyst grows on the substrate, as opposed to coating commercial nanoparticles. [60]. Cu, Zn (as ZnO), Ag, and Au electrodes were prepared using this method. Those GDEs were prepared by sputtering a 100-300 nm layer of the specific metal onto different commercial GDLs in a vacuum environment (10^{-6} torr) at a deposition rate of 1 $\text{Å} \cdot \text{s}^{-}1$ under 10 sccm Ar, the total pressure of 2 mTorr and RT. The commercial GDL Sigracet 39BB from the company SGL was used in all the experiments as it is the most common substrate used in CO_2 electrolysis studies and facilitates comparison with other experiments. Other experiments, where I sputtered Cu into different commercial GDLs, were conducted to select the best substrate for this thesis based on the physical and mechanical properties of the GDLs (Appendix A.1.3).

- Metal co-sputtering in commercial GDLs: The tandem Cu/[M] (M: Ag, Au, ZnO) were prepared using the same settings on single-metal but sputtered simultaneously, controlling the metal compositions but keeping the CL thickness the same value.

- Sputtering of independent layers into commercial GDLs: As part of the tandem catalyst studies (Chapter 5), two independent layers were sputtered using the layer-by-layer deposition, modifying the thickness of each different layer but keeping the total catalyst layer thickness constant.

Coating nanoparticles (NPs) in commercial GDLs

The bare electrodes using this approach were prepared using drop-casting and spray coating (airbrush) techniques. Catalysts ink consisted of a mixed solution of the Cu, Ag, ZnO, or Au nanoparticles (20 mg of the powder), Nafion ionomer solution as a binder (80 µL), and the defined water:isopropanol solution solvent (1-3 mL), and then sonicated for 1 hour. Next, the catalyst was airbrushed or drop-casted onto the substrate uniformly until the desired loading was reached and finally dried at 80-105°C for 24 hours.

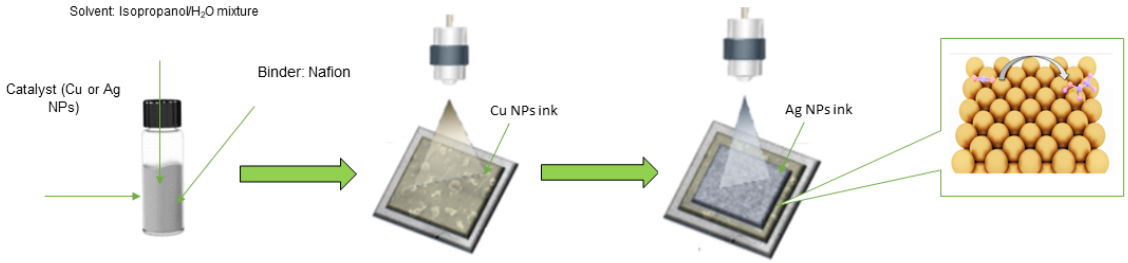

Figure 3.5: Schematic representation of the electrode synthesis with NPs through air-brushing of tandem catalyst following layer-by-layer approach)

On the other hand, the tandem catalysts using this synthesis approach were fabricated by sequentially spraying Cu and Ag (ZnO or Au) nanoparticles on the carbon paper using the same ink suspension method described previously, and the amount of catalyst of the respective ink-controlled the loading. Two types of tandem electrodes were prepared, where the first consisted of keeping the total mass loading at 1 $mg \cdot cm^{-2}$ and varying the Cu, Ag, and Au loadings from 0.1-0.9 $mg \cdot cm^{-2}$ using the layer-by-layer deposition. An alternate method uses a mixed solution to deposit both metals in one layer by controlling the mass loading of each metal using the electrode's weight and area. A comparison of these different methods is described in more detail in Chapter 5, where I evaluated the effect of the preparation method and the metal loading on the CO_2E performance.

Cu-electrodes for ATR-SEIRAS experiments

Experiments for ATR-SEIRAS (Chapter 4) required a different preparation method through a preliminary chemical deposition of Au thin film (60 nm) in a silicon wafer and further sputtering a 100 nm Cu layer. Dr. Wanyu Deng did the synthesis of these electrodes here at DTU.

Au film electrodes were deposited directly on a Si prism used in situ for ATR-

SEIRAS, following the proposed methodology by Miyake et al [117]. Initially, the Si substrate was polished using a polishing machine (YUZHOU PG-2B, 650 r/min) with 0.05 m Al_2O_3 polishing powder for 10 minutes and further immersed in Piranha solution (3:1 volume ratio H_2SO_4:H_2O_2) for 1 hour to clean the organic contaminants before deposition. Then, to improve the adhesion of Au film, the film was immersed in the reflecting plane of the crystal in 40% NH4F solution for approximately two minutes to remove the oxide layer and generate a hydrogen-terminated surface. The reflecting plane of Si crystal was then immersed in a mixture of 1 mL of 2% HF and 3 mL of Au plating solution containing 0.1050 g NaOH, 0.2276 g $HAuCl_4$, 0.1337 g NH_4Cl, 0.9845 g Na_2SO_3, and 0.6205 g $Na_2SO_3 \cdot 5H_2O$ at a constant volume of 100 mL for 4 minutes at 50°C. Finally, the Si crystal was cleaned with pure water before the Cu deposition.

3.3.2 Ag-electrocatalyst

Experiments from Chapter 6 (AEMs testing) and Chapter 7 (introduction of the recycling line) were conducted using a commercial Ag-porous membrane. The commercial Ag porous membrane with a nominal pore size of 1.2 µm (purity 99.97%) was purchased from Sterlitech Inc.

3.3.3 Electrodes prepared with ionomer layer

Different types of AEIs (MPIP, MPY, TMA, TMIMID from the University of Surrey), Sustainion XI-9 (Dioxide Materials, alkaline ionomer 5% in ethanol), and CEIs (perfluorinated ion-exchange resin and PTFE) were used to cast onto Cu-GDEs. To prepare stock solutions for casting onto the substrate, the ionomer solutions were diluted with isopropyl alcohol (Sigma-Aldrich, 99.9%) and a water mixture. The stock solutions were then drop-cast onto the electrode at concentrations at 5-50 $\mu g_{ionomer} \cdot cm^{-2}$ before being dried at room temperature for 1 hour.

3.4 AEM synthesis

The synthesis of the AEMs was conducted by Dr. Terry Wilson from the University of Surrey, a partner from SelectCO2 under the supervision of Prof. John Varcoe. A detailed description of the synthesis method with all the intermediate steps is found in the paper attached to this manuscript [79].

The RG-AEMs were synthesized via the radiation-grafting peroxidation method. ETFE was selected as a substrate rather than LDPE and HDPE, as quick screening CO_2E cell tests showed that ETFE-based RG-AEMs avoid to a major extent, the H_2 generation. The VBC was grafted onto electron-beamed ETFE films (40 kGy total doses, 4.5 MeV electron beam) by immersing them in N_2 purged (O_2 free) aqueous dispersion of VBC (5 %vol) in 1-octyl-2-pyrrolidone (1 %vol) and heating

at 70°C for 24 h. After thorough washing in toluene/acetone and drying, batches of RG-membrane [designated ETFE-g-p(VBC)] were obtained with a degree of grafting (dog) = 79 % for the variant made from 25 µm thick ETFE and a dog = 68 % for the variant made from 50 µm thick ETFE. ETFE-g-p(VBC) samples were then aminated separately with either the aqueous trimethylamine (45 %mass, room temperature, 24 h), N-methylpyrrolidine (50 %vol, 60°C, 18 h), or N-methylpiperidine (15 %vol, 60°C, 18 h), yielding the desired RG-AEMs.

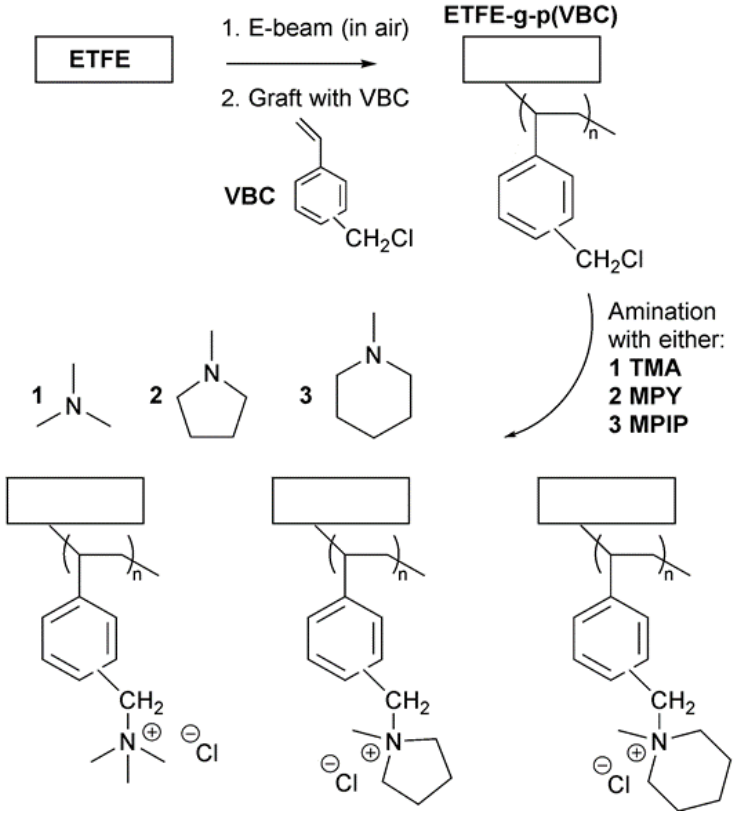

Figure 3.6: An outline of the synthesis of the RG-AEMs supplied with the three different amination agents. The Cl anions can be easily exchanged for any other anion desired (e.g., CO_3^{2-}, HCO_3^-) by multiple (at least 3 ×) submersions in aqueous salt solutions (1.0 M). Image adapted from my Manuscript found in Reference [79]

After the amination, the RG-AEMs were washed multiple times in UPW and soaked in aqueous NaCl (1 M) solutions for 1 h (with at least three solution changes during this period) to ensure the pure Cl^- anion form. After thoroughly washing with UPW for at least 1 h (with multiple changes in UPW) to remove all excess co- and counter-ions, they were stored in UPW until use. The Cl^- form RG-AEMs can be converted into the predominant HCO_3^- form (with trace amounts of CO_3^{2-} anions) by immersion in aqueous $KHCO_3$ (1 M) for 1 h followed by thorough washing with UPW (to remove excess co- and counter-ions).

Further AEMs were developed by tuning their mechanical properties by modifying their chemistry. Those membranes were developed from RG-MPIP with various ion-

exchange capacities (IEC): MPIP-1.7 and MPIP-2.2, alongside a batch of MPIP-based RG-AEM made with a standard amination process (using an excess of N-methylpiperidine) and a new amination process (with controlled 1.1 %mol excess). Cross-linked versions by introducing N,N,N',N'-tetramethylhexane-1,6–diamine at 5 and 10 mol% content (TMHDA) were also manufactured.

3.5 Electrochemical setup

Experiments at RT

My electrochemical system consisted of mass flow controllers, the cell electrolyzer, two electrolyte storage tanks, a pumping system, a water trap for the CO_2 off-gas, the in-situ gas chromatography (GC), and an ex-situ HPLC system. At MEA, I could avoid using a catholyte, but in principle, the system is versatile to be adapted for flow cells (by adding another catholyte pump). A volumetric flow controller sets the CO_2 feeding rate in the cathode with a defined flow rate (20-50 mL $\cdot$ min^{-}1, MKS, or Red-y from Voegtlin). The catholyte and/or the anolyte were fed with 0.1-1 M electrolyte ($KHCO_3$ or $CsHCO_3$ and recirculated continuously at an approximated 40 mL $\cdot$ min^{-}1 rate using a diaphragm pump (KFL-pump).

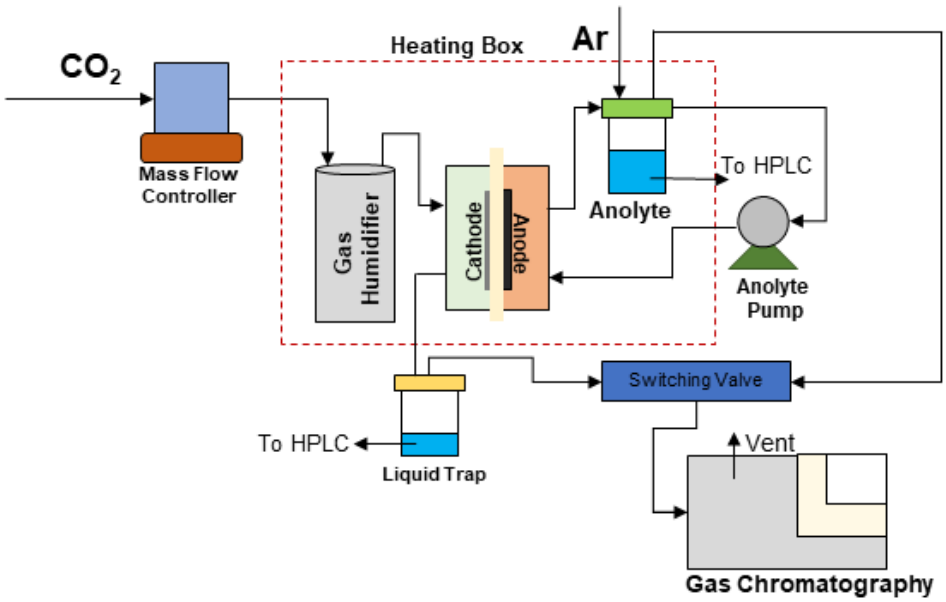

Figure 3.7: Scheme of the reaction setup used in this thesis work (backpressure regulators or MFM aren't shown in the figure but placed after the E-cell and the GC).

Next to the cathode compartment, a water trap was installed on the outlet line from the cathodic gas to avoid water, obstructing the liquid products from going into the GC line and collecting liquid samples. The CO_2-electrolyzer was connected to an external potentiostat as an external power source (Bio-Logic VSP 300 with booster up to 4A) to control the current densities. Reference conditions for the gas

flows were defined as 293.15 K and 1 bar. For experiments using the recycling line, an additional diaphragm pump (KFL pump) was added at the outlet line of the cathode compartment (Appendix A.1.7).

Experiments at elevated temperature

For the controlled-temperature experiments with an MEA setup, CO_2 (AGA, purity 4.5) was supplied to the cathode flow fields with a flow rate of 40 mL $\cdot$ min^{-1} using a volumetric flow controller (Red-y from Voegtlin) and further humidified by sparging into a container filled with Millipore water. 0.1 M electrolyte reservoir was fed to the anode and recirculated continuously using a diaphragm pump (KNF) with a flow rate of approximately 10 mL $\cdot$ min^{-1}. Gas products on the anolyte were measured by purging Ar (at 30 mL $\cdot$ min^{-1}), allowing gaseous anolyte products to be carried along for further analysis. The cell and all the reaction components were placed in a heating oven with a PSU/box interfaced coupled to Raspberry Pi as a PID controller, which my colleague Dr. Asger Moss made at DTU (Figure 3.8)

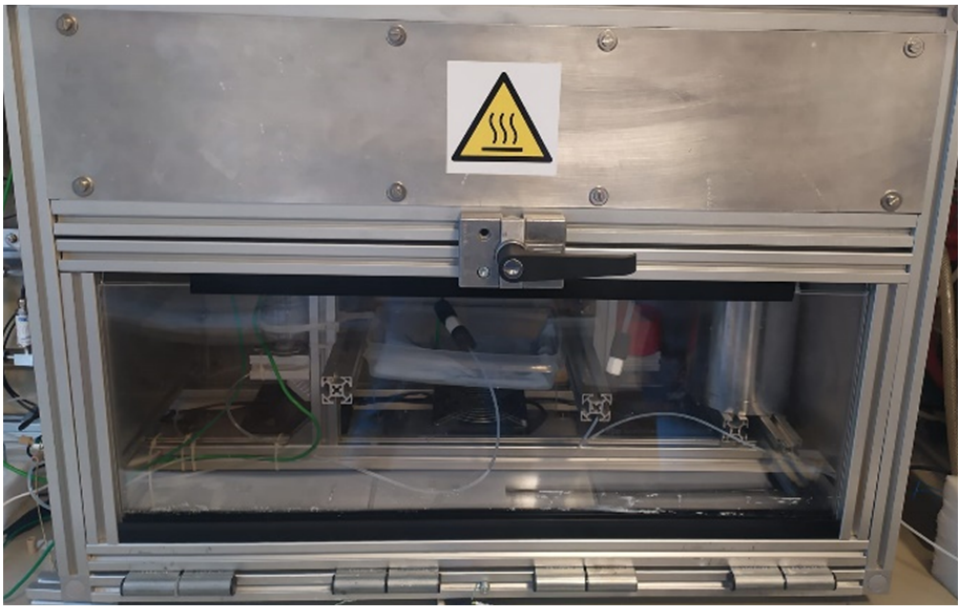

Figure 3.8: Image of the self-made heating box used for elevated temperatures

A 230 heater (GPIO pin) was connected to thermocouples for temperature measurement, and a homemade Python program was developed to control and regulate the reaction system's temperature. Thermocouples were placed in the electrochemical cell (cathode and anode flow fields), the humidifier, inlet, and outlet streams, the heating plates, and the electrolyte reservoirs. The experiments using different heating methods were achieved by preheating the anolyte with a heating plate coupled with a self-made temperature controller or heating rods attached directly to the electrolyzer and controlled with a homemade temperature controller, simulating the effect of the commercial heating tape.

Experiments using ATR-SEIRAS technique

For ATR-SEIRAS experiments, 0.1 M $KHCO_3$ aqueous solution was CO-saturated and preheated to the desired temperatures (20-80°C) to be further filled in the catholyte and anolyte chambers. A mixture of CO/Ar (MKS flow controller) was fed to the cathode compartment at rates between 5-10 mL $\cdot$ min^{-1} depending on the operational temperature, varying the partial pressure to keep the CO concentration in the catholyte chamber constant. The electrochemical cell was connected to a Bruker spectrometer equipped with an MCT detector, and a Pike Technologies VeeMAX III ATR accessory was employed for the electrochemical ATR-SEIRAS. All spectra were collected with a 4 cm^{-1} resolution and 16 scans. The reference spectrum was measured at -0.9 V vs. Ag/AgCl in Ar-saturated $KHCO_3$. In addition, experiments were conducted using chronoamperometry (CA) between -0.9 to -1.5 V vs.Ag/AgCl using a Bio-Logic VSP 200 potentiostat at different temperatures, and the CO peak in the IR spectra was detected at approximately 2050 cm^{-1}.

3.6 Electrochemical techniques

Multiple standard electrochemical methods were implemented throughout this thesis. This section will briefly describe the principle of these techniques and the information I can extract from them.

-Cyclic Voltammetry (CV): a powerful and popular electrochemical technique commonly employed to investigate the molecular species' reduction/oxidation processes and electron transfer-initiated chemical reactions. CV varies the potential linearly at a specific rate (scan rate) compared to RE, and current response is recorded and linked to adsorption and reaction processes at the electrode surface [118]. CV changes can be correlated to the Nernst equation, as it predicts how the system will respond to a change of species concentration or charge at the electrode potential (Eq.3.6.1).

$$E = E^0 + \frac{RT}{nF} \cdot ln\frac{c_O}{c_R} \tag{3.6.1}$$

In this work, CVs were used to reveal the oxidation and reduction processes of a monolayer of a specific metal. For example, bulk copper electrodes in alkaline solutions revealed the different steps of Cu oxidation (formation of Cu_2O and CuO_x) and its further reduction to metallic Cu^0 at backward scan.

-Linear Sweep voltammetry (LSV): LSV is an electrochemical technique used to measure the current response of a reduction/oxidation electroactive species to a linear potential sweep (the potential is scanned from a lower limit to an upper limit) using a specified scanning rate (v). In principle, the LSV operates like CV, but the potential is not back-scanned to the starting point [119]. For my study, I

implemented LSV to correlate the changes in the cathode activity (current density) at different scanned potentials by the modification of the electrode surface (ionomer addition) or the effect of the operating condition (temperature).

- Chronopotentiometry (CP) and Chronoamperiometry (CA): CP is a galvanostatic method in which the current at the working electrode is held constant for a given time while recording the resulting potential (in MEA experiments, it corresponds to E_{cell}). CP is used to investigate the time-dependence of the CO_2R mechanism and was the technique used for all my experiments presented in this thesis (Figure 3.9 presents an example measurement of a CP plot) at ranges between 50-300 $mA \cdot cm^{-2}$ in intervals of 50 $mA \cdot cm^{-2}$. I mostly conducted CO_2R through this technique, where the charged passed (Q) is used to calculate the Faradaic Efficiency, partial current density, and Energy Efficiency. As explained in Chapter 1, I linked those metrics to the selectivity or activity toward a desired product.

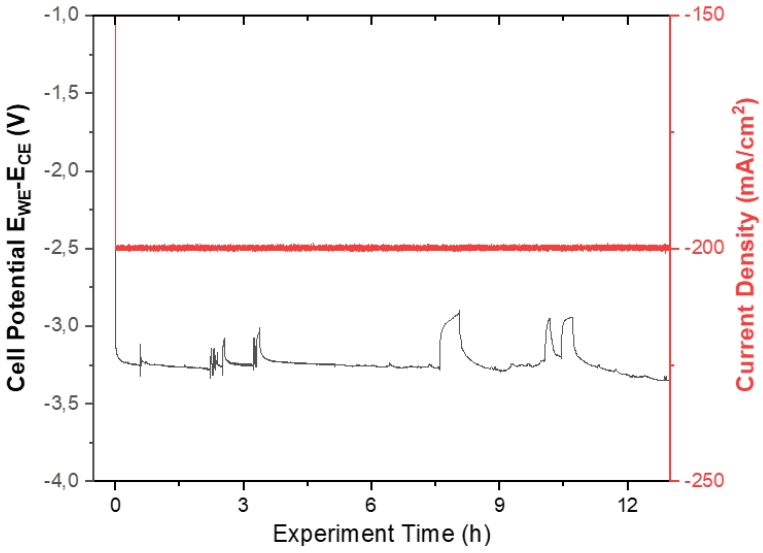

Figure 3.9: Example data of a CP plot. The black line corresponded to the cell potential (left y-axis). Red line is the total current density (right x-axis). I selected this experiment as the potential fluctuations due to flooding/salt precipitate formation are visible.

Oppositely, in chronoamperometry (CA), the potential is set, and the current is recorded over a time range. Without the presence of a RE (as there isn't an ionic contact), it isn't viable to do CA, as it isn't possible to control the WE potential. There are, however, some limitations to performing CP experiments. In the first place, electrochemical reactions depend on the potentials applied, so controlling the potential makes sense. Moreover, the logarithmic dependence between the current density and the overpotential might make it difficult to detect minimal variations in the onset potentials and overpotentials with such techniques. In our research group, we have proposed using a RE in the anode compartment or a new cell design with apertures in both cathode and anode flow fields to place the RE or thermocouples to overcome such limitations.

Capacitance cycling: this is a method used to estimate the electrochemically active surface area (ECSA) or measure the electrode-electrolyte interface's double-layer capacitance (DLC). For this thesis, I didn't measure the ECSA. I instead used the DLC capacitance measurements to correlate the GDE-electrowetting (an essential parameter in GDEs since it determines the amount of catalyst in contact with the electrolyte) and the performance, serving as an indicator of the electrode flooding.

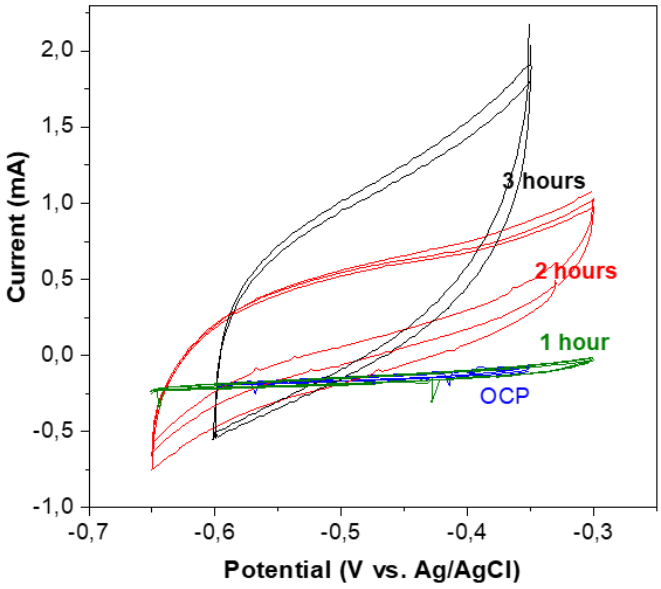

Figure 3.10: Example of CV screening in the non-faradaic region at different reaction times to measure the capacitance of Cu-GDE at 20 $mV \cdot s^{-1}$.

DLC can be measured by conducting CVs at potentials where non-faradaic processes occur (typically 100 mV window from OCV) and using different scanning rates. At these potentials, any measured current can be directly correlated to the charge of the electrochemical double layer and can be estimated as the ratio between the charging current (i_c) and the scan rate (v) [22].

$$C_{DLC} = \frac{i_c}{v} \tag{3.6.2}$$

Electrochemical Impedance Spectroscopy (EIS): EIS is a powerful method of characterizing the electrical properties of materials. It works by measuring the impedance of a material as a function of the frequency, applying an alternating current (AC) signal to the material, and measuring the resulting voltage. The impedance consists of a real part (Z_r) linked to the resistance and an imaginary part (Z_{im}). The impedance variation with the frequency is displayed using the Nyquist plot, displaying Z_{im} vs. Z_r at different angular frequencies (w).

The theory behind the impedance methodology is to find analogies between the E-cell, networks of resistors, inductors, and capacitors that behave like the studied electrochemical cell. The Randles circuit is typically used to describe the elec-

trochemical process and consists of a circuit with a resistor (Rs) associated with the solution resistance and connected in series with the double-layer capacitor and impedance of faradaic reactions (Z_f). Such impedance consists of a charge transfer resistor and the Warburg impedance associated with mass transfer resistances [120].

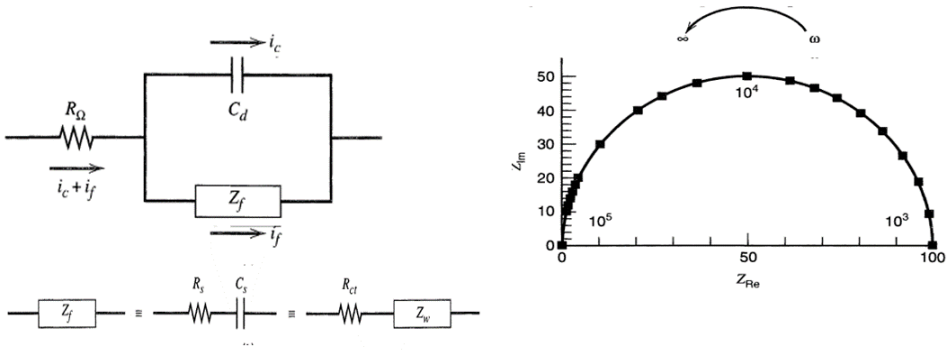

Figure 3.11: Schematic representation of EIS experiment a). Randles circuit, and b). Corresponding Nyquist plot.

The values of different resistors and capacitors can be obtained from the Nyquist plot. The solution resistance, the only real term, is obtained from the interception with the x-axis, C_{DL} corresponding to the middle of the half circle. The second interception is the sum of the solution and charge-transfer resistances. I used the EIS technique mainly to assess the effect of temperature on ionic conductivity and solution resistance at different temperatures by checking the first cross-section with the axis. Hence, galvanostatic EIS (GEIS) was used at different frequencies (1 Hz^{-1} MHz) to measure the solution resistances (0.1-10 Ω) depending on the cell configuration or electrolyte concentration.

Current Interrupt (CI): CI method can be used to estimate the uncompensated resistance (R_u) in a setup. This technique involves measuring at OCV and applying a current step at certain times, and calculating the ohmic resistances by taking the ratio of measured voltage and current (Ohm's Law). The potentiostat (Bio-Logic VSP 300 with booster unit) can compensate for 85% of the ohmic drop ("known as compensated resistances R_C"), The remaining should be compensated manually. In this work, the reported potentials are not IR compensated and just reported as obtained by the EC-Lab software ($E_{measured}$). However, the correction can be done using the following equation:

$$E_{cell} = E_{measured} - I \cdot R \tag{3.6.3}$$

3.7 Product quantification

Quantification of all the derived products from CO_2R is crucial to have an overview of the catalyst selectivity and the overall performance. In this section, I will

describe the two methods used for product analysis, gas chromatography (GC) for gas products and high-performance liquid chromatography (HPLC) for liquid products.

3.7.1 Gas Chromatography (GC)

A gas chromatograph (GC) is an instrument that separates and analyzes volatile compounds. A gas sample is transported through a heated column filled with an inert material, like silica, by an inert carrier gas. As the sample passes through the column, the compounds are separated based on their properties and interaction with the column. The compounds then pass through a detector which measures the amount and identity of the compound [121]. The separation process in a GC is based on the interaction between the sample and the column, which depends on the polarity or van der Waals interaction. Compounds with weak-interaction strength reach the detector first, and so on. The detector produces an electrical signal converted into a peak on the chromatogram. The position and height of each peak at a specific time (retention time) indicate the amount and identity of the compounds in the sample.

Cathodic gas products were analyzed with a gas chromatograph (PerkinElmer Clarus 590) coupled with a thermal conductivity detector (TCD), equipped with the Molecular Sieve 13x, and HayeSep Q packed column using Argon (Linde 5N) as the carrier gas. The GC was also used for analyzing CO_2 gas products at the cathode and O_2 and CO_2 at the anode size using a switching valve to measure products at both compartments. My GC system consisted of the following components:

- Thermal conductivity detector (TCD): the TCD utilizes differences in thermal conductivity to generate the peak signal at the chromatograph. It usually consists of two gas channels, one for a gas sample and the other for the reference gas. A filament burns in each channel, and a signal is created whenever there is a change in thermal conductivity compared to the reference. All gas compounds (CO_2, CO, H_2, C_2H_4, C_2H_6, C_3H_8, and C_3H_6) can be detected using a TCD, however, the sensitivity can vary significantly, especially for longer-chain hydrocarbons. To avoid this, GCs might have a flame ionization detector with a hydrogen flame to ionize organic compounds (CH-species). Therefore, FID can only detect oxidizable organic compounds but with high sensitivity (depending on the oxidation states and number of carbon atoms in the molecule).
- Carrier gas: Ar was selected as carrier gas (regulated with a Swagelok BPR), since it is inert and has high thermal conductivity (26.5 $mW \cdot m^{-1} \cdot K^{-1}$ compared to 271 $mW \cdot m^{-1} \cdot K^{-1}$ at 500 K), helping to increase the sensitivity towards H_2, and other gases. The standard carrier gas flow for my experiments

was 10 mL · min^{-1}.

- Temperature: The column temperature influences product retention. Increasing the temperature might decrease the retention time of a specific product. While it is an effective method to accelerate the gas measurement, it might compromise how well separated the gases are. For all my measurements, a heating ramp method was used to facilitate the separation without compromising the detection (initial temperature was 60 °C and kept for 3 min. Subsequently, it was increased to 80 °C at 10 °C · min^{-1} and kept for the rest of the measurement).

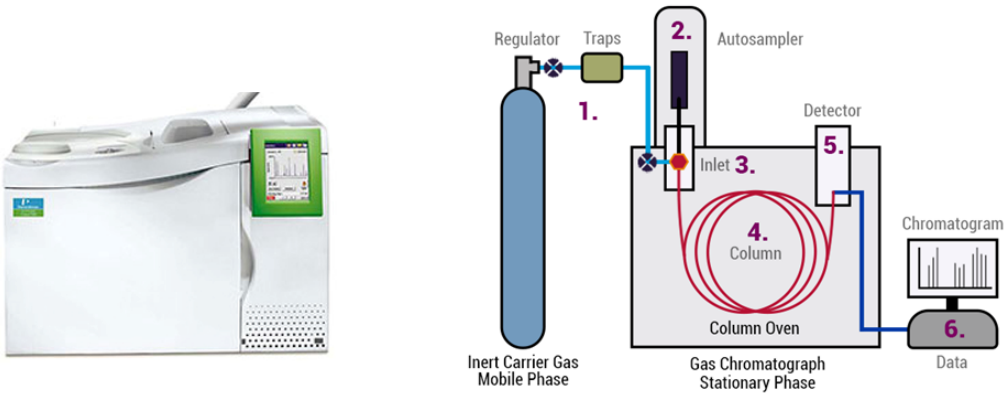

Figure 3.12: Picture of the Clarus 590 GC used in this thesis and scheme of the different GC components. Images adapted from References [122], [123].

3.7.2 High-performance liquid chromatography (HPLC)

The HPLC process is analogous to a GC since it involves passing a mixture of compounds through a packed column containing a stationary phase such as C_{18} bonded silica. As the sample passes through the column, the compounds separate based on their chemical and physical properties. The separation process in an HPLC is based on the different diffusion rates of the compounds in the mixture across the column [124].

The HPLC unit is comprised of several components, such as a pumping unit to flow the mobile phase at a specific rate; a degassing unit to remove dissolved air and gas bubbles, which may interfere with proper operation by introducing fluctuations in the flow rate or baseline noise/drift; a sample injector designed to introduce either standard solutions or samples into the system through a needle; columns that are placed within column ovens for temperature control during separation processes; and detector units used in conjunction with workstations for quantifying and processing chromatograms so that products can be identified and measured.

In my measurements, the liquid products are quantified using an ex-situ HPLC unit from both reaction compartments after CO_2 electrolysis (cathode and anode). The

cathode products are collected from a water trap filled with water (20 mL), while the anode products are collected from the anolyte (60 mL from the reservoir). Collecting products in both compartments is necessary as liquid products tend to cross the membrane (via electro-osmotic drag, diffusion, or electromigration) or across the GDE (evaporation). Throughout this thesis, I described the liquid products of cathode and anode as a whole, except when I was interested in evaluating product crossover, in which case I differentiated those from cathode and anode. Just with the HPLC, I could quantify all the liquid-phase products precisely, and I have designed a closed system for collecting our liquid samples, preventing some evaporation of volatile products.

For my measurements, 2 mL of solutions are prepared, placed in HPLC-designed vials, and used for further quantification. The HPLC unit was the Agilent 1260 Infinity II which consists of an autosampler, quaternary pump (up to 400 bar), a column (Aminex HPX-87H packed column with a cross-linked resin in hydrogen form), and two detectors (RID: refractive index detector and DAD: diode array detector). I used 5 mM H_2SO_4 as mobile phase (polar solvent with an apolar column), and preliminary calibrations were done to estimate the concentration in the samples and were done by preparing different dilutions (1:10-1:100000 for each of the liquid CO_2-derived products, e.g., ethanol, formate, acetate, n-propanol). The analysis method is around 1 hour per sample, and the reason behind it is the number of different products and the necessity of having a self-contained chromatograph with a well-defined peak for each compound. Although one detector is slightly more sensitive to a compound, both detectors provide the same results once the compound is measured. Normally, DAD detectors have higher sensitivity towards organic molecules with πbonds, while RID has higher to alcohols and carboxylic acids.

The concentration and the Faradaic Efficiency can be measured by quantifying the peak area for each detected product (this applies to GC and HPLC):

$$C_i = \frac{A}{CF_i} \tag{3.7.1}$$

$$FE_i = \frac{z \cdot c_i \cdot V_r \cdot F}{Q} \tag{3.7.2}$$

Where A_i is the peak area, CF_i is the calibration factor for each compound, z corresponds to the number of transferred electrons, c_i is the concentration (measured with the chromatograph plot), V_r is the reservoir volume (cathode or anode), F is the Faraday's constant (96485 $C \cdot eq^{-1}$), and Q is the transferred charge. In general, the liquid products range between 20-30% of the total products. The calibration factor and retention time of these methods are found in Appendix A.1.3. To obtain

these values, I previously plotted the peak area at a specific concentration value and got the slope through a linear fitting.

3.8 Measurement of the RG-AEM properties (membrane characterization)

A comprehensive characterization of the synthesized membranes' associated mechanical, thermal, and chemical properties was required to establish a correlation between those properties and performance.

Raman Spectroscopy: Raman spectra were recorded on dry samples of the ETFE-g-p(VBC) and final RG-AEMs using a Renishaw InVia Reflex Raman Microscope equipped with a 785 nm IR laser and a 20× ($N_A = 0.40$) objective. All Raman data was collected, and the baseline was corrected using Renishaw WiRE Software (Renishaw PLC, UK), with normalization and integration of band intensities conducted using Spectragryph (Spectroscopy Ninja, Germany).

Ion-exchange capacities (IEC): The IECs were determined using potentiometric AgCl precipitation titrations. For each RG-AEM in the Cl^- form, a dehydrated known dry mass (m_{dry}) sample was immersed in 25 mL aqueous $NaNO_3$ solution (1.2 M) and continuously stirred for 16 h. Subsequently, the solution (still containing the RG-AEM sample) was acidified with aqueous 2 mL HNO_3 (2 M) and titrated against aqueous $AgNO_3$ standard solution (0.02000 ± 0.00006 M). A Metrohm 848 Titrino Plus autotitrator equipped with an Ag/AgCl Titrode was used for the dynamic equivalence point titrations (DET). The endpoint was calculated as the peak maxima in the first differential plot of potential vs. titrant volume data.

$$IEC = \frac{E_p \cdot C_s}{m_{dry}} \tag{3.8.1}$$

where E_p represents the endpoint volume, C_s is the $AgNO_3$ standard concentration solution, and m_dry is the mass of the dry RG-AEM(Cl^-) sample under analysis. This procedure was undertaken on n = 3 samples of each RG-AEM.

Water uptake (WU) and through-plane swelling (TPS): A RG-AEM(Cl^-) sample was removed from UPW storage, and the excess surface water was removed by blotting with a filter paper. The hydrated mass (m_{hyd}) and thickness (T_{hyd}) were recorded immediately. Masses were recorded on a 4 decimal place (0.1 mg) analytical balance, and thicknesses were recorded using an outside digital micrometer (precision of ± 2 µm). The RG-AEM(Cl^-) sample was dried under reduced pressure at 50 °C (vacuum oven) for 18 h before the dehydrated mass (m_{hyd}) and thickness (T_{hyd}) were recorded. All measurements were conducted on n = 3 samples of each RG-AEM(Cl^-). The gravimetric water uptake, through-plane swelling (TPS), and hydration number (λ)

are calculated as follows:

$$WU = \frac{(m_{hyd} - m_{dry})}{m_{dry}} \tag{3.8.2}$$

$$TPS = \frac{(T_{hyd} - T_{dry})}{T_{dry}} \tag{3.8.3}$$

$$\lambda = \frac{WU}{IEC \cdot M_w} \tag{3.8.4}$$

where M_w corresponds to the molecular mass of water. The area of swelling values was calculated the same way as TPS values but using the hydrated and dry areas measured simultaneously as the thicknesses.

Ionic conductivity: the in-plane and Cl^- and HCO_3^- anion conductivities of fully hydrated RG-AEM samples between room temperature and 80 °C were measured using a Solartron 1260/1287 combination controlled by ZPlot/ZView software (Scribner Associates, USA). Impedance spectra were collected over a frequency range of 1.0 – 106 Hz (10 mV a.c. amplitude) with the samples mounted in a 4-probe BekkTech BT-112 test cell (Alvatek, UK). Test cells containing samples of the Cl^- and HCO_3^- RG-AEM forms were then submerged in UPW. The ionic resistance values, taken as low-frequency x-(real)-axis intercepts in the collected Nyquist plots, were used to calculate the conductivity.

$$\sigma = \frac{L}{R \cdot w \cdot T} \tag{3.8.5}$$

where L corresponds to the working electrode distances (0.425 cm), and w and T are the width and thickness of the RG-AEM samples, respectively.

3.9 Electrode characterization

3.9.1 X-ray photoelectron spectroscopy (XPS)

XPS is a valuable technique used to observe the elemental composition and chemical state of materials on the surface of a sample, apart from H and He [125]. The XPS relies on the photoelectric effect, as it utilizes X-ray radiation to excite electrons from the sample surface, which are then detected and analyzed for their kinetic energy. With the relation between the incoming X-ray ($h \cdot v$), the binding energy of the electron at the sample surface, and the work function of the electron energy analyzer, the resulting kinetic energy can be calculated:

$$E_k = h \cdot v - E_b - \phi \tag{3.9.1}$$

The binding energy is the energy of the electrons attracted to the nucleus (E_b), the photon energy is the energy of the X-ray photons used by the spectrometer ($h \cdot v$), and the kinetic energy is the energy of the ejected electrons from the sample. The work function is a correction factor for the instrument and correlates to the minimum energy required to eject an electron from an atom (Φ). The work function and photon energy are known, and the detector measures the kinetic energy, leaving the binding energy as the only unknown [126]. When the binding energy is lower for higher orbitals since less energy is required to eject electrons from further away from the nucleus. Furthermore, the binding energy can vary from atom to atom, depending on their environment and the bonds they partake in, allowing XPS to measure a material's chemical shifts. Figure 3.13 shows an example of an XPS survey spectrum for a Cu-based electrocatalyst.

As a surface-sensitive technique, it can only examine the top 1-10 nm from the sample surface. I used this technique mainly to detect foreign impurities on the cathode after electrolysis, corroborate the presence of different metallic species (co-sputtering approach), or after coating with binder/ionomer agents.

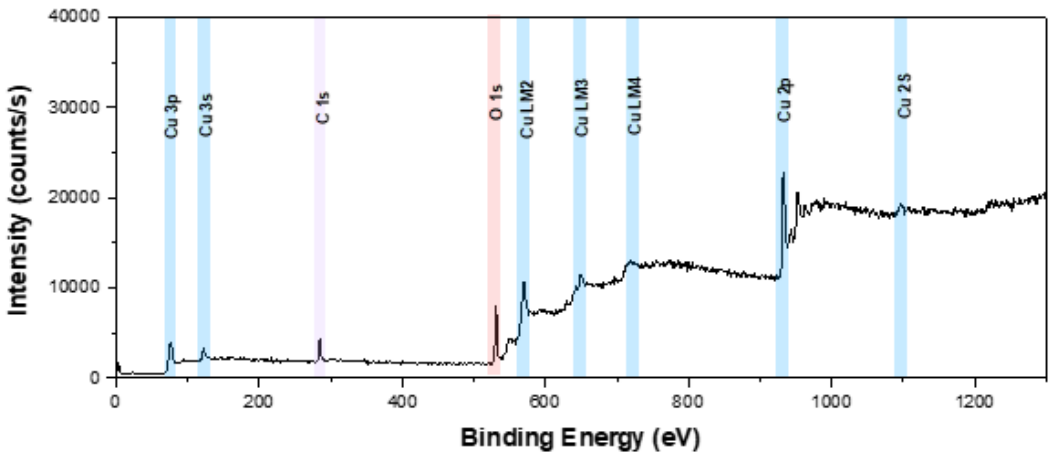

Figure 3.13: Example of the XPS survey spectrum for Cu-GDE prepared by PVD method.

3.9.2 Scanning electron microscope (SEM)

SEM is an electron microscope that produces images of a sample surface by scanning it with a focused beam of electrons. The electrons interact with the sample to produce a variety of signals, including visible light and secondary electrons, which are detected and used to produce a high-resolution image of the sample surface [127]. SEMs are powerful tools for investigating samples' microscopic structure and chemical composition since their images can be magnified up to 100000 times and can image samples in three dimensions, allowing for a deeper understanding of a sample morphology. Additionally, the SEM can provide quantitative information with cathodoluminescence and backscattered electron imaging, which can measure

sample properties such as electrical, optical, and magnetic parameters.

SEM is used to image and analyze the surface properties of a wide range of samples, providing information on topography, composition, and structure [128]. For my thesis work, I used the SEM technique to study the morphology of the catalyst layer for Cu-based electrodes (Figure 3.14 showed examples of different sputtered Cu layers in different substrates) and cross-sectional SEM imagining to observe the GDE structure and identify the different layers coated through the tandem catalyst approach.

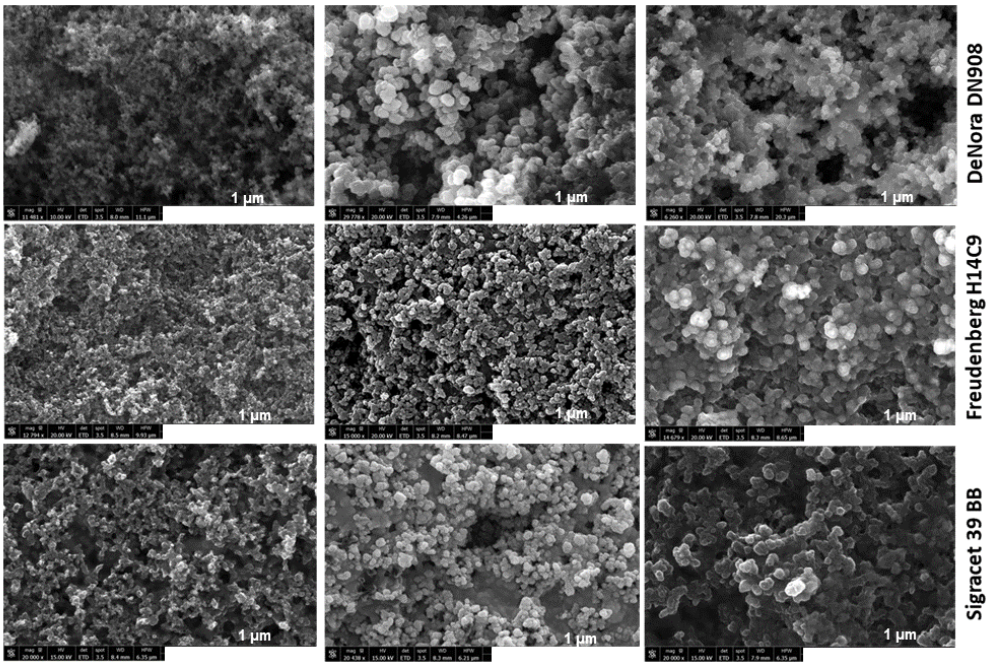

Figure 3.14: An example of SEM images of Cu-GDE using different commercial GDLs (DN909, H14C9, and 39BB). a) GDL, b). Cu catalyst before the electrochemical reaction, c). Post-reaction GDEs after experiments at 200 mA $\cdot$ cm^{-2}.

3.9.3 Electron-Diffraction X-ray spectroscopy (EDX)

EDX is an analytical technique used to identify the composition of a material by measuring the diffraction of a beam of electrons as they interact with the material. This method works by firing a beam of electrons at the material, then measuring the degree of diffraction as they interact with the material's structure. The material's atomic structure can be determined through diffraction, which can then be used to identify its composition [129]. In general, the EDX method is a powerful and flexible technique that has been used extensively, as it is a non-destructive method that does not require sample preparation and can be used to analyze a wide range of materials, including metals, ceramics, polymers, and semiconductors. In addition, the EDX method is ideal for analyzing materials on the nanoscale since it can be used to determine the composition of a material in extremely small surface areas.

I combined this technique with cross-sectional SEM to differentiate the Cu and tandem electrodes' different layers and components for my thesis.

3.10 Selection of operating parameters and conditions for this thesis

This section sets the standard operating parameters for testing electrochemical CO_2 reduction catalysts, gas diffusion electrodes, and membranes used in this thesis work. This aims to provide consistency between different studies conducted during my Ph.D. and a straightforward comparison of the effectiveness of each suggested strategy and the current state of the art.

- The standard electrolyte concentration will be 0.1M $KHCO_3$ (the effect of electrolyte concentration has been presented in this chapter's Appendix A.1.3).
- The CV scan rate will be 20 $mV \cdot s^{-1}$. For DLC, scan rates will be between 10-60 $mV \cdot s^{-1}$.
- The standard catalyst loading for nanoparticles will be 1 $mg \cdot cm^{-2}$ (selected after the studies on the effect of loading conducted in Chapter 5), and CL through sputtering will be between 100-150 nm.
- The used gas diffusion layer will be commercial Sigracet 39BB (see Results of GDL comparison for CO_2 electrolysis attached in Appendix A.1.3r). I used Sustainion X37-50 Grade RT and RG-MPIP AEM for experiments where anion exchange membranes are needed. Preliminary studies comparing different membranes are also found in Appendix A.1.3.
- The standard anode was the commercial IrO_2 on carbon paper from Dioxide Materials. Other anodes have been tested for this thesis work (commercial DN300 and Ni foam). An anode comparison is included in Appendix A.1.3.
- The standard geometric surface area of the cathode will be 2.25 cm^2, the anode will be 4 cm^2, and the AEM will be 7.4 cm^2.
- The operating conditions will be ambient conditions (except for studies focusing on understanding temperature and pressure effects).
- The standard zero-gap CO_2 electrolyzer reactor will be those described in Section 3.2, and flow cells will be the Teflon-based cell (Figure 3.4).
- To measure the flow at the outlet, I used a bleed line (such as N_2) as an internal standard or a volumetric flow meter (Defender 530).
- Inlet CO_2 feeding rate will be set at 30 $mL \cdot min^{-1}$. However, different flow rates are expected to be used throughout the project, potentially leading to a new standard (see results of the effect of CO_2 feeding rates in Appendix A.1.3).

- The relative humidity of the inlet CO_2 will be 100% unless specifically stated otherwise.
- The standard test duration will either be 1 hr, 2hr, 4hr, 10 hr, 24hr, 100 hr, or 200 hr. The testing duration should differ for different catalysts, gas diffusion layers, and membranes since some materials will be more stable than others (also depending on the strategy).
- Operating cell potentials, current densities, and product selectivity will be recorded for all experiments. When multiple current densities are tested on the same catalyst, it is also suggested to sweep the current density between 50-300 $mA \cdot cm^{-2}$ at intervals of 50 $mA \cdot cm^{-2}$ to study the mass transfer limits for CO_2 electrolysis.

Chapter 4

Insights into the temperature effects on CO_2 electrolysis

Contribution

I performed ATR-SEIRAS experiments with Dr. Wanyu Deng, while Dr.Asger Moss built the heating oven used in the study (Figure 3.8). I conducted all the experiments, and this study resulted in a manuscript attached to the Appendix.

4.1 Chapter Overview

Temperature is expected to play a role in CO_2R kinetics and mass transport, as discussed in Chapter 2. Additionally, the operation of CO_2 electrolyzers at elevated temperatures should be entailed due to the produced resistive heat from activation overpotential and ohmic losses at industrially relevant conditions. Few systematic researches have been conducted to investigate the temperature effects on CO_2E despite studies incorporating temperature-dependent experiments or computational models [130]. Thus, in this chapter, I presented a holistic and systematic study of temperature effects on CO_2E on Cu-based electrocatalysts. I conducted electrochemical measurements, partial pressure experiments, and in-situ ATR-SEIRAS studies to evaluate how diffusion, solubility, kinetics, and mass transport vary with temperature and influence performance. In addition, I assessed the effects of different heating methods, together with a long-term experiment at elevated temperatures.

4.2 Temperature effects on the cathode activity

First, I evaluated the effects of temperature on cathode activity using LSV techniques (scanning rate 20 $mV \cdot s^{-1}$). The polarization curves at different operating conditions show that temperature significantly affects the cathodic activity, with the total current density increasing approximately 3.0-fold at 80°C compared to ambient conditions (RT). While the scanning time of the polarization curves is too short to detect CO_2 products, longer-term tests at similar temperatures and even slightly elevated current densities show that CO_2R mechanism dominates over HER, at least initially, before GDE degradation occurs (the linear sweeps can be used as a proxy for CO_2 reduction activity). Furthermore, higher temperatures can affect

the primary CO_2RR, reducing the activation overpotentials required to drive them and lowering the thermodynamic cell potentials ($E^0{}_i$). Nevertheless, a calculation of the thermodynamic potentials at different temperatures showed that temperature effects are minor (e.g., 20 mV for CO_2R to CO and 37 mV for major C_2H_4 from 20°C to 80°C), indicating that overpotentials have a more significant influence on temperature than thermodynamic potentials [131]. (Table A3 from Appendix A.1.4).

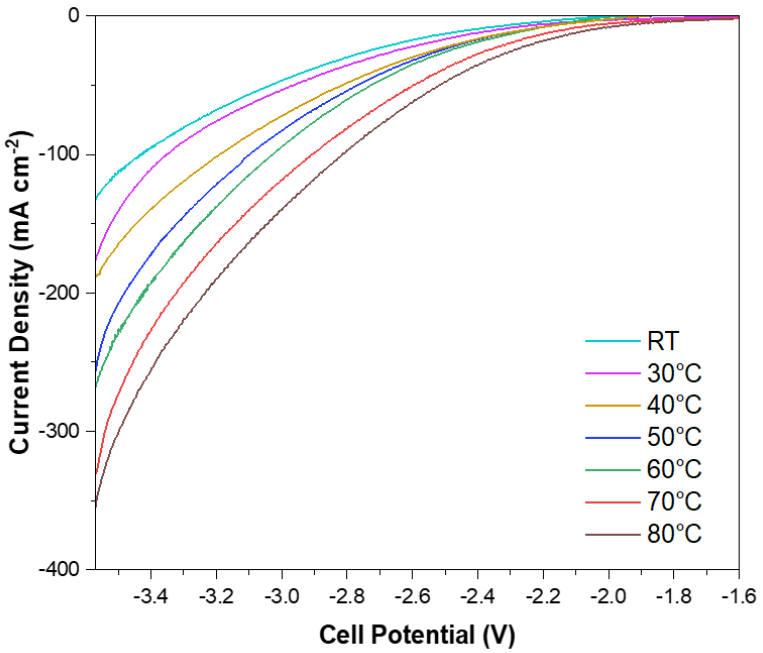

Figure 4.1: Temperature effects on the current density and cell potential at different operating temperatures for CO_2R using LSV measurements.

Chronopotentiometry experiments at different current densities and temperatures showed that operating at higher temperatures decrease both cell potential and ohmic resistance in CO_2E (Figure 4.2a). During my experiments, I observed a decrease in E_{cell} as the temperature increased (e.g., 500 mV voltage drop from RT to 80°C at 200 $mA \cdot cm^{-2}$). The ohmic resistances also decreased similarly (e.g., 720 mΩ at RT to 400 mΩ at 200 $mA \cdot cm^{-2}$). The changes in these parameters at elevated temperatures may be attributed to improved CO_2RR kinetics (Butler-Volmer equation) or enhanced gas diffusivity and ion conductivity, resulting in lower overpotentials attributed to effects on the GDE (decrease in diffusion layer thickness), AEM (conductance), and electrolyte.

A decrease in the ohmic resistance and cell potential may also result from an increase in the ionic conductivity. Nevertheless, measurements of the ohmic resistances (through GE impedance spectroscopy) and the analysis of the high-frequency resistance (HFR) showed a value of less than 600 $m\Omega \cdot cm^2$ when the temperature was elevated, resulting in only 120 mV overpotential reduction (Figure 4.2b). As a result, the overall cell potential change might be attributed to a higher extent to an

increase in the CO_2R reaction rates rather than ionic conductivity changes in the system [132].

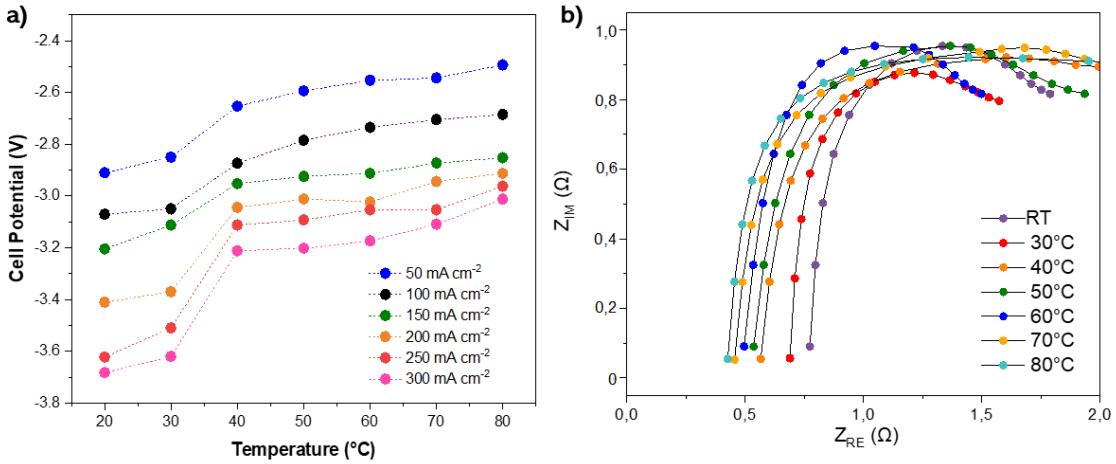

Figure 4.2: a). Cell potential profiles as a function of the total current density and b). Galvano-electro impedance spectroscopy (GEIS) for CO_2 electrolysis at 200 mA $\cdot$ cm^{-2} for different operating temperatures. (High-frequency region indicates potential variations of the ionic conductivity).

4.3 Effect of temperature on product distribution

This section investigated the effect of temperature on product selectivity by testing fresh Cu-GDEs at different temperatures and current densities. As shown in Figure 4.3, Faradaic Efficiencies of CO and C_{2+} products did not differ significantly at temperatures below 40°C from RT (e.g., 15% and 43% at room temperature versus 17% and 47%, respectively, at 40°C). However, when the temperature was raised to 60°C, the CO selectivity increased dramatically, with Faradaic Efficiencies above 40% at all current densities. While this section presents the results of just four different temperatures, I have also measured 30, 50, and 70°C, identifying the threshold temperature for visible effects between 40 and 50°C (details of all screened temperatures are included in the manuscript attached to this thesis).

A shift toward CO at elevated temperatures can be explained by temperature-dependent CO_2R kinetics and a preference for faster desorption from the surface over CO-CO coupling to C_{2+} products (further corroborated in the ATR-SEIRAS experiments). On the other hand, when CO selectivity increases, ethylene selectivity decreases disproportionately compared with other liquid C_{2+} compounds. It seemed the ethylene selectivity decreased at high temperatures when the CO coverage is expected to be low, suggesting that *CO coverage may not be a dominant factor for ethylene production over these conditions [52] (similar effects were observed varying *CO surface coverage through backpressure experiments). Moreover, CH_4 was shown to be suppressed at higher temperatures, in agreement with previous

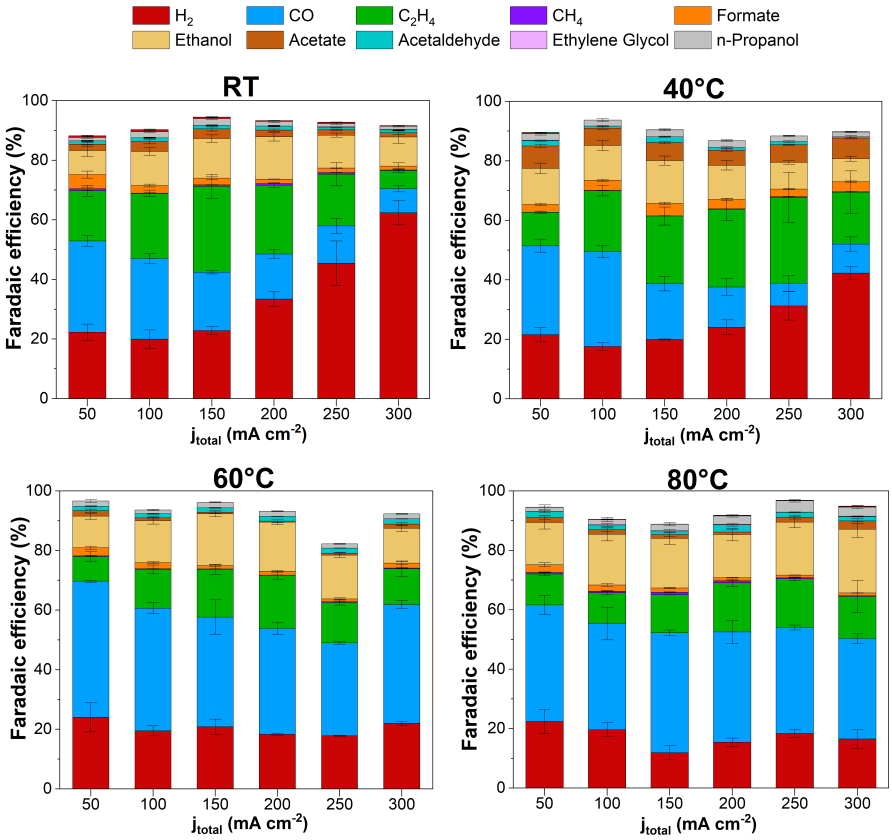

Figure 4.3: Temperature effects on the product distribution for CO_2R over Cu-based electrocatalysts at different temperatures and current densities.

studies in the field, most likely due to the adverse effects of temperature on proton shuttling and the stabilization of its intermediates [103].

Further selectivity trends are observed as a function of temperature for CO and C_{2+} products by plotting the C_{2+}/CO ratio (Figure 4.4a). It is known that CO dominates over C_{2+} products at low overpotentials in CO_2E. When the overpotential is high, CO binds strongly to the surface, facilitating the CO-CO coupling, explaining why the C_{2+}/CO ratio increases with total current density [133]. Increasing the temperature also changed the C_{2+}/CO ratio, reaching its maximum at 40°C and decreasing at 80°C. A decrease in the C_{2+}/CO ratio above 40°C may be attributed to the desorption of CO at these temperature ranges. Because CO appears to be relatively well bound to Cu at 40°C, the increase of C_{2+}/CO ratio is likely a consequence of an enhancement of the CO-CO coupling, since CO-CO coupling is an electrochemical reaction, so the temperature should influence its rate.

On the other hand, H_2 exhibits an exciting trend. Moreover, as discussed in Chapter 2, there might be abrupt shifts towards HER at industrially relevant conditions, attributed to GDE flooding and salt precipitation, thus significantly distorting CO_2R selectivity [86]. In my experiments, HER selectivity dominates at low operating

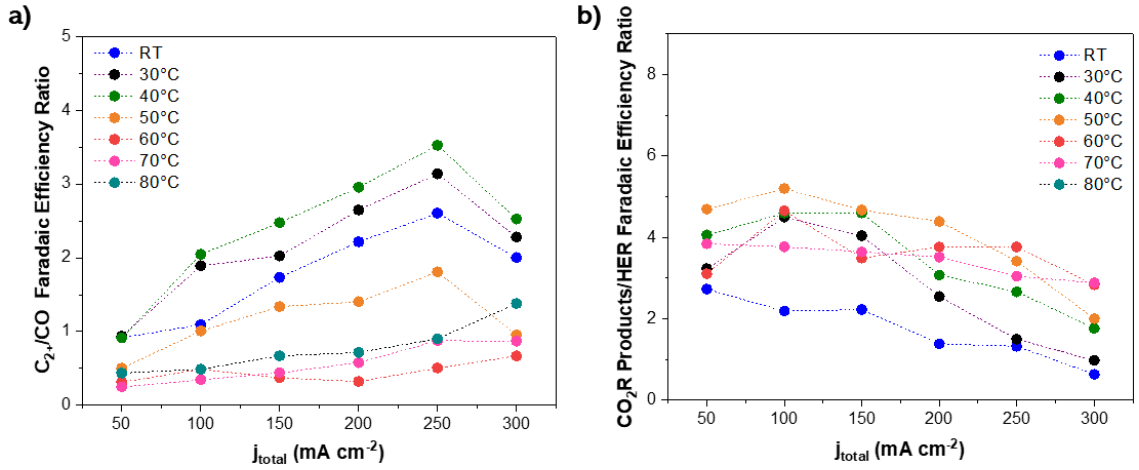

Figure 4.4: a). C_{2+}/CO Faradaic Efficiency ratio, b). CO_2-derived products/H_2 Faradaic Efficiency ratio as a function of the temperature and total current densities.

temperatures, as expected. The excessive H_2 usually indicates cathode flooding and concomitant mass transfer issues, clearly indicating limited CO_2 mass transport [84]. However, by operating at temperatures higher than 50°C, the HER selectivity surprisingly declined even while operating at j_{total}>200 mA $\cdot$ cm^{-2} and longer-experimental time (FE_{HER}<20% for all the tested conditions). The decrease of the CO_2R/HER ratio by raising the temperature using MEA-cells (Figure 4.4b) indicates that HER might not be primarily determined by CO_2 mass transport limitations but rather by water management.

Studying the water management and electrode flooding in CO_2 electrolysis devices is complex, as they depend on several factors, including the membrane. AEMs do not directly affect catalytic activity in MEAs, but they can affect the local reaction environment and water transport, influencing the product selectivity, especially when CO_2-reduced products vs. H_2 [107]. Although water transport in MEAs is difficult to predict due to its transient nature and reliance on AEM properties, there are water-transport mechanisms that are temperature-dependent.

Generally, a temperature rise will increase electroosmotic drag and diffusion-driven fluxes, accelerating the ion transport and water uptake across the membrane. As a result, water penetration into the cathode-GDE might decrease [80]. Furthermore, the ionomers' water content is intrinsically affected by temperature, which can alter AEM hydration and favor hydraulic permeation to the anode [134]. Nevertheless, it is possible that such variations could cause a water imbalance in the system, dragging water towards the cathode, since the increase in water consumption (from electrochemical reactions) favored at elevated temperatures could also facilitate back-diffusion. As I did not observe flooding in my high-temperature experiments (supported with capacitance measurements), I may assume that diffusion, hydraulic permeation, and electroosmotic drag fluxes are greater than back diffusion flux.

Further simulations and modeling of MEA overall water transport mechanisms are needed before such conclusions can be drawn.

Moreover, operating at elevated temperatures with fully humidified cathodes (RH) results in higher water content in the humidified instreams (e.g., for 100% RH cathode inlets, H_2O content at 25 °C is 3% by mol, whereas at 80 °C is 43%). Therefore, the concentration of water and CO_2 is expected to be affected by temperature in humidified inlet flow. In contrast, preliminary experiments indicated negligible differences at different relative humidities, as I just observed a slight increase in HER selectivity at high temperatures and low relative humidity (results of this study are included in the Appendix section of the attached manuscript).

Another factor that could affect H_2 selectivity is salt solubility. A well-known fact is that carbonate formation from the acid/base CO_2 equilibria results in salt precipitation of $KHCO_3$. Salt deposition blocks flow fields and thus causes primary water to drag across the AEM to reach the cathode-GDE, favoring hydrogen selectivity [85]. Therefore, as the salt solubility increases with temperature, higher operating CO_2 electrolysis should have fewer issues with salt deposition and concomitantly less HER. To enhance the stability of CO_2E, strategies such as operating at low electrolyte concentrations or switching from K-based salts to Cs should be coupled with an elevated operating temperature.

4.4 Effects of temperature on product's crossover

Product crossover is a significant issue in CO_2E, as 40% of liquid products can cross the AEMs due to diffusion and electromigration [90]. Figure 4.5 shows the effects on ethanol selectivity as a function of temperature and trends in the crossover of this compound. I focused on ethanol, a volatile compound, and the major liquid C_{2+} generated from CO_2R.

At different temperatures, no major variations were observed in the ethanol selectivity (Figure 4.5a). It was initially expected that increasing the temperature would increase ethanol selectivity due to their lower reaction order and higher transfer coefficient than other CO_2R-derived products. Nonetheless, this did not occur since selectivity trends in MEA are also influenced by surface coverage concentrations (faster CO desorption) and mass transport mechanisms, which may have stronger influences than these kinetics effects.

The temperature effects on ethanol have been observed in a substantial way through the product crossover since temperature increases result in lower crossover through the AEM, resulting in higher cathode concentrations. Figure 4.5b shows a linear relationship between temperature rise and decrease in crossover ratio, indicating that ethanol evaporation through the GDE is favored at higher temperatures over

diffusion and electroosmotic drag through the anode.

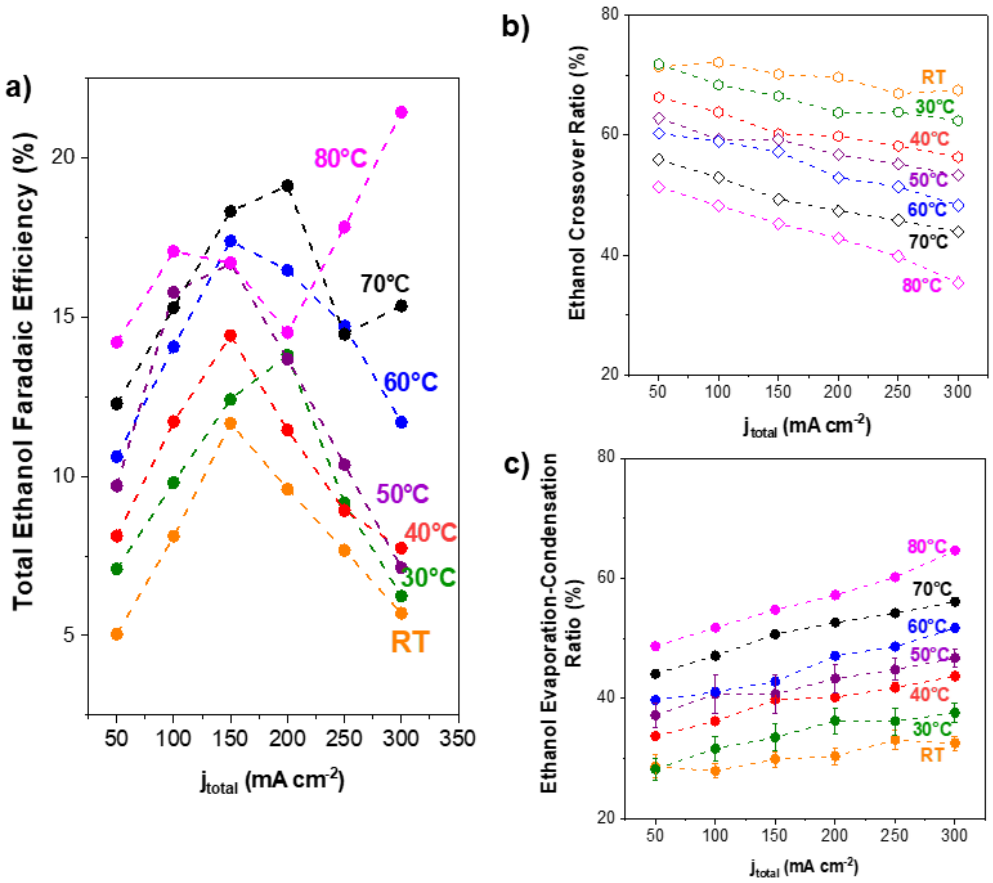

Figure 4.5: a). Effect of temperature in the ethanol selectivity at different total current densities b). Ethanol crossover ratio as a function of the operating temperature and the current density, and c). The evaporation rate of ethanol across the cathode-GDE is a function of the temperature.

During this study, I observed a decreased ethanol crossover rate across the AEM (28% at RT vs. 54% at 60 °C of the ethanol found in the liquid trap at the cathode). Similar results were reported by the Stinton group, with crossover rates increasing at high temperatures, but Faradaic Efficiency did not change significantly [91]. Furthermore, negatively charged compounds (e.g., $HCOO^-$ or acetate) do not alter their crossover rate, as they are affected by electromigration across AEM and don't have a vapor pressure. The selectivity of formate and acetate slightly decreased at temperatures higher than 60 °C, as oxidation of those compounds at the anode might be favorable under these conditions.

4.5 Temperature effect on CO_2 utilization and mass transport

Higher temperatures contribute to faster CO_2 mass transport in the system due to increased CO_2 diffusion and a decrease in the electrolyte viscosity; however, this is counterbalanced by reduced CO_2 solubility (Figure 2.4 in Chapter 2). I conducted partial pressure experiments to determine which effect was more significant during the operation. I varied the CO_2 partial pressure (p_{CO2}) using Ar at different current densities and temperatures, keeping constant the CO_2 concentration. Using Henry's law to calculate the concentration of CO_2 at 80 °C and 1 bar as standard, I adjusted the CO_2/Ar ratio for all experiments at the measured temperatures to match the same concentration during all experiments. The results of the variation in partial pressure in major gas product distribution are shown in Figure 4.6.

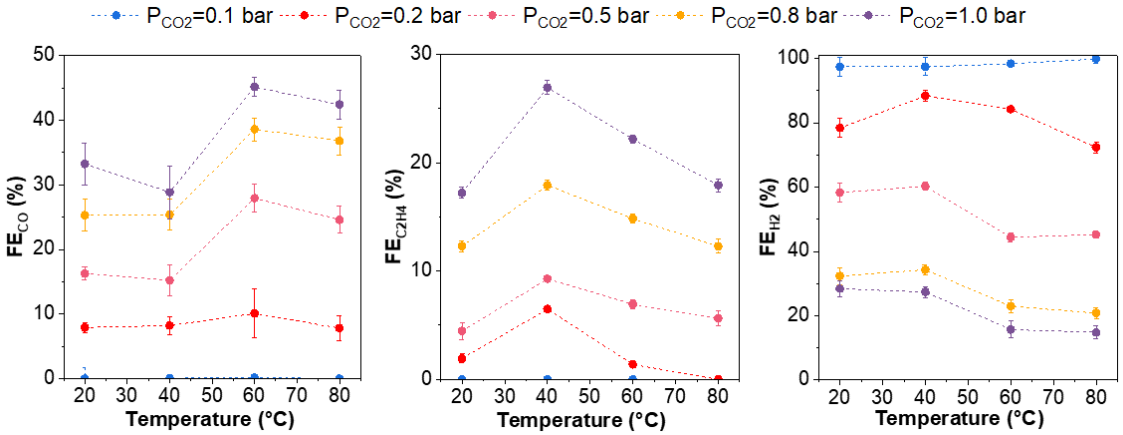

Figure 4.6: Temperature effects in CO_2 availability and mass transport at different partial pressures.

I found increased selectivity towards carbon-derived products and lower HER at p_{CO2} and temperatures above 0.5 bar and 60°C, suggesting that a decreased CO_2 concentration at the surface may not be a limiting factor for CO_2R. Furthermore, the temperature did not significantly influence HER selectivity when p_{CO2} was below 0.5 bar, as CO_2 was depleted from the catalyst surface. If anything, there is a slight decrease in HER selectivity at higher temperatures. Regarding product selectivity, ethylene decreased by reducing the p_{CO2} (FE_{C2H4}=26% at p_{CO2}=1bar vs.FE_{C2H4} =4% at p_{CO2}=0.2 bar), as previously reported in the literature [135]. Interestingly, while the C_{2+}/CO ratio varied quite substantially with temperature transitioning between 40 to 60°C, the partial pressure actually has minimal effect on the C_{2+}/CO ratio.

To examine the effect of temperature on CO_2 mass transport, I simplified the thin film flooded agglomeration model using Faraday's law and Fick's law to estimate

the limiting current density ($j_{MAX,CO2}$) [55]. In CO_2-depleted conditions (with CO_2 at the center of the agglomerate dropping to zero), HER will dominate the limiting current density (Eq.4.1).

$$j_{MAX,CO2} = \frac{D_{CO2}}{r} \cdot c_{CO2} \cdot F \cdot z \tag{4.5.1}$$

D_{CO2} corresponds to the CO_2 diffusion ($m^2 \cdot s^{-1}$), c_{CO2} the aqueous CO_2 concentration, r the agglomerate radius, F the Faraday's constant, and z the number of electrons of the charge transfer reaction. The CO_2 solubility and diffusion calculation are taken from empirical equations described by Arquer et al. [63]. The porosity and tortuosity of the agglomerate were setting it up following Weng et al. As diffusion and charge transfer reactions happen simultaneously, the estimation of the limiting current density is only an approximation [134].

A temperature increase from RT to 80°C increased the limiting current density from 240 to 320 $mA \cdot cm^{-2}$ (Table 4.1). Notably, CO_2 solubility and diffusivity can be correlated with the limiting current density. From 20°C to 40°C, $j_{CO2,MAX}$ only slightly changed, possibly because CO_2 solubility overrode diffusion enhancement. Furthermore, when the temperature exceeds 50°C, there is a significant increase in the limiting current as the CO_2 diffusion is greater than its solubility decrease (Figure 4.7), supporting the observation of enhanced CO_2 mass transport at high temperatures. Finally, the results of this calculation were combined with product selectivity (Figure 4.3), showing that even at higher current densities, the system would not be operating in limiting current density regimes at elevated temperatures (the dominant HER (60%) at room temperature dropped to 15% at 80°C under 300 $mA \cdot cm^{-2}$).

Table 4.1: CO_2 concentration in aqueous solution and diffusion as a function of operating temperature

Temperature (°C)	$j_{MAX,CO2}$ ($mA \cdot cm^{-2}$)
20	240
30	239
40	243
50	254
60	270
70	292
80	320

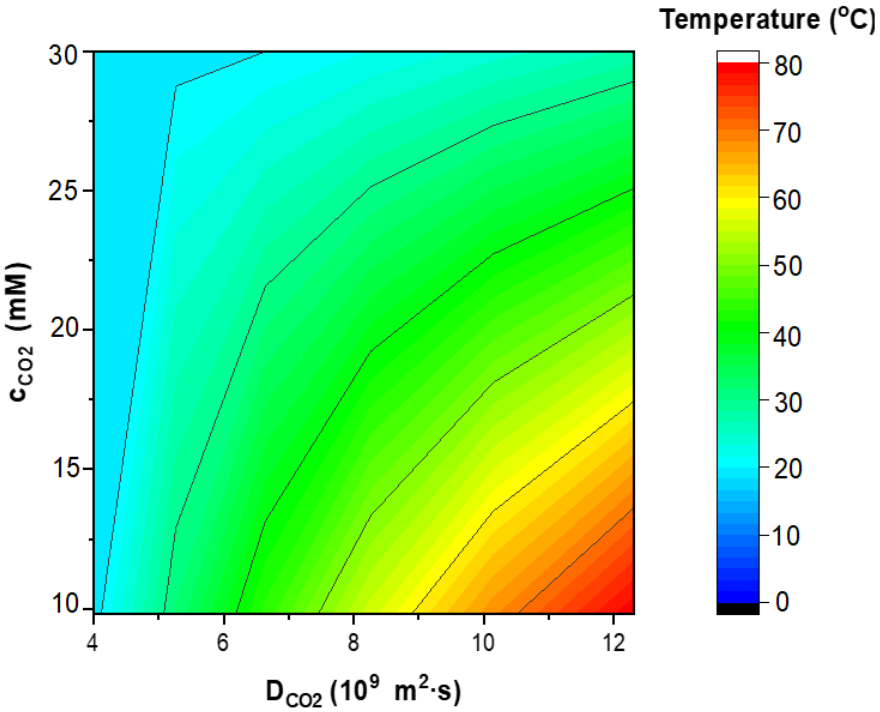

Figure 4.7: Contour plot of the effect of temperature on the CO_2 solubility and diffusion. Data obtained from equations A2.1 and A2.2 in Appendix A.1.2).

4.6 Fundamental studies using ATR-SEIRAS

The protocol and setting for performing ATR-SEIRAS are described in Chapter 3. Because it is well-known that CO_2 electrolysis involves an intermediate CO product on Cu electrocatalyst, this approach was used to analyze CO adsorption on Cu as the effect of temperature. Figure 4.8 shows in-situ ATR-SEIRA spectra for CO signal at different working potentials (vs. RHE) and temperatures. According to the results, the CO peak intensity and position decreased with increasing cathodic potentials, regardless of the operational temperature, due to chemical changes caused by bonding changes between the adsorbed CO and the surface, or the Stark effect, which occurs when the dipoles interact with the electric field [136]. However, those effects appeared to be enhanced when the temperature was raised, as both the intensity area and stretching frequency of the CO peak decreased at all measured potentials.

Although CO coverage was not quantified, ATR-SEIRAS spectra can estimate CO concentration. No significant differences exist between ambient conditions and 40°C at less reductive potentials (-0.5 V vs. RHE), as peaks do not decrease in intensity, suggesting saturated CO concentrations. The peak intensity was notoriously reduced at very reductive potentials (>-0.9 V vs. RHE), but this may be on the verge of further reduction towards C_{2+}. Additionally, experiments at 60°C showed a significant decline in peak intensity due to the weakening of CO binding

strength, enhanced CO desorption, and decreased CO concentration. In agreement with previous findings, CO-CO coupled selectivity (i.e., C_{2+} products) is favored at lower temperatures, while CO selectivity is enhanced at higher temperatures.

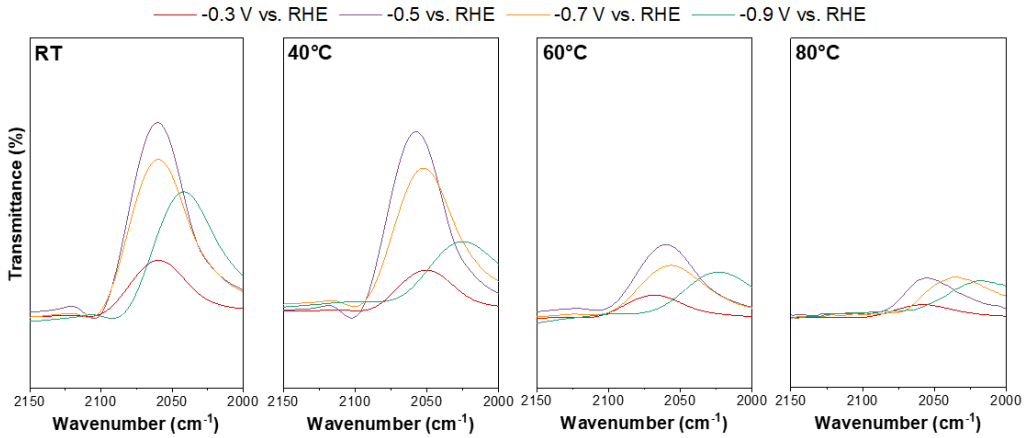

Figure 4.8: ATR-SEIRAS CO adsorption peak for COR at different potentials and temperatures.

4.7 Effect of the heating method on CO_2 electrolysis

The lack of a standardized protocol and method for determining proper electrolyzer heating in CO_2E makes comparing studies at high temperatures challenging [11]. I conducted a study to analyze the impact of cell heating methods on results. For this, I implemented two additional heating methods. The first involved heating only the anolyte reservoir (60 mL) with a heating plate to the desired temperature while the other elements of the reaction system remained at room temperature. The idea behind this was that the anolyte, with its high heat capacity, would be able to keep the electrolyzer at a uniform temperature. The second method involved connecting heating rods to the cathode and anode's flow fields and inserting a thermocouple into the reactor, simulating the effect of commercial heating tape. This enabled the reactor to operate at the given temperature.

The experiments were run at temperatures >60°C, as variations in product selectivity were more noticeable at higher temperatures. Results from Figure 4.9 showed a few notable differences in the product distribution between the three heating methods. While only slight differences can be seen between the direct cell heating method and the use of the heating box (i.e., results from Figure 4.3, which was the heating method used for the experiments), significant variations are found when comparing those obtained from electrolyte heating, especially with regards to C_{2+} and increased H_2 selectivity. Furthermore, when measuring the cell temperature during these experiments, I found that the experiment with the anolyte heated to 60°C had a cell temperature of 28°C, the 70°C anolyte had a cell temperature of 32°C,

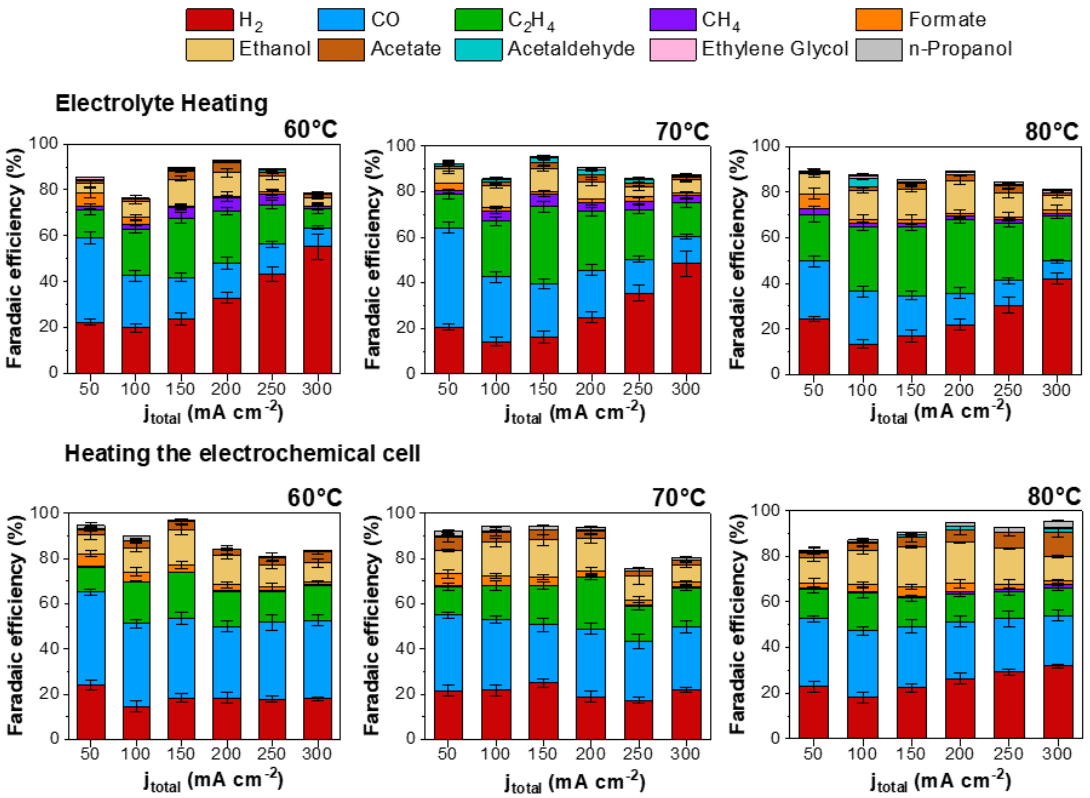

Figure 4.9: Effect of the cell heating in the product distribution using two different methods at different operating temperatures.

and the 80°C anolyte had a cell temperature of 35°C, showing how insufficient this method is for cell heating. These results remarked the importance of proper heating as an inconsistent method might mislead some conclusions on the temperature effects in mass transport and product distribution.

As previously mentioned, CO_2 electrolysis could generate heat from the charge transfer or electrical resistances (resistive heating). Corral et al. established that alterations in temperature inside the electrolyzer affect the CO_2 concentration at the gas-liquid interface, thus limiting CO_2 mass transport [137]. They reported a temperature increase of 7°C to 24°C between 300 to 500 $mA \cdot cm^{-2}$ for CO_2R, which they attributed to the heat released from exothermic reactions at the surface. Bearing this in mind, a customized MEA cell was used to precisely measure the temperature near the GDE (with multiple holes for placing thermocouples in different cell sections). In my experiments at 300 $mA \cdot cm^{-2}$ and E_{cell}= -3.58 V, the estimated thermoneutral potential close to 1.5V and the electrode area of 2.25 cm^2, generated an ohmic heat production of 1.4 W. This led to a temperature rise of 3 °C at the cathode (changes of temperature and the released heated are found in the Appendix A.1.4). Given the insignificant change in the reactor, it is evident that any temperature fluctuations caused by resistive heating will be insignificant.

In industrial scale-up, this phenomenon remains relevant since resistive heating is dominant at elevated temperatures at larger-size electrolyzers.

4.8 Long-term stability of CO_2R at elevated temperatures

By carrying out experiments over a long period of time (50 hours) at elevated temperatures, I monitored product distribution and stability. Figure 4.10 displays electrolysis's cell potential and product distribution at 60°C and 150 $mA \cdot cm^{-2}$. The Faraday efficiency of the gas products was determined by taking the average of the simultaneous injections in the GC, while the liquid products were determined by regularly collecting samples from the anolyte and cathode. To avoid any potential evaporation of the anolyte, a larger reservoir (400 mL) was used compared to the standard 60 mL used in all other experiments, and continuous operation was maintained to increase GDE durability.

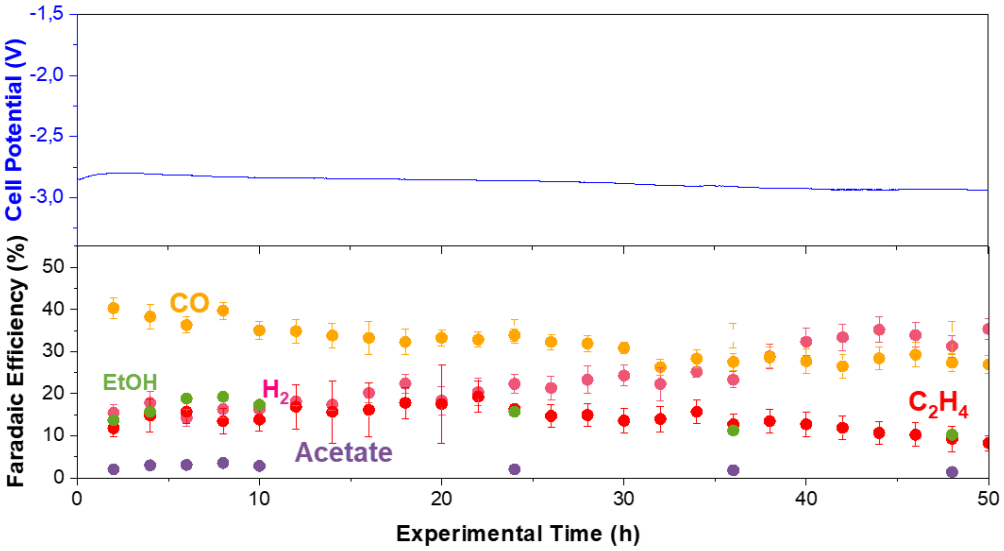

Figure 4.10: Long-term stability test at 60°C and 150 $mA \cdot cm^{-2}$ using Cu-electrocatalyst.

The device's operating potential stayed constant during the entire operation, with an initial potential of -2.8 V and a slight increase of 100 mV after 50 hours. Initially, CO was the primary product at 39%, but this decreased over the 50-hour test to 25%. The ethylene selectivity fluctuated between 10-20% throughout the experiment. Initially, ethanol was relatively high at nearly 20%, though this decayed quickly to 10%, at which time it remained relatively stable; this might be attributed to crossover and further oxidation at the anode. HER increased from 15% to 38% at the end of the experiment, suggesting that flooding might occur even by operating at higher temperatures for a longer experimental time.

The CO_2 electrolyzer ran for 55 hours before a sudden rise in potential led to the short-circuiting of the cell. Such phenomena were determined to be caused by low

membrane hydration, which contributed to the chemical degradation rather than limited CO_2 mass transport. Even though this study showed that temperature might be a powerful strategy for overcoming CO_2 mass transport limitations, maintaining CO_2R at MEA for extended periods still remains challenging.

4.9 Summary

By performing a systematic study, I examined the effects of temperature on zero-gap CO_2 electrolysis and summarized the most interesting findings of this study:

- Operating at elevated temperatures increased CO_2R activity and decreased the cell potential (3-fold in total current density from RT to 80 °C with 500 mV potential drop).
- At temperatures >50°C, a selectivity shift towards CO (FE_{CO}>40%) was observed at industrially relevant conditions due to the weakening of the CO binding strength to the surface. ATR-SEIRAS measurements support the trend of faster CO desorption at elevated temperatures.
- Operating at higher temperatures (>50°C) suppresses significantly HER (e.g., 15.0% at 300 $mA \cdot cm^{-2}$ at 80°C) and delays the GDE flooding (low capacitance), increasing the CO_2R durability. These effects are associated with enhanced CO_2 mass transport, water management, AEM stability, and higher salt solubility at these conditions.
- Higher temperatures enhanced the mass transport of CO_2, resulting in a higher limiting current density and demonstrating that enhanced diffusion effects might overcome those from reduced CO_2 solubility during the performance.
- Temperature also seemed beneficial in reducing product crossover, inhibiting the volatile compounds crossover by favoring its evaporation through the GDE.
- Heating methods heavily influence catalytic performance in these experiments, and incorrect heating might lead to a misinterpretation of temperature effects in CO_2E.
- Although resistive heating might not cause significant temperature rises in small electrochemical cells, it does at industrial scales.
- This study highlights the benefits of operating CO_2R at elevated temperatures under industrially relevant conditions to reduce energy consumption and improve stability (50 hours experiment). Furthermore, these findings provide strategies for combining these benefits with designing and optimizing selective electrocatalysts, GDEs, and AEMs to address current limitations in this field.

Chapter 5

Tandem catalyst approach for CO_2 electrolysis

Contribution

Ph.D. candidate Clara Brunn helped me through the XPS characterization (found in the Appendix from this Chapter). As for the rest, I performed all the synthesis, characterization, and testing of the experiments presented here.

5.1 Chapter Overview

CO_2R is a multi-electron transfer mechanism that produces various hydrocarbons and oxygenated products on Cu electrocatalysts. However, Cu still suffers from narrow selectivity, and production rates for C_{2+} products at high current densities [40]. Several strategies have been used to control the selectivity using Cu electrodes, including surface modification, morphology control, use of single atoms, or bimetallic catalysts to tune the d-band position [11]. While the CO_2R activity has been improved with these methods, the selectivity for specific C_{2+} products (e.g., ethanol) has not significantly improved compared to commercial Cu nanoparticles. Designing new catalysts and electrodes is key to simultaneously achieving selectivity, yield, and energy efficiency of a specific product at the industrial scale.

An exciting approach for tuning the selectivity towards C_{2+} products is combining Cu with a CO-producing catalyst, known as tandem catalysis, which increases CO local concentration and can reduce overpotentials [100]. The coupling of Cu with Ni–N–C, Ag, Zn, or Au at the catalyst layer maximizes the CO-CO coupling reaction rate by increasing CO flux at the surface, thereby improving the selectivity and production rate of C_{2+} compounds. However, the metal loading and the spatial arrangement of the catalyst layers determine the optimal catalyst preparation. Consequently, controlling these parameters during synthesis is necessary to achieve the atomically optimum location of active sites and CO_2E performance.

This chapter studies the rational design of tandem catalysts by coating two independent layers of commercial nanoparticles or sputtering them through the layer-by-layer electrode preparation technique (using Ag, ZnO, and Au as co-catalysts). Initial studies were conducted to determine the effect of fabrication methods, mass loading, and composition ratios in tandem catalysts. Cross-section SEM character-

ization help to verify the design principle of tandem catalysts after the electrode preparation. Electrochemical tests assess the benefits of adding a CO-selective layer through gas mass transfer (CO utilization), product selectivity, and branching ratio between C_{2+} products.

5.2 Effect of the synthesis method and electrolyzer configuration for tandem-based electrodes

5.2.1 Comparison of the preparation method

I considered two techniques for electrode synthesis: a two-dimensional (2D) thin film and a 3D nanoparticulate layer. Detailed information for the fabrication can be found in Chapter 3, Section 3.3. In principle, the 2D structures (sputtering) enhance the activity and selectivity, maintaining a uniform local reaction environment since the catalyst grows on the substrate, as opposed to coating commercial nanoparticles-electrodes. A preliminary study conducted by Li et al. reported high selectivity of Cu/Ag thin films towards ethanol (41% with $Cu_{0.86}/Ag_{0.14}$ at 250 mA $\cdot$ cm^{-2}), which makes this synthesis method attractive for tandem applications [138]. Furthermore, I also prepared 3D nanoparticle-based electrodes, as it is one of the most widely used methods to coat the electrocatalysts (with thick active layers of 1-10 µm) and might offer insight into the performance of my electrodes in comparison to the current state of the art.

Before evaluating the effect of the different methods in our prepared-tandem electrodes, it was necessary to perform benchmark experiments of Cu-GDE synthesized by sputtering or deposited by spray-coating to see if there are significant effects between the preparation method and decouple from those expected from the tandem catalysts. A comparison between the electrode preparation using these two different preparation methods can be found in Figure 5.1.

For this experiment, the Cu thickness and the Cu-mass loading were maintained at 100 nm and 1 mg $\cdot$ cm^{-2}, respectively. Effects on the CL thickness and mass loading were evaluated in a further section of this chapter. However, a preliminary comparison of the effects of these methods on the product distribution at different current densities showed that there were no significant differences between both methods at lower current densities 50-200 mA $\cdot$ cm^{-2} (FE_{C2H4} =34% for the sputtered sample, whereas 36% for the NP sample at 200 mA $\cdot$ cm^{-2}). At higher current densities (>200 mA $\cdot$ cm^{-2}), higher selectivity towards HER was observed in the samples prepared with NPs compared to the sputtered sample. I tentatively attributed the high HER to an insistent particle distribution during the spray-coating and low surface active sites for CO_2R. Since there was no significant difference between those synthesis methods at low-current density regime (applied conditions for further

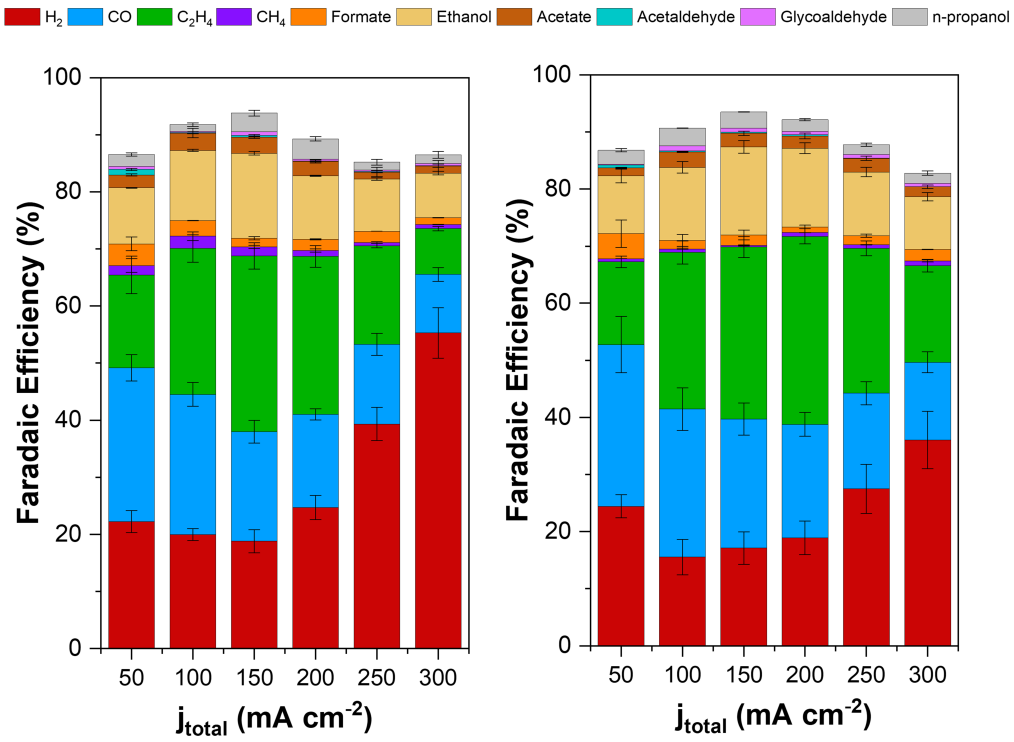

Figure 5.1: Product distribution of Cu-based electrodes on Sigracet 39BB prepared by different methods a) Sputtering (CL: 100 nm) and b) by spray-coating (1 mg $\cdot$ cm^{-2}).

experiments as I ensured a stable performance without compromising the threshold of industrial relevant conditions), I selected coating commercial nanoparticles to prepare my electrodes, as it is simpler to become industrially scalable method than the sputtered counterpart.

Nevertheless, since the sputtered GDE was closely comparable to the nanoparticulate GDE, I did a quick survey testing the potential for preparing our tandem catalyst through different methods. As shown in Figure 5.2, I considered alternatives for electrode preparation and measured partial current densities for different products at 150 mA $\cdot$ cm^{-2} for two hours each. Bare Cu (from sputtering and nanoparticles) showed slight differences compared to the results shown in Figure 5.1 (those conducted at shorter reaction time), but there were used as benchmark samples. Initially, I considered using Ag as a co-catalyst through different electrode approaches, including the layer-by-layer, co-sputtering, or deposition of the co-catalyst in the MPL, keeping the Cu/Ag 50:50 ratio. Loadings and thickness for both approaches were the same as those used in Figure 5.1. Catalyst screening between the different electrodes (product distribution and cell potential) is found in Figure 5.2.

From these results, I could see some exciting trends between samples. I want to point out that measurements from Figure 5.2 represent a preliminary evaluation of the potential application of tandem catalysts in my reaction system, meaning

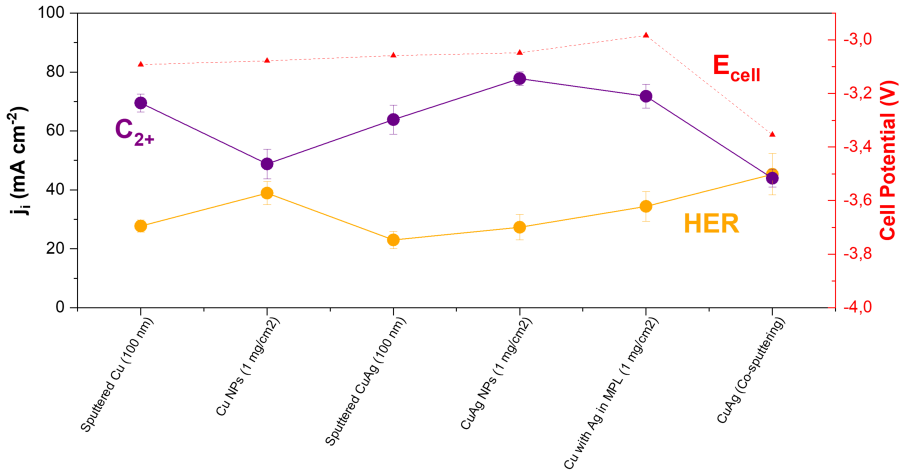

Figure 5.2: Preliminary studies and catalysts screening in terms of the partial current density of main products and cell potential of the different approaches for electrode preparation.

no synthesis parameter has been fully optimized. The layer-by-layer approach (Cu/Ag) seemed the best method for preparing the tandem catalyst compared to co-sputtering or deposition of one layer at the MPS and the other in the MPS of the GDL (j_{C2+}=77 mA $\cdot$ cm^{-2} compared to 40 mA $\cdot$ cm^{-2} from co-sputtering). From these results, I did not observe any synergistic effect with the simultaneous co-sputtering of Cu and Ag, showing that they might have independent effects. In addition, it seemed that the nanoparticulate approach was better than the sputtered one in the layer-by-layer approach, as partial current density for C_{2+} is higher in this case (j_{C2+}=77 mA $\cdot$ cm^{-2} vs. j_{C2+}=64 mA $\cdot$ cm^{-2}), supporting my selection on using commercial NPs.

5.2.2 Comparison of the effect of the 3D nanostructured layer fabrication method

As previously explained, the efficiency of the tandem catalysts depends primarily on the spatial arrangement and distribution of the catalyst layer on the carbon support, so the preparation method should maximize homogeneity [139]. Two methods of applying NPs coating have been used, air-brushing with a spray gun and drop-casting. While these methods worked well for thick layers, making thinner ones is challenging. Additionally, the catalyst layer was applied manually to the GDL, which does not always ensure the same uniformity. Different studies have reported these synthesis methods for their electrode preparation, so these two fabrication methods are selected in this study to compare their effect on the catalytic performance [140]. The drop-casting was carried out in different sections of the GDL, trying to cover all the geometric area with the CL, while the spray coating with the airbrush was dispersed throughout all the electrode area, providing a more

homogeneous distribution onto the GDE (details about the methodology are found in synthesis section of Chapter 3) [141]. Figure 5.3 presents the result of the gas-product distribution of the other bare electrodes (total loading of 1.0 $mg \cdot cm^{-2}$) prepared for both methods at different current densities.

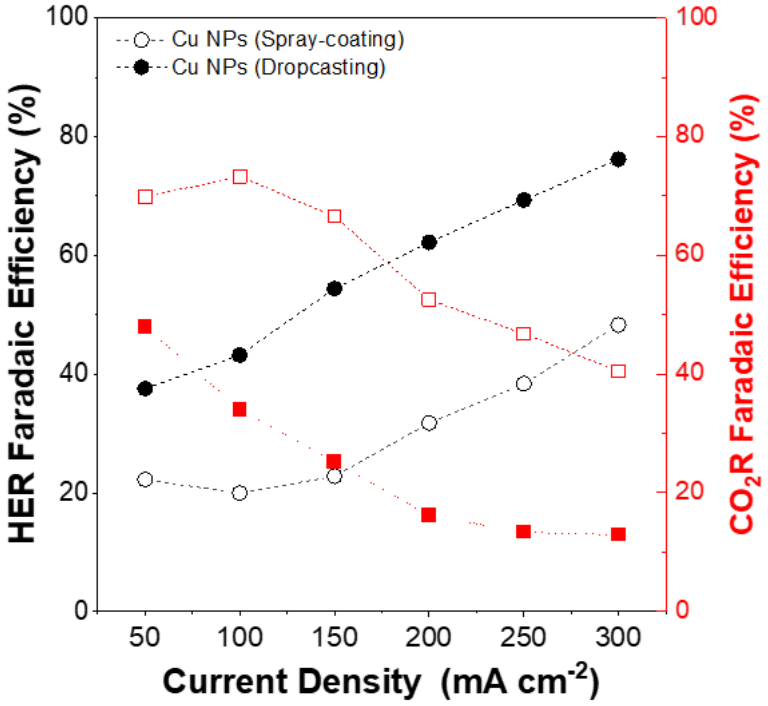

Figure 5.3: HER and CO_2RR selectivity of bare Cu-NPs electrodes on SG39BB prepared by drop-casting and spray-coating.

The results indicate a significant difference between the two preparation methods based on their trends in selectivity. In contrast to spray-coating at the same current density, drop-casting only resulted in 28% selectivity for CO_2R products when compared with 65% selectivity achieved by spray-coating. This might be explained by better catalyst uniformity with the second method. Additionally, samples prepared by drop casting displayed accelerated HER at all tested current densities (almost twice the ratio as samples prepared by spray coating). Many attempts have been made to optimize the electrode preparation method, including alternate studies using spray coating and conditions that ensure distribution on the electrode. However, reproducibility issues might limit this synthesis method, as the same loading cannot guarantee the same CL thickness. In contrast, the isopropanol (IPA):H_2O ratio in the ink during suspension preparation and the drying temperature might have effects during the electrode synthesis[142]. The IPA:H_2O depends on the hydrophobicity/porosity of the substrate, so I used a higher ratio (95:5 IPA:H_2O) for porous substrates and 50:50 for less-porous GDLs.

5.2.3 Mass transport on tandem electrodes: comparison of different tandem approaches

I investigated the mass transport of CO_2 and CO across the different CLs to determine the optimal thickness and distribution of the catalyst layers. An analysis through CO_2 transport modeling has been conducted within the GDE. Based on a total loading of 1 $mg \cdot cm^{-2}$ (corresponding to a thickness of around 2 µm), it was estimated that 60-80% of the initial CO_2 concentration could pass through the thick catalyst layer between 0.1 and 0.5 A [98]. Hence, the system will not be mass transport limited since there is still enough CO_2 left to transport to the top Ag catalyst layer for reduction into CO during electrolysis.

GDEs prepared with Ag, or Au layers on top of the Cu catalyst layer simulate simultaneous conversion between CL/electrolyte and CL/GDL interfaces (layer-by-layer). In these electrodes, electrochemical CO_2 to CO reduction occurs in the CO selective layer, and the produced CO molecules are subsequently fed into the Cu layer for further conversion to C_{2+}. This approach is based on the assumption that CO self-diffusion in porous electrodes (1.93 x 10^{-5} $m^2 \cdot s^{-1}$) is much greater than its diffusion coefficient in water (2.13 x 10^{-9} $m^2 \cdot s^{-1}$) [98], meaning that CO gas molecules generated on the CO-selective layer diffuse backward much faster into the Cu catalyst layer than they diffuse forward into the liquid electrolyte, thus providing a basis for efficient CO utilization. I used the terms Cu/Ag to refer to tandem catalysts prepared by the layer-by-layer method, where Cu represents the metal at the bottom, and Ag represents the metal at the top.

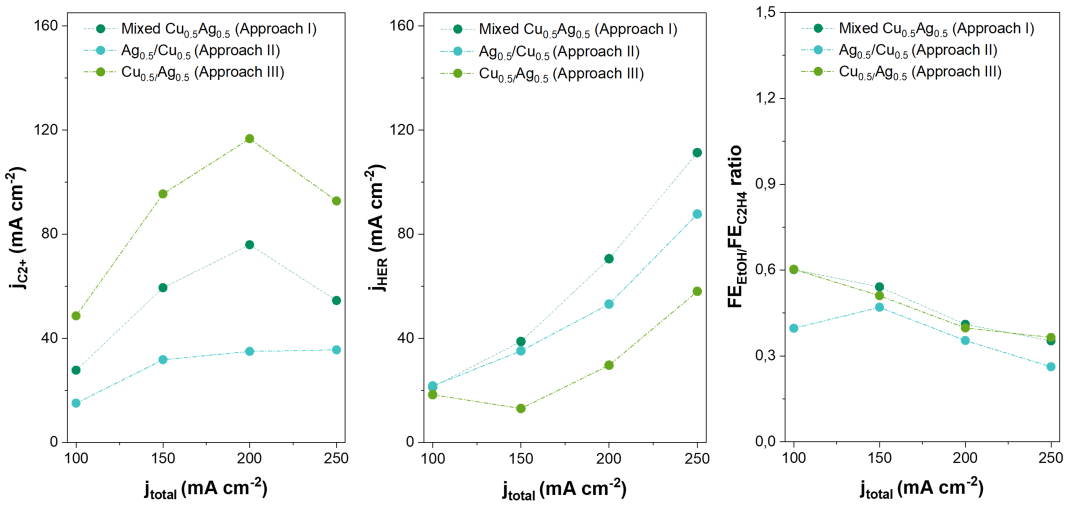

Figure 5.4: Comparison of different performances of Two-layer GDE with Cu on top, Ag on top, and nanoparticle mixture of Cu-Ag electrodes. a) C_{2+} partial current density, HER partial current density, and c) Branching ratio between ethylene and ethanol.

Tandem catalysts with different spatial arrangements were prepared to understand the role of coupling two layers in the selectivity of major C_{2+} products. Those

included two-layer electrodes $Cu_{0.5}/Ag_{0.5}$, $Ag_{0.5}/Cu_{0.5}$ and mixed Cu and Ag, composed by a unique catalyst layer of mixed nanoparticles physically and randomly disperse with the same mass composition and loading (co-deposition). The $Ag_{0.5}/Cu_{0.5}$ is prepared with a reverse structure comprising the bottom Ag catalyst layer and top Cu catalyst layer, where it is expected that most of the supplementary CO gas molecules diffuse backward through the MPL instead of forward to the top Cu catalyst layer, resulting in low utilization efficiency of supplementary CO (inverse layer). Figure 5.4 shows the catalyst screening results and the gas product distribution at different tandem catalysts from three different approaches at 200 $mA \cdot cm^{-2}$, where the respective loadings for Cu and Ag catalysts were kept the same for the three samples.

$Cu_{0.5}/Ag_{0.5}$ tandem electrode exhibits higher j_{C2+} value than those fabricated by reverse structure and CuAg mixture. With the Ag-layer on top of the catalyst layer, C_{2+} selectivity was slightly improved compared to bare Cu nanoparticles (Figure 5.1), however, it is evident that these electrodes had low CO utilization since the CO Faradaic Efficiency for tandem catalysts was around 25-35% at 150 $mA \cdot cm^{-2}$. The electrode with the Cu-layer on top ($Ag_{0.5}/Cu_{0.5}$) exhibited the lowest j_{C2+} among all three electrodes. Based on these results, the proposed tandem electrode structure layer-by-layer with Ag on top and Cu on the bottom appeared to have the ideal CO_2/CO mass transport behavior to improve gas transport across the electrode and maximize its utilization. The branching ratios between ethylene and ethanol in the attempt to synthesize a selective catalyst did not differ significantly between the three electrodes, demonstrating ethylene as the major C_{2+} product.

These results raise interesting questions about using tandem catalysts to improve C_{2+} rates. Did I fabricate tandem catalysts with optimal loadings? What is the proper molar composition of metals? Finally, am I using the proper CO-selective catalyst to maximize the Cu synergy with the co-catalyst? In the following sections, I will discuss a series of experiments to address these questions and optimize the tandem approach.

5.2.4 Effect of mass loading and catalyst thickness

The mass loading of the catalyst in the substrate determines the number of active sites and the CL thickness of the layer, which significantly impacts the kinetic reaction and mass transport [93]. Before optimizing the tandem catalyst loading, I would like to ensure that the electrode loadings for which I am preparing them are appropriate. As a result, I studied the effect of mass loading on bare copper electrodes. Since the loading measurement is an approximated estimation (relation weight of the GDE before and after the coating of each layer and the geometric area), I prepared electrodes with loadings that were not close in magnitude to see a more general impact of this factor on the catalysis.

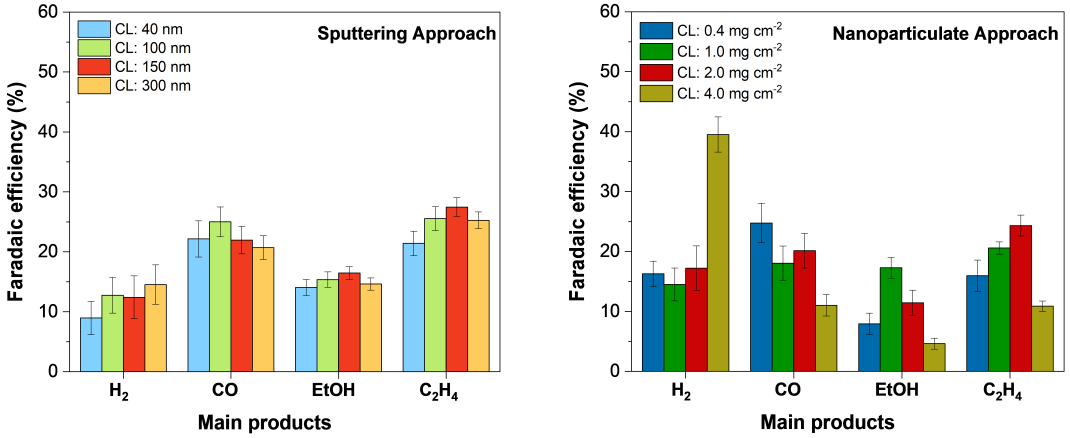

Figure 5.5: Effect of the catalyst layer thickness and mass loading in product selectivity of electrodes prepared by sputtering and nanoparticulate approaches.

The influence of catalyst loading on selectivity for major products on Cu-electrodes was examined by sputtering (40-300 nm) and coating NPs (0.4-4 mg $\cdot$ cm^{-2}) at 150 mA $\cdot$ cm^{-2} (Figure 5.5). The selectivity of sputtered samples did not differ with different CL thicknesses. An explanation for such consistency between the samples can be found in the homogeneous deposition of Cu at the CL and the presence of a thin layer to ensure proper diffusion of CO_2 through the GDE. In contrast, commercial nanoparticle loading showed an interesting pattern. Catalyst mass loading greater than 2.0 mg $\cdot$ cm^{-2} decreased selectivity towards carbon products (below 26%), favoring the HER (40%). Therefore, I expected that higher mass loading would result in limited CO_2R performance, as the CO_2 mass transport in the CL is insufficient (this loading represents a thicker layer equivalent to 3-5 µm). Furthermore, low loadings showed higher CO selectivity, presumably due to fewer active sites for C_{2+} products (CO-CO coupling depends on the proximity between active sites). An optimal value for the total mass loading of the catalysis layer was found at 1.0 mg $\cdot$ cm^{-2}, which agrees with values as total loadings reported in the literature for tandem electrodes [100].

5.3 Electrode Characterization

The characterization of the tandem electrodes was conducted with planar and the cross-sectional scanning electron microscope (SEM), energy-dispersive X-ray spectroscopy (EDX) elemental mapping, and XPS. Figure 5.6 shows the planar images of the CL and cross-sectional SEM and EDS mapping images of a representative Cu/Ag tandem electrode with Cu and Ag loadings of 0.5 and 0.5 mg $\cdot$ cm^{-2}, respectively. The Ag and Cu layers, the Nafion, and the MPL diffusion layer are well-defined EDS mapping. Post-reaction characterization of these samples didn't present any major effect on the cross-sectional imaging but some more pronounced effects on the CL

morphology due to microenvironment effects during electrolysis. At the same time, any interfacial alloying or particle agglomeration wasn't observed between phases, as expected, due to the thermodynamically favored separation between Cu and Ag layers [143].

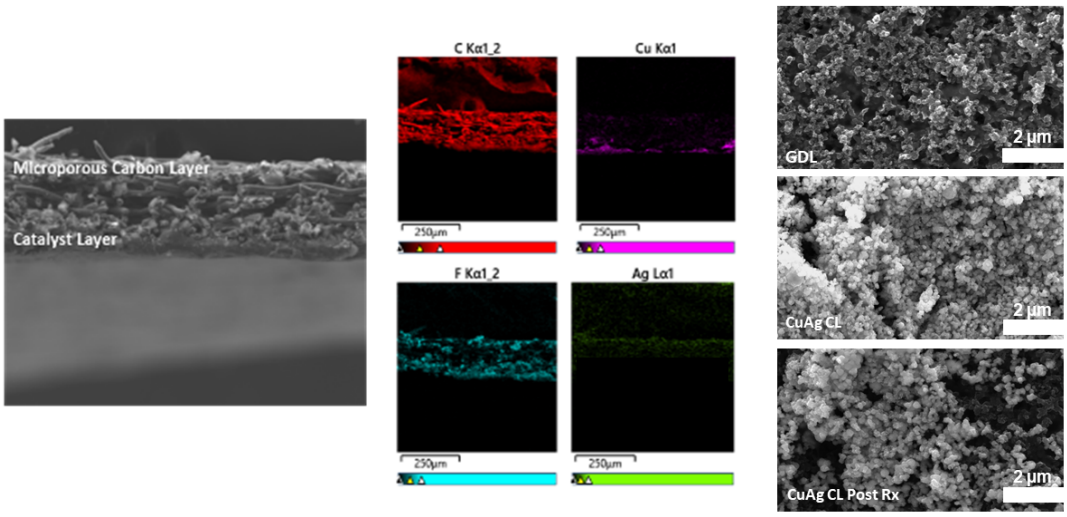

Figure 5.6: SEM cross-sectional images of tandem electrodes a) Cross-sectional SEM image of Cu/Ag catalyst b) EDS Mapping of a Cu/Ag tandem electrode with two catalyst layers c) Morphology of the cathode GDE at different reaction stages.

XPS was conducted to check impurities at the surface. Therefore, an XPS scan was conducted on a bare Cu electrode, which revealed the presence of adventitious copper, carbon, and oxygen and high-intensity peaks that indicated fluorine, possibly due to the Nafion layer used as a binder (Appendix A.1.5). Nonetheless, no impurities or other metals that might interfere with the CO_2R were observed within the limit of detection of the XPS analysis. The XPS angle-resolved use could be limited by the depth of XPS being < 10 nm, depending upon the material and the kinetic energy of the electron being measured, making difficult the measurement of composition and thickness of the different layers or using this technique for the tandem catalysts. For this reason, SEM cross-section was the implemented technique to characterize the composition of such layers.

5.4 Performance of Tandem Electrodes with Cu and CO-Selective catalyst layers

As mentioned in the previous section, the CO_2R is an adsorption and reaction process that occurs on the active sites of a catalyst surface. Varying the composition might improve its performance for C_{2+} products in gas-phase electrolyzers. While it has been extensively studied in Ag and Cu-based catalysts, research into non-Cu-based, bimetallic, or tandem catalysts is limited, calling for further research in the optimization of catalysts [141, 75]. This section presented results concerning Cu/Ag

tandem catalysts prepared layer-by-layer, focusing on the effect of loading and the effect of the CO-selective catalyst.

5.4.1 Catalyst Screening Tandem Electrodes and the effect of the Ag-loading on the C_{2+} production

Compared to the bare Cu electrode at the same loading and active area, the increase in local CO flux generated by the tandem Ag layer may reduce the potential for C_{2+} formation since the CO formed on the top layer should be further reduced on Cu, balancing the CO productivity and consumption. The CO in the Ag-catalyst layer was added to the generated CO by the Cu layer itself, increasing the local concentration of CO near the Cu sites and the CO utilization range, given the enhanced mass transport behavior.

Some Cu/Ag tandem electrodes were fabricated utilizing this principle, setting the total mass loading of 1.0 $mg \cdot cm^{-2}$ and varying the Cu and Ag loadings (0.1-0.9 $mg \cdot cm^{-2}$) proportionately. Samples are labeled as Cu_a/Ag_b (where a and b are the metal composition). Figure 5.7a illustrates the Faradaic Efficiency for multiple tandem catalysts with different molar compositions under the same testing conditions. Figure 5.7b illustrates HER, CO, and C_{2+} partial current densities as a function of the Ag-loading. Figure 5.7c illustrates the ratio between ethanol and ethylene branching as a function of cell potential for the main tandem catalysts.

Under the same operating conditions, tandem electrodes incorporating commercial Cu and Ag nanoparticles achieved an increased C_{2+} Faradaic Efficiencies compared to bare Cu (nanoparticulate and sputtered samples). Among all of the prepared samples, $Cu_{0.8}/Ag_{0.2}$ showed the highest C_{2+} selectivity (ethanol and ethylene as main products) at 150 $mA \cdot cm^{-2}$ at 67% and E_{WE} = -3.6 V (although $Cu_{0.6}/Ag_{0.4}$ also showed a similar selectivity with 59%, still higher than the 46% with bare Cu electrodes). It is possible to correlate the poor performance of tandem $Cu_{0.4}/Ag_{0.6}$ and $Cu_{0.2}/Ag_{0.8}$ with an HER enhancement due to the ineffective use of the surface area on these structures and its location far from the interface, as well as the presence of thicker Ag-layers (Figure 5.7b). These results suggest that low Ag-loading might lead to insufficient CO supply (despite not being observed in my results), whereas an increase in the Ag-loading reduces Cu-active sites and C_{2+} selectivity. In the same manner, partial current densities (j_{C2+}) increased when the Cu/Ag ratio varies between 1-4, where $Cu_{0.8}/Ag_{0.2}$ had a maximum value of approximately 95 $mA \cdot cm^{-2}$.

In this study, the optimal values obtained agreed with those reported by Shen et al., who showed the same tendency in the variation of CO-selective layers in ethylene selectivity [98]. Alternatively, differences between samples with low loadings could be seen by operating at a constant cell potential (Figure 5.7c). For this approach,

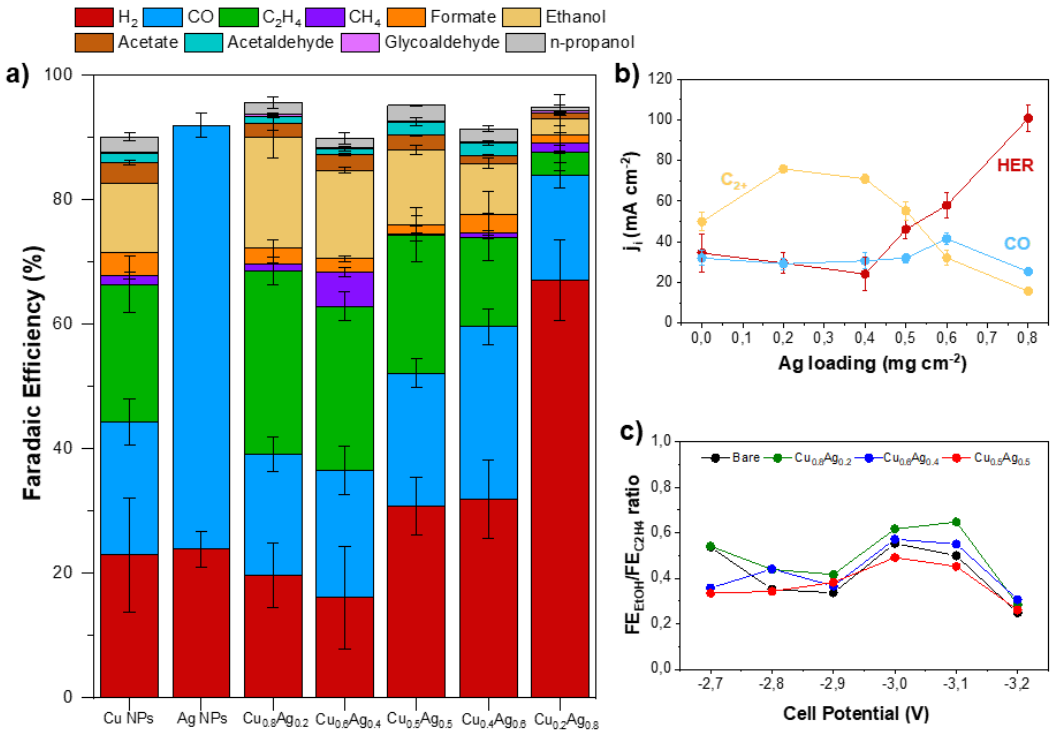

Figure 5.7: Catalyst screening of different Cu/Ag-tandem catalysts varying the Ag loading prepared by layer-by-layer approach a). The product distribution of gas-and liquid products at different electrodes b) Effect of the Ag loading in the partial current density for different products. c). Branching ratio between ethylene and ethanol at different cell potentials.

I switched from the Teflon flow cell to the MEA cell (to take advantage of the reduced cell resistance and evaluate reproducibility in another cell configuration). Even though no major differences were observed (similar product distribution trends were seen between different cell configurations with similar ethanol/ethylene ratios), low Ag-loading appeared to favor the formation of oxygenate over ethylene at cell potentials below -3.1 V. While there were some variations in C_{2+} oxygenate species, no significant improvements were observed because the tandem catalysts are made using Cu, and Ag nanoparticles that seem to favor C_{2+} gas products over liquid products (ethylene), as reported in literature [98, 99].

5.4.2 Role of different CO-selective catalysts in product selectivity for tandem electrodes

I extended the design of tandem electrodes to involve more active CO generation catalysts, such as ZnO and Au to demonstrate the effect of the "CO-selective layer" on product distribution. Figure 5.8 illustrates the results of testing a series of tandem electrodes at different current densities (Cu loading of 0.8 mg $\cdot$ cm^{-2} and ZnO, Au

or Ag loading of 0.2 mg · cm^{-2}).

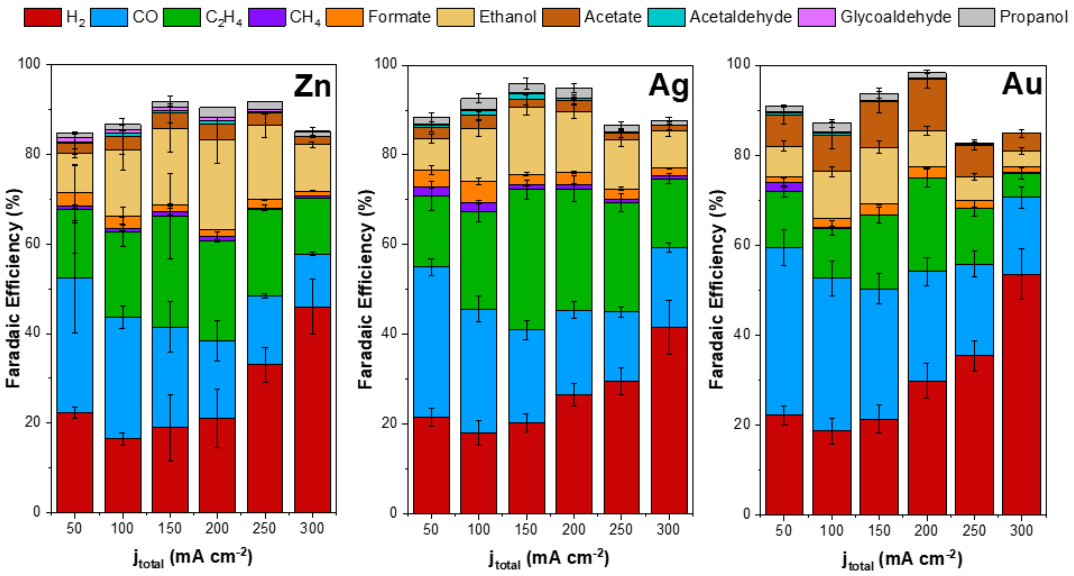

Figure 5.8: Product distribution through the synthesis of different tandem catalysts varying the "CO-selective" catalysts, keeping its loading at 0.2 mg · cm^{-2} as a function of current density.

Compared to $Cu_{0.8}/Ag_{0.2}$, $Cu_{0.8}/Au_{0.2}$ and $Cu_{0.8}/ZnO_{0.2}$ tandem electrodes exhibited a reduced selectivity toward C_{2+} products (e.g., 64% for $Cu_{0.8}/Ag_{0.2}$, compared to 52% for $Cu_{0.8}/Zn_{0.2}$ and 53% for $Cu_{0.8}/Au_{0.2}$) at 150 mA · cm^{-2}. Au, as a co-catalyst, was found to have higher selectivity toward CO at all the tested current densities, which may be due to the strong CO binding at the surface compared to the other metals. Moreover, interesting trends in product distribution were observed with the different catalysts, with Ag-layers favoring C_2H_4 (35% at 150 mA · cm^{-2}), Zn-layers favoring ethanol formation (23% at 150 mA · cm^{-2}), and Au-layers favoring acetate formation (12% at 150 mA · cm^{-2}). The effect of the co-catalyst on the branching ratio between C_{2+} products is still not fully understood in these approaches, but it demonstrates how metal synergies are crucial to the mechanisms and distribution of C_{2+} selected tandem catalysts, opening new research directions.

5.5 Studies over Cu/ZnO tandem catalyst in MEA-type cell

Due to recent interest in tuning the selectivity of oxygenates (ethanol) over ethylene, I focused on studying more in detail the effect of ZnO loading in layer-by-layer tandem electrodes. I performed these experiments in MEA to verify the reproducibility between configurations again, but primarily to couple this approach with the effects of temperature, as studied in Chapter 4 with the configuration. Figure 5.9 shows the partial current density and branching ratios between ethanol/ethylene at different cell potentials.

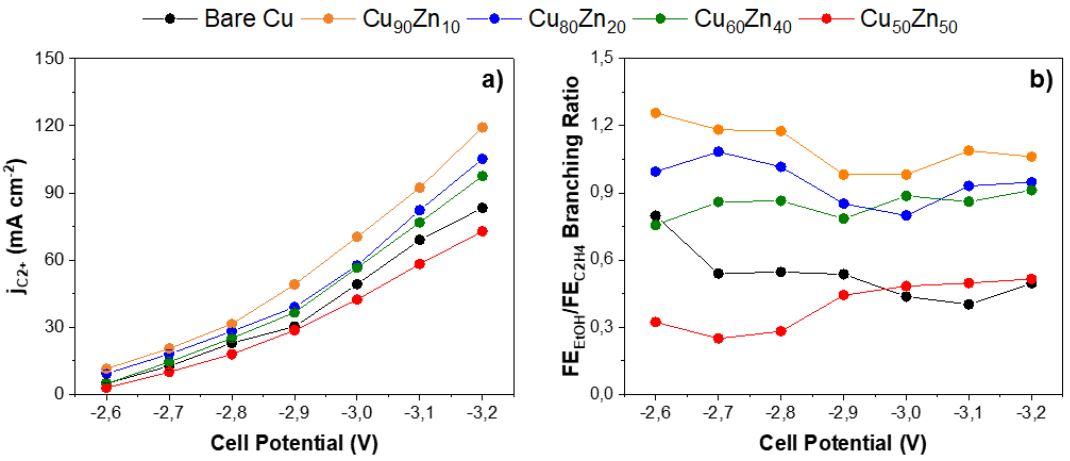

Figure 5.9: Comparison of performance of Cu/ZnO tandem catalysts varying the metal loading. a). Effect of the ZnO loading in the partial current density of C_{2+} products and b) Branching ratio between ethylene and ethanol at different cell potentials as a function of the ZnO loading.

Modifying Cu/ZnO tandem electrodes' molar composition enhanced their activity and selectivity towards C_{2+} products. Optimal compositions of such electrodes were found at $Cu_{0.9}/ZnO_{0.1}$ with a selectivity of 25% for ethanol at -3.1 V and a j_{C2+} of 1.4 times greater than bare Cu (Figure 5.9a). Increasing Zn composition led to a shift from ethanol to CO in all potential ranges, which was explained by more Zn-active sites present. Additionally, as shown in Figure 5.8, using Zn as a co-catalyst improved the ethanol/ethylene ratio (Figure 5.9b). At lower cell potentials, $Cu_{0.9}/ZnO_{0.1}$ and $Cu_{0.8}/ZnO_{0.2}$ had ratios of 1.3 and 1.4, indicating ethanol was more selective than ethylene, which was consistent with literature trends explaining that ethanol is favored at low potentials and ethylene at higher potentials (decline of the branching ratio to 1.03 and 0.95) [138, 144]. Still, $Cu_{0.9}/ZnO_{0.1}$ seemed to be the most promising composition as it showed a higher selectivity for ethanol than ethylene while maintaining a high C_{2+} activity.

5.6 Long-Term Stability of Tandem Electrodes

For practical applications, stability is just as relevant as activity and selectivity. The stability of tandem electrodes has been examined using Cu/ZnO ($Cu_{0.9}/ZnO_{0.1}$) electrocatalysts at 200 mA $\cdot$ cm^{-2}, incorporating temperature and the MEA configuration.

Over the course of the experiment, the tandem electrode maintained stable operation (-2.8 V) with only minor changes in selectivity for main products (and presumably activity). A maximum ethanol selectivity of 25% was achieved within the first two hours and then decreased to 20% after 10 hours. CO remains the main product, and I do not attribute it directly to the tandem approach but instead to the effects

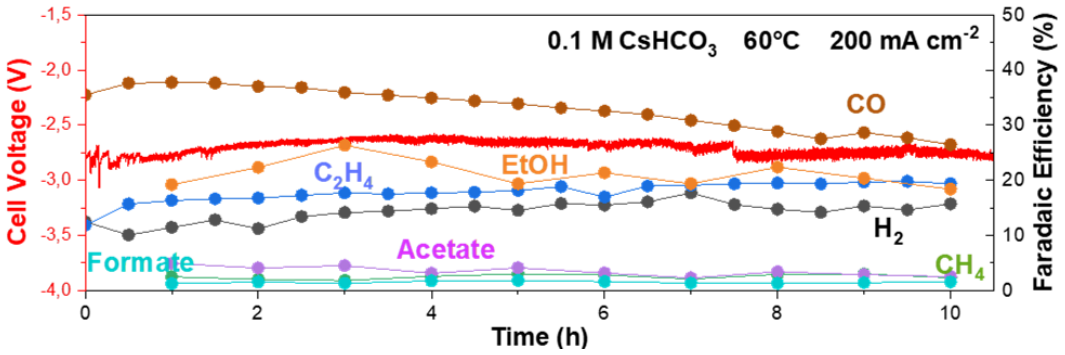

Figure 5.10: Long term experiment of $Cu_{0.9}/ZnO_{0.1}$ at elevated temperatures (60°C) at 200 mA $\cdot$ cm^{-2}.

of temperature (as described in Chapter 4). A longer-term performance evaluation of the tandem catalyst is required to determine its stability over time. Nevertheless, the results in Figure 5.10 indicate that tandem catalysts can produce highly C_{2+}-selective products (even ethanol over ethylene) for extended periods.

5.7 Summary

Using tandem catalysts improved the selectivity of C_{2+} compared to bare Cu electrodes, although they did not surpass the current state-of-the-art selectivity (for example, the Cu/Ag electrode with 85% tandem catalyst in literature [98] compared to 67% from my experiments towards C_{2+} at 150 mA $\cdot$ cm^{-2}). My studies with tandem catalyst provided some exciting trends and results that I will summarize as follow:

- Preparation of electrodes through sputtering and commercial nanoparticles gave similar performances while working at current densities below 200 mA $\cdot$ cm^{-2}. However, when preparing a tandem catalyst, the use of nanoparticles seemed to improve the selectivity towards C_{2+} compared to the preparation of a tandem catalyst through sputtering.
- Coating the NPs into commercial GDL using spray-coating seemed to be better than drop-casting as it provides a more homogeneous distribution of the NPs in the CL.
- The synthesis of tandem catalysts with the selective CO-layer on top, creating two-independent layers in a GDE seemed to maximize the CO utilization by increasing the CO local concentration and improving the gas transport across the different layers.
- The catalyst layer thickness seemed not to have a big effect on sputtered samples at the prepared thickness compared to the commercial NPs loading through an ink suspension. Optimal values for the latest were found at 1.0

$mg \cdot cm^{-2}$.

- SEM-cross-sectional coupled with EDX showed well-separated layers of both metals. XPS characterization technique is limited for this application, as XPS angle-resolve depth can reach just 10 nm.
- SEM Loading of the CO-selective layer seemed to have an effect on the product distribution. High loading enhanced the HER selectivity due to the presence of thicker Ag CL or inefficient use of active sites, while a low loading might lead to insufficient CO supply. The optimal loading of tandem catalyst in my experiments was found at $Cu_{0.8}/Ag_{0.2}$ with FE_{C2+}=67% at 150 $mA \cdot cm^{-2}$.
- Results between different cell configurations are comparable and reproducible, obtained similar trends by switching from a flow cell with a catholyte layer to an MEA.
- The use of different metals as CO-selective layers showed interesting trends in product distribution. The use of Ag seemed to favor selectivity towards C_2H_4 (35% at 150 $mA \cdot cm^{-2}$), ZnO to ethanol (23% at 150 $mA \cdot cm^{-2}$), and Au to acetate (12% at 150 $mA \cdot cm^{-2}$). Still, Cu/Ag-tandem catalyst exhibited the highest selectivity towards C_{2+} of those samples.
- Using ZnO as a co-catalyst helped to favor ethanol production over ethylene with branching ratios higher than 1.0 (using $Cu_{0.9}/ZnO_{0.1}$).
- Long-term test coupling the tandem approach with operation at elevated temperature improved the selectivity towards ethanol while ensuring a stable operation for 10h.

Chapter 6

Developing anion exchange membranes for CO_2 electrolysis

Contribution

Dr. Terry Wilson and Prof. John Varcoe at the University of Surrey conducted AEM synthesis and characterization. Bjørt Óladóttir conducted preliminary experiments on these membranes and confirmed potential application for CO_2 electrolysis using other designs of MEA-electrolyzer. Asger Moss built the reaction heating oven to evaluate the membrane's stability at elevated temperatures. As for the rest, I conducted all the studies and measurements.

6.1 Chapter overview

Recent studies have focused on improving catalytic activity and selectivity for CO_2 reduction and the concomitant anodic reaction. Yet, even though the membrane plays an important role in cell potential and electrolyzer performance, less attention has been paid to it. Understanding how the ionomeric components in the membrane affect the water/ion transport mechanisms will enable improvements in the operation of CO_2Es, providing new tools for further research and development [80].

This chapter evaluates the effectiveness of QA-based AEMs with zero-gap (MEA) electrolysis and industrially relevant current densities for CO_2 reduction. These membranes were prepared using a radiation-grafting technique, where vinylbenzyl chloride (VBC) monomer was co-grafted onto electron-beam activated ethylene-co-tetrafluoroethylene (ETFE) films, followed by amination with either trimethylamine (TMA), N-methyl-pyrrolidine (MPY), or N-methylpiperidine (MPIP) groups [79]. To improve membrane properties, further strategies were considered, such as altering the IEC by varying the chemistry, the proportion of hydrophobic units, functionalization level, or reinforcement and cross-linking. [145, 146].

In the first section, I discussed the synthesis and characterization of the RG-AEMs and correlated their physical properties to their expected performance. Afterward, I investigated the effect of different headgroup chemistries on CO_2E using various electrocatalysts and operation conditions. By comparing these ETFE-AEMs and commercial membranes, I highlighted the advantages of these RG-AEMs, which are chemically stable and provide adequate ionic/water transport. Additionally, I

carried out long-term experiments to demonstrate the stability of CO_2 electrolyzer operation using RG-AEMs. Last, I examine membranes with modified properties (adding cross-linking agents or varying the concentration of the amine group during the amination process) and the effects on CO_2E performance.

6.2 Membrane characterization

6.2.1 Raman Spectroscopy

The ETFE-g-p(VBC) intermediate membrane was subjected to Raman spectra at 30 random sites on ETFE-g-p(VBC) intermediate membranes (laser spot size ca. 2 µm, while penetrating a few µm into the sample), and the integrated area ratios (areas of the 1612 cm^{-1} bands normalized to the 835 cm^{-1} bands) were calculated to measure grafting homogeneity. The spectra presented in Figure 6.1 confirm grafting (79% dog) of pre-aminated intermediate with characteristic bands at 835 and 1444 cm^{-1} (due to the ETFE substrate's $–CF_2–$ and $–CH_2–$ groups), a poly(VBC)-derived band at 1612 cm^{-1} (aromatic ring quadrant mode), and a band at 1267 cm^{-1} (due to the $–CH_2Cl$ groups in the grafted poly(VBC) chains). In addition, the Raman spectra of all RG-AEMs confirm successful amination, based on the disappearance of the poly(VBC)-($–CH_2Cl$)-derived band at 1267 cm^{-1}, and the appearance of diagnostic bands for each of the QA groups (756 and 976 cm^{-1} for TMA, 899 cm^{-1} for MPY, and 704 and 1273 cm^{-1} for MPIP).

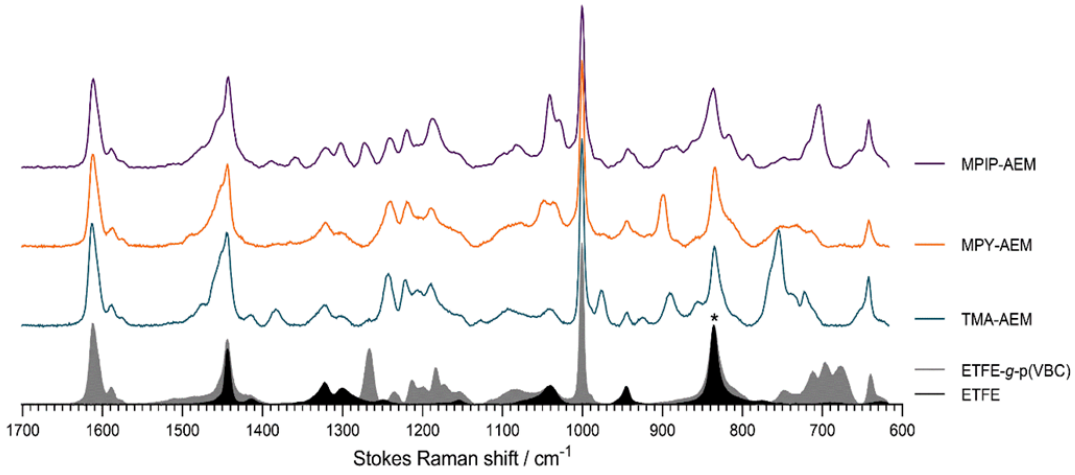

Figure 6.1: Raman spectra of the 25 µm thick ETFE substrate film (black filled) and the resulting ETFE-g-p(VBC) intermediate grafted membrane (gray filled, an average of n = 30 spectra taken at random spots across both surfaces), and the final aminated RG-AEMs with line spectra (average of n = 10 spectra taken at random spots across both surfaces) stacked higher in the order TMA-AEM (teal), MPY-AEM (orange), and MPIP-AEM (purple). Laser wavelength = 785 nm. * Spectra normalized to the intensity of the ETFE-derived band at 835 cm^{-1} to aid visual comparison.

6.2.2 Mechanical and transport properties for synthesized RG-AEMs

RG-AEMs have been characterized in the Cl^- form to confirm their ex-situ behavior, and Table 6.1 summarizes a few of their common physical properties as obtained from 25 µm ETFE films with three different amine groups.

These results show that adding different QA groups to polymer backbones results in a significant change in water content (and swelling) and a less significant change in electrochemical conductivity and ionic conductivity (in-plane measurements with the RG-AEM samples immersed in water at 25 °C). MPIP- and MPY-AEMs exhibit greater WU than TMA-AEMs, due to their hydrophilic nature, as reported previously. Heterocyclic-QAs are expected to form ionic clusters segregated into hydrophilic and hydrophobic phases, leading to enhanced WU values. While higher water content variants might be beneficial, they tend to swell more [147]. Generally, higher IECs and moderate WU AEMs lead to better performance (lower cell potentials and optimized water transport) in CO_2E.

Table 6.1: Key Properties for the Synthetized RG-AEMs Made from 25 µm ETFE Films at Room Temperature in the Cl^- Form

Properties	**TMA-AEM**	**MPY-AEM**	**MPIP-AEM**
IEC ($mmol \cdot g^{-1}$)	2.20 ± 0.02	2.07 ± 0.05	2.09 ± 0.07
Fully hydrated thickness (µm)	56 ± 2	72 ± 2	69 ± 3
σ_{Cl^-} at room temperature ($mS \cdot cm^{-1}$)	18 ± 1	23 ± 2	18 ± 1
Area swelling on hydration (%)	19 ± 3	32 ± 10	47 ± 18
Gravimetric WU (% wt.)	33 ± 1	82 ± 13	85 ± 19
λ(H_2O molecules per exchange site)	8 ± 1	22 ± 4	23± 5

6.2.3 Measurements of the ionic-conductivity

The in-plane Cl^- and HCO_3^- anion conductivities of fully hydrated RG-AEM samples between room temperature and 80 °C were measured. Values are reported in Cl^- form RG-AEMs before any alkaline reagent exposure that risks trace degradations and changes in nano/micro-morphology. However, I also quantified the ionic conductivity in values for HCO_3^-, as it is one of the main ion carriers in CO_2E.

Results for the different synthesized membranes and comparison with commercial Sustainion X37-50 RT are presented in Figure 6.2. For the 25 µm ETFE RG-AEMs, a comparison of the measured HCO_3^- conductivities above 80 °C showed that the MPIP-AEM had slightly lower values than the TMA- and MPY-AEMs. RG-AEMs display higher conductivities than Sustainion due to ion mobility and diffusivity differences between ions and the AEM microchannel structure. In addition, it is expected that Sustainion degrades at elevated temperatures, resulting in low membrane conductivity [92].

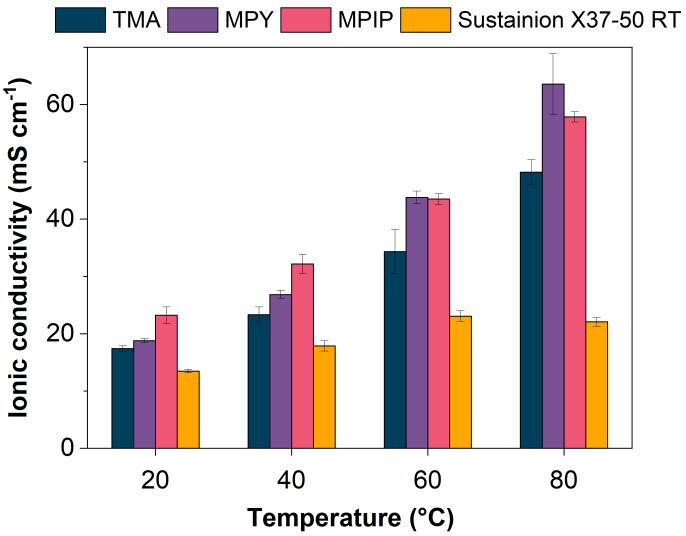

Figure 6.2: In-plane HCO_3^- conductivities (in water) for MPIP, TMA, and MPY-AEMs (made from 25 µm ETFE) and Sustainion X37-50 RT at different temperatures.

6.3 Electrochemical testing

Results of CO_2 electrolysis with different AEMs over Ag-electrocatalysts are shown in Figure 6.3. The experiments were carried out in galvanostatic mode at different current densities ranging from 100 to 300 mA $\cdot$ cm^{-2}, with CO and H_2 being the primary products. The total Faradaic Efficiencies were less than 100% due to unaccounted formate ($HCOO^-$) being transported to the anolyte (ca. 20%) [64].

Both MPY-AEM and MPIP-AEM showed similar product selectivities, with the MPIP-AEM reaching a maximum CO production rate of 5.6 mmol $\cdot$ h^{-1} $\cdot$ cm^{-2} at 200 mA $\cdot$ cm^{-2} (E_{cell}=-3.1 V). With these two RG-AEMs, the selectivity towards CO was favored at total current densities $<$ 250 mA $\cdot$ cm^{-2} (FE_{CO} = 70–87%), but less so at 300 mA $\cdot$ cm^{-2} (FE_{CO} $<$ 60%), where HER dominate due to either cathode flooding or localized mass transfer issues. MPY-AEM exhibits noticeably lower FE_{CO} values than MPIP-AEM at >200 mA $\cdot$ cm^{-2}. In comparison, lower WU TMA-AEM exhibits smaller CO selectivities compared to MPY- and MPIP-AEM with FE_{CO} $<$ 50% at $>$ 200 mA $\cdot$ cm^{-2} (along with 250 mV additional overpotential).

Water management can be affected by the nature of the AEM (e.g., QA chemistry) and the water content. To assess the effects of each RG-AEM, I used the metrics water uptake (WU) and the hydration number (λ). It is critical to emphasize that these are average bulk properties, which cannot provide information regarding the nano/micro-distribution of water-containing channels within hydrophilic-hydrophobic phase-separated AEMs, but they provide insights into the net water transport within CO_2E cells. Generally, water crosses the AEM by electro-osmotic drag (cathode to anode) and by diffusion or hydraulic permeation (anode to cath-

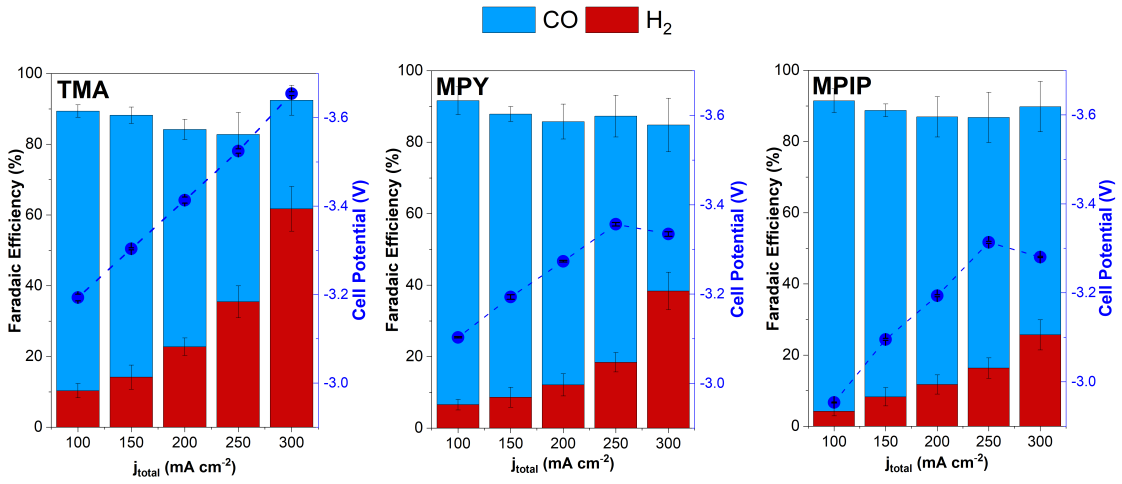

Figure 6.3: Product distribution and cell potentials at room temperature for CO_2E with the different RG-AEMs (made from 25 µm ETFE) as a function of the total current density using Ag electrocatalysts and 0.1 M HCO_3^-: TMA-, MPY-, and MPIP-AEM.

ode). For our low WU TMA-AEM (λ= 8), we observed a faster cathode flooding at $j_{total} > 200$ mA $\cdot$ cm^{-2} compared to the higher WU MPY- and MPIP-AEMs (λ> 22), potentially caused by a rise in the water flux to the cathode or a possible decrease in the electroosmotic drag coefficient.

MPIP-AEM and MPY-AEM exhibit a counter-intuitive phenomenon when switching between 250 mA $\cdot$ cm^{-2} and 300 mA $\cdot$ cm^{-2}, as the cell potential drops at higher current densities. A similar phenomenon was observed when the device was starved for CO_2, resulting in an inability to form carbonate anions and a switch to predominate OH^- anion formation. AEMs are most conductible when in their OH^- form, so an increase in their OH^- ion concentration reduces the cell potential [80]. However, this starving of CO_2 also entails CO_2 electrolysis becoming less selective in favor of HER. Moreover, incorporating heterocyclic-QA groups may provide a phase-separated morphology with a more efficient ion transport framework with the electrostatic repulsion of self-aggregated QA groups within hydrophilic domains, resulting in preferential OH^- transport of the type of Grotthuss (weakening OH binding to the cationic sites) [148]. The evaluation of the anodic CO_2/O_2 discharge ratios in RG-AEMs showed a decline in the ratio at higher current densities, confirming the switch to OH^- (Appendix A.1.6).

6.4 Evaluating the thickness effect on water transport and CO_2 electrolysis performance

On the other hand, significant differences between RG-AEMs were observed from different ETFE substrate thicknesses (25 µm vs. 50 µm). Those fabricated from thicker 50 µm ETFE had a lower degree of grafting (68% compared to 79% for 25

µm ETFE). Figure 6.4a showed the results of the j_{CO} for RG-AEMs with different functionalized groups and thicknesses.

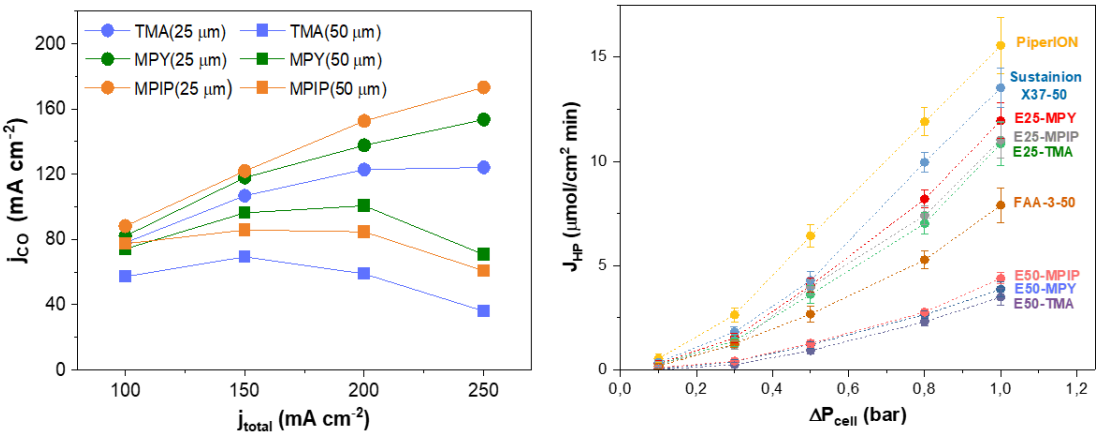

Figure 6.4: a). Effect of thickness on the CO partial current density for the RG-AEMs made from 25 and 50 µm ETFE substrate films, and b). Hydraulic water permeation as a function of pressure gradient for different AEMs.

These results showed that reducing RG-AEM thicknesses increased selectivity and activity independently of the headgroup. Moreover, thicker membranes (50 µm ETFE) appeared to enhance electrode flooding as opposed to thinner membranes (25 µm ETFE), due to increased water accumulation at the cathode. For those membranes, a rise in cell potential to compensate for the higher ohmic resistance may accelerate the loss of the GDE hydrophilicity. In addition, the higher IECs for the thinner RG-AEMs led to higher water contents and Cl^- conductivities (at 25 °C) compared to thicker analogs, and the lower water contents of the thicker versions led to lower CO_2E performances

Similarly, the thickness of the membrane can also influence overall water transport at high current densities since it can influence the hydraulic permeation flux (J_{HP}) across the AEM (Figure 6.4b) [107]. I recognize that accurately measuring hydraulic water permeation across the membrane in this MEA is difficult. In gas-fed CO_2 electrolysis, it is necessary to consider the impact of other water transport(electroosmotic drag and diffusion fluxes) and vapor (from the humidified gas and liquid phases) mechanisms. To do this, it would be necessary to conduct independent studies of the hydraulic permeation between phases, depending on the operating conditions, as it wouldn't be possible to decouple the effect of each individual mechanism just by studying one mechanism [149]. Nevertheless, I conducted additional ex-situ measurements of water permeation for our various membranes by using a reservoir below the electrochemical cell (assembled just with AEM and gaskets in between to prevent any potential GDE effects) and a water reservoir above the cell with a pressure controller that applied Ar-gas pressure.

Membranes with low water content and uptake (such as TMA) appear to have

lower water permeability since they have hydrophilic channels with smaller and less segregated channels. Membranes with higher water content are expected to provide expanded and interconnected water channels, enhancing water permeability, as observed for membranes with cyclic QA (MPIP or MPY), Sustainion X37-50 RT, and PiperION. In addition, membranes with water content might improve ion mobility, favoring the Grotthuss mechanism (structural diffusion by cleavage of hydrogen bonds with neighboring hydration shells) and vehicular processes (surface-site hopping) as water molecules interact with the functional groups in the polymer, which could also enhance permeability [80].

In terms of thickness, there is a direct correlation between thickness and water permeation. The water permeability results showed that increasing membrane thickness increases the hydraulic water permeation flux. PiperION (the thinnest measured membrane) exhibited the highest value, while E50-TMA was the lowest. It is expected that thinner AEMs provide better performance towards CO_2R as they tend to favor the water back-convective flux from the cathode to the anode, resulting in more even through-plane water distribution and increasing the hydration in the membrane locally [107].

6.5 Comparison of RG-AEMs with commercial membranes

6.5.1 Studies in terms of cell potentials and product selectivity

I conducted comparative studies with other commercial AEMs (Figure 6.5) to demonstrate the potential benefits and applicability of this newly developed generation of ETFE-based RG-AEMs for CO_2E.

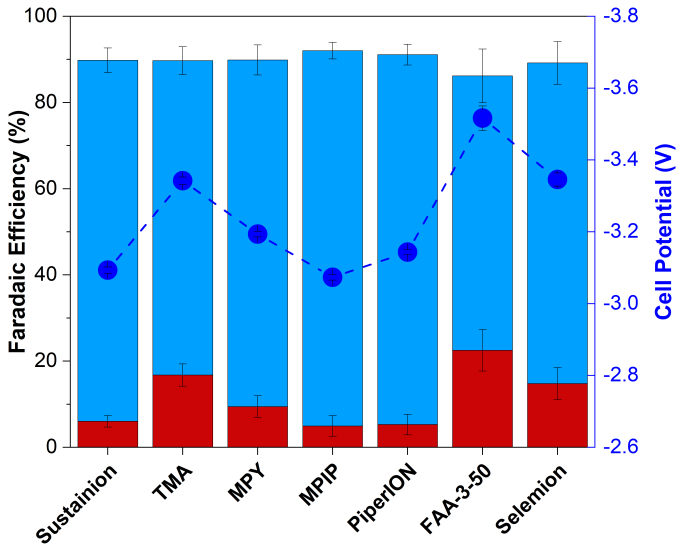

Figure 6.5: Product distribution and cell potentials for CO_2E cells operating at j_{total} = 150 mA · cm^{-2} at RT with different AEMs.

Based on the results, MPIP-AEM is comparable to the best commercial membranes, with MPY-AEM only slightly behind. However, under the same experimental conditions at room temperature, FAA-3-50, Selemion AMV, and TMA-AEM appear less competitive regarding cell potential and selectivity. MPIP-AEM had high FE_{CO} values with low cell potentials, similar to Sustainion® X37-50 RT and PiperION. TMA-AEM and Fumasep FAA-3, however, showed higher cell potentials (270 mV and 500 mV higher than MPIP-AEM, respectively). Compared to all the AEMs tested, which had different chemistries, cation transfer numbers, and thickness, it isn't easy to compare their performance directly [23]. However, it can be discerned that the AEMs with lower WUs (Fumasep® FAA-3-50, TMA-AEM, and Selemion® AMV) showed higher potentials and lower CO selectivities, consistent with arguments made vide supra (on the effect of the hydrophobic nature of the headgroups) [111].

6.5.2 Chemical and thermal stability of AEMs

As mentioned in Chapter 4, any potential commercial CO_2 electrolyzer would require operating at temperatures significantly above ambient temperatures due to its generated resistive heat. In addition, temperature influences the water management and ionic conductivity across the AEM (Figure 6.2). However, excessive temperatures may compromise the stability of AEMs due to alkali-derived degradation of the QA groups (or polymer backbones). Therefore, I conducted experiments at different operating temperatures to assess the thermal stability of MPIP-AEM compared to Sustainion® X37-50 RT (Figure 6.6).

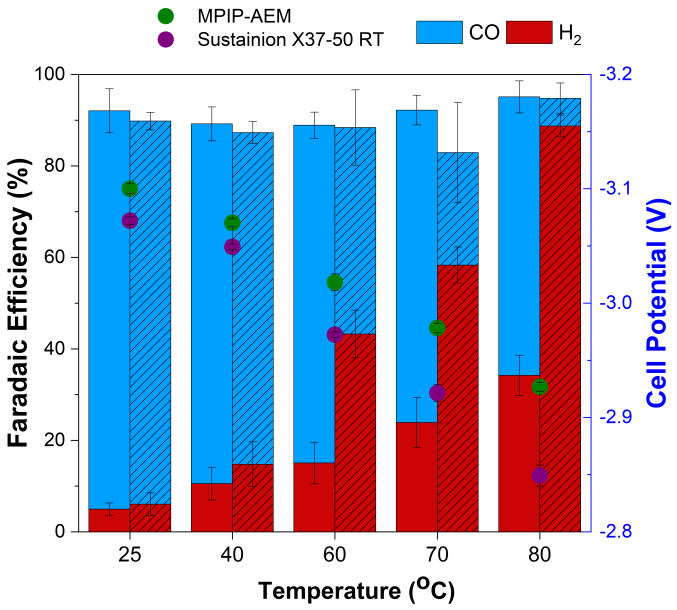

Figure 6.6: Effect of the operating temperature on the cell potential and Faradaic Efficiency for both AEMs E25-MPIP and Sustainion X37-50 RT.

At lower temperatures (< 40 °C), the MPIP-AEM resulted in slightly higher operating potentials and similar H_2 selectivity compared to Sustainion® X37-50 RT. In contrast, MPIP membranes exhibited a consistent trend at 60°C in terms of CO_2-reduced products vs. HER, compared to Sustainion® as it exhibited an increase in H_2 selectivity. The cell potential with Sustainion® also declined more rapidly at this temperature [150]. While a decrease in potential is generally favorable, this may indicate that the AEM has stability issues (degradation of functional groups and/or mechanical modifications), leading to the electrode flooding. Figure 6.2 also hints Sustainion® AEM degradation above 60 °C as the conductivity starts to decrease above this temperature. The MPIP-AEM was stable even at higher temperatures, as I could even perform experiments at 90 °C, still with stable performance (Appendix A.1.6).

6.5.3 Product crossover

A final feature was investigating the product crossover across the AEM. This experiment compared the MPIP-AEM developed in this work with different commercial membranes. A switch to sputtered Cu catalyst led to a range of C_1 and C_{2+} products, allowing a better understanding of the crossover properties of the various AEMs (Figure 6.7).

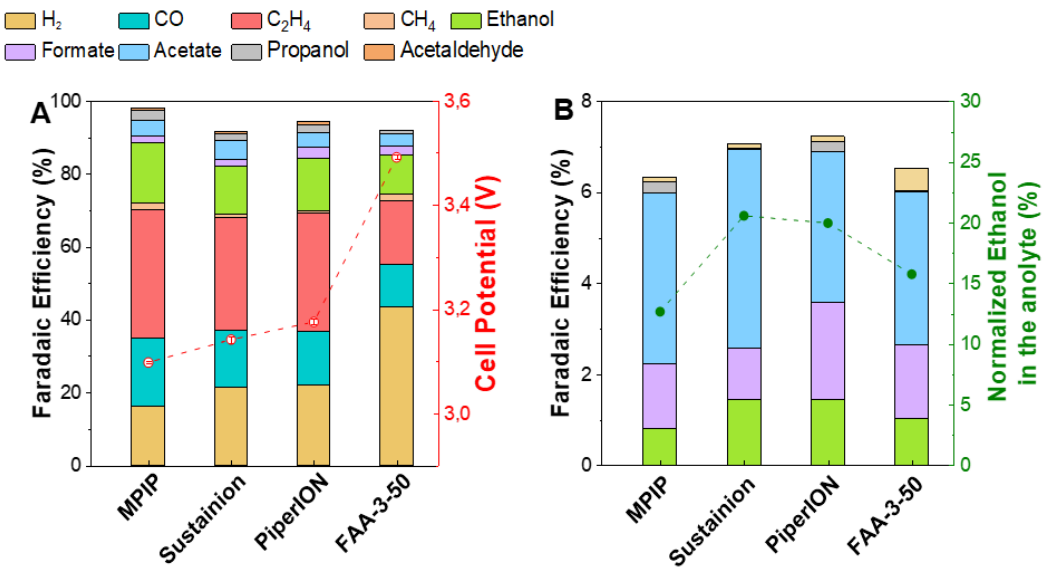

Figure 6.7: a) Product distribution and cell potentials obtained with a CO_2E cell containing a Cu catalyst and various AEMs, when operating at 150 $mA \cdot cm^{-2}$ at RT b) Product distributions detected at the anode. The right-hand axis relates the anodic ethanol Faradaic Efficiency as a function of the total ethanol FE.

It was reassuring to observe that all AEMs showed similar selectivity for experiments with similar potentials. The only notable exception was HER selectivity, which was expected to be primarily related to in-situ water management. FAA-3-50 gave the

highest HER selectivity, with MPIP-AEM giving the lowest. In contrast, the liquid crossover was similar across all the AEMs tested. Using an MEA approach, any volatile liquid product (e.g., ethanol, allyl alcohol, and propanol) can evaporate from the GDE. Despite minor differences, MPIP-AEM had the lowest ethanol crossover compared to the commercial membranes, demonstrating some potential benefits of the RG-AEM morphology and chemistry in regulating neutral product crossover. In contrast, there were no notable differences in (negatively charged) acetate and formate crossover among the different AEMs.

6.6 Long-term experiment for RG-MPIP AEM

As I intend to test the efficacy of these newly developed membranes under industrially relevant conditions, I chose the RG-MPIP membrane for long-term experiments due to its versatility in terms of conductivity and water management. The down-selected MPIP-AEM was tested at RT for 200 hours (Figure 6.8). The results showed only minor oscillations in the cell potential (ca. 100 mV) and stable CO selectivity (FE_{CO} = 80–85%).

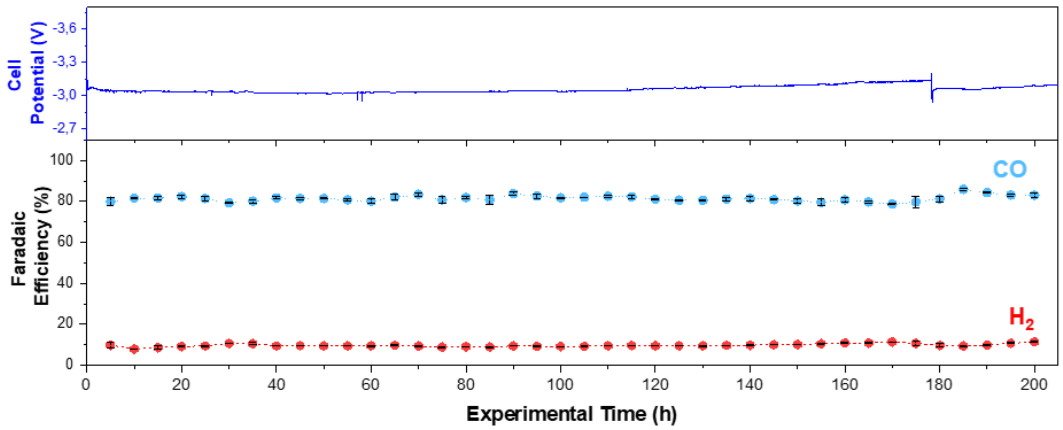

Figure 6.8: 200 h long-term stability test of a room-temperature CO_2E cell operating at 150 mA $\cdot$ cm^{-2} and containing the MPIP-AEM (Ag-based electrocatalyst and 0.1 M $KHCO_3$ anolyte).

A similar experiment with Sustainion® X37-50 RT showed less stability, with HER increasing over 100 hours (Appendix A.1.6). While my results do not show the stable operation with Sustainion® reported in the literature, the experiment was replicated multiple times, yielding the same trend. It should be noted that RG-AEMs are substantially easier to handle (more flexible and mechanically robust, without the addition of extrinsic plasticizers) compared to the Sustainion® X37-50 RT, which may contribute to the unsuccessful durability tests with this membrane.

6.7 Modifying AEM properties

Adding N-methylpiperidinium (MPIP) functionalized QA group has demonstrated a positive effect in the CO_2E. Therefore, further improvements to this AEM are considered to optimize its mechanical and chemical properties. This section correlates CO_2E trends with the membrane microstructure by understanding the effect of IEC in membranes with the same functionalized group, the benefits of introducing covalent crosslinking agents into RG-AEMs and evaluating the effect of amine abundance on final amination effects. Results in this section are just a baseline of possible strategies for first batches with modified features. These provided insight into optimizing them and have led to further research on the topic.

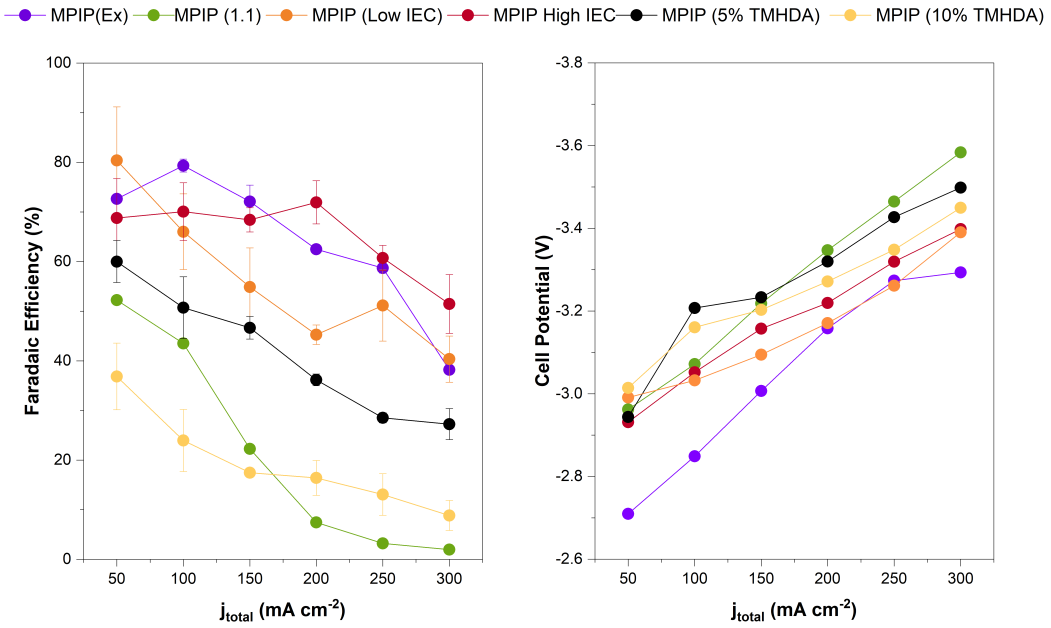

Figure 6.9: Different strategies to improve the MPIP-AEM performance through the addition of crosslinking agents, varying the amination composition ratio and the IEC.

Firstly, based on the amination method, I will address the effects on performance. CP results showed a higher operating potential for the sample with the stoichiometric amount (MPIP 1.1) than MPIP(EX). The phenomenon might result from limited ion transport across the membrane (electrowetting and intramolecular interactions between functionalized groups. MPIP(EX) measurements exhibited higher selectivities for CO_2 products (maximum FE_{CO}= 82%). At the same time, an abrupt shift to HER is visible in the sample MPIP(1.1) at current densities above 100 $mA \cdot cm^{-2}$. Those differences could be explained by the membranes' different IEC and ion conductivity. As expected, low amination content has a negative effect on CO_2E.

By contrast, I observed differences in the performance when TMHDA was added as a crosslinking agent. Adding 10% mol THMDA to the membrane decreased

CO selectivity by 20-40%, compared with adding 5%, which failed to exhibit any benefit in CO_2E. As a result, adding a covalent crosslinking agent might have a limited effect on this application. However, the MPIP-AEM crosslinking method has not been optimized, so further studies are needed to determine its effect. Finally, two different membranes with IEC were tested (low IEC=1.7 $mmol \cdot g^{-1}$ and high IEC=2.3 $mmol \cdot g^{-1}$). Results showed a minor difference in cell potentials, while AEM with higher IEC exhibit slightly higher CO selectivity above 100 $mA \cdot cm^{-2}$. However, even though the membrane with higher IEC showed similar results to MPIP(EX), the higher IEC can cause excessive swelling, diluting the charge carrier concentration and reducing conductivity and mechanical robustness.

6.8 Summary

In this Chapter, I presented a new AEM generation for CO_2E. Through characterization and electrochemical testing, the following conclusion could be drawn:

- QA groups (TMA, MPIP, and MPY) in ETFE substate have exhibited desired transport, chemical, and mechanical properties, including high IEC (above 2 $mmol \cdot g^{-1}$), ionic conductivities, moderate water uptake, and low ohmic resistances ($< 0.6\ \Omega \cdot cm^2$).
- Tailored properties of these membranes make them suitable for CO_2E in MEA configurations. Their mechanical flexibility and robustness make them easily handled during cell assembly, whereas they provide comparable performance to commercial membranes.
- Operation using thinner membranes with MPIP-headgroup yielded the highest CO selectivity (>80%) over Ag-electrocatalysts at higher current densities (E_{cell}=-2.9-3.3 V), owing to improved water and ionic transport within the system.
- The use of cycloaliphatic headgroups in RG-AEMs proved thermal and chemical stability under different reaction conditions (e.g., operation temperatures, electrolyte) and, to some extent, reduced the product crossover.
- RG-MPIP achieved stable operation for 200 h at 150 $mA \cdot cm^{-2}$ with high CO selectivity (80-85%) at RT conditions.
- Different strategies for improving the mechanical and chemical properties of RG-MPIP AEMs did not exhibit the expected results. The addition of crosslinking agents or the control of amine composition increased the cell potential and enhanced HER. However, IEC variations did not show significant differences between the membranes (as those values were higher enough).

Chapter 7

Other strategies to improve the CO_2E performance

Contribution

Dr. Asger Moss designed the control system to adjust the reflux ratio and measure the streams across the reaction system. Dr- Terry Wilson and Prof. John Varcoe synthesized and characterized the ionomers powders at the University of Surrey.

7.1 Chapter Overview

Current low CO_2 conversion rates and limited performance at long operational times contribute to the inability of CO_2E to be commercialized and implemented on an industrial scale. Therefore, I proposed additional alternatives besides those in Chapters 4-6 to address the limitations regarding stability and conversion. By incorporating both ionic functionalities (hydrophobic and hydrophilic units), ionomers might help increase gas transport and improve reaction microenvironments in CO_2E. As part of this study, I evaluated different CEIs and AEIs (same ionomer units used in AEM synthesis). I coated them onto Cu-GDEs to quantify their effects on gas transport, product distribution, and stability. Another strategy involves the addition of a recycling line after the cell to enhance CO_2 conversion, similar to most current industrial processes. A recycling loop increases CO_2 conversion to more highly reduced species than a single-pass operation by selectively consuming unreacted CO_2 and operating at lower overpotentials [151]. Therefore, part of this chapter will evaluate the effect of implementing a recycling line and study the operational viability regarding CO_2 conversion and stability. Lastly, I evaluated the effect of pressure on CO_2 coverage and water management in MEA systems.

7.2 Use of ionomers for CO_2E

This section describes the effects of AEIs (anion exchange ionomers that contain QA and imidazolium-based groups) and CEIs (cation exchange ionomers composed of perflourosulfonic acid groups) on a catalyst layer to gain insight into the interactions at the ionomer-catalyst interface and their subsequent effect on CO_2E. To achieve this, I prepared Cu-based catalysts coated with an ionomer layer. Their surface morphology, product distribution, and measurements of activity and capacitance

during the operation were evaluated by characterization and electrochemical testing. These coatings can facilitate gas transport, activity, and GDE durability by creating an optimal microenvironment, thereby reducing electrode flooding and improving mass transport rates and kinetic performance. The approach described here can be a general guideline for improving gas-fed electrolysis operations.

7.2.1 Properties and characterization of the ionomers

Nafion was used as CEI, while the tested AEIs corresponded to commercial vinylbenzyl methylimidazolium (Sustainion XA-9) in suspension, PTFE, and synthesized trimethylammonium (TMA), benzyl-N-methylpyrrolidinium (MPY), benzyl-N-methylpiperidinum (MPIP). These ionomers were synthesized via radiation grafting (the same way AEMs were prepared) and aminated with TMA, MPY, and MPIP. Table 7.1 summarizes some physical properties of the RG-AEIs. The lower IECs are attributed to the increased molecular masses of the larger quaternary ammonium head groups. In addition, the contact angle measurements are presented for the prepared AEI (other values were taken from the literature for comparison a:[152], b:[88], c:[153]; P.S stands for particle size).

Table 7.1: Key properties of ionomers used in this study

Properties	TMA	MPY	MPIP	Nafion[a]	XI-9[b]	PTFE[c]
IEC mmol $\cdot$ g^{-1}	2.09 $\pm$ 0.1	2.00 $\pm$ 0.1	1.85 $\pm$ 0.1	0.93	1.2	N.S
P.S (µm)	1.96 $\pm$ 0.2	1.11 $\pm$ 0.1	1.18 $\pm$ 0.1	N.S	N.S	2.0
C.Angle (°)	98 $\pm$ 5	107$\pm$ 6	103 $\pm$ 2	120 $\pm$ 5	>90	135

As expected, the results of the measured IEC were similar to those found in Table 6.1. As evidenced by contact angle measurements, all ionomers conferred a hydrophobic nature on the GDE due to their polymeric structure, as indicated by the fact that all samples had water contact angles greater than 90°. XPS characterization of the ionomers revealed the presence of principal ionic groups, which can be used to verify the coating in the CL and determine if contaminants are present at the surface after the coating (e.g., Nafion has fluorine groups, whereas RG-AEIs have Cl^- features due to their -CH_2Cl groups). Finally, some cross-sectional SEM coupled with EDX was performed on the GDE, consisting of interwoven MPS (carbon fibers) with an MPL and CL, to verify the presence of the top layer of the ionomer.

7.2.2 Effects of the coated-ionomer and mass loading

Ionomers serve various functions in the CL, including immobilization of the catalyst particles on the GDL surface (binder), modulation of wettability, formation of porous structures to improve mass transfers, and improvement in ionic conductivity.

To evaluate the role of ionomers, commercial GDLs were sprayed with homogenized catalyst inks containing Cu nanoparticles, IEI (ionic-exchange ionomer), and IPA:water to form catalyst layers (maintaining a total loading of 1 $mg \cdot cm^{-2}$).

At first, I investigated how ionomer-coated Cu affects CO_2R by performing linear sweep voltammetry (LSV) at different potentials to compare the activity of bare Cu with various Cu/ionomer catalysts (Figure 7.1a). According to polarization curves, all catalysts containing ionomers significantly enhanced the CO_2R current (2-fold increase in total current). I found that adding ionomers increased the activity by two-fold for Cu/PTFE, 2.8-fold for Cu/Nafion, and three-fold for Cu/MPIP compared with Cu-GDE.

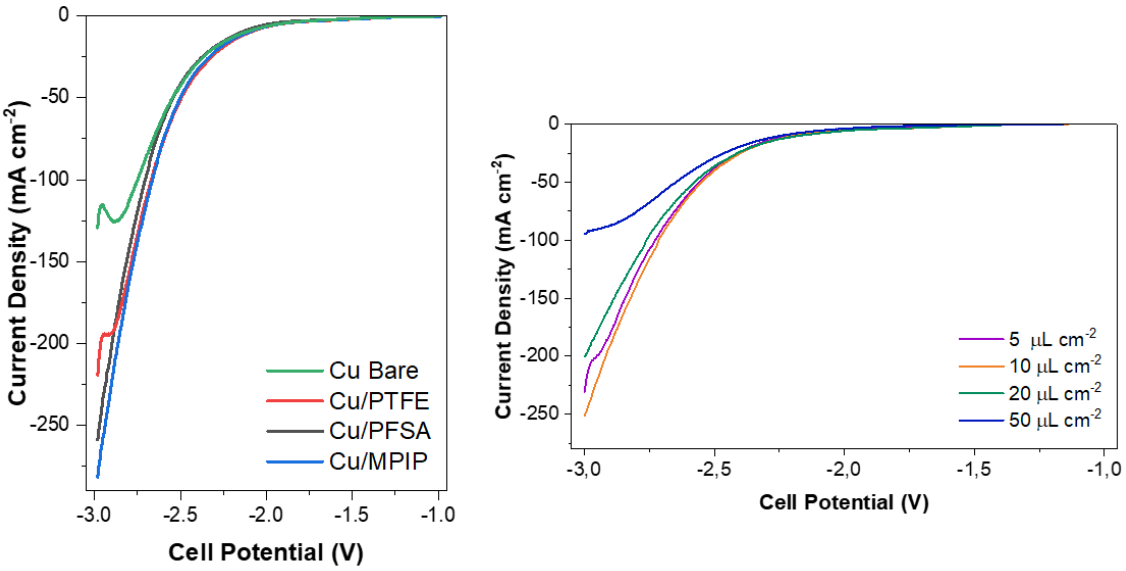

Figure 7.1: Catalyst screening through polarization curve a). Effect of different CEI and AEIs in Cu-GDE b). Effect of the ionomer loading in the catalyst activity.

While LSV scan time is short of conducting product analysis, in further sections, I could corroborate that even at 200 $mA \cdot cm^{-2}$, samples with HER remained below 10%, compared to bare Cu, which increases up to 60%. I attributed the activity enhancement to hydrophobicity, transport enhancement, and electric field effects from adding ionomers. Although I did not study the reason behind this increase in current density, literature reports have shown that PFSA or QA ions promote CO_2R through specific non-covalent interactions with CO_2 intermediates (*CO stabilization). The effect of gas availability on gas transport has been confirmed by Garcia de Arquer et al. [63] and Møller et al.[93] through different reaction mechanisms (COR or ORR), showing such effect and reduced ionic resistance.

By tuning the Cu/ionomer loading, I can assess the effect of the ionomer layer thickness. For that, I used Cu/Nafion for this study, as it has been a well-studied ionomer for CO_2R. The dramatic impact of ionomer loading on the synthesized electrodes was found to be independent of the ionomer´s chemistry (Figure 7.1b).

By increasing the loading by 10 /textmu m $\cdot$ cm−2, the current density increases to 250 mA $\cdot$ cm^{-2} at -3 V. Loadings above 20 textmu m $\cdot$ cm−2 result in lower performance, likely due to increased diffusion resistance, as increasing quantities of ionomer in the catalytic layer represent a barrier to the mass transport of reactive species.

7.2.3 Effect of the ionomer layer in product distribution

A preliminary indicator of the effect on CO_2 availability is product quantification. I performed CP experiments at cell 200 mA $\cdot$ cm^{-2} for two hours for each sample. I chose this condition, as in my research group, we have found it as a threshold for GDE-flooding. According to Figure 7.2, slight differences were observed in the selectivity of C_1 and C_2+ for electrodes with the ionomer compared to bare Cu-GDE. The use of TMA and MPY ionomers seemed to enhance the HER, related to their high WU and IEC (FE_{HER}=>35%). MPIP, PTFE, and Nafion showed higher selectivity towards carbon products than bare-Cu.

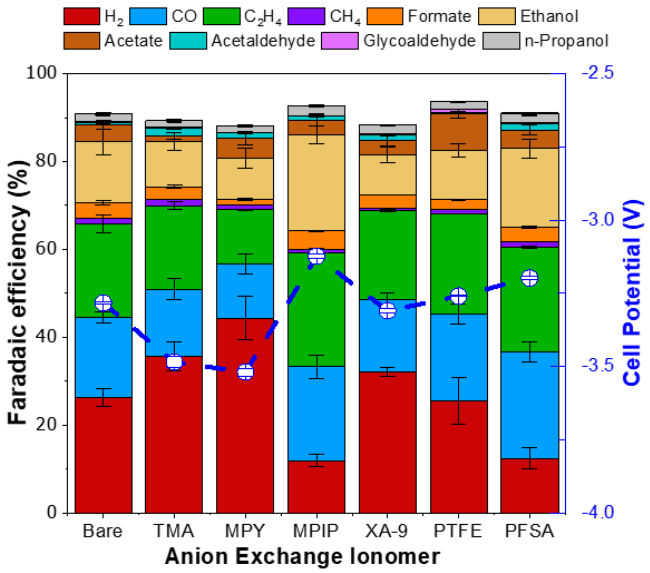

Figure 7.2: Product Distribution of CO_2 with Cu-based electrodes coated with different ionomers at 200 mA $\cdot$ cm^{-2}.

Interestingly, minor differences have been seen between using CEIs or AEIs, as product distribution towards Cu-MPIP and Cu-Nafion didn't show any major difference in selectivity and cell potential. In theory, the chemistry effect of different ionomers should promote different effects, as reported in literature [113]. AEI should increase the local ratio of CO_2/H_2O, while CEI prevents carbonate species from entering the catalyst's microenvironment. Nevertheless, the enhanced selectivity of C_{2+} products using MPIP and Nafion ionomers can be explained by Donnan exclusion at the interface between Cu and the ionomer. The difference between these ionomers is

the background charge, which is positive for MPIP and negative for Nafion. Despite MPIP's affinity for anions, its hydrophobicity features and heterocyclic QA groups (moderate WU) regulate the water penetration into its GDE, which means it could delay flooding. Nafion is expected to exclude anions from the surface, resulting in a higher local pH due to accumulated CO_2R-generated OH^- at the Cu surface, which favors the C_{2+} selectivity [63].

7.2.4 Effects of the ionomers on double layer capacitance

I can correlate the CO_2 mass transport, electrowetting, and electrode flooding by double-layer capacitance (DLC) measurements. My experiments here were divided into two groups, one with just Cu-GDE and testing at different current densities, and another with varying NP/ionomer compositions (10-50% wt.) and studying how they affected the capacitance by varying MPIP loadings.

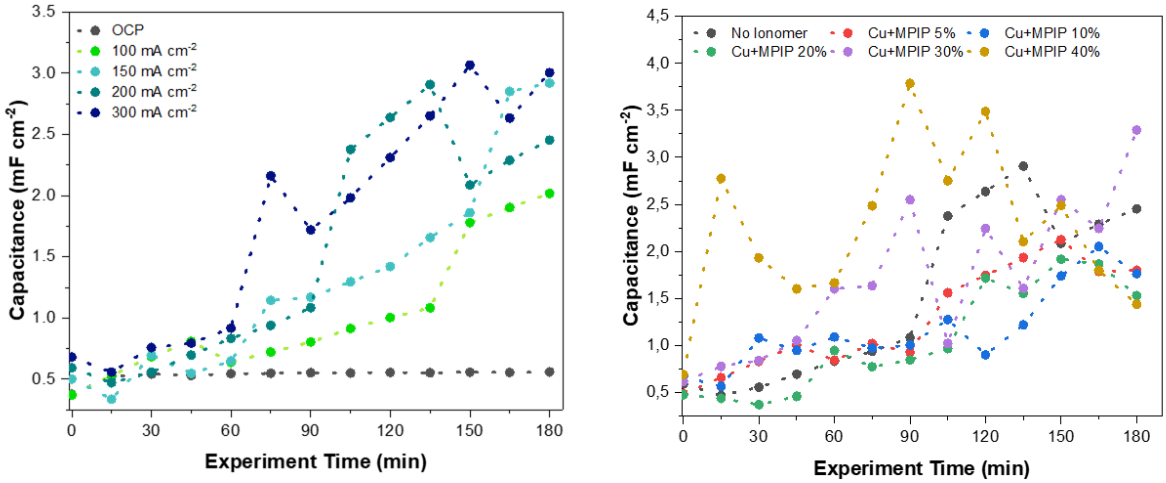

Figure 7.3: Tracking the electrode flooding by DLC measurements as a function of the ionomer content and current density.

The degree of wetting is an essential parameter in GDE because it determines the amount of catalyst that comes into contact with the electrolyte. As a result, I measured DLC after electrolysis at each current density to determine how adding an ionomer affects electrode flooding. When not using ionomers, I found a direct correlation between current density, capacitance, and flooding, similar to the observations reported by Leonard et al.[84]. A rise in capacitance at current densities above 200 $mA \cdot cm^{-2}$ using bare Cu can be attributed to high electrowetting and GDE flooding (spikes in capacitance corresponded to an increase in HER, based on product quantification). However, the capacitance of the electrode decreases when the ionomer is added. The ionomer might reduce the water/electrolyte viscosity and surface tension at the surface, allowing less water penetration through the catalyst layer. Furthermore, samples containing more than 20% wt. resulted in an increase in DLC, which could be explained as higher ionomer loading might block the pores

and active sites in the CL. Comparison of bare Cu with Cu/MPIP 10% wt. (2.87 $mF \cdot cm^{-2}$vs. 1.17 $mF \cdot cm^{-2}$) showed more than 2.5 fold increase in the capacitance. The low capacitance at such loading may be caused by hydrophobic backbones orienting themselves toward the copper surface on its surface beforehand, decreasing the overall charge on its surface. Variations at higher MPIP loadings (>20 wt%.) may be caused by the orientation of hydrophobic and hydrophilic functionalities in the ionomers, making hydrochannels accessible, promoting water penetration and enhanced charging in the DLC.

7.2.5 Long-term experiment

The stability of tandem electrodes has been examined using Cu/MPIP(10%) -GDE at 200 $mA \cdot cm^{-2}$, incorporating temperature, at the same conditions as the other long-term experiment done for the tandem catalyst in section 5.6.

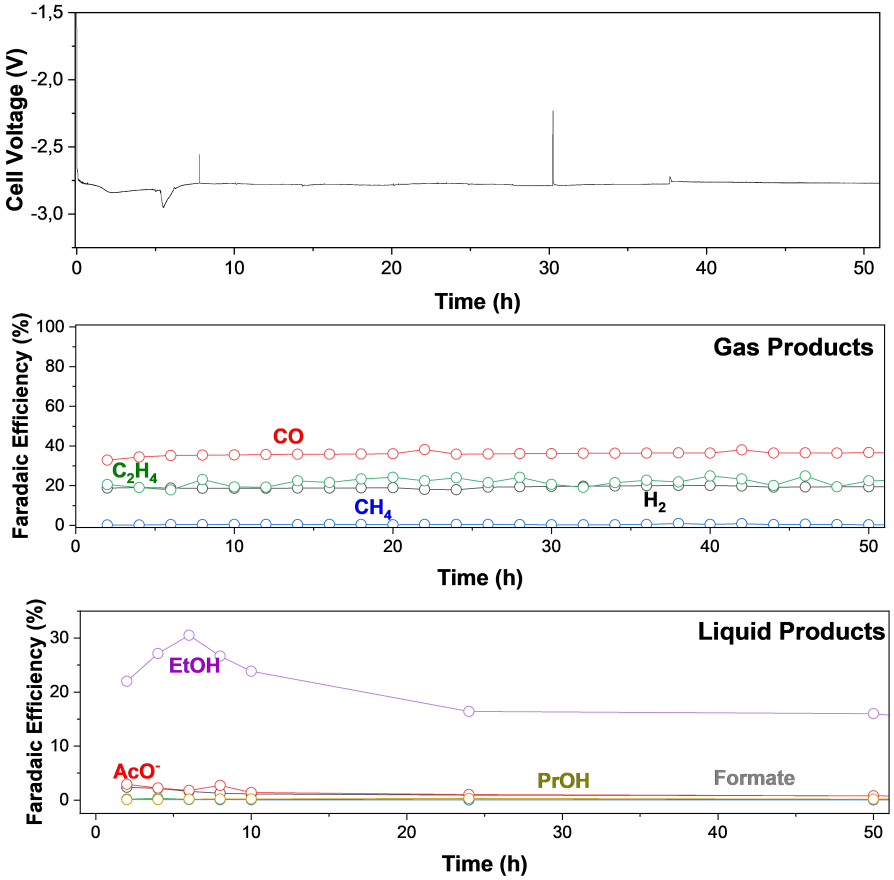

Figure 7.4: Long-term experiment of Cu-GDE with 10% wt. MPIP coupled operated at elevated temperatures (60°C) at 200 $mA \cdot cm^{-2}$ and 0.1 M $CsHCO_3$.

Over the 50 hours, the tandem electrode maintained stable operation (-2.76 V) with only minor changes in selectivity for main products. Due to the ionomer and operating at elevated temperatures, the HER was kept below 20%. The maximum ethanol selectivity was achieved in the first six hours and then decreased to 18%

after 50 hours, while ethylene selectivity kept stable (22%) over the experiment. Like the stability test results in Figure 5.10, CO remains the main product, and I attribute it to temperature rather than the ionomer itself. A failure in the GC equipment ended the experiment after 50 h, rather than an electrochemical effect, which encouraged its use of this strategy for further stability testing (as I coupled in an experiment in Chapter 8).

7.3 Introducing a recycling line in CO_2E

Throughout this section, I examined the effects of recycling lines under varying operating conditions, including reflux ratios (between the inlet and outlet flow lines), CO_2 feeding rates, and current densities. The experiments have been conducted using MEA-type cells and Ag electrodes since they primarily produce CO, simplifying the analysis of other possible products formed by side reactions. At first, I conducted CO_2 single-pass experiments to understand better the mechanism's nature, including its relationship with feeding rate and partial current density. Further experiments focused on implementing a closed-loop system, using a pumping system and valves to ensure some control of the flow fed directly back into the cell. Finally, optimal conditions were implemented to evaluate the effect of recycling in long-term experiments.

7.3.1 CO_2 single-pass conversion studies

$CO2_2$ single-pass conversion experiments were conducted to demonstrate the effect of feeding rates and current density. Figure 7.5a shows the Faradaic efficiency of CO at different current densities and flow rates, and Figure 7.5b is the fraction of CO_2 converted to CO. The compositions of the gaseous products were taken from the last three measurements.

Results of these measurements indicate a proportional relationship between the CO_2 feeding rate and the conversion of CO_2 to CO. This is consistent with the findings of Jeng and Jiao [94]. As observed in Figure 7.5b, operations at lower current densities (<50 mA $\cdot$ cm^{-2}) provided similar CO partial current densities (j_{CO}) regardless of the CO_2 inlet feeding rates as the CO_2E is controlled by kinetics and ohmic resistances in this region. At higher current densities, j_{CO} depend on the feed rate, showing a clear dependence on CO_2 mass transport, as operation beyond 150 mA $\cdot$ cm^{-2}, j_{CO} decrease significantly, likely due to mass transfer limitations [86].

By integrating electrochemical and homogeneous reactions, it is possible that for each CO_2 converted to CO, another one is consumed by carbonate formation in parallel. This phenomenon happens under the assumption that all produced hydroxyl groups combine with CO_2 to form carbonates, setting a practical, theoretical

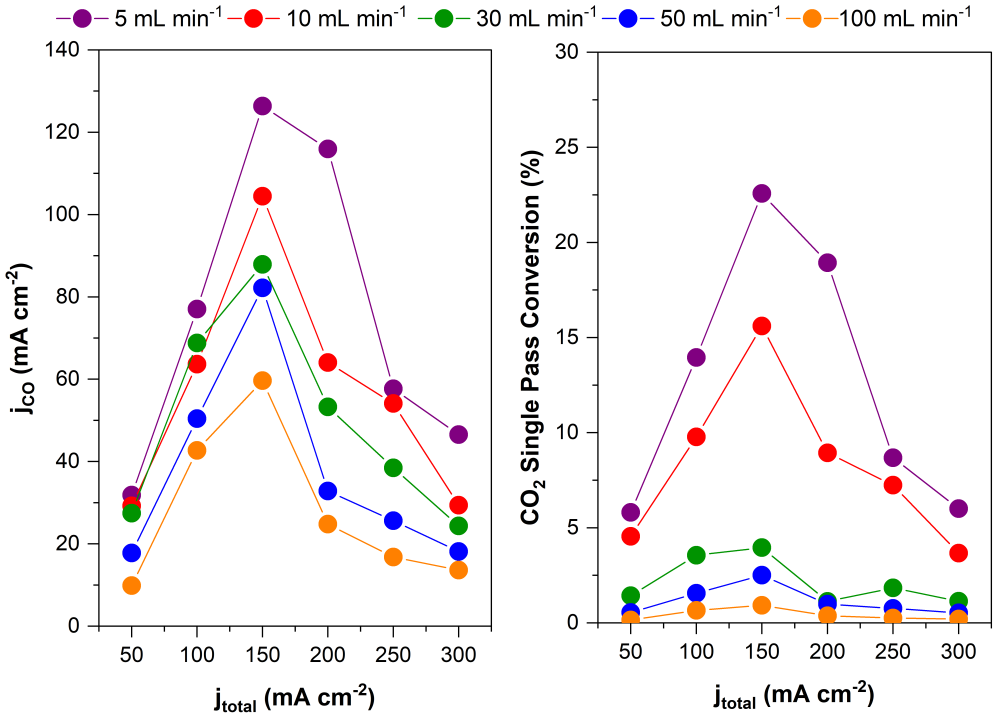

Figure 7.5: CO_2R at different CO_2 feeding rates and current density: (a) CO partial current density and (b) CO_2 single-pass conversion to CO.

limit of 50% CO_2 conversion to CO as it was also described by Jeng and Jiao, using Ag-electrocatalyst [94]. The experimental results support the previous statement, where the maximum achieved value was 23% at 5 mL $\cdot$ min^{-1} and 150 mA $\cdot$ cm^{-2}. However, the CO_2 conversion for my experiments is lower than those reported in the literature, likely to differences in the cell's configuration and reaction conditions.

7.3.2 Effect of the Reflux Ratio

Using a recycling line is expected to improve the conversion of the unreacted CO_2 of the single-pass, thus overcoming the limitations of the CO_2R. Initially, the outlet flow introduced back into the inlet CO_2 flow is controlled by the reflux ratio (RR), defined as R=F_7/F_5 (see Appendix A.1.7 for general balance). These experiments were repeated twice using a new anode, cathode, and AEM to verify reproducibility and isolate inherent errors. For each run, the inlet CO_2 flow was 50 mL $\cdot$ min^{-1}, operating in galvanostatic mode at 100 mA $\cdot$ cm^{-2} for two hours. A comparison of Faradaic Efficiency at five different reflux ratios is shown in Figure 7.6.

Performance presented similar selectivities for all RR, with CO being 70% to 80% and H_2 being 10-15% (the remaining Faradaic Efficiency is likely to be formate). These results indicate that the reflux ratio (and regeneration line) had a negligible effect on the selectivity and the production rate, compared to the experiments of the single-pass at the defined conditions (maximum CO production rate of 3.5 mmol $\cdot$ h^{-1} $\cdot$ cm^{-2} with the recycling loop (RR=1.5) vs. 3.2 mmol $\cdot$ h^{-1} $\cdot$ cm^{-2} with-

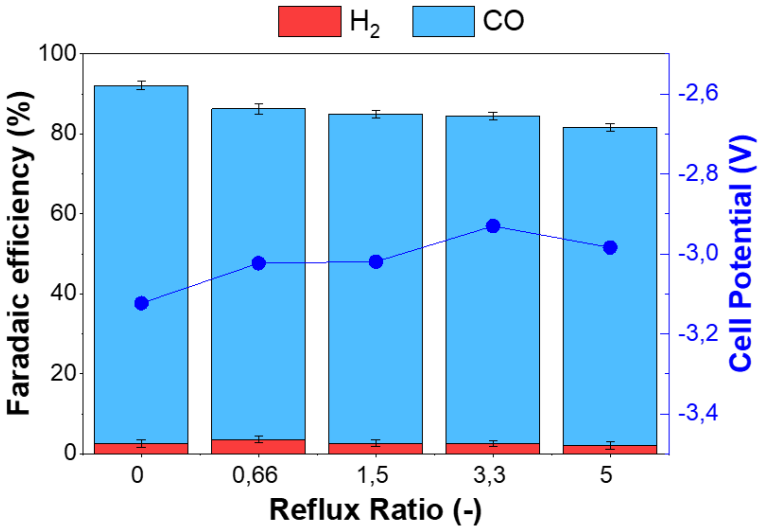

Figure 7.6: Effect of the reflux ratio in CO_2 selectivity to CO at 150 mA $\cdot$ cm^{-2}

out at 100 mA $\cdot$ cm^{-2}).

Such small variations could be correlated to the coverage of the adsorbed CO_2 at the surface. Such parameter can be expressed as $\Theta_{CO2} = \Theta^* \cdot [CO_2] \cdot \exp(-E_{CO2}/R \cdot T)$, where Θ^* is the coverage of available sites, $[CO_2]$ is the CO_2 local concentration, E_{CO2} is the CO_2 adsorption energy and T is the temperature [44]. Adding the recycling loop could increase the coverage of $*CO_2$ on the catalyst surface and CO formation at the beginning. However, if the saturation coverage is reached, it is possible that the flux reaching the catalyst layer (CL) could be sufficient to get to the active sites, meaning that the unreacted CO_2 cannot be adsorbed in the surface, and it cannot react before being desorbed [136]. Further studies on the recycling line will focus on its effect on operating at high current densities and different feeding rates.

7.3.3 Effect of adding the recycling line

Function of current densities

The following section focused on studying the influence of the current density at three different conditions (no reflux and RR=1.5 and 3.0). These experiments consisted of catalytic screening at different current densities (50-300 mA $\cdot$ cm^{-2}) for two hours for each run (Figure 7.7)

Studies on the effect of current density on CO formation showed that the loop line increased selectivity for CO in the range of 50-100 mA $\cdot$ cm^{-2} over the CO_2 single-pass experiments. Nevertheless, at current densities of 200 mA $\cdot$ cm^{-2}, the recycling loop increases HER selectivity, as reintroducing unreacted CO_2 and CO into the cell at high pH conditions might accelerate the carbonation rate rather than CO_2R. On the other hand, I performed additional experiments at different feeding rates

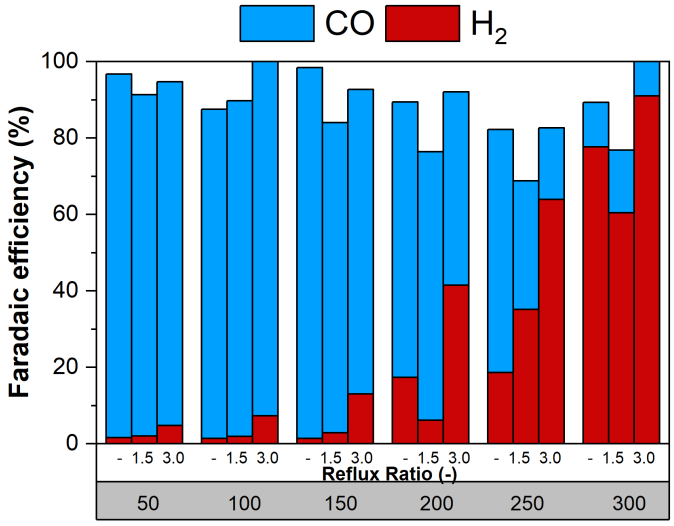

Figure 7.7: Comparing the performance between single-pass experiments and adding the recycling line at different reflux ratios and current densities.

(adjusting the RR) and current densities to support the trend. The conversions towards CO are reported without crossover effects (CO_2 to carbonate formation, but can easily be divided by two), and flows reported do not correspond to the initial feeding rate but rather the flow in the system after including the recycling line (feeding rate plus this value multiplied by the reflux ratio).

As shown in Figure 7.8, up to 38% CO_2 was converted to CO (76% without crossover effects) when an inlet flow of 5 $mL \cdot min^{-1}$ was applied at 200 $mA \cdot cm^{-2}$. This increased CO selectivity is likely due to improved gas diffusivity and CO_2 availability from the recycling loop at such conditions. In contrast, when the current density is higher than 200 $mA \cdot cm^{-2}$, there is an increase in H_2 output due to a CO_2 mass transport-limitation regime. Decreasing the CO selectivity at such conditions using the recycling loop could be explained since the unreacted CO_2 and the produced CO from the recycling loop would have fewer active sites (pore blockage, H-adsorption, or water management) to adsorb on. Consequently, the unreacted CO_2 will interact with the OH^- due to the current-induced build-up of alkalinity near the electrode surface, enhancing the carbonate formation. While it is evident that the recycling loop affects the conversion of CO_2 to CO, it also promotes the formation of carbonates, which resulted in an operation being limited to salt precipitation.

7.3.4 CO_2R performance with the recycling loop at the low CO_2 feeding rates

As observed in Figure 7.8, operations adding the recycling loop are limited below 200 $mA \cdot cm^{-2}$. Initially, I conducted CP between 50-200 $mA \cdot cm^{-2}$ using the same feeding rate (e.g., 10 $mL \cdot min^{-1}$ just with the feeding rate vs. 10 $mL \cdot min^{-1}$ with the addition of the recycling loop, Figure 7.9a). This experiment aimed to

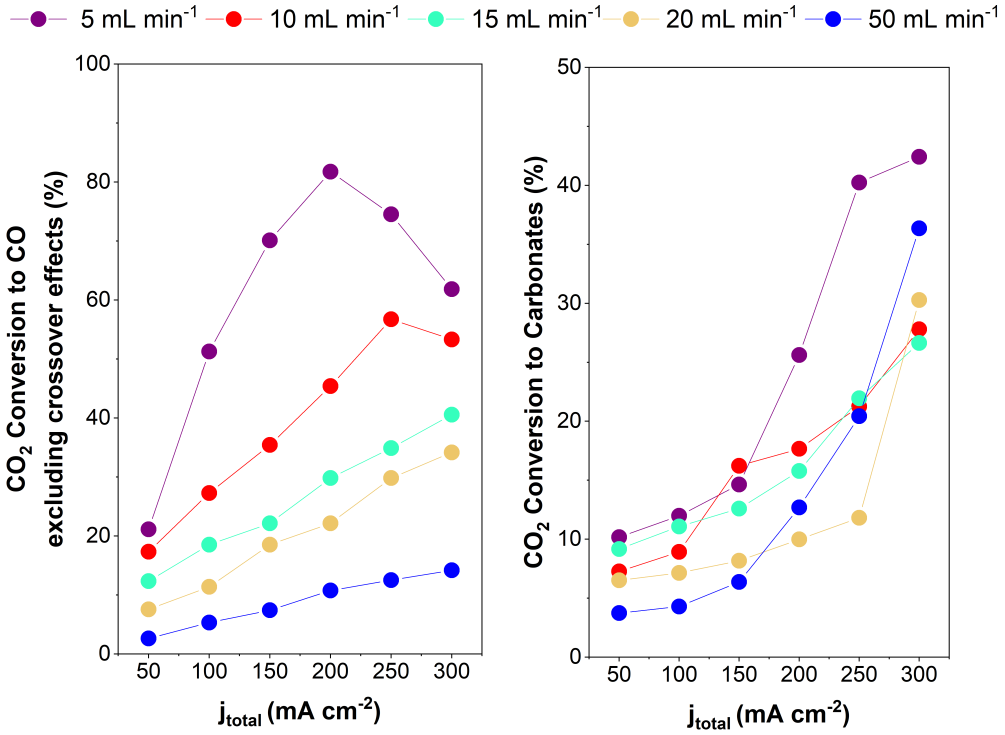

Figure 7.8: Study of the CO_2 conversion as a function of CO_2 feeding rate and current density towards a).CO and b).carbonates.

determine if reducing feeding rates and extending residence times might improve CO_2 conversion. Three different CO_2 feeding rates (5-15 mL $\cdot$ min^{-1}) were tested, and the experiment time for each of these measurements was approximately 4 hours, where error bars represent an average of the last three GC injections (Figure 7.9b).

Results from Figure 7.9 showed that the maximum conversion of CO_2 to CO is around 27% at 100 mA $\cdot$ cm^{-2} versus 15% for single-pass experiments. Adding a recycling loop improved CO conversion and Faradaic Efficiency. However, comparing results between both different approaches exhibits surprisingly different trends. For example, between 100 and 150 mA $\cdot$ cm^{-2}, a positive effect is visible using a recycling loop, where CO selectivity increases. This can be explained by increased local CO_2 concentrations resulting from improved transport and a reduced pH gradient at the interface. Likewise, it is interesting that at 50 mA $\cdot$ cm^{-2}, the loop has no significant effect on CO selectivity, although there are no significant engineering limitations (i.e., mass transfer) under those conditions. Further measurements (capacitance and capillary pressure) can clarify why it is advantageous to use a recycling line under these conditions.

Several challenges were encountered in translating these results from porous Ag membranes to carbon paper-based GDLs. The performance of recycling loops with GDLs was limited by the instability of the GDE (GDE flooding and electrowetting) after short operating times, as previously reported in the literature but apparently

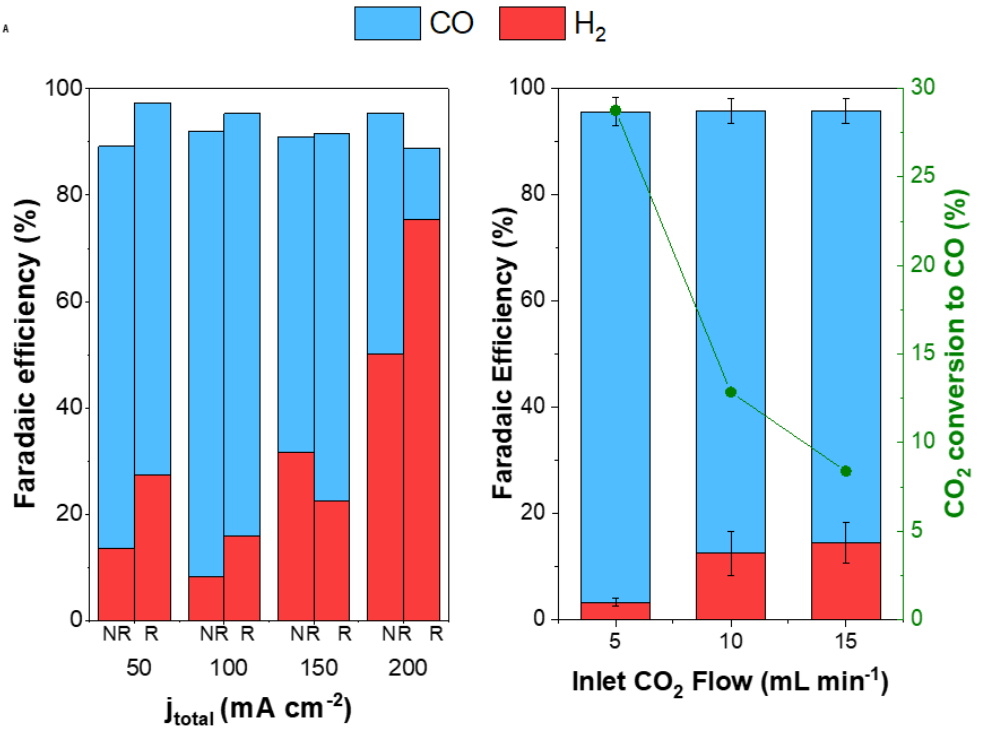

Figure 7.9: Electrochemical CO_2 reduction at low CO_2 feeding rate a) Product distribution at different current densities and comparison between single-pass and recycling line configurations at 5 mL $\cdot$ min^{-1} b). Faradaic Efficiency and conversion at different feeding rates.

less evident in single-pass experiments. The cause of the limited performance is unclear, but it may be related to GDE's inherent characteristics (e.g., porosity), which limit recycling loop implementation. Yet, in porous substrates (Ag-GDL), it seemed that the recycling loop might have some benefit in improving CO_2 conversion to some extent.

7.3.5 Long-term experiment

Having defined all the optimal operating conditions, a "stability test" was performed, where a constant current density was applied, and products were quantified every ca.20 minutes for 6-10 hours. During the first three hours, CO production gradually increased before reaching a maximum value of 31%, remaining stable for 1 hour. Afterward, the decay continued until another plateau was reached at 24-27% and remained there for the rest of the experiment.

Even though FE_{CO}=31% was achieved with 100 mA $\cdot$ cm^{-2} using the recycling loop, this value is below the theoretical limit, meaning that I have low CO_2 utilization or the carbonate formation still has a significant effect on the loop on CO_2 consumption in neutral and alkaline media. Further studies on a detailed carbon balance and crossover will provide more insight into the above statement and provide new alternatives to overcome the current limitations of the recycling loop line. While

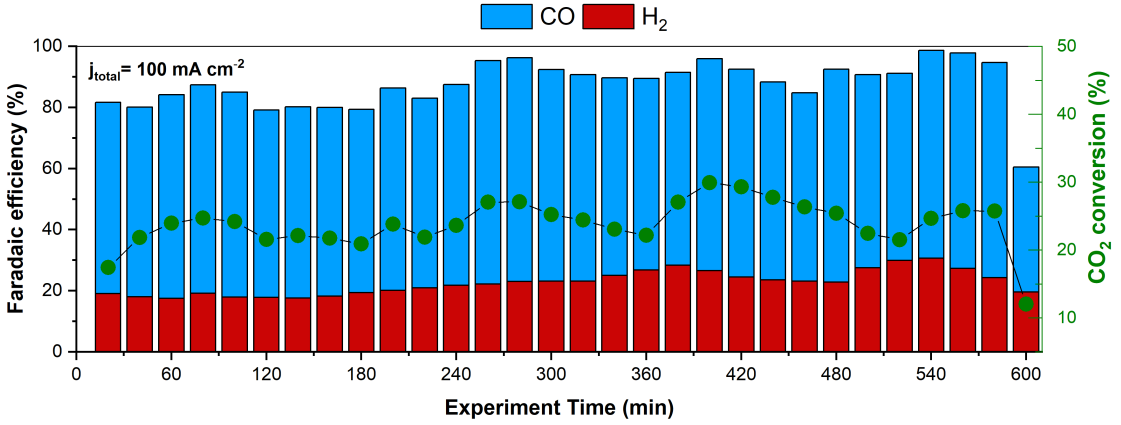

Figure 7.10: CO_2 conversion profile at longer-time experiment at 100 mA $\cdot$ cm^{-2}

it was possible to estimate how much carbonate is produced, it is still necessary to make more precise measurements to determine to what extent the recycling loop contributes to carbonate formation. Furthermore, modifications to the substrate, such as improving hydrophobicity or gas-ion transport, may help overcome these limitations in the CO_2 conversion process in single-pass experiments or implement the recycling line to enhance the selectivity for C_{2+}.

7.4 Manipulating the backpressure

It has been shown that the partial pressure of CO_2 directly influences the rate of CO_2 mass transfer to the electrode surface due to the relationship between CO_2 solubility and solvent solubility[16]. Nevertheless, operating CO_2 electrolyzers at high pressure requires balancing the pressure between the cathode and anode to prevent damage to the AEM and maintain reliable operation. Pressure imbalances can be caused by gas products formed at the cathode or anode, even at ambient pressure, or by backpressure from the attached in-situ gas chromatograph, affecting water transport and mechanical AEM robustness [54].

The possibility of using thicker membranes to reduce pressure gradients has been suggested [107]. However, I demonstrated that thicker AEMs increase the resistance losses and cause water imbalances, accelerating flooding, due to higher hydraulic permeation gradients (see Chapter 6 for a detailed description of such phenomena). Therefore, manipulating the backpressure across both channels of the electrolyzer has been implemented to manipulate $*CO_2$ coverage at the electrode surface (by increasing CO_2 feed concentration) and mitigate flooding effects. Thus, I conducted a study in which I varied the backpressure (0-1000 mbar in both channels) to control water drag and enhance GDE stability.

7.4.1 Experimental Setup

A description of the reaction setup can be found in Chapter 3, which was the same one used for this set of experiments. It is necessary, however, to make some modifications, including adding two backpressure regulators at the gas outlet streams of the electrolyzer.

Backpressure regulators: A set of Equilibar LF Series Precision dome-loaded backpressure regulators from the Dutch company Pressure Solutions were mounted in the system. They do not measure the pressure directly in the gas stream but instead regulate the flow using a diaphragm. The diaphragm is opened only when the pressure of the regulated gas is greater than the externally controlled pilot pressure. The regulators, which can be used for gases and liquids, were constructed with diaphragm material PGL4.2 and mounted after the cell. To control the pilot pressure, a dual valve pressure controller model PCS-DRP70 was utilized, and the electronics have been replaced with a more robust system from Widgetlords Electronics.

Application of cell's backpressure: Pressure sensors were used to monitor the cell pressure, and the applied backpressure to the system is defined by the difference between the cathode (p_{cat}) and anode (p_{an}). In the first set of experiments, the pressure difference was varied between 0-1000 mbar, and electrolysis was performed at 200 $mA \cdot cm^{-2}$. Such experiments allowed me to see the threshold pressure at which pressure would cause water to penetrate the GDE and evaluate whether there was any visible effect on the mechanical strength of the membrane. Further studies focused on varying the pressure difference in the different reaction channels, the feeding rate, and operation long-term to evaluate the effects on product selectivity and stability (linked to the switch towards HER).

7.4.2 Screening of different cell backpressure in MEA systems

First of all, I examined the effects of backpressure on local CO_2 concentration and CO_2R activity. In Figure 7.11, the Faradaic Efficiency of gas products is depicted as a function of cell overpressure (backpressure). Specifically, I study the selectivity of three products: H_2, which I link to GDE failure and low CO_2R activity, CO (as the primary intermediate towards C_{2+}), and C_2H_4 (an indicator of C_{2+} selectivity). Each measurement at different was conducted at 200 $mA \cdot cm^{-2}$ for two hours.

At overpressure below 500 mbar, the HER selectivity is suppressed by less than 20%, whereas in the base case (no overpressure), the HER was already around 35% in just two hours, and becoming dominant over time. A cell overpressure threshold of 600 mbar defined the maximum point in my system where I observed HER shifts (from 11% at 100 mbar to 25% at 600 mbar, even to 46% at 1 bar overpressure). The selectivity towards CO with 28% was found at 200 mbar, while the selectivity

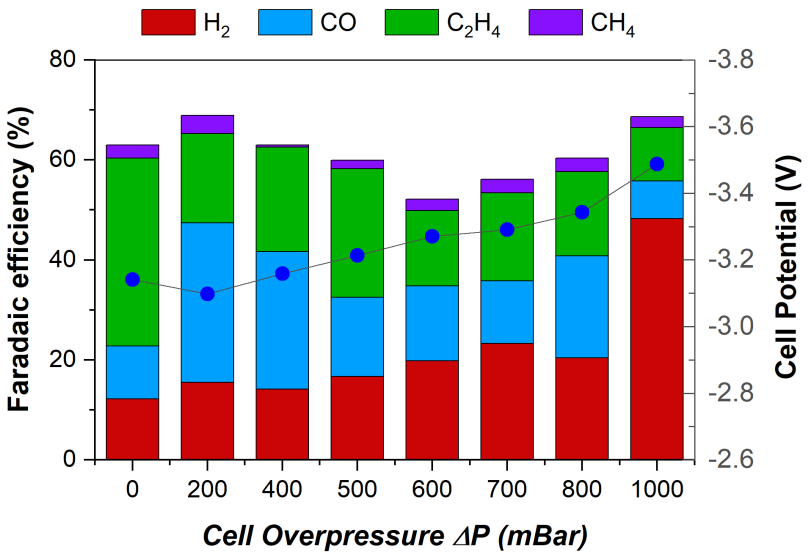

Figure 7.11: Product distribution and cell potential by applying different cell overpressure through regulation.

towards C_2H_4 did not change significantly due to the effect of backpressure (20-25% from 200 mbar).

Generally, there are two main reasons for variations in product selectivity due to the effect of backpressure. The first effect is on the local CO_2 concentration, where a rise in partial pressure will enhance $*CO_2$ coverage, and the HER (site-blocking effects) will be suppressed, leading to a preference for carbon-based products [46]. Another possibility might be that the backpressure keeps a high capillary pressure (linked to GDE electrowetting), minimizing electrode flooding.

On the other hand, I observed a switch from C_2H_4 to CO selectivity between 100 and 200 mbar. Although this variation has not been fully explained, it supports the observation (from temperature effect studies) that *CO coverage may not be the dominant factor for C_2H_4 formation. Instead, in agreement with previous literature reports, CO selectivity increased at higher pressures, which I attribute to a low residence time for CO_2 at the electrode surface and the adsorbate-adsorbate repulsion at the electrode surface [135, 52].

7.4.3 Effect of the applied backpressure in MEA systems

After discovering an optimal cell overpressure for my reaction system (100-200 mbar), I wanted to determine if it affected the channel where I applied backpressure. Therefore, I conducted an experiment in which I applied a 200 mbar difference and altered the range in which channel the higher backpressure was implemented (cathode vs. anode channel). Product distribution at 300 $mA \cdot cm^{-2}$ is shown in Figure 7.12, where the pressure varies in each channel, but the difference is kept

constant.

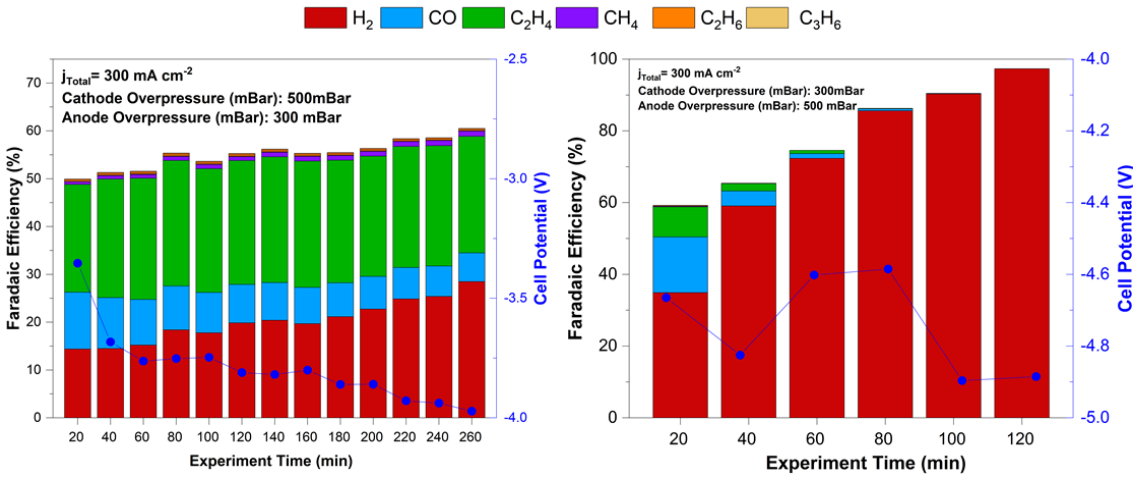

Figure 7.12: Comparison of the effect of the applied backpressure by implementing: a) Higher cathode overpressure and b) Higher anode overpressure, keeping the same pressure difference at the cell.

Results with higher cathode overpressure showed stable selectivity towards gas products (FEH_2<10%, FE_{CO}= 20-25%, and FE_{C2H4}= 22-27%) after four hours of operation. Alternatively, experiments with higher anodic overpressure showed limited stability due to an accelerated loss of CO_2R activity (after 20 minutes, I already observed dominant HER with less than 20% FE of carbon products, followed by dominance exceeding 80% after 1 hour). The differences in hydrodynamic pressures in the system may explain the differences in trends between these experiments. In MEAs, sufficient water flux must be provided at the cathode side to maintain CO_2R, while excess water must be removed to avoid GDE flooding. I use the HER enhancement as indicator for water drag and flooding across the system. Increasing the pressure on the anode chamber can result in a substantial amount of water being dragged to the cathode, which may result in a loss of GDE-hydrophilicity (water penetration), as experiments applied to the anode showed a higher HER than experiments performed on the cathode.

Furthermore, the experiments with larger anode overpressures also showed higher potential. This phenomenon can be attributed to a higher bubble formation rate (caused by the OER and the inlet pressurization), which increases ohmic losses and alters the cell potential measurement (E_{cell}=-3.3 V vs. E_{cell}=-3.9 V at 100 min between the different experiments) [54]. Overall, the shifts observed here illustrate the effect of backpressure on capillary pressure and water transport, as well as the importance of increasing the overpressure in the cathode channel to improve the stability and selectivity of the system[104].

7.4.4 Combined effects of backpressure and CO_2 utilization by decreasing the inlet flow rate

As previously shown, backpressure favors CO over C_2H_4. To evaluate the coupled effects between changes in CO_2 concentration and backpressure, I operated at low CO_2 feed flow rate and longer-time to determine if a longer residence time and optimum surface coverage for C_{2+} could be achieved. For example, by reducing the inlet flow rate from 50 mL $\cdot$ min^{-1} to 10 mL $\cdot$ min^{-1}, the bulk CO_2 gas concentration was reduced from 81.9 to 33.3 mol%, respectively. Therefore, having low CO_2 concentrations at the surface, I could evaluate if the applied backpressure could switch the selectivity towards C_{2+}.

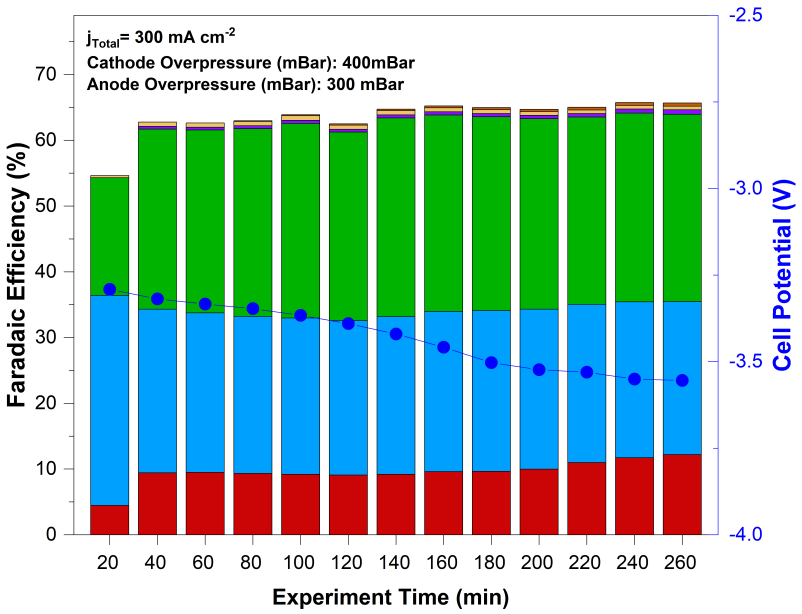

Figure 7.13: Effect of the applied and low CO_2 feeding rate in product distribution and cell potentials.

The FE_{CO} decreased from 24% to 10% when the CO_2 flow rate was reduced from 40 mL $\cdot$ min^{-1} to 10 mL $\cdot$ min^{-1}, as shown in Figures 7.12 and 7.13. Interestingly, a drop in selectivity towards CO seemed to be accelerated under combined backpressure and low flow rates (from 15% to 7% after 2 hours). Backpressure enhances CO production at higher flow rates, whereas it appears to have a contrary effect at lower flow rates. This suggests that the surface coverage at combined and low flow rates offers an environment where *CO does not desorb but further reacts towards C_{2+} products [136]. Additionally, when low flow rates and backpressure were combined, FE_{C2H4} increased from 23% to 28%. There was a slight increase in HER after 4 hours in the experiment with a higher flow rate (21% versus 10%), but it was still significantly lower than those without using backpressure. These observations suggest that HER could be suppressed when there is a high CO_2 local concentration at the surface.

7.4.5 Long-term experiment

To evaluate the effect of backpressure in long-term, I conducted electrolysis for 10 hours at 200 mA · cm^{-2} to evaluate whether backpressure maintains its effects on CO_2 coverage and flooding. According to Figure 7.14, stable CO_2R activity was observed for 300 min before shifts towards HER were observed. The results suggest that backpressure is primarily responsible for increasing local CO_2 concentration instead of reducing electrode flooding, as limited CO_2 mass transport and salt precipitates were observed after disassembly. Therefore, applying pressure in the system can be considered an alternative when scaling up the operation. Still, it shouldn't be the only one and should be used with other strategies.

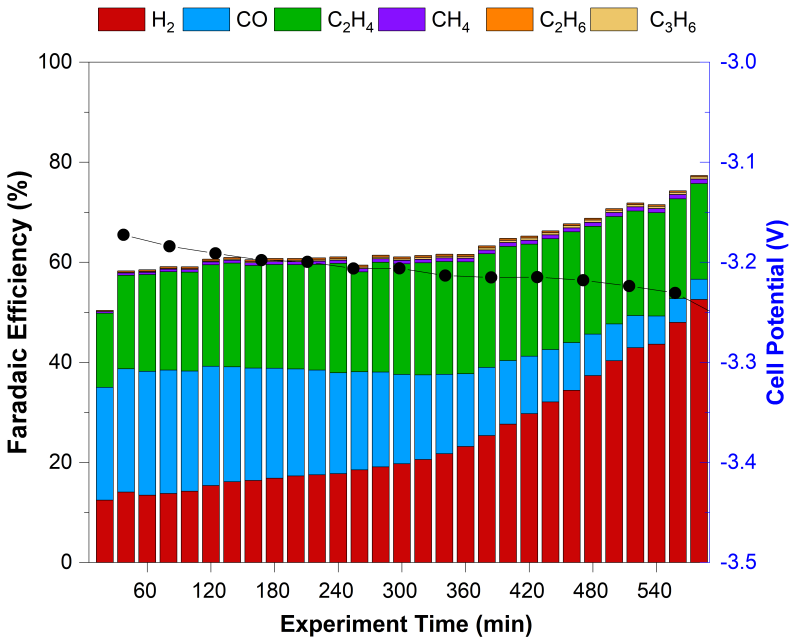

Figure 7.14: Long-term experiment to evaluate effects of backpressure in the CO_2 electrolysis stability.

7.5 Summary

Throughout this chapter, I studied different strategies to improve the electrode's stability and CO_2 conversion. Based on the results, the following conclusions for each alternative were drawn:

- Adding ionomers into the Cu-GDE enhances the catalyst activity (an increase of at least 2-fold), independent of the ionomer's chemistry.
- The ionomer loading plays a crucial role in this approach, where minor changes (e.g., 10 to 20 µm · cm^{-2}) significantly influence performance, DLC, and selectivity. In addition, some reproducibility issues might be faced when there isn't a standardized method for the electrode synthesis for this approach.

- The ionomers slightly affect product selectivity (TMA and MPIP enhanced HER compared to MPIP, PFTE, and PFSA). Interestingly, I didn't observe different effects by using CEI vs. AEI, as both seemed to positively stabilize CO-intermediates, decrease water penetration, or avoid carbonate formation.
- Coupling ionomers with a performance at elevated temperatures ensured a stable operation of 50 h with Cu-GDEs with selectivity towards carbon-products higher than 80% at 200 $mA \cdot cm^{-2}$.
- Decreasing the CO_2 feeding rate improved the CO_2 without bordering on mass transfer limitations. The magnitude of the reflux ratio didn't influence the product selectivity and the cell potential.
- The addition of the recycling loop seemed to improve the CO_2 conversion at current densities below 200 $mA \cdot cm^{-2}$. However, its implementation is limited due to GDE flooding, catalyst deactivation, and possible enhancement of side reactions (HER or carbonate formation).
- The application of the recycling loop was limited by changing the catalyst substrate to commercial GDLs, independent of the operation conditions.
- Further measurements of capacitance and capillarity pressure are necessary to determine the actual effect of the recycling line on water transport and electrowetting.
- Manipulating the backpressure (below 600 mbar) mitigates the HER, favoring the selectivity towards carbon products.
- A shift between CO to ethylene was observed from 100 to 200 mbar, suggesting the *CO coverage might not be a determining factor.
- It is important to ensure that slight overpressure at the cathode is applied to tune the water management and capillary pressure on the system.

Chapter 8

Conclusions and general discussion

When I started this Ph.D. project, I faced a lot of uncertainty and limitations while operating my electrochemical reactor. Regardless of the electrocatalyst, the operation was limited (less than two hours), as I usually observed HER spike, GDE flooding, or salt precipitation in my MEA or catholyte flow cells (e.g., Figure 2.2). Regardless of cathode, anode, or membrane, this problem kept escalating, and although sometimes I achieved high selectivity (e.g., 50% towards C_2H_4 in MEA at 150 $mA \cdot cm^{-2}$), I could not maintain that performance for long-term. As a result, I examined the influence of multiple parameters and proposed strategies for the current challenges. These strategies must, of course, have an effect that is visible during operation. But most importantly, they must be easy to scale and implement since CO_2 electrolysis is expected to become commercially viable in the near future.

Consequently, operational conditions and engineering factors were studied in relation to performance. Initially, I evaluated the effect of different parameters, including selecting the appropriate GDE, anode, electrolyzer configuration, AEM, or electrolyte, on product distribution, cell potential, and current density towards CO_2R. While I have stated in this thesis that I didn't optimize these parameters, I could observe that each element of the electrolyzer contributes to the overall cell potential (which is directly linked to energy consumption). Therefore, I used the materials with the highest benefits during operation (commercial-carbon-based GDL with low through-out pressure, AEM with high IEC and moderate WU, stable electrocatalyst/materials at high current densities and alkaline conditions). In this way, I can analyze multiple strategies more systematically and simultaneously guarantee reproducibility across experiments and in comparison with the literature.

However, choosing the appropriate reaction components is insufficient to resolve all problems encountered during electrolysis. Therefore, I took some of the most relevant challenges in the field (based on the current state-of-the-art) and explored some alternatives, including operation at elevated temperatures, the use of Cu-based tandem catalysts, synthesis of AEM suitable for CO_2 reduction, implementation of ionomers, manipulating the cell's back pressure or adding a recycling line to the reaction system. Initially, I was driven to investigate these strategies as they had not been widely discussed, which gave me the opportunity to examine their effects on CO_2E. In addition, they provide potential alternatives in terms of improving CO_2R kinetics and mass transport, selectivity, water management, or CO_2 conversion under industrially relevant conditions.

In Chapter 4, I conducted a systematic study to analyze the effects of temperature on zero-gap CO_2 electrolysis, focusing on selectivity, activity, and overall performance. I found that elevating the temperature increased the activity towards CO_2R while lowering the cell potential and ohmic resistances. Interestingly, operation at temperatures above 50°C resulted in high selectivity toward CO (>40%), likely caused by a weakening of the binding strength of CO to the surface, which favored desorption, and was further corroborated by ATR-SEIRAS measurements. I found that in MEA systems, elevated temperature suppressed the HER (15% at 80°C compared to 60% at RT at 300 $mA \cdot cm^{-2}$) and delayed GDE flooding, attributed to a combination of effects coming from the AEM, CO_2 diffusion, and electrowetting. Using this approach, I achieved long-term operation with minor changes in selectivity or cell potential (<-3 V) while having an energy efficiency (EE) of 28% compared to the usual 15-20% at RT. However, there are still challenges with selectivity towards C_{2+}, which require combining this strategy with selective electrocatalysts, operating conditions, and AEMs to overcome current limitations.

To enhance the selectivity towards C_{2+}, I implemented tandem catalysts prepared by coating two independent layers in the CL, which is expected to increase the local CO concentration and gas transport. In Chapter 5, preliminary studies set up the optimal loading, fabrication method, and spatial arrangement showed the benefits by implementing this layer. Using CO-selective catalysts at the top layer improved the C_{2+} products (67%) compared to bare Cu (generally between 50-55% by using Ag with an optimal loading of 0.2 $mg \cdot cm^{-2}$). In addition, using different metals in the CL influenced the product distribution, with ZnO being the catalyst that favors ethanol over ethylene. Finally, the long-term experiment showed a stable C_{2+} selectivity, highlighting the approach's benefits.

As I was operating in MEA, the AEM played a significant role in the reaction environment and water management. Therefore, in Chapter 6, I presented the study of a new generation of AEMs for CO_2E applications. The use of QA (TMA, MPIP, and MPY) as headgroups in ETFE substrates exhibited desired transport, chemical, and mechanical properties, including high IEC (above 2 $mmol \cdot g^{-1}$), ionic conductivities, moderate water uptake, and low ohmic resistances ($< 0.6\ \Omega \cdot cm^2$), achieving stable operations (>200 h) with stable selectivity towards carbon-products (>80% at 150 $mA \cdot cm^{-2}$) and comparable performance to commercial ones. Heterocyclic groups (MPIP) provide membranes with thermal and chemical stability, allowing operation at elevated temperatures without signs of degradation, a significant issue in current AEMs. Despite the superior performance of this membrane, we (in collaboration with the University of Surrey) proposed methods to tune the mechanical properties, such as cross-linking or optimizing the amine compositions. These modifications didn't produce the expected stability and water transport results, but they provided insight into which strategies should be explored further in this field.

Finally, in Chapter 7, I study additional strategies to improve stability and CO_2 conversion. I employed ionomers since they have been reported in the literature to enhance catalytic activity (establishing the current state of the art). Using different IEIs, I showed improvement in the current density for CO_2R (at least 2-fold compared to bare Cu) and the ability to improve CO_2 availability by adding the ionomer next to the electrode surface without compromising product selectivity or stability. Using a recycling line seemed interesting, as it could maximize CO utilization in the system. However, minor differences were observed by applying this line compared to single-pass experiments. Furthermore, such an approach was limited to operation below 100 $mA \cdot cm^{-2}$ and porous substrates, as the changes in these factors showed accelerated electrode flooding, GDE degradation, and HER selectivity. In addition, I studied the effect of manipulating the backpressure on selectivity and water management, showing that a slight overpressure might overcome current selectivity and GDE stability issues for long-term operation, favoring water management and CO_2 local concentration.

As each proposed strategy showed benefits during its implementation, the next logical step is to pair these strategies in a single long-term experiment to evaluate how they improve stability and CO_2E performance. In the experiment presented in Figure 8.1, I coupled the following strategies: performance at elevated temperature (60ºC), use of MPIP-AEM, 100 mbar overpressure, the use of MPIP (10%wt.) ionomer coated in the GDE and using 0.1 M $CsHCO_3$ as electrolyte.

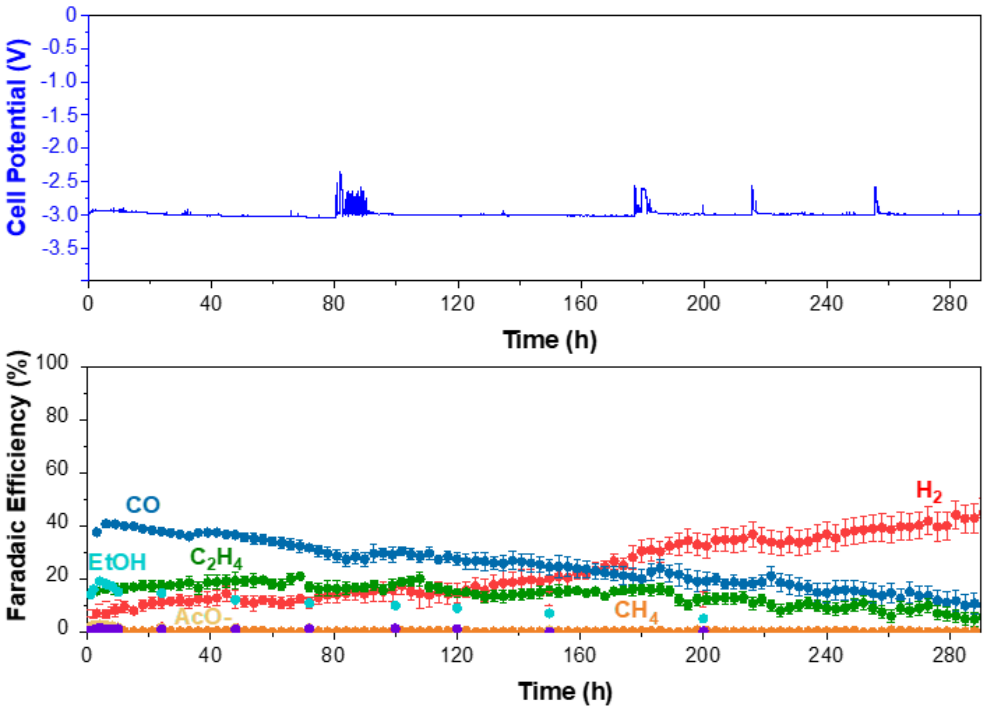

Figure 8.1: Long-term test coupling multiple strategies: Operation at 60°C, sputtered Cu-GDE, MPIP-AEM, MPIP-ionomer, 0.1 M $CsHCO_3$, and 100 mbar at 200 $mA \cdot cm^{-2}$.

The results showed a stable operation for around 200 h towards CO_2R at industrially relevant conditions. My stability goals have been exceeded compared to when I began this Ph.D. This operation is among the most stable at industrially relevant conditions (based on Wakerley et al. [40]). Even so, this experiment demonstrated CO_2E's current limitations and challenges. In my experiment, which lasted for almost 300 hours, I observed a slight shift in product distribution from CO_2-derived products to HER after 190 hours, with HER dominating after 205 hours. In other words, even if all these strategies lead to improved long-term performance, they are not sufficient to guarantee prolonged operation. Inadequacies in GDE substrates, anode materials, AEM degradation, and other factors might contribute to this shift and should be studied extensively (e.g., using PTFE as a substrate). As expected, CO was the primary product throughout the operation, with selectivity exceeding 30% due to the temperature's effect on weakening CO from the surface and its desorption. While CO is a product of CO_2R, other technologies, such as SOFC present prolonged stability with even higher selectivity than this approach. Therefore, it is necessary to find a catalyst capable of accelerating CO-CO coupling under these conditions. On the other hand, tandem catalysts can enhance C_{2+}, but they may not be a suitable approach under these conditions since their principle focuses on increasing local CO and has not shown any benefits when combined with other strategies. Fundamental studies might be an excellent alternative to finding the right electrocatalyst and remark on the necessity for both research lines to ensure operability at industrially relevant conditions of CO_2E.

Outlook and prospect for future research

The zero-gap electrolysis of CO_2 opens a pathway for carbon capture, renewable energy storage, and the production of chemicals and fuels. To make it cost-effective, electrolysis must occur at a rate that offsets capital costs while minimizing electrical energy lost as heat and internal resistances. However, more research is necessary to discover practical electrochemical configurations that operate at high current densities (>100 mA $\cdot$ cm^{-2}, ideally >1 A $\cdot$ cm^{-2}) for the long term. Temperature experiments with thermal and chemically stable materials should be conducted to evaluate heating resistance and its effect on CO_2/CO electrolysis. Additionally, ionomers should be explored further through bilayer films, or new alternatives to CO_2 conversion should be explored, such as using permeable regeneration layers to increase single-pass conversion efficiency. Moreover, Faradaic Efficiency should not be the only factor in determining the practical use of CO_2 electrolyzers for industrial applications. Energy Efficiency, stability, and logistical challenges should also be considered, along with rational electrode design, electrolyzer engineering, and optimal operating conditions to achieve scalability.

Bibliography

[1] Zhu Liu et al. "Monitoring global carbon emissions in 2021". In: *Nature Reviews Earth & Environment* 3.4 (2022), pp. 217–219.

[2] Gunnar Luderer et al. "Residual fossil CO_2 emissions in 1.5–2 C pathways". In: *Nature Climate Change* 8.7 (2018), pp. 626–633.

[3] Carl-Friedrich Schleussner et al. "Science and policy characteristics of the Paris Agreement temperature goal". In: *Nature Climate Change* 6.9 (2016), pp. 827–835.

[4] Vivian Scott and Oliver Geden. "The challenge of carbon dioxide removal for EU policy-making". In: *Nature Energy* 3.5 (2018), pp. 350–352.

[5] Pierre Friedlingstein et al. "Persistent growth of CO_2 emissions and implications for reaching climate targets". In: *Nature geoscience* 7.10 (2014), pp. 709–715.

[6] N RE. "The race to recycle carbon dioxide". In: *Nature* 603 (2022).

[7] Annette Alcasabas et al. "A Comparison of Different Approaches to the Conversion of Carbon Dioxide into Useful Products: Part I: CO_2 reduction by electrocatalytic, thermocatalytic and biological routes". In: *Johnson Matthey Technology Review* 65.2 (2021), pp. 180–196.

[8] Stéphanie Bouckaert et al. "Net Zero by 2050: A Roadmap for the Global Energy Sector". In: (2021).

[9] Jan Wyndorps, Hesam Ostovari, and Niklas Von der Assen. "Is electrochemical CO_2 reduction the future technology for power-to-chemicals? An environmental comparison with H 2-based pathways". In: *Sustainable Energy & Fuels* 5.22 (2021), pp. 5748–5761.

[10] Phil De Luna et al. "What would it take for renewably powered electrosynthesis to displace petrochemical processes?" In: *Science* 364.6438 (2019), eaav3506.

[11] Stephanie Nitopi et al. "Progress and perspectives of electrochemical CO_2 reduction on copper in aqueous electrolyte". In: *Chemical reviews* 119.12 (2019), pp. 7610–7672.

[12] Chi Chen, Juliet F Khosrowabadi Kotyk, and Stafford W Sheehan. "Progress toward commercial application of electrochemical carbon dioxide reduction". In: *Chem* 4.11 (2018), pp. 2571–2586.

[13] Shulin Zhao et al. "Advances in Sn-based catalysts for electrochemical CO_2 reduction". In: *Nano-Micro Letters* 11.1 (2019), pp. 1–19.

[14] Dunfeng Gao et al. "Enhancing CO_2 electroreduction with the metal–oxide interface". In: *Journal of the American Chemical Society* 139.16 (2017), pp. 5652–5655.

[15] Ting Ouyang et al. "Nanostructures for electrocatalytic CO_2 reduction". In: *Chemistry–A European Journal* 26.62 (2020), pp. 14024–14035.

[16] Sahil Garg et al. "Advances and challenges in electrochemical CO_2 reduction processes: an engineering and design perspective looking beyond new catalyst materials". In: *Journal of Materials Chemistry A* 8.4 (2020), pp. 1511–1544.

[17] Karen Chan. “A few basic concepts in electrochemical carbon dioxide reduction”. In: *Nature Communications* 11.1 (2020), pp. 1–4.

[18] Woong Choi, Yun Jeong Hwang, et al. “Catalyst design strategies for stable electrochemical CO_2 reduction reaction”. In: *Journal of Materials Chemistry A* 8.31 (2020), pp. 15341–15357.

[19] Shreya Sarkar and Sebastian C Chirambatte Peter. “Catalyst designing strategies for electrochemical CO_2 reduction: A perspective”. In: *Progress in Energy* (2022).

[20] Yoshio Hori, Katsuhei Kikuchi, and Shin Suzuki. “Production of CO and CH4 in electrochemical reduction of CO_2 at metal electrodes in aqueous hydrogencarbonate solution”. In: *Chemistry Letters* 14.11 (1985), pp. 1695–1698.

[21] Alexander Bagger et al. “Electrochemical CO_2 reduction: a classification problem”. In: *ChemPhysChem* 18.22 (2017), pp. 3266–3273.

[22] Ezra L Clark et al. “Standards and protocols for data acquisition and reporting for studies of the electrochemical reduction of carbon dioxide”. In: *Acs Catalysis* 8.7 (2018), pp. 6560–6570.

[23] Balázs Endrődi et al. “High carbonate ion conductance of a robust PiperION membrane allows industrial current density and conversion in a zero-gap carbon dioxide electrolyzer cell”. In: *Energy & Environmental Science* 13.11 (2020), pp. 4098–4105.

[24] Akansha Goyal et al. “Competition between CO_2 reduction and hydrogen evolution on a gold electrode under well-defined mass transport conditions”. In: *Journal of the American Chemical Society* 142.9 (2020), pp. 4154–4161.

[25] Beomil Kim et al. “Over a 15.9% solar-to-CO conversion from dilute CO_2 streams catalyzed by gold nanoclusters exhibiting a high CO_2 binding affinity”. In: *ACS Energy Letters* 5.3 (2019), pp. 749–757.

[26] Qisi Chen, Panagiotis Tsiakaras, and Peikang Shen. “Electrochemical Reduction of Carbon Dioxide: Recent Advances on Au-Based Nanocatalysts”. In: *Catalysts* 12.11 (2022), p. 1348.

[27] Xiaoxu Sun. “Achieving Selective and Efficient Electrocatalytic Activity for CO_2 Reduction on N-Doped Graphene”. In: *Frontiers in Chemistry* 9 (2021), p. 734460.

[28] Ana Sofia Varela, Wen Ju, and Peter Strasser. “Molecular nitrogen–carbon catalysts, solid metal organic framework catalysts, and solid metal/nitrogen-doped carbon (MNC) catalysts for the electrochemical CO_2 reduction”. In: *Advanced Energy Materials* 8.30 (2018), p. 1703614.

[29] Xing Zhang et al. “Highly selective and active CO_2 reduction electrocatalysts based on cobalt phthalocyanine/carbon nanotube hybrid structures”. In: *Nature communications* 8.1 (2017), pp. 1–8.

[30] Wen Luo et al. “Electrochemical reconstruction of ZnO for selective reduction of CO_2 to CO”. In: *Applied Catalysis B: Environmental* 273 (2020), p. 119060.

[31] Ruperto G Mariano et al. “Selective increase in CO_2 electroreduction activity at grain-boundary surface terminations”. In: *Science* 358.6367 (2017), pp. 1187–1192.

[32] Janis Timoshenko et al. “Steering the structure and selectivity of CO_2 electroreduction catalysts by potential pulses”. In: *Nature Catalysis* 5.4 (2022), pp. 259–267.

[33] Huali Wu et al. “Improved electrochemical conversion of CO_2 to multicarbon products by using molecular doping”. In: *Nature Communications* 12.1 (2021), pp. 1–11.

[34] Jiang Li et al. “Screening binary alloys for electrochemical CO_2 reduction towards multi-carbon products”. In: *Journal of Materials Chemistry A* 10.30 (2022), pp. 16171–16181.

[35] Gian Luca De Gregorio et al. “Facet-dependent selectivity of Cu catalysts in electrochemical CO_2 reduction at commercially viable current densities”. In: *ACS catalysis* 10.9 (2020), pp. 4854–4862.

[36] Tsu-Chin Chou et al. “Controlling the oxidation state of the Cu electrode and reaction intermediates for electrochemical CO_2 reduction to ethylene”. In: *Journal of the American Chemical Society* 142.6 (2020), pp. 2857–2867.

[37] Jofrey J Masana et al. “Influence of halide ions on the electrochemical reduction of carbon dioxide over a copper surface”. In: *Journal of Materials Chemistry A* 10.3 (2022), pp. 1086–1104.

[38] Alexander Bagger et al. “Electrochemical CO_2 reduction: classifying Cu facets”. In: *Acs Catalysis* 9.9 (2019), pp. 7894–7899.

[39] Yuhang Wang et al. “Catalyst synthesis under CO_2 electroreduction favours faceting and promotes renewable fuels electrosynthesis”. In: *Nature Catalysis* 3.2 (2020), pp. 98–106.

[40] David Wakerley et al. “Gas diffusion electrodes, reactor designs and key metrics of low-temperature CO_2 electrolysers”. In: *Nature Energy* 7.2 (2022), pp. 130–143.

[41] Georg Kastlunger and Karen Chan. *SelectCO$_2$ D7.5: Pathways towards CO, ethylene, ethanol on Cu Facets*. Technical University of Denmark, 2022.

[42] Xinyan Liu et al. “Understanding trends in electrochemical carbon dioxide reduction rates”. In: *Nature communications* 8.1 (2017), pp. 1–7.

[43] Xinyan Liu et al. “pH effects on the electrochemical reduction of CO (2) towards C2 products on stepped copper”. In: *Nature communications* 10.1 (2019), pp. 1–10.

[44] Wanyu Deng et al. “Unraveling the rate-limiting step of two-electron transfer electrochemical reduction of carbon dioxide”. In: *Nature communications* 13.1 (2022), pp. 1–9.

[45] Marilia Moura de Salles Pupo and Ruud Kortlever. “Electrolyte effects on the electrochemical reduction of CO_2”. In: *ChemPhysChem* 20.22 (2019), pp. 2926–2935.

[46] Mariana CO Monteiro et al. “Absence of CO_2 electroreduction on copper, gold and silver electrodes without metal cations in solution”. In: *Nature Catalysis* 4.8 (2021), pp. 654–662.

[47] Stefan Ringe et al. “Understanding cation effects in electrochemical CO_2 reduction”. In: *Energy & Environmental Science* 12.10 (2019), pp. 3001–3014.

[48] Gumaa A El-Nagar et al. “Unintended cation crossover influences CO_2 reduction activity in Cu-based zero-gap electrolysers”. In: (2022).

[49] Akira Murata and Yoshio Hori. "Product selectivity affected by cationic species in electrochemical reduction of CO_2 and CO at a Cu electrode". In: *Bulletin of the Chemical Society of Japan* 64.1 (1991), pp. 123–127.

[50] Joaquin Resasco et al. "Effects of Anion Identity and Concentration on Electrochemical Reduction of CO_2". In: *ChemElectroChem* 5 (2018), pp. 1064–1072.

[51] Federica Proietto et al. "Electrochemical conversion of pressurized CO_2 at simple silver-based cathodes in undivided cells: study of the effect of pressure and other operative parameters". In: *Journal of Applied Electrochemistry* 51.2 (2021), pp. 267–282.

[52] Hakhyeon Song et al. "Activation of C2H4 reaction pathways in electrochemical CO_2 reduction under low CO_2 partial pressure". In: *Applied Catalysis B: Environmental* 272 (2020), p. 119049.

[53] Mahinder Ramdin et al. "High pressure electrochemical reduction of CO_2 to formic acid/formate: a comparison between bipolar membranes and cation exchange membranes". In: *Industrial & engineering chemistry research* 58.5 (2019), pp. 1834–1847.

[54] Baran Sahin et al. "Controlling Product Distribution of CO_2 Reduction on CuO-Based Gas Diffusion Electrodes by Manipulating Back Pressure". In: *Energy Technology* (2022), p. 2200972.

[55] Armin Löwe et al. "Influence of temperature on the performance of gas diffusion electrodes in the CO_2 reduction reaction". In: *ChemElectroChem* 6.17 (2019), pp. 4497–4506.

[56] Sandra Hernandez-Aldave and Enrico Andreoli. "Fundamentals of gas diffusion electrodes and electrolysers for carbon dioxide utilisation: Challenges and opportunities". In: *Catalysts* 10.6 (2020), p. 713.

[57] Ádám Vass et al. "Anode Catalysts in CO_2 Electrolysis: Challenges and Untapped Opportunities". In: *ACS catalysis* 12.2 (2022), pp. 1037–1051.

[58] Thomas Burdyny and Wilson A Smith. "CO_2 reduction on gas-diffusion electrodes and why catalytic performance must be assessed at commercially-relevant conditions". In: *Energy & Environmental Science* 12.5 (2019), pp. 1442–1453.

[59] Roger Lin et al. "Electrochemical reactors for CO_2 conversion". In: *Catalysts* 10.5 (2020), p. 473.

[60] Eric W Lees et al. "Gas diffusion electrodes and membranes for CO_2 reduction electrolysers". In: *Nature Reviews Materials* 7.1 (2022), pp. 55–64.

[61] Siddhartha Subramanian et al. "Geometric Catalyst Utilization in Zero-Gap CO_2 Electrolyzers". In: *ACS Energy Letters* 8.1 (2022), pp. 222–229.

[62] Christine M Gabardo et al. "Continuous carbon dioxide electroreduction to concentrated multi-carbon products using a membrane electrode assembly". In: *Joule* 3.11 (2019), pp. 2777–2791.

[63] F Pelayo García de Arquer et al. "CO_2 electrolysis to multicarbon products at activities greater than 1 A cm- 2". In: *Science* 367.6478 (2020), pp. 661–666.

[64] Gastón O Larrazábal et al. “Analysis of mass flows and membrane cross-over in CO_2 reduction at high current densities in an MEA-type electrolyzer”. In: *ACS applied materials & interfaces* 11.44 (2019), pp. 41281–41288.

[65] Jing-Jing Lv et al. “A highly porous copper electrocatalyst for carbon dioxide reduction”. In: *Advanced Materials* 30.49 (2018), p. 1803111.

[66] Song Jin et al. “Advances and challenges for the electrochemical reduction of CO_2 to CO: from fundamentals to industrialization”. In: *Angewandte Chemie* 133.38 (2021), pp. 20795–20816.

[67] Matthew Jouny, Wesley Luc, and Feng Jiao. “General techno-economic analysis of CO_2 electrolysis systems”. In: *Industrial & Engineering Chemistry Research* 57.6 (2018), pp. 2165–2177.

[68] Haeun Shin, Kentaro U Hansen, and Feng Jiao. “Techno-economic assessment of low-temperature carbon dioxide electrolysis”. In: *Nature Sustainability* 4.10 (2021), pp. 911–919.

[69] Parameswaram Ganji et al. “Toward commercial carbon dioxide electrolysis”. In: *Advanced Sustainable Systems* 4.8 (2020), p. 2000096.

[70] Brian Seger, Marc Robert, and Feng Jiao. “Best practices for electrochemical reduction of carbon dioxide”. In: *Nature Sustainability* (2023), pp. 1–3.

[71] Xu Lu et al. “A high performance dual electrolyte microfluidic reactor for the utilization of CO_2”. In: *Applied energy* 194 (2017), pp. 549–559.

[72] Ivan Grigioni et al. “CO_2 electroreduction to formate at a partial current density of 930 mA cm–2 with InP colloidal quantum dot derived catalysts”. In: *ACS Energy Letters* 6.1 (2020), pp. 79–84.

[73] Chuan Xia et al. “Continuous production of pure liquid fuel solutions via electrocatalytic CO_2 reduction using solid-electrolyte devices”. In: *Nature Energy* 4.9 (2019), pp. 776–785.

[74] Jun Li et al. “Copper adparticle enabled selective electrosynthesis of n-propanol”. In: *Nature communications* 9.1 (2018), pp. 1–9.

[75] Lei Fan et al. “Strategies in catalysts and electrolyzer design for electrochemical CO_2 reduction toward C2+ products”. In: *Science advances* 6.8 (2020), eaay3111.

[76] Hesamoddin Rabiee et al. “Gas diffusion electrodes (GDEs) for electrochemical reduction of carbon dioxide, carbon monoxide, and dinitrogen to value-added products: a review”. In: *Energy & Environmental Science* 14.4 (2021), pp. 1959–2008.

[77] Alina Gawel et al. “Electrochemical CO_2 reduction-The macroscopic world of electrode design, reactor concepts & economic aspects”. In: *Iscience* (2022), p. 104011.

[78] Danielle A Salvatore et al. “Designing anion exchange membranes for CO_2 electrolysers”. In: *Nature Energy* 6.4 (2021), pp. 339–348.

[79] Carlos A Giron Rodriguez et al. “Influence of Headgroups in Ethylene-Tetrafluoroethylene-Based Radiation-Grafted Anion Exchange Membranes for CO_2 Electrolysis”. In: *ACS Sustainable Chemistry & Engineering* (2023).

[80] Sahil Garg et al. “How membrane characteristics influence the performance of CO_2 and CO electrolysis”. In: *Energy & Environmental Science* 15.11 (2022), pp. 4440–4469.

[81] Nia J Harmon and Hailiang Wang. “Electrochemical CO_2 Reduction in the Presence of Impurities: Influences and Mitigation Strategies”. In: *Angewandte Chemie International Edition* (2022), e202213782.

[82] Byung Hee Ko et al. “The impact of nitrogen oxides on electrochemical carbon dioxide reduction”. In: *Nature communications* 11.1 (2020), pp. 1–9.

[83] McLain E Leonard et al. “Investigating electrode flooding in a flowing electrolyte, gas-fed carbon dioxide electrolyzer”. In: *ChemSusChem* 13.2 (2020), pp. 400–411.

[84] McLain E Leonard et al. “Editors’ choice—Flooded by success: on the role of electrode wettability in CO_2 electrolyzers that generate liquid products”. In: *Journal of The Electrochemical Society* 167.12 (2020), p. 124521.

[85] Mark Sassenburg et al. “Zero-Gap Electrochemical CO_2 Reduction Cells: Challenges and Operational Strategies for Prevention of Salt Precipitation”. In: *ACS Energy Letters* 8 (2022), pp. 321–331.

[86] Asger Moss et al. “In Operando investigations of oscillatory water and carbonate effects in MEA-based CO_2 electrolysis devices”. In: (2022).

[87] Yueyuan Gu et al. “Long-term-stability continuous flow CO_2 reduction electrolysers with high current efficiency”. In: *Sustainable Energy & Fuels* 5.3 (2021), pp. 758–766.

[88] Zengcai Liu et al. “CO_2 electrolysis to CO and O2 at high selectivity, stability and efficiency using sustainion membranes”. In: *Journal of The Electrochemical Society* 165.15 (2018), J3371.

[89] Ming Ma et al. “Insights into the carbon balance for CO_2 electroreduction on Cu using gas diffusion electrode reactor designs”. In: *Energy & Environmental Science* 13.3 (2020), pp. 977–985.

[90] Jie Zhang, Wen Luo, and Andreas Züttel. “Crossover of liquid products from electrochemical CO_2 reduction through gas diffusion electrode and anion exchange membrane”. In: *Journal of catalysis* 385 (2020), pp. 140–145.

[91] Rui Kai Miao et al. “Electroosmotic flow steers neutral products and enables concentrated ethanol electroproduction from CO_2”. In: *Joule* 5.10 (2021), pp. 2742–2753.

[92] Danielle Salvatore and Curtis P Berlinguette. “Voltage matters when reducing CO_2 in an electrochemical flow cell”. In: *ACS Energy Letters* 5.1 (2019), pp. 215–220.

[93] Tim Möller et al. “The product selectivity zones in gas diffusion electrodes during the electrocatalytic reduction of CO_2”. In: *Energy & Environmental Science* 14.11 (2021), pp. 5995–6006.

[94] Emily Jeng and Feng Jiao. “Investigation of CO_2 single-pass conversion in a flow electrolyzer”. In: *Reaction Chemistry & Engineering* 5.9 (2020), pp. 1768–1775.

[95] Cao-Thang Dinh, Yuguang C Li, and Edward H Sargent. “Boosting the single-pass conversion for renewable chemical electrosynthesis”. In: *Joule* 3.1 (2019), pp. 13–15.

[96] Colin P O'Brien et al. "Single pass CO_2 conversion exceeding 85% in the electrosynthesis of multicarbon products via local CO_2 regeneration". In: *ACS Energy Letters* 6.8 (2021), pp. 2952–2959.

[97] Tianyu Zhang et al. "Enhance CO_2-to-C2+ products yield through spatial management of CO transport in Cu/ZnO tandem electrodes". In: *Journal of catalysis* 387 (2020), pp. 163–169.

[98] Xiaojie She et al. "Tandem electrodes for carbon dioxide reduction into C2+ products at simultaneously high production efficiency and rate". In: *Cell Reports Physical Science* 1.4 (2020), p. 100051.

[99] Chubai Chen et al. "Cu-Ag tandem catalysts for high-rate CO_2 electrolysis toward multicarbons". In: *Joule* 4.8 (2020), pp. 1688–1699.

[100] Jie Zhang et al. "Tandem effect of Ag@ C@ Cu catalysts enhances ethanol selectivity for electrochemical CO_2 reduction in flow reactors". In: *Cell Reports Physical Science* 3.7 (2022), p. 100949.

[101] Min Wang et al. "Tandem electrocatalytic CO_2 reduction with Fe-porphyrins and Cu nanocubes enhances ethylene production". In: *Chemical Science* 13.43 (2022), pp. 12673–12680.

[102] Carlos G Morales-Guio et al. "Improved CO_2 reduction activity towards C2+ alcohols on a tandem gold on copper electrocatalyst". In: *Nature Catalysis* 1.10 (2018), pp. 764–771.

[103] Yixu Zong, Pongkarn Chakthranont, and Jin Suntivich. "Temperature Effect of CO_2 Reduction Electrocatalysis on Copper: Potential Dependency of Activation Energy". In: *Journal of Electrochemical Energy Conversion and Storage* 17.4 (2020), p. 041007.

[104] Lien-Chun Weng, Alexis T Bell, and Adam Z Weber. "Towards membrane-electrode assembly systems for CO_2 reduction: a modeling study". In: *Energy & Environmental Science* 12.6 (2019), pp. 1950–1968.

[105] Marijn A Blommaert et al. "Orientation of a bipolar membrane determines the dominant ion and carbonic species transport in membrane electrode assemblies for CO_2 reduction". In: *Journal of Materials Chemistry A* 9.18 (2021), pp. 11179–11186.

[106] Danika G Wheeler et al. "Quantification of water transport in a CO_2 electrolyzer". In: *Energy & Environmental Science* 13.12 (2020), pp. 5126–5134.

[107] Angelica Reyes et al. "Managing hydration at the cathode enables efficient CO_2 electrolysis at commercially relevant current densities". In: *ACS Energy Letters* 5.5 (2020), pp. 1612–1618.

[108] John R Varcoe et al. "Anion-exchange membranes in electrochemical energy systems". In: *Energy & environmental science* 7.10 (2014), pp. 3135–3191.

[109] Robert B Kutz et al. "Sustainion imidazolium-functionalized polymers for carbon dioxide electrolysis". In: *Energy Technology* 5.6 (2017), pp. 929–936.

[110] Ana Laura Gonçalves Biancolli et al. "ETFE-based anion-exchange membrane ionomer powders for alkaline membrane fuel cells: a first performance compari-

son of head-group chemistry". In: *Journal of Materials Chemistry A* 6.47 (2018), pp. 24330–24341.

[111] Bjorn Hasa et al. "Benchmarking anion-exchange membranes for electrocatalytic carbon monoxide reduction". In: *Chem Catalysis* (2022), p. 100450.

[112] Kentaro U Hansen and Feng Jiao. "Creating the right environment". In: *Nature Energy* 6.11 (2021), pp. 1005–1006.

[113] Chanyeon Kim et al. "Tailored catalyst microenvironments for CO_2 electroreduction to multicarbon products on copper using bilayer ionomer coatings". In: *Nature Energy* 6.11 (2021), pp. 1026–1034.

[114] Abebe Reda Woldu et al. "Electrochemical reduction of CO_2: Two-or three-electrode configuration". In: *International Journal of Energy Research* 44.1 (2020), pp. 548–559.

[115] Sudipto Saha et al. "Electrodeposition fabrication of chalcogenide thin films for photovoltaic applications". In: *Electrochem* 1.3 (2020), pp. 286–321.

[116] Kai Liu, Wilson A Smith, and Thomas Burdyny. "Introductory guide to assembling and operating gas diffusion electrodes for electrochemical CO_2 reduction". In: *ACS energy letters* 4.3 (2019), pp. 639–643.

[117] Hiroto Miyake, Shen Ye, and Masatoshi Osawa. "Electroless deposition of gold thin films on silicon for surface-enhanced infrared spectroelectrochemistry". In: *Electrochemistry Communications* 4.12 (2002), pp. 973–977.

[118] Noémie Elgrishi et al. "A practical beginner's guide to cyclic voltammetry". In: *Journal of chemical education* 95.2 (2018), pp. 197–206.

[119] Vernon D Parker. "Linear sweep and cyclic voltammetry". In: *Comprehensive Chemical Kinetics*. Vol. 26. Elsevier, 1986, pp. 145–202.

[120] Thomas F Fuller and John N Harb. *Electrochemical engineering*. John Wiley & Sons, 2018.

[121] Harold M McNair, James M Miller, and Nicholas H Snow. *Basic gas chromatography*. John Wiley & Sons, 2019.

[122] PerkinElmer. *Gas Chromatography Explained: What It Is and How It Works*. 2022. URL: https://blog.perkinelmer.com/posts/gas-chromatography-explained-what-it-is-and-how-it-works (visited on 01/10/2022).

[123] Technotechnologies. *Clarus 590*. 2019. URL: https://technovn.vn/product/may-sac-ky-khi-gc-clarus-590-perkinelmer-man-hinh-cam-ung/.

[124] Frank Steiner, Carsten Paul, and Michael Dong. "HPLC autosamplers: Perspectives, principles, and practices". In: *LCGC North America* 37.8 (2019), pp. 514–529.

[125] Mark A Isaacs et al. "Advanced XPS characterization: XPS-based multi-technique analyses for comprehensive understanding of functional materials". In: *Materials Chemistry Frontiers* 5.22 (2021), pp. 7931–7963.

[126] Ib Chorkendorff and Johannes W Niemantsverdriet. *Concepts of modern catalysis and kinetics*. John Wiley & Sons, 2017.

[127] Kalsoom Akhtar et al. “Scanning electron microscopy: Principle and applications in nanomaterials characterization”. In: *Handbook of materials characterization*. Springer, 2018, pp. 113–145.

[128] Azad Mohammed and Avin Abdullah. “Scanning electron microscopy (SEM): A review”. In: *Proceedings of the 2018 International Conference on Hydraulics and Pneumatics—HERVEX, Băile Govora, Romania*. 2018, pp. 7–9.

[129] Daisuke Shindo et al. “Energy dispersive x-ray spectroscopy”. In: *Analytical electron microscopy for materials science* (2002), pp. 81–102.

[130] Rainer Küngas. “electrochemical CO_2 reduction for CO production: comparison of low-and high-temperature electrolysis technologies”. In: *Journal of The Electrochemical Society* 167.4 (2020), p. 044508.

[131] Rafaël E Vos and Marc TM Koper. “The Effect of Temperature on the Cation-Promoted Electrochemical CO_2 Reduction on Gold”. In: *ChemElectroChem* 9.13 (2022), e202200239.

[132] Zhenglei Yin et al. “An alkaline polymer electrolyte CO_2 electrolyzer operated with pure water”. In: *Energy & Environmental Science* 12.8 (2019), pp. 2455–2462.

[133] Feihan Yu et al. “Electrochemical CO_2 reduction: from catalysts to reactive thermodynamics and kinetics”. In: *Carbon Capture Science & Technology* (2022), p. 100081.

[134] Lien-Chun Weng, Alexis T Bell, and Adam Z Weber. “A systematic analysis of Cu-based membrane-electrode assemblies for CO_2 reduction through multiphysics simulation”. In: *Energy & Environmental Science* 13.10 (2020), pp. 3592–3606.

[135] Mozhgan Moradzaman, Carlos Sánchez Martínez, and Guido Mul. “Effect of partial pressure on product selectivity in Cu-catalyzed electrochemical reduction of CO_2”. In: *Sustainable Energy & Fuels* 4.10 (2020), pp. 5195–5202.

[136] Elizabeth R Corson et al. “In situ ATR–SEIRAS of carbon dioxide reduction at a plasmonic silver cathode”. In: *Journal of the American Chemical Society* 142.27 (2020), pp. 11750–11762.

[137] Daniel Corral et al. “Advanced manufacturing for electrosynthesis of fuels and chemicals from CO_2”. In: *Energy & Environmental Science* 14.5 (2021), pp. 3064–3074.

[138] Yuguang C Li et al. “Binding site diversity promotes CO_2 electroreduction to ethanol”. In: *Journal of the American Chemical Society* 141.21 (2019), pp. 8584–8591.

[139] Di Niu et al. “Cu2O-Ag Tandem Catalysts for Selective Electrochemical Reduction of CO_2 to C2 Products”. In: *Molecules* 26.8 (2021), p. 2175.

[140] Huei-Ru “Molly” Jhong, Fikile R Brushett, and Paul JA Kenis. “The effects of catalyst layer deposition methodology on electrode performance”. In: *Advanced Energy Materials* 3.5 (2013), pp. 589–599.

[141] Ying Chuan Tan et al. “Modulating local CO_2 concentration as a general strategy for enhancing C- C coupling in CO_2 electroreduction”. In: *Joule* 4.5 (2020), pp. 1104–1120.

[142] Liniker de Sousa et al. “Optimizing the Ink Formulation for Preparation of Cu-Based Gas Diffusion Electrodes Yielding Ethylene in Electroreduction of CO_2”. In: *ACS ES&T Engineering* 1.12 (2021), pp. 1649–1658.

[143] Ezra L Clark et al. “Electrochemical CO_2 reduction over compressively strained CuAg surface alloys with enhanced multi-carbon oxygenate selectivity”. In: *Journal of the American Chemical Society* 139.44 (2017), pp. 15848–15857.

[144] Hilmar Guzmán et al. “CO_2 conversion to alcohols over Cu/ZnO catalysts: prospective synergies between electrocatalytic and thermocatalytic routes”. In: *ACS Applied Materials & Interfaces* 14.1 (2021), pp. 517–530.

[145] Jinghui Li et al. “Probe Into the Influence of Crosslinking on CO_2 Permeation of Membranes”. In: *Scientific reports* 7.1 (2017), pp. 1–11.

[146] Lianqin Wang et al. “Radiation-grafted anion-exchange membranes: the switch from low-to high-density polyethylene leads to remarkably enhanced fuel cell performance”. In: *Energy & Environmental Science* 12.5 (2019), pp. 1575–1579.

[147] Tianchi Zhou et al. “A review of radiation-grafted polymer electrolyte membranes for alkaline polymer electrolyte membrane fuel cells”. In: *Journal of Power Sources* 293 (2015), pp. 946–975.

[148] Yubin He et al. “A novel methodology to synthesize highly conductive anion exchange membranes”. In: *Scientific reports* 5.1 (2015), pp. 1–7.

[149] Xiaoyan Luo et al. “Water permeation through anion exchange membranes”. In: *Journal of Power Sources* 375 (2018), pp. 442–451.

[150] Kyle N Grew, Xiaoming Ren, and Deryn Chu. “Effects of temperature and carbon dioxide on anion exchange membrane conductivity”. In: *Electrochemical and Solid-State Letters* 14.12 (2011), B127.

[151] Mahinder Ramdin et al. “Electroreduction of CO_2/CO to C2 products: process modeling, downstream separation, system integration, and economic analysis”. In: *Industrial & engineering chemistry research* 60.49 (2021), pp. 17862–17880.

[152] R Sigwadi et al. “The proton conductivity and mechanical properties of Nafion®/ZrP nanocomposite membrane”. In: *Heliyon* 5.8 (2019), e02240.

[153] Kai Junge Puring et al. “Electrochemical CO2 reduction: tailoring catalyst layers in gas diffusion electrodes”. In: *Advanced Sustainable Systems* 5.1 (2021), p. 2000088.

Appendix A

Appendix A

Appendix A.2: Appendant to Chapter 2

Equations for estimating the effect of temperature in transport properties involved in CO_2E (taken from [63]):

CO_2 solubility

$$c_{CO2} = H_{CO2} \cdot c_{CO2,gas} \tag{A.0.1}$$

$$H_{CO2}(mM \cdot atm^{-1}) = 93.4517 \cdot \frac{100}{T[K]} - 60.2409 + (23.3585 \cdot \frac{T[K]}{100}) \tag{A.0.2}$$

CO_2 diffusion

$$D_{CO2} = 2.17 \cdot 10^{-4} \cdot e^{\frac{-2345}{\frac{1}{T[K]} + \frac{1}{T_{ref}}}} \tag{A.0.3}$$

Overall Water balance (take from [80]):

$$J_W = J_{diff} - J_{EOD} \pm J_{HP} - J_{W,CO2} - J_{W,eff} \tag{A.0.4}$$

Where J_{diff} is the diffusion flux, J_{EOD} is the electroosmotic drag flux, J_{HP} the hydraulic permeation flux, $J_{W,CO2}$ is the flux associated with water production/consumption from charge transfer and neutralization equations and $J_{W,eff}$ overall inlet and outlet of water in the system

Appendix A.3: Appendant to Chapter 3

Materials

ETFE polymer films (ethylene-tetrafluoroethylene, 25 µm thickness) were supplied by Nowofol Kunststoffprodukte GmbH (Germany). VBC (97% purity, a mixture of 3- and 4-ionomers, 700–1100 ppm nitromethane or 50–100 ppm tert-butylcatechol inhibitors) was purchased from Sigma Aldrich and used as supplied without any inhibitor removal prior to use in the grafting mixtures. In addition, 1-octyl-2-pyrrolidone dispersant, N-methylpiperidine (99% purity), trimethylamine (99%), N-methylpyrrolidine (88%), and acetone were purchased from Sigma-Aldrich (Merck). $AgNO_3$ titration standard analytical solutions (.02000 ± 0.00006 M) were purchased from Honeywell-Fluka. The ultra-pure water (UPW) used throughout this study was

generated using a Purity water purification system (resistivity = 18.2 M ·).

Commercial AEMs Selemion® AMV, Fumasep® FAA-3-50, and PiperION) were purchased from FuelCellStore, while Sustainion® X37-50 RT was purchased from Dioxide Materials. $KHCO_3$ or $CsHCO_3$ (Sigma-Aldrich 99.995% trace metal basis) and KOH (Sigma-Aldrich 99.95% trace metal basis) were used as an electrolyte for cell testing or membrane activation solutions. For ATR-SEIRAS, $HAuCl_4$ (98.0%), NH_4Cl (99.0%), Na_2SO_3 $Na_2S_2O_3 \cdot 5H_2O$ (98%), and NaOH from Alfa Aesar (China) Chemical Co., Ltd, AR to prepare the Au-films.

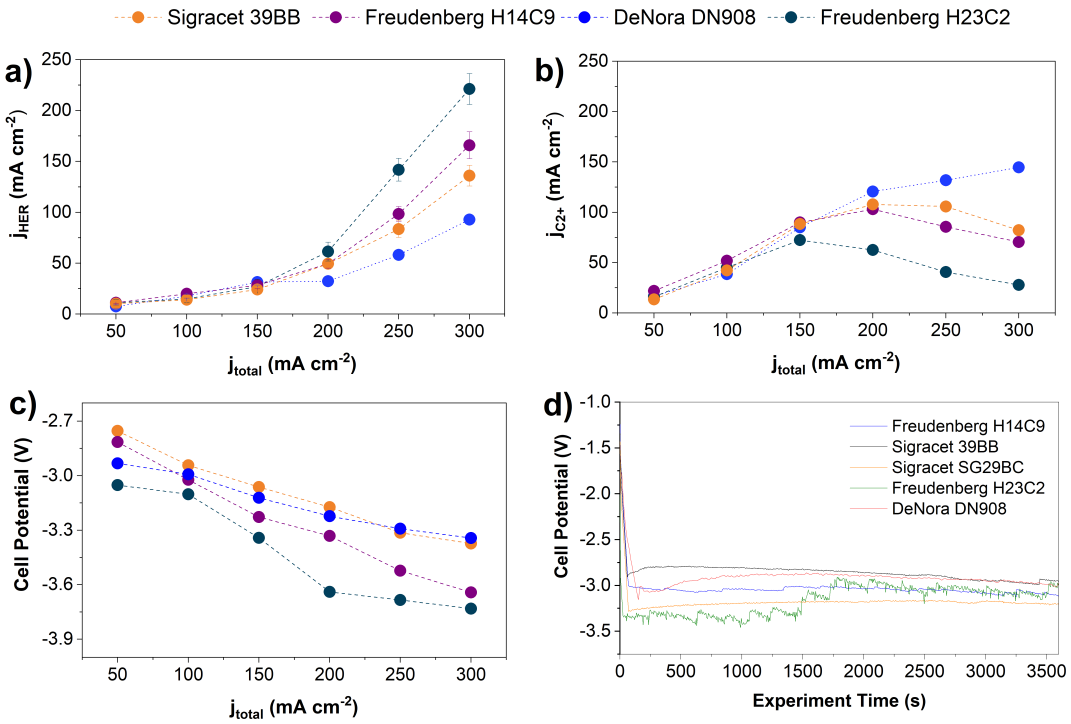

Fig. A.1: Screening of different Commercial GDLs

Although this section focuses on the study of ethanol, initial studies using the zero-gap configuration are conducted to study the effect of compression, thickness, cell potential, and product selectivity on the four different GDEs Sigracet 39BB, Freudenberg H23C2 and H14C9 and DeNora DN908), despite the limitation of the liquid quantification using this approach.

The Figure shows the partial current densities as a function of the applied current density (A-C), and the cell voltage profile (D).

Comparison between cell configurations in terms of product selectivity and stability

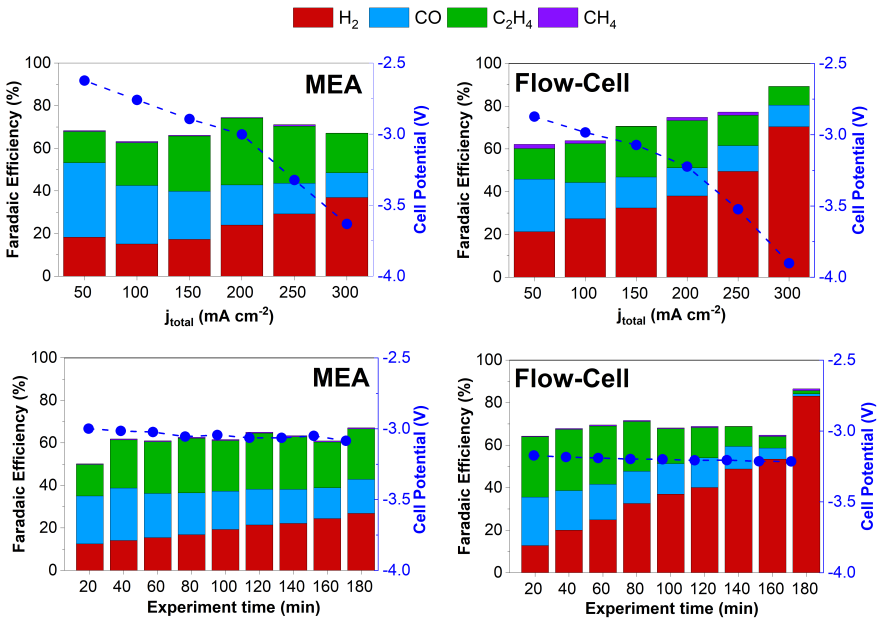

Figure A.2: Comparison of cell configuration MEA vs. Catholyte flow cell

AEM screening for CO_2E

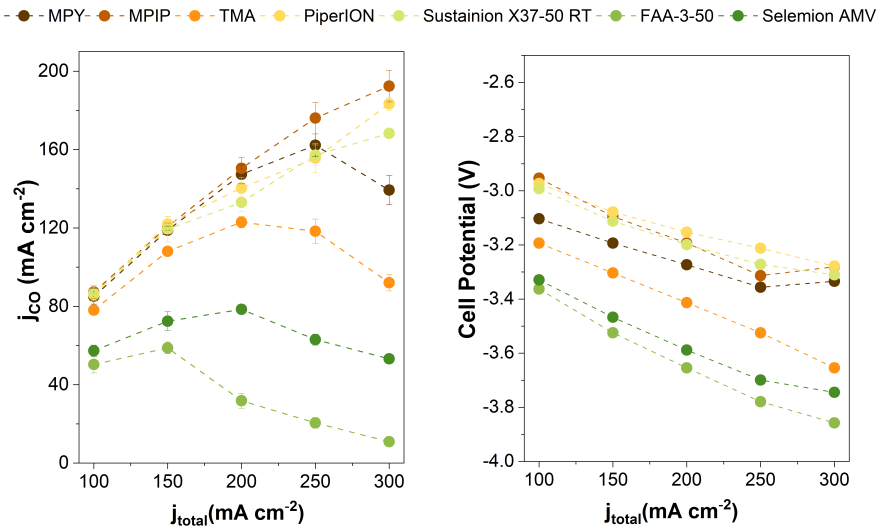

Figure A.3: Screening of different AEM and effect on j_{CO}

Anode screening for CO_2E

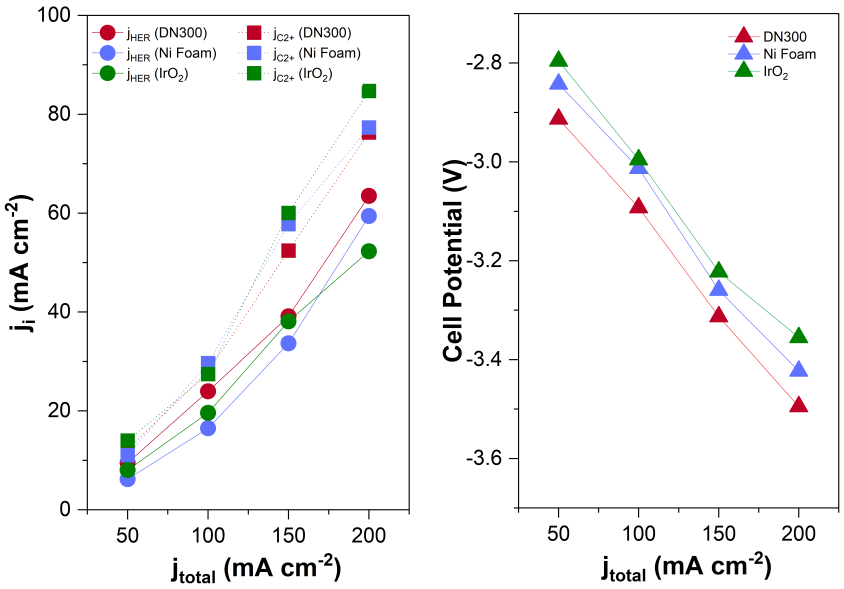

Figure A.4: Screening of different anodes and effects in selectivity and cell potentials

Effect of the CO_2 Feeding Rate

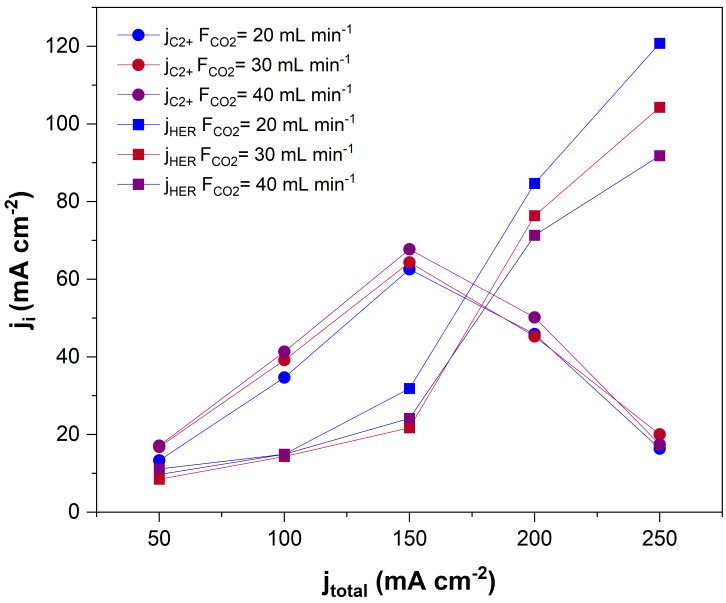

Figure A.5: Effect of the CO_2 Feeding Rate

Table A.1: Calibration Data for HPLC (DAD Detector)

Compound	RT (min)	Calibration Factor (uV.s/mol%)
Glyoxal	19.451	0.0031176
Glycoaldehyde	23.438	0.0022864
Formate	26.567	0.26605
Acetate	28.74	0.21086
Ethylene Glycol	30.82	0.004831
Hydroxyacetone	32.533	0.96651
Acetaldehyde	34.962	0.030397
Methanol	36.124	1.06196
Allyl Alcohol	41.204	1.20
Acetone	41.966	1.198
Propionaldehyde	43.109	4.83E-03

Electrolyte concentration

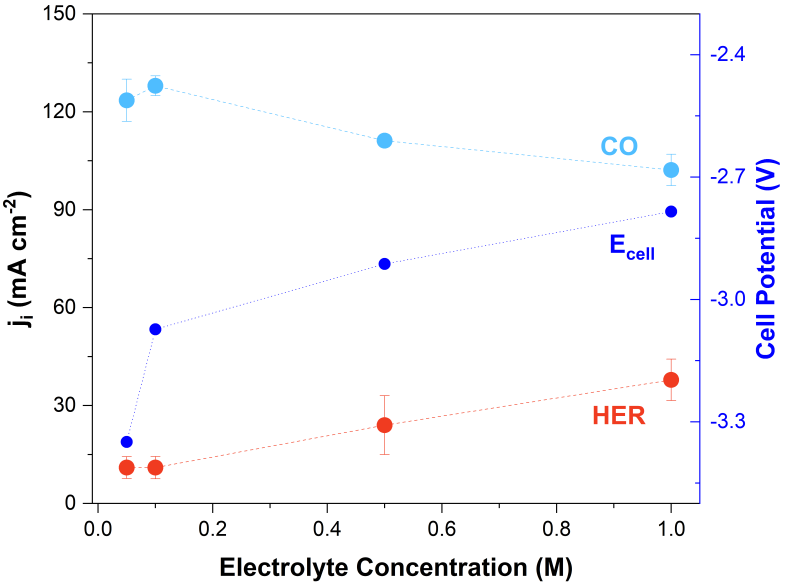

Figure A.6: Effect of the electrolyte concentration

Table A.2: Calibration Data for HPLC (RID Detector)

Compound	RT (min)	Calibration Factor (uV.s/mol%)
Glyoxal	19.744	23.079
Glycoaldehyde	23.729	65.129
Formaldehyde	26.17	2.732
Formate	26.86	17.089
Acetate	29.033	25.785
Ethylene Glycol	20.082	48.781
Hydroxyacetone	32.574	47.525
Acetaldehyde	34.962	12.969
Methanol	36.684	3.5469
Allyl Alcohol	41.497	41.57
Ethanol	41.546	21.923
Acetone	42.261	22.568
Propionaldehyde	43.39	19.155
Propanol	51.069	29.671

Effect of the different electrolyzers

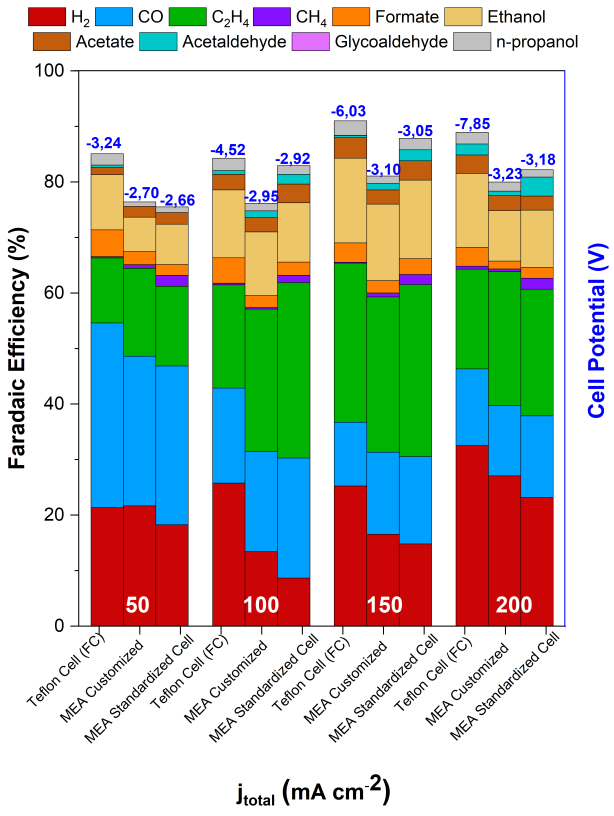

Figure A.7: Effect of the electrolyzer type used in this thesis

Appendix A.4: Appendant to Chapter 4

Table A.3: Effect of temperature in the standard potentials for different CO_2R products

T(°C)	E° CO (V)	E° C2H4 (V)	E° EtOH (V)	E° PrOH (V)	E° CH4 (V)
20	-0.104	0.081	0.080	0.096	0.171
30	-0.108	0.075	0.074	0.090	0.165
40	-0.112	0.069	0.068	0.083	0.160
50	-0.116	0.062	0.062	0.077	0.155
60	-0.120	0.056	0.056	0.070	0.150
70	-0.123	0.050	0.049	0.063	0.144
80	-0.127	0.044	0.043	0.057	0.139

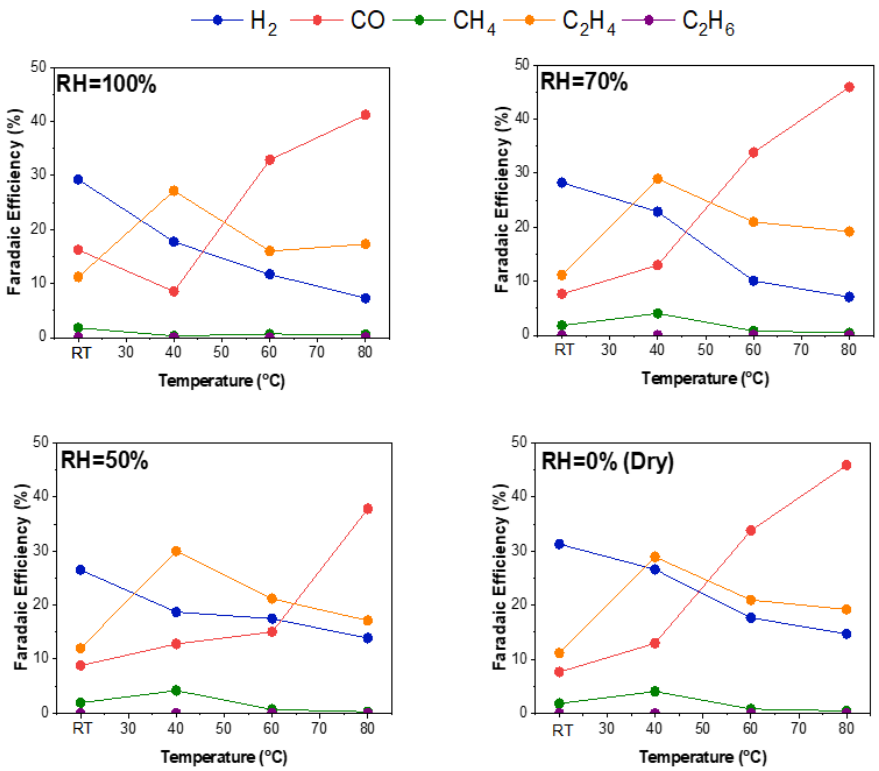

Figure A.8: Effect of the relative humidity (different humidity in CO_2 feeding rate) in the product distribution of gas-products for CO_2 electrolysis as a function of the temperature. A) 100%, b) 50%, c) 70%, and d) Dry

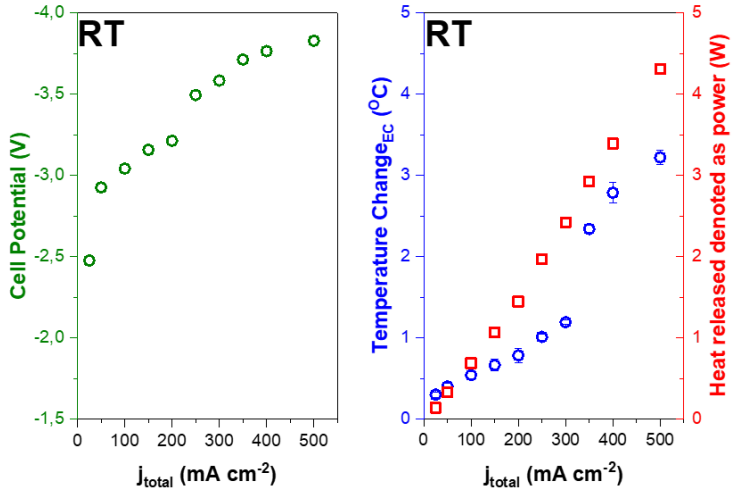

Figure A.9: Cell potential as function of j_{total} and power for CO_2E

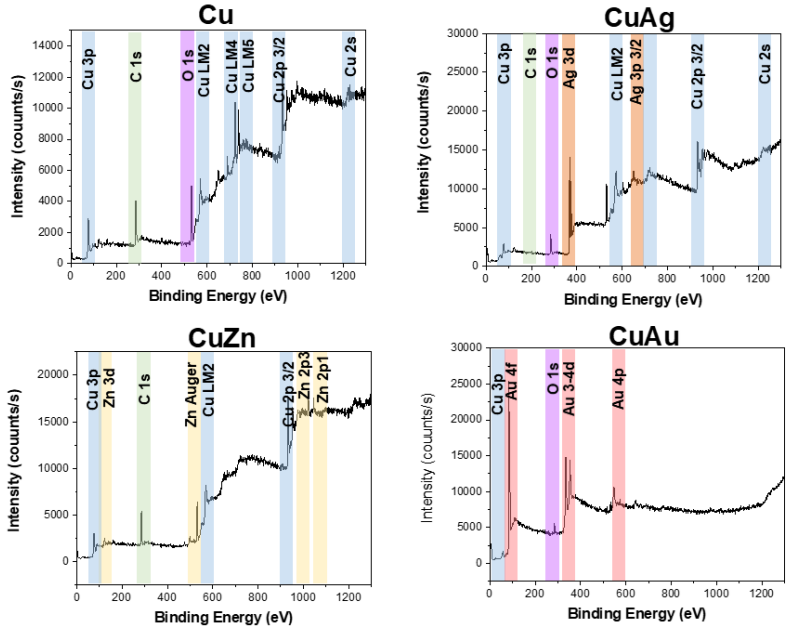

Figure A.10: XPS survey spectrum for tandem catalysts through co-sputtering

Appendix A.6: Appendant to Chapter 6

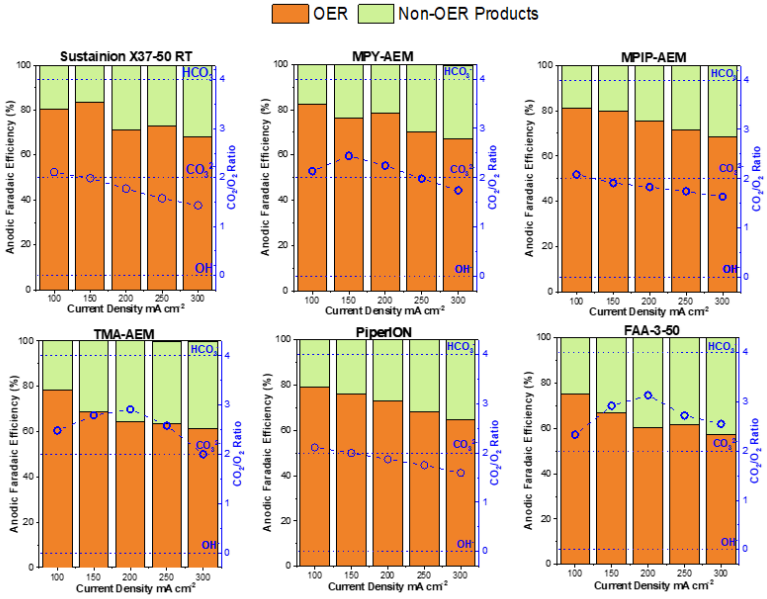

Figure A.11: CO_2/O_2 ratio evolved over the anode as a function of total current density for different AEMs

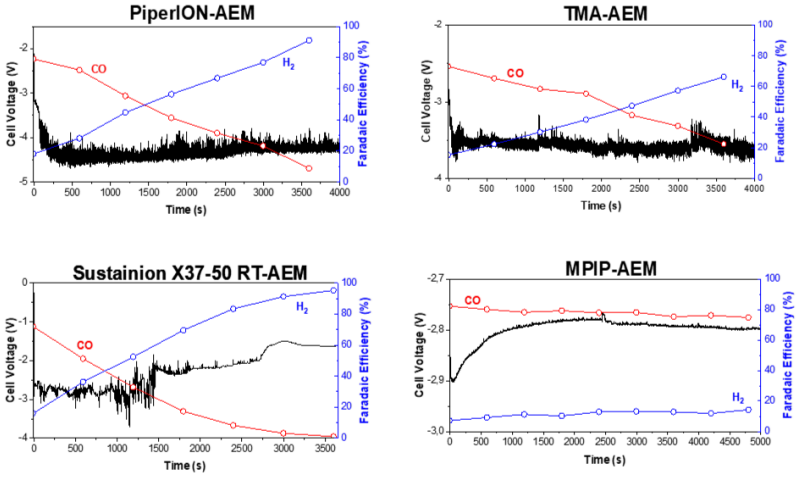

Figure A.12: Effect of temperature CO_2-electrolysis performance for AEMs at 90°C

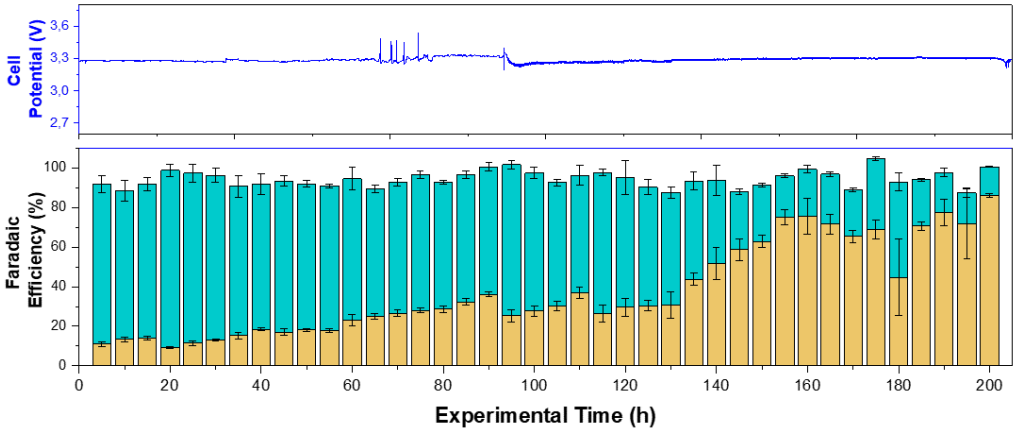

Figure A.13: 200h-stability test using Sutainion X37-50 RT

Appendix A.7: Appendant to Chapter 7

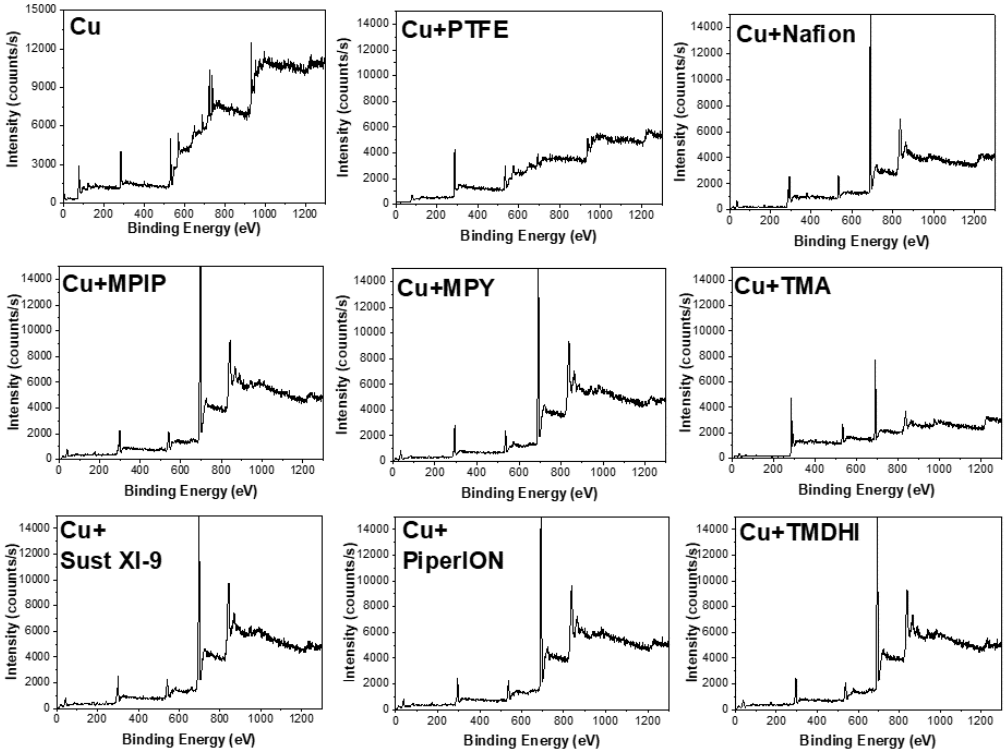

Figure A.14: XPS survey spectrum for Cu-GDEs for the ionomers

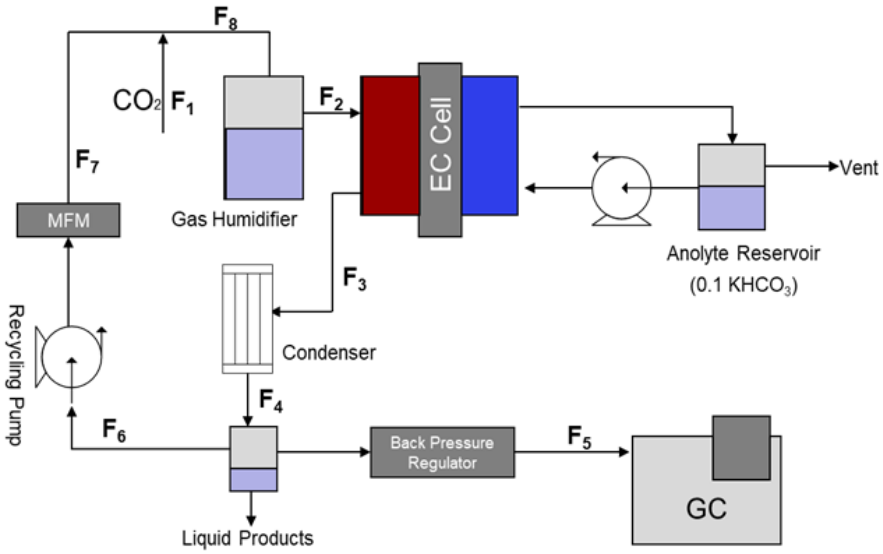

Figure A.15: Scheme of the reaction setup with the recycling loop

General balance equations

$$F_1 + F_7 = F_8 \tag{A.0.5}$$

Reflux Ratio

$$RR = F_7/F_5 \tag{A.0.6}$$

Appendix A

Appendix B

Publications

Paper I

Influence of headgroups in ETFE-based radiation-grafted anion exchange membranes for CO_2 electrolysis

Carlos A. Giron Rodriguez, Bjørt Oladottir Joensen, Asger B. Moss, Gaston Larrazabal, Daniel K. Whelligan, Brian Seger, John R. Varcoe, and Terry Wilson. ACS Sustainable Chemistry and Engineering, 2023.

ACS Sustainable Chemistry & Engineering

pubs.acs.org/journal/ascecg

Research Article

Influence of Headgroups in Ethylene-Tetrafluoroethylene-Based Radiation-Grafted Anion Exchange Membranes for CO_2 Electrolysis

Carlos A. Giron Rodriguez, Bjørt Óladottir Joensen, Asger Barkholt Moss, Gastón O. Larrazábal, Daniel K. Whelligan, Brian Seger,* John R. Varcoe,* and Terry R. Willson

Cite This: https://doi.org/10.1021/acssuschemeng.2c06205

Read Online

ACCESS | Metrics & More | Article Recommendations | Supporting Information

ABSTRACT: The performance of zero-gap CO_2 electrolysis (CO_2E) is significantly influenced by the membrane's chemical structure and physical properties due to its effects on the local reaction environment and water/ion transport. Radiation-grafted anion-exchange membranes (RG-AEM) have demonstrated high ionic conductivity and durability, making them a promising alternative for CO_2E. These membranes were fabricated using two different thicknesses of ethylene-tetrafluoroethylene polymer substrates (25 and 50 μm) and three different headgroup chemistries: benzyl-trimethylammonium, benzyl-*N*-methylpyrrolidinium, and benzyl-*N*-methylpiperidinium (MPIP). Our membrane characterization and testing in zero-gap cells over Ag electrocatalysts under commercially relevant conditions showed correlations between the water uptake, ionic conductivity, hydration, and cationic-head groups with the CO_2E efficiency. The thinner 25 μm-based AEM with the MPIP-headgroup (ion-exchange capacities of 2.1 ± 0.1 mmol g^{-1}) provided balanced in situ test characteristics with lower cell potentials, high CO selectivity, reduced liquid product crossover, and enhanced water management while maintaining stable operation compared to the commercial AEMs. The CO_2 electrolyzer with an MPIP-AEM operated for over 200 h at 150 mA cm^{-2} with CO selectivities up to 80% and low cell potentials (around 3.1 V) while also demonstrating high conductivities and chemical stability during performance at elevated temperatures (above 60 °C).

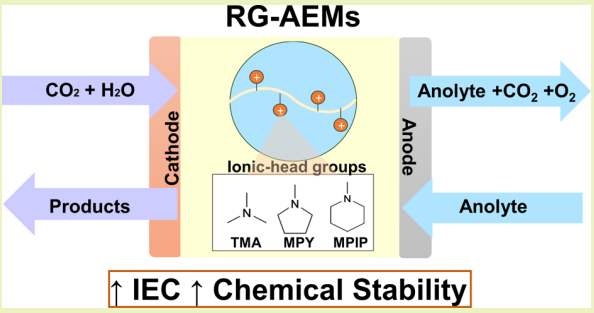

KEYWORDS: *electrochemical CO_2 reduction, anion exchange membrane (AEM), cationic functional group, ion transport, zero-gap approach, ion exchange capacity*

INTRODUCTION

Driven by renewable sources, CO_2 electrolysis (CO_2E) is a promising approach to convert greenhouse gases into chemical feedstocks, providing a decentralized alternative to help close the carbon cycle.[1−4] However, intensifying the operation at an industrial scale requires high current densities (>100 mA cm^{-2}) and a long-term stable system to ensure low capital costs and techno-economic viability.[5−7] The use of gas-diffusion electrodes (GDEs) in membrane electrode assemblies (MEAs) or flow-cell configurations has proven to perform effectively under commercially relevant conditions, overcoming the CO_2 transport limitations inherent to fundamental H-cell research studies.[5,8−10]

While recent studies have focused on improving catalytic activity and selectivity of CO_2 reduction,[11−14] durability, and anode activity,[15−17] lesser attention has been given to the membrane, yet this contributes substantially to the overall cell voltage and electrolyzer performance.[18−20] Understanding how the ionomeric components affect water/ion transport mechanisms will enable improvements in stable CO_2E operation, providing new tools for future research and development.

Ion exchange membranes (IEMs) typically have charged functional groups branching off a polymeric backbone.[21] Anion exchange membranes (AEMs) have positively charged functional groups, allowing negatively charged ions to conduct, whereas cation exchange membranes (CEMs) have negatively charged functional groups, allowing cations to conduct. In terms of CO_2E, if the catalyst is not in direct contact with the ionomeric components (e.g., flow cells with a catholyte layer), they do not affect catalytic selectivity.[22] However, having an electrolyte between the catalyst and membrane will add a substantial overpotential, and thus, it is more efficient to have an intimate catalyst/membrane interaction (e.g., an MEA configuration). CEMs are well known to promote mainly hydrogen evolution reaction (HER), whereas AEMs allow high selectivity to CO_2 reduction products. Conversely, AEMs have

Received: October 17, 2022
Revised: January 3, 2023

the issue where they primarily conduct CO_2-derived HCO_3^-/CO_3^{2-} anions (rather than OH^- anions) during CO_2 electrolysis, leading to an anodic product gas comprising a mixture of CO_2 and O_2, effectively mitigating the environmental benefit from developing CO_2E technologies.[23] It is generally believed that solving this problem is more straightforward than improving the poor selectivities obtained with CEMs; thus, AEM-based cells currently appear most promising for CO_2 electrolysis. The state-of-the-art CO_2E cells with AEMs have reached high selectivities toward carbon-derived products (>95% for CO and 80% for C_{2+} products)[23] and low cell potentials (<3.0 V) at high current densities (>100 mA cm^{-2}), but they exhibit limited stability.[24]

The AEMs in this study were fabricated using another approach known as radiation grafting. This method involves the exposure of commercial substrate films to high-energy radiation to generate active sites (peroxide groups) that co-polymerize functional vinyl monomers to produce radiation-grafted copolymers (RG).[25] The advantages of the radiation-grafting method include the preparation of IEMs without the need for a film formation step, the ability to compare different headgroup chemistries by post-graft functionalization of a single batch of RG membranes (with a single degree of grafting), yielding RG-IEMs with comparable ion-exchange capacities (IECs),[26] and the ability to modify substrate films of the same type/chemistry (e.g., polyethylene) but with different intrinsic morphologies (crystallinities), resulting in IEMs with tailored water uptakes (WU) and transport properties.[27]

The mechanical and electrochemical properties of AEMs are known to be influenced by the cationic headgroups and the nature of the polymeric backbone.[28−30] The development of hydrated ionic domains in IEMs governs the ionic and water transport during CO_2E[31−33] and will affect water management in the system. Optimizing such attributes will prevent electrode flooding, maintain adequate conductivity, and minimize the levels of salt precipitation at the cathode.[34,35]

Parameters like the WU and the hydration number (λ, the number of water molecules per ion-exchange site) are linked to water transport and can influence product crossover and ion mobility.[20,36] The IEC (defined as the amount of charged groups bound to the polymer normalized to the mass of the dehydrated membrane in a specific anion form) is a fundamental characterization metric for IEM performance, which can often be correlated with ionic conductivity or water transport properties. Even though higher IECs are often desired, excessive amounts of cationic groups can disproportionally increase the WU, causing excessive swelling, which will dilute the charge carrier concentration and reduce conductivity and mechanical robustness.[37] In general, AEMs for CO_2 electrolysis should have a high enough IEC to yield high ionic conductivity with moderate water uptakes to ensure restrained degrees of swelling and acceptable mechanical properties, along with good stability in high pH environments, and low permeabilities to gases, CO_2 reduction products, and electrolysis intermediates.[19]

With stable polymer backbones (generally without heteroatom links, such as ether groups), an AEM's stability toward nucleophilic OH^- anions (especially at elevated temperatures) is dictated by the cationic group and its hydration, where different headgroups will affect the ionic conductivity, hydration levels, and chemical stability.[26,28,30,38] For example, AEMs functionalized with trimethylammonium groups have yielded promising thermo-chemical stabilities in both water and CO_2 electrolyzers.[37] AEMs based on imidazolium-functional groups also have high OH^- conductivities and long-term operando performances;[39] hence, they are becoming the benchmark AEM for CO_2E, despite stability limitations at temperatures higher than 60 °C. In addition, cycloaliphatic quaternary ammonium (QA) chemistries (e.g., *N*-methylpiperidinium) have been identified as alkali-stable when hydrated.[40,41] In a recent study, Ponce-González et al. showed that such chemistries could be introduced into RG-AEMs, yielding promising fuel cell performances.[42]

Herein, we use the radiation-grafting synthetic platform to conduct a screening of AEM headgroup chemistry for potential CO_2E applications. RG-AEMs were fabricated by co-grafting vinylbenzyl chloride (VBC) monomers onto electron-beam-activated ethylene-co-tetrafluoroethylene (ETFE) polymer films, followed by amination with either trimethylamine, *N*-methylpyrrolidine, or *N*-methylpiperidine, to yield benzyltrimethylammonium (TMA), benzyl-*N*-methylpyrrolidinium (MPY), and benzyl-*N*-methylpiperidinium (MPIP) RG-AEMs, respectively.[26,42] This study investigates the effectiveness of such RG-AEMs for CO_2 electrolyzers, using the zero-gap (MEA) approach at current densities >100 mA cm^{-2}. A scheme of the synthesis method via is shown in Figure 1, while a detailed description of the synthesis and characterization methods is found in the Supporting Information (SI).

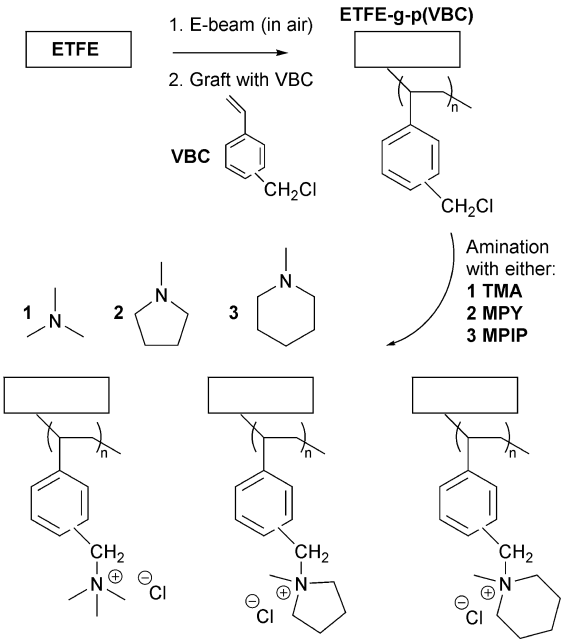

Figure 1. Synthesis of the RG-AEMs with TMA-, MPY-, and MPIP-functionalized groups in the Cl^- form. The Cl^- anions can be easily exchanged for any other anion desired (HCO_3^{2-}/CO_3^{2-}) via multiple (at least 3×) submersions in aqueous solutions (≥1 M).

RESULTS AND DISCUSSION

Electrode Characterization. Commercially porous Ag membranes with a nominal pore size diameter of 1.2 μm and a thickness of 50 μm and sputtered Cu-GDEs (150 nm) were characterized by XPS and SEM. During the survey scan, carbon and oxygen were detected in the Ag membranes, along with minor peaks indicating chlorine, perhaps related to the formation of AgCl during the electrode preparation. In

https://doi.org/10.1021/acssuschemeng.2c06205
ACS Sustainable Chem. Eng. XXXX, XXX, XXX−XXX

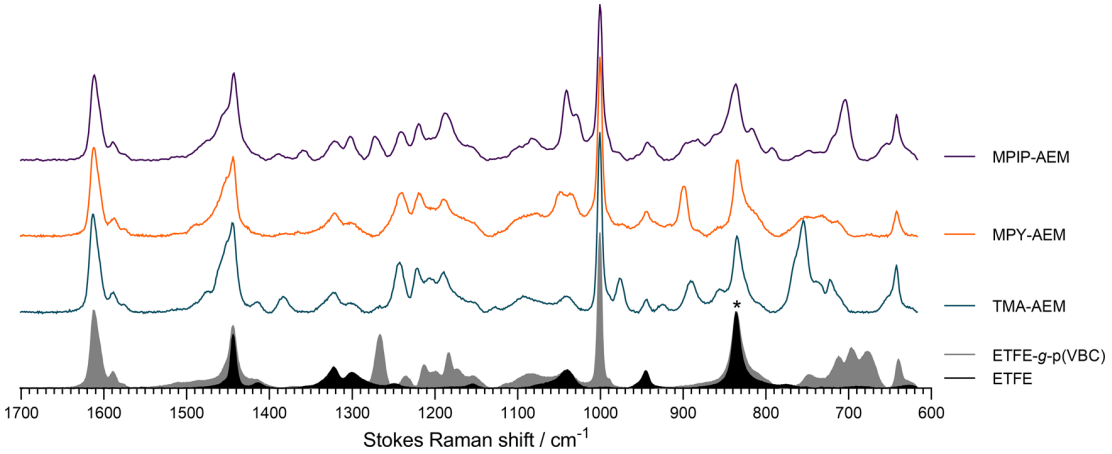

Figure 2. Raman spectra of the 25 μm thick ETFE substrate film (black filled) and the resulting ETFE-g-p(VBC) intermediate grafted membrane (gray filled, average of n = 30 spectra taken at random spots across both surfaces), and the final aminated RG-AEMs with line spectra (average of n = 10 spectra taken at random spots across both surfaces) stacked higher in the order TMA-AEM (teal), MPY-AEM (orange), and MPIP-AEM (purple). Laser wavelength = 785 nm. * Spectra normalized to the intensity of the ETFE-derived band at 835 cm^{-1} to aid visual comparison. A description of this characterization method can be found in the SI.

Table 1. Key Properties for the Synthetized RG-AEMs Made from 25 μm ETFE Films at Room Temperature (Cl^- Form)[a,b]

head group	IEC (mmol g^{-1})	σ_{Cl^-} (mS cm^{-1})	T_{hyd} (μm)	WU (%)	TPS (%)	λ	area swelling (%)
TMA-AEM	2.20 ± 0.02	18 ± 1	56 ± 2	33 ± 1	8 ± 4	8 ± 1	19 ± 3
MPY-AEM	2.07 ± 0.05	23 ± 2	72 ± 2	82 ± 13	46 ± 5	22 ± 4	32 ± 10
MPIP-AEM	2.09 ± 0.07	18 ± 1	69 ± 3	85 ± 19	41 ± 14	23 ± 5	47 ± 18

[a]The in-plane ionic conductivities (σ_{Cl^-}) in water were measured at 25 °C [b]Errors in λ values were calculated from errors in IEC and WU using standard error propagation rules.

contrast, as expected, Cu-GDEs showed copper, carbon, and oxygen features (Figure S4). In such measurements, no metallic impurities were observed within the limits of XPS sensitivity that would interfere with the CO_2E. The SEM images of Cu-GDEs exhibited a spherical morphology (Figure S5), with some roughness variations between the fresh and the postreaction samples.

Raman Characterization. The spectra for the pre-aminated ETFE-g-p(VBC) intermediate membrane (degree of grafting 79%) made using the 25 μm ETFE substrate confirms grafting (Figure 2) with characteristic features including bands at 835 and 1444 cm^{-1} (due to the presence of $-CF_2-$ and $-CH_2-$ groups in the ETFE substrate, respectively), a grafted poly(VBC)-derived band at 1612 cm^{-1} (aromatic ring quadrant mode), and a band at 1267 cm^{-1} (due to the $-CH_2Cl$ groups in the grafted poly(VBC) chains).[26] Raman spectra were collected at 30 random surface sites across both surfaces of the ETFE-g-p(VBC) intermediate membrane (laser spot size ca. 2 μm, while penetrating a few μm into the sample), and the integrated area ratios (areas of the 1612 cm^{-1} bands normalized to the areas of the 835 cm^{-1} bands) were calculated to gauge grafting homogeneity. The band area ratio was recorded as 1.30 ± 0.13, which yields a relative standard deviation = 10%, a quasi-measure of a small but acceptable amount of grafting inhomogeneity (Figure S2). In addition, the Raman spectra of all RG-AEMs confirm successful amination with each amine (Figure 2), based on the disappearance of the poly(VBC)-($-CH_2Cl$)-derived band at 1267 cm^{-1} and the appearance of diagnostic bands for each of the QA groups (756 and 976 cm^{-1} for TMA, 899 cm^{-1} for MPY, and 704 and 1273 cm^{-1} for MPIP).

Physical Properties of RG-AEMs. The RG-AEMs were characterized for key properties in the Cl^- forms to confirm that the ex situ behaviors were as expected. The fundamental physical properties of the ETFE-based RG-AEMs made from 25 μm ETFE films and the three different amines (the equivalent data for the RG-AEMs made from the 50 μm ETFE can be found in Table S3) are summarized. Our results show that incorporating different QA groups onto polymer backbones has a significant effect on the water contents (and swelling) and a lesser effect on the IEC and ionic conductivity (in-plane measurements with the RG-AEM samples submerged in water at 25 °C). MPIP- and MPY-AEMs exhibit higher WU than TMA-AEMs, due to their hydrophilic nature, as reported previously.[42] In accordance with these results, Koronka et al. reported that AEMs with heterocyclic-QAs would form ionic clusters with more segregated hydrophilic/hydrophobic phases and better channels to transport water, leading to enhanced WU values.[43] The higher water content variants also tend to swell more (Table 1). For CO_2E applications, higher IECs and WU AEMs generally lead to higher in situ performances.[44]

For the RG-AEMs made from 25 μm ETFE, a comparison of the measured Cl^- conductivities above 80 °C showed that the MPIP-AEM (Figure 3A) had slightly lower values than the TMA- and MPY-AEMs. We always initially report that values for Cl^- form RG-AEMs before any alkaline reagent exposure that risks trace degradations and changes in the nano/micro-morphology. The conductivities of the RG-AEMs in the predominant HCO_3^- were all comparable and slightly lower compared to the Cl^- forms (A), owing to differences in ion mobility and diffusivity between ions with different charge densities and hydrated radius.[42,45]

https://doi.org/10.1021/acssuschemeng.2c06205
ACS Sustainable Chem. Eng. XXXX, XXX, XXX−XXX

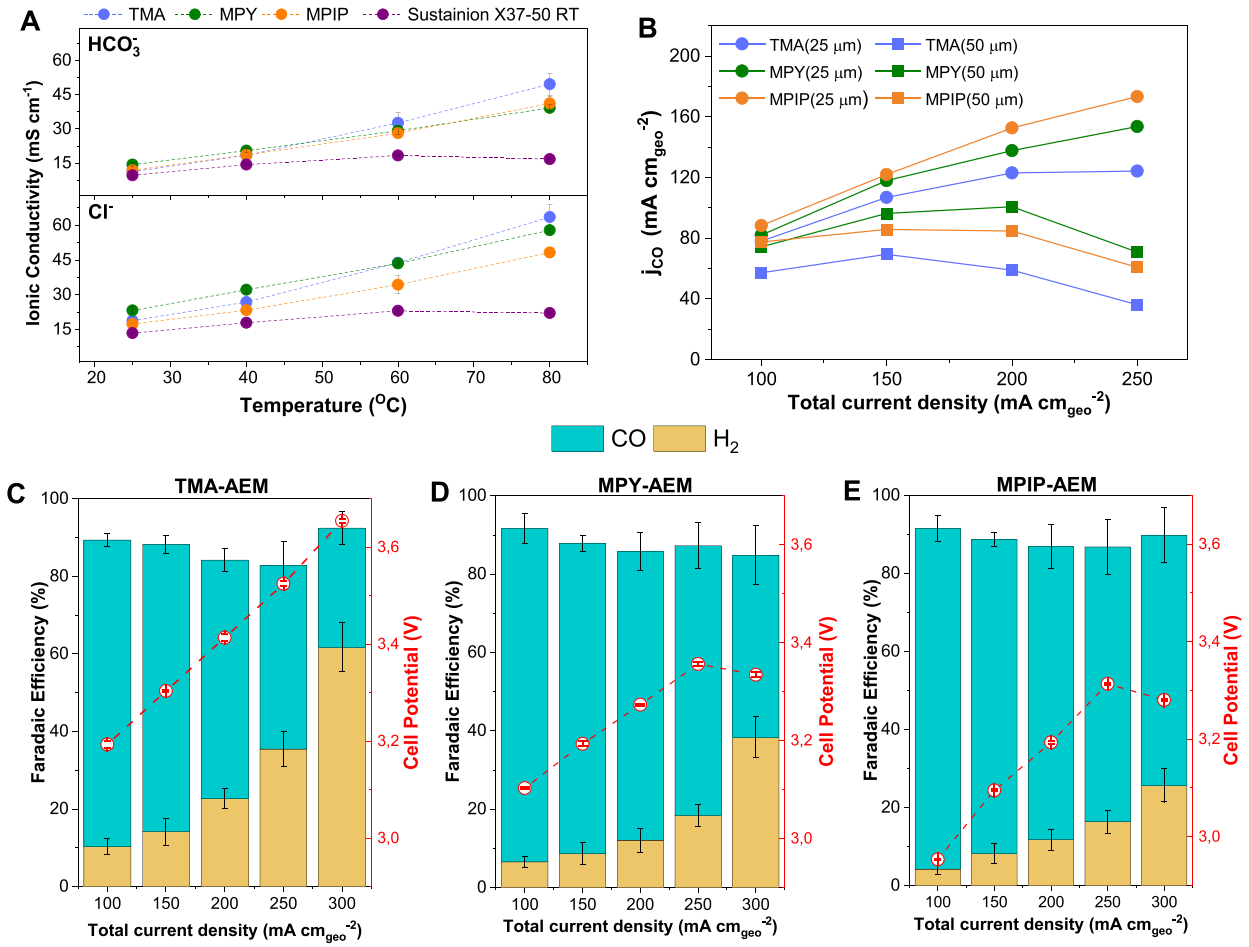

Figure 3. (A) In-plane Cl^- and HCO_3^- conductivities (in water) for MPIP-, TMA-, and MPY-AEMs (made from 25 μm ETFE) and Sustainion X37-50 RT at different temperatures. (B) Effect of thickness on the CO partial current density for the RG-AEMs made from 25 and 50 μm ETFE substrate films (as indicated in the legend). (C–E) Product distribution and cell potentials at room temperature for CO_2E with the different RG-AEMs (made from 25 μm ETFE) as a function of the total current density using Ag electrocatalysts (0.1 M $KHCO_3$ anolyte): (C) TMA-AEM, (D) MPY-AEM, and (E) MPIP-AEM. The error bars represent the standard error of the mean for three independent cell tests.

On the other hand, significant differences were observed between these RG-AEMs and those fabricated from thicker 50 μm ETFE (Table S3). The ETFE-g-p(VBC) intermediate membrane made with 50 μm ETFE had a lower degree of grafting (68% compared to 79% with the version made with 25 μm ETFE). The quantitative Raman analysis (Figure S2) also confirmed the lower DOG (degree of grafting) for the thicker ETFE-g-p(VBC) membrane. The higher IECs for the thinner RG-AEMs lead to higher water contents and Cl^- conductivities (at 25 °C) compared to thicker analogues. The lower water contents of the thicker versions led to lower CO_2E performances (B). Hence, all subsequent testing was performed with the thinner RG-AEMs made from the 25 μm thick ETFE.

Electrochemical Performance. Figure 3(C–E) also shows the results of CO_2E over Ag electrocatalysts with different RG-AEMs. The experiments were carried out in galvanostatic mode at different current densities ranging from 100 to 300 mA cm^{-2}, with CO and H_2 observed to be the primary products. The total FE was less than 100% due to unaccounted formate ($HCOO^-$) being transported to the anolyte (Table S5 and Figure S6). Electro-generated formate is difficult to quantify because of its negative charge, making it susceptible to cross-over through the AEM by covalently bound positive charges and further oxidized to CO_2 at the anode. In a detailed study of AEM cross-over using the same setup and Ag-electrocatalyst, Larrazábal et al. reported that the FEs toward $HCOO^-$ are ca. 20% at higher current densities, which matches the unaccounted-for product FE in this work.[46]

While it is not believed that AEMs themselves directly affect catalytic activity, they do modify the local environment around the cathode catalysts for zero-gap MEA-type cells, particularly in terms of water management, which affects both pH and the mass transfer rates of the CO_2 at the catalyst's surface.[47] Thus, indirectly, AEMs can substantially affect product selectivity, especially related to CO_2-reduced product(s) vs H_2. Both MPY-AEM (Figure 3D) and MPIP-AEM (Figure 3E) showed similar product selectivities, with the MPIP-AEM reaching a maximum CO production rate of 5.6 mmol h^{-1} cm^{-2} at 200 mA cm^{-2} (cell voltage of 3.1 V). With these two RG-AEMs, the selectivity toward CO was favored at total current densities <250 mA cm^{-2} (FE_{CO} = 70–87%), but less so at 300 mA cm^{-2} (FE_{CO} < 60%), where HER starts to dominate due to either the cathode flooding or localized mass transfer issues.[48] MPY-AEM starts to exhibit noticeably lower FE_{CO} values compared to MPIP-AEM at >200 mA cm^{-2}. In comparison, lower WU TMA-AEM (Figure 3C) exhibits smaller FE_{CO} values at all current densities compared to MPY- and MPIP-AEM with

https://doi.org/10.1021/acssuschemeng.2c06205
ACS Sustainable Chem. Eng. XXXX, XXX, XXX–XXX

FE_{CO} < 50% at >200 mA cm^{-2} (along with higher cell potentials).

Water management, the subject of many previous studies on CO_2E, can be influenced by the nature of the AEM (e.g., QA chemistry)[20,49−51] and a given AEM's water content.[52] It is essential to highlight that WU and the hydration number (λ) are average bulk properties, which does not provide information regarding the nano/micro-distribution of the water-containing channels inside hydrophilic−hydrophobic phase-segregated AEMs. However, λ or WU values still provide insights into the net water transport within CO_2E cells. Generally, water crosses the AEM by electro-osmotic drag (cathode to anode) and by diffusion or hydraulic permeation (anode to cathode). For our low WU TMA-AEM (λ = 8), we observed faster cathode flooding at j_{total} > 200 mA cm^{-2} compared to the higher WU MPY- and MPIP-AEMs (λ > 22), potentially caused by a rise in the water flux to the cathode or a possible decrease in the electro-osmotic drag coefficient.[53] Similarly, the thickness of the membrane can also influence overall water transport at high current densities since it can influence the hydraulic permeation flux (J_{HP}) across the AEM (Figure S10). Our results showed that reducing RG-AEM thicknesses increased selectivity and activity independently of the headgroup (Figure 3B).[20] Moreover, thicker membranes (50 μm ETFE) appeared to enhance electrode flooding as opposed to thinner membranes (25 μm ETFE), due to increased water accumulation at the cathode. For those membranes, a rise in cell potential to compensate for the higher ohmic resistance may accelerate the loss of the GDE hydrophilicity, altering the J_{HP}. An in-depth description of the effect of the AEMs properties on water transport can be found in our recent review paper, which explored the effects of membrane characteristics on CO_2E performance in MEAs.[54]

A comparison of the cell potentials and resistances was performed to understand what caused the difference in performance between the RG-AEMs. Under similar conditions, the measured cell potential (2.9−3.6 V) and resistance (0.2−0.6 Ω cm^2) were similar to those in the literature for Ag-cathode MEAs.[46,55,56] Current interrupt measurements (Figure S7) show that the in situ through-plane TMA-AEM resistance of 600 mΩ cm^2 is significantly higher than that for MPY-AEM (350 mΩ cm^2) and MPIP-AEM (220 mΩ cm^2). This contrasts the ex situ HCO_3^- conductivities (Figure 3A), which were similar for all three RG-AEMs; however, only in-plane ex situ measurements were made as it is challenging to get reliable ex situ through-plane conductivities with such thin and highly conductive RG-AEMs. Additionally, even though the RG-AEMs were ion-exchanged in aqueous HCO_3^- solutions, the anions present will be a mixture of HCO_3^- and CO_3^{2-} (plus traces of OH^-) due to the equilibria between these anions. At room temperature, the conductivity values for HCO_3^--exchanged RG-AEMs are equivalent to ASRs of 150−250 mΩ cm^2, which is lower than the in situ values measured (the latter include contact resistances and ionic resistances in the electrodes). Hence, through-plane in situ resistance measurements can be more insightful since relative through-plane resistance trends can be discerned when comparing identical cell set-ups containing different RG-AEMs.

For MPIP-AEM and MPY-AEM, a counter-intuitive phenomenon is observed when transitioning between 250 and 300 mA cm^{-2}. The voltage decreases as the cells are pushed to a higher current density. This has been observed previously due to the starvation of CO_2, resulting in the inability of carbonate anions to form and therefore a switch to predominate OH^- anion formation.[46] This allows the more highly conductive OH^- anions to increase in concentration in the AEM, which decreases the device potential as AEMs are most conductive in their OH^- forms. However, this starving of CO_2 also entails CO_2 electrolysis selectivity decreases in favor of HER. Moreover, incorporating heterocyclic QA groups could provide a hydrophilic−hydrophobic phase-separated morphology with a more efficient ion transport framework due to the electrostatic repulsion of self-aggregated QA groups within hydrophilic domains, resulting in preferential Grotthus-type OH^- transport (weakening the OH^- binding to the cationic sites).[57−59] To validate that the RG-AEMs switched to OH^- conduction, the anodic CO_2/O_2 discharge ratios were measured where they showed a decrease in the ratio at higher current densities, proving this switch to OH^- transfer (Figure S9).

To demonstrate the potential benefits and applicability of this new generation of ETFE-based RG-AEMs for CO_2E, we conducted comparative studies with other commercial AEMs (Figure 4). Based on our results, MPIP-AEM is competitive

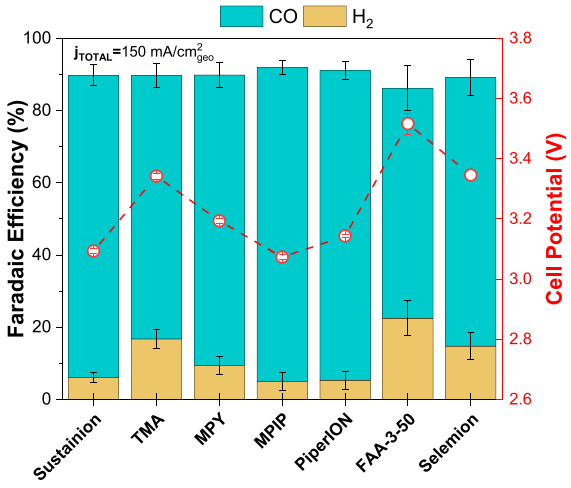

Figure 4. Product distribution and cell potentials for CO_2E cells operating at j_{total} = 150 mA cm^{-2} at room temperature when containing different AEMs (aqueous 0.1 M $KHCO_3$ anolyte and Ag electrocatalyst). Sustainion stands for X37-50 RT and Selemion stands for AMV. Error bars represent the standard error of the mean for three independent cell tests for each AEM.

with the best commercial membranes, with MPY-AEM being only slightly behind. FAA-3-50, Selemion AMV, and TMA-AEM appear less competitive in terms of cell potential and selectivity under the same experimental conditions at room temperature. The MPIP-AEM reported high FE_{CO} values with low cell potentials, similar to values obtained with Sustainion X37-50 RT and PiperION. In contrast, TMA-AEM and Fumasep FAA-3-50 showed higher cell potentials (270 and 500 mV higher than those of the MPIP-AEM). The fact that all the AEMs tested had different chemistries, cation transfer numbers, and even thickness makes a more direct performance comparison difficult. However, it can be discerned that the AEMs with lower WUs (Fumasep FAA-3-50, TMA-AEM, and Selemion AMV) showed higher potentials and lower CO selectivities, consistent with arguments made vide supra (on the effect of the hydrophobic nature of the headgroups).[20,35]

https://doi.org/10.1021/acssuschemeng.2c06205
ACS Sustainable Chem. Eng. XXXX, XXX, XXX−XXX

Additionally, we examined the effect of the anolyte concentration (0.05, 0.1, and 1.0 M) on product distributions, cell potentials, and resistances. By increasing the anolyte concentration, we observed a decrease in the ohmic resistances and a concomitant decrease in cell potential (Figure S11). Such behavior is expected since a higher electrolyte concentration enhances ionic conductivity in the cell. The magnitude of this effect did not appear to be AEM-dependent; thus, the trends discussed in this paper are expected to hold with other anolyte concentrations.

The resistive heat produced from any potential commercial CO_2 electrolyzer entails the necessity of operating at temperatures notably above ambient conditions (>50 °C);[60] therefore, it is essential to investigate the temperature effects in CO_2E. Also, elevated temperatures improve CO_2 reduction kinetics and the ionic conductivity of AEMs (Figure 3A), improving energy efficiencies.[61] However, excessive temperatures may compromise AEM stabilities due to alkali-derived degradation of the QA groups (or polymer backbones). Hence, we performed experiments at increasing temperatures to compare the thermal stability of MPIP-AEM against the benchmark Sustainion X37-50 RT (Figure 5).

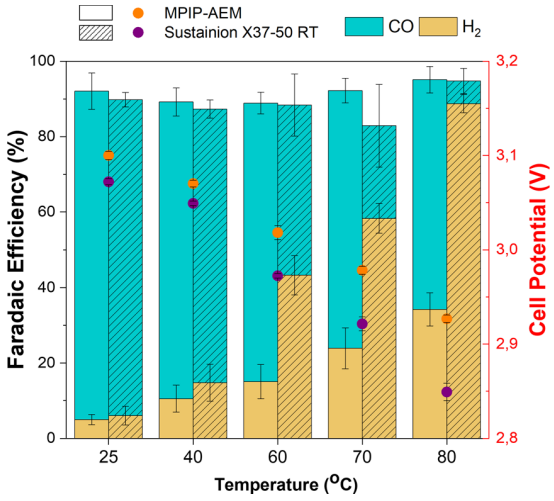

Figure 5. Effect of the operating temperature on the cell potential and Faradaic efficiency for both AEMs E_{25}-MPIP and Sustainion X37-50 RT. An Ag electrocatalyst was used as the cathode, and the current density was held at 150 mA cm^{-2} for this experiment. Error bars represent the standard error of the mean for three independent measurements.

At lower temperatures (<40 °C), the MPIP-AEM resulted in slightly higher operating potentials and similar H_2 selectivity compared to Sustainion X37-50 RT. However, at 60 °C, the MPIP followed a consistent trajectory in terms of CO_2-reduced product(s) vs HER as previously discussed. In contrast, Sustainion yielded disproportionate increases in H_2 selectivity. The cell voltage with Sustainion also commenced more rapid decreases at this temperature. While a decrease in device potential is generally good, this decrease may indicate that the AEM has stability issues (degradation of functional groups and/or mechanical modifications), leading to flooding. Figure 3A also hints the Sustainion AEM degradation above 60 °C as the conductivity starts to decrease above this temperature.

To further investigate the water management effects using the RG-AEMs (MPIP-, MPY-, and TMA-AEM), 24 h tests were employed at 25 °C. All RG-AEMs gave a stable performance with high FE_{CO} (>80%) and constant cell potential throughout the experiments (Figure S12). In addition, the HER remained at a constant level for all AEMs (FE_{HER} = 11−15% for TMA-AEM compared to 3−6% for MPIP-AEM). To further test MPIP-AEM durability, they were tested at 60 °C over 24 h, with again no signs of degradation (Figure S13).

It was then decided to test the down-selected MPIP-AEM over 200 h at room temperature (Figure 6). This test showed only minor oscillations in the cell voltage (ca. 100 mV) and stable CO selectivity (FE_{CO} = 80−85%). However, the same experiment with Sustainion X37-50 RT showed less stability, with HER increases occurring over 100 h (Figure S14). While our results do not show the stable operation with Sustainion reported in the literature,[62] the experiment was replicated multiple times, yielding the same trend. It should be noted that RG-AEMs are substantially easier to handle (more flexible and mechanically robust, without the addition of extrinsic plasticizers) compared to the Sustainion X37-50 RT, which may contribute to the unsuccessful durability tests with this AEMs.

A final feature that was investigated relates to product cross-over across the AEM (when conducting CO_2 reduction on Cu enabling C_{2+} products). It has been demonstrated that ca. 40% of liquid products can cross the AEMs, caused mainly by diffusion and electromigration.[33] This experiment aimed to compare the MPIP-AEM developed in this work with different commercial membranes. A switch to the sputtered Cu catalyst led to a CO_2E cell that produced a range of C_1 and C_{2+} products, allowing a better understanding of the cross-over properties of the various AEMs.

Figure 7A shows the results of Cu cathode CO_2E testing of cells containing various AEMs operating at a constant current density (150 mA cm^{-2}). With the similar potentials of all devices, it was reassuring to observe that the general selectivity of all AEMs was consistent. The only notable exception was HER selectivity, which was expected to be primarily related to in situ water management. Regarding H_2 selectivity, FAA-3-50 gave the highest amount, with MPIP-AEM giving the lowest. In contrast, Figure 7B shows that the liquid cross-over is similar across all the AEMs tested. Since we are using a zero-gap MEA cell, any volatile liquid product (e.g., ethanol, allyl alcohol, and propanol) can evaporate from the GDE (and will be found mainly in the liquid trap with only traces making their way to the anolyte). We observed that MPIP-AEM had the lowest ethanol cross-over compared to the commercial membranes, demonstrating some potential benefits of the RG-AEM morphology and chemistry in regulating neutral product cross-over. Meanwhile, differences in (negatively charged) acetate and formate cross-over were not that noticeable between the different AEMs.

CONCLUSIONS

In this study, RG-AEMs were fabricated from ETFE substrate films of different thicknesses with TMA, MPY, and MPIP quaternary ammonium groups for CO_2 electrolysis under commercially relevant conditions. These RG-AEMs exhibited desired transport, chemical, and mechanical properties, including high IEC (above 2 mmol·g^{-1}), ionic conductivities, moderate water uptake, and low ohmic resistances (<0.6 Ω·cm^2). The tailored properties of these membranes make them suitable for CO_2E in MEA configurations, as their mechanical

https://doi.org/10.1021/acssuschemeng.2c06205
ACS Sustainable Chem. Eng. XXXX, XXX, XXX−XXX

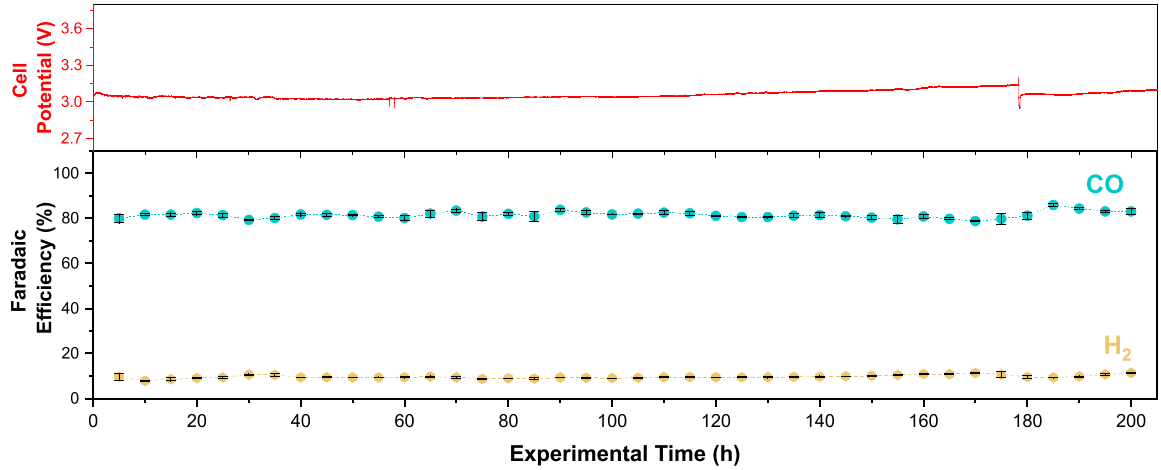

Figure 6. 200 h long-term stability test of a room-temperature CO_2E cell operating at 150 mA cm^{-2} and containing the MPIP-AEM (Ag-based electrocatalyst and 0.1 M $KHCO_3$ anolyte). Error bars represent the standard error of the mean for the measurements within 5 h intervals.

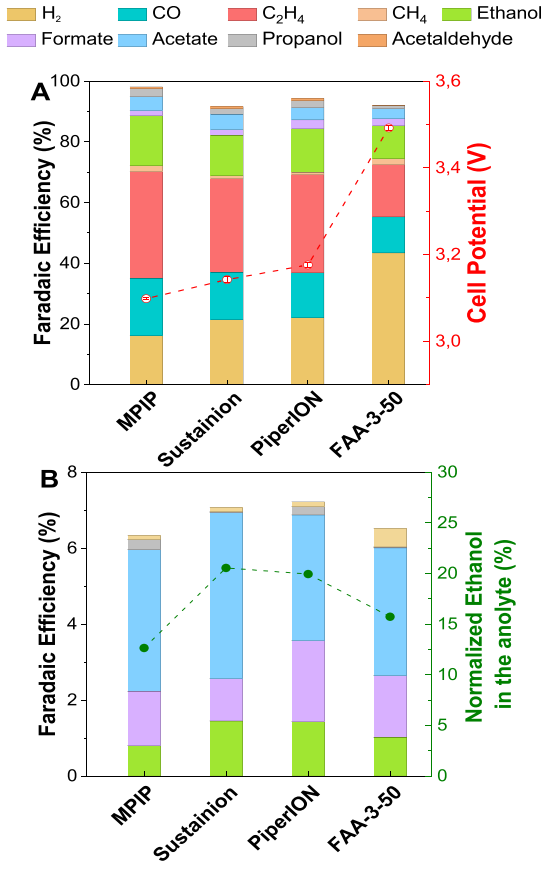

Figure 7. (A) Product distribution and cell potentials obtained with a CO_2E cell containing a Cu catalyst and various AEMs, when operating at 150 mA cm^{-2} and room temperature. (B) Product distributions detected at the anode. The right-hand axis relates the anodic ethanol Faradaic efficiency as a function of the total ethanol Faradaic efficiency. Sustainion membrane corresponds to X37-50 RT.

flexibility and robustness make them easily handled during cell assembly while providing long-term stable performance. The operation using thinner membranes with MPIP-head groups yielded the highest CO selectivity (>80%) over Ag-electrocatalysts at higher current densities (with E_{cell} = 2.9−3.3 V), owing to improved water and ionic transport within the system. The use of cycloaliphatic headgroups in RG-AEMs proved thermal and chemical stability under different reaction conditions (e.g., operation temperatures and electrolyte), reducing product cross-over and achieving stable operation for at least 200 h for CO_2E to CO at 150 mA cm^{-2} with high selectivity (80−85%) under RT conditions. Our RG-AEMs exhibit a wide range of properties similar to common commercial AEMs, including the tantalizing possibility of operating at elevated temperatures (80 °C) and demonstrating the potential of a new generation of AEMs for electrochemical CO_2 reduction applications.

■ ASSOCIATED CONTENT

Supporting Information

The Supporting Information is available free of charge at https://pubs.acs.org/doi/10.1021/acssuschemeng.2c06205.

Synthesis method of RG-AEMs; metrics for RG-AEM characterization; Raman spectroscopy description; preparation and characterization of Cu electrodes; cell configuration; and electrochemical tests; chemical structures of the membranes; information on key properties of common AEMs and our synthesized membranes; XPS and SEM figures of the catalyst; scheme of the reaction setup and electrochemical cell; calculation procedures for FEs and partial current density; HPLC analysis of products; electrochemical tests of 50 μm of RG-AEM and commercial membranes at different current densities; analysis of the CO_2/O_2 ratio at the anode; measurements on the effect of electrolyte concentrations; and stability tests (PDF)

■ AUTHOR INFORMATION

Corresponding Authors

Brian Seger − *Surface Physics and Catalysis (SurfCat) Section, Department of Physics, Technical University of Denmark, 2800 Kgs. Lyngby, Denmark;* orcid.org/0000-0002-0036-095X; Email: brse@fysik.dtu.dk

John R. Varcoe − *School of Chemistry and Chemical Engineering, University of Surrey, Guildford GU2 7XH, U.K.;* orcid.org/0000-0001-9898-0235; Email: j.varcoe@surrey.ac.uk

https://doi.org/10.1021/acssuschemeng.2c06205
ACS Sustainable Chem. Eng. XXXX, XXX, XXX−XXX

Authors

Carlos A. Giron Rodriguez − *Surface Physics and Catalysis (SurfCat) Section, Department of Physics, Technical University of Denmark, 2800 Kgs. Lyngby, Denmark;* orcid.org/0000-0002-0175-0052

Bjørt Óladottir Joensen − *Surface Physics and Catalysis (SurfCat) Section, Department of Physics, Technical University of Denmark, 2800 Kgs. Lyngby, Denmark*

Asger Barkholt Moss − *Surface Physics and Catalysis (SurfCat) Section, Department of Physics, Technical University of Denmark, 2800 Kgs. Lyngby, Denmark*

Gastón O. Larrazábal − *Surface Physics and Catalysis (SurfCat) Section, Department of Physics, Technical University of Denmark, 2800 Kgs. Lyngby, Denmark;* orcid.org/0000-0003-4218-3514

Daniel K. Whelligan − *School of Chemistry and Chemical Engineering, University of Surrey, Guildford GU2 7XH, U.K.*

Terry R. Willson − *School of Chemistry and Chemical Engineering, University of Surrey, Guildford GU2 7XH, U.K.*

Complete contact information is available at: https://pubs.acs.org/10.1021/acssuschemeng.2c06205

Notes

The authors declare no competing financial interest.

The raw data collected by the University of Surrey and presented in Figure 2 and Table 1 are available at DOI 10.6084/m9.figshare.21802473 (CC-BY)

■ ACKNOWLEDGMENTS

This research was primarily funded by the European Union's Horizon 2020 research and innovation program under grant agreement No. 851441 (project SELECTCO2). SURFCAT funded the resources for the catalyst characterization techniques at DTU. We want to thank the Villum Center for the science of sustainable fuels and chemicals (V-Sustain No. 9455) at DTU for their contribution to the research area of electrocatalysis. The resources used for the membrane conductivity experiments were funded by Engineering and Physical Sciences Research Council (EPSRC UK) grant EP/T009233/1. The Raman microscope was funded by EPSRC grant EP/M022749/1. We thank Dr. Friedrich Menges for granting a free use Spectragryph license (https://www.effemm2.de/spectragryph/index.html).

■ REFERENCES

(1) Vasileff, A.; Zheng, Y.; Qiao, S. Z. Carbon Solving Carbon's Problems: Recent Progress of Nanostructured Carbon-Based Catalysts for the Electrochemical Reduction of CO_2. *Adv. Energy Mater.* **2017**, *7*, No. 1700759.

(2) Quadrelli, E. A.; Centi, G.; Duplan, J. L.; Perathoner, S. Carbon Dioxide Recycling: Emerging Large-Scale Technologies with Industrial Potential. *ChemSusChem* **2011**, *4*, 1194−1215.

(3) De Luna, P.; Hahn, C.; Higgins, D.; Jaffer, S. A.; Jaramillo, T. F.; Sargent, E. H. What Would It Take for Renewably Powered Electrosynthesis to Displace Petrochemical Processes? *Science* **2019**, *364*, No. eaav3506.

(4) Zheng, Y.; Vasileff, A.; Zhou, X.; Jiao, Y.; Jaroniec, M.; Qiao, S. Z. Understanding the Roadmap for Electrochemical Reduction of CO_2 to Multi-Carbon Oxygenates and Hydrocarbons on Copper-Based Catalysts. *J. Am. Chem. Soc.* **2019**, *141*, 7646−7659.

(5) Burdyny, T.; Smith, W. A. CO_2 Reduction on Gas-Diffusion Electrodes and Why Catalytic Performance Must Be Assessed at Commercially-Relevant Conditions. *Energy Environ. Sci.* **2019**, *12*, 1442−1453.

(6) Chen, C.; Khosrowabadi Kotyk, J. F.; Sheehan, S. W. Progress toward Commercial Application of Electrochemical Carbon Dioxide Reduction. *Chem* **2018**, *4*, 2571−2586.

(7) Jouny, M.; Luc, W.; Jiao, F. General Techno-Economic Analysis of CO_2 Electrolysis Systems. *Ind. Eng. Chem. Res.* **2018**, *57*, 2165−2177.

(8) Ozden, A.; Li, F.; Garcia De Arquer, F. P.; Rosas-Hernández, A.; Thevenon, A.; Wang, Y.; Hung, S. F.; Wang, X.; Chen, B.; Li, J.; Wicks, J.; Luo, M.; Wang, Z.; Agapie, T.; Peters, J. C.; Sargent, E. H.; Sinton, D. High-Rate and Efficient Ethylene Electrosynthesis Using a Catalyst/Promoter/Transport Layer. *ACS Energy Lett.* **2020**, *5*, 2811−2818.

(9) Lee, J.; Lim, J.; Roh, C. W.; Whang, H. S.; Lee, H. Electrochemical CO_2 Reduction Using Alkaline Membrane Electrode Assembly on Various Metal Electrodes. *J. CO2 Util.* **2019**, *31*, 244−250.

(10) Lin, R.; Guo, J.; Li, X.; Patel, P.; Seifitokaldani, A. Electrochemical Reactors for CO_2 Conversion. *Catalysis* **2020**, *10*, 473.

(11) De Gregorio, G. L.; Burdyny, T.; Loiudice, A.; Iyengar, P.; Smith, W. A.; Buonsanti, R. Facet-Dependent Selectivity of Cu Catalysts in Electrochemical CO_2 Reduction at Commercially Viable Current Densities. *ACS Catal.* **2020**, *10*, 4854−4862.

(12) Varela, A. S.; Kroschel, M.; Reier, T.; Strasser, P. Controlling the Selectivity of CO_2 Electroreduction on Copper: The Effect of the Electrolyte Concentration and the Importance of the Local PH. *Catal. Today* **2016**, *260*, 8−13.

(13) Chen, C.; Yan, X.; Liu, S.; Wu, Y.; Wan, Q.; Sun, X.; Zhu, Q.; Liu, H.; Ma, J.; Zheng, L.; Wu, H.; Han, B. Highly Efficient Electroreduction of CO_2 to C_{2+} Alcohols on Heterogeneous Dual Active Sites. *Angew. Chem., Int. Ed.* **2020**, *59*, 16459−16464.

(14) Tomboc, G. M.; Choi, S.; Kwon, T.; Hwang, Y. J.; Lee, K. Potential Link between Cu Surface and Selective CO_2 Electroreduction: Perspective on Future Electrocatalyst Designs. *Adv. Mater.* **2020**, *32*, No. 1908398.

(15) Luc, W.; Rosen, J.; Jiao, F. An Ir-Based Anode for a Practical CO_2 Electrolyzer. *Catal. Today* **2017**, *288*, 79−84.

(16) Verma, S.; Lu, S.; Kenis, P. J. A. Co-Electrolysis of CO_2 and Glycerol as a Pathway to Carbon Chemicals with Improved Technoeconomics Due to Low Electricity Consumption. *Nat. Energy* **2019**, *4*, 466−474.

(17) Vass, Á.; Kormányos, A.; Kószo, Z.; Endrődi, B.; Janáky, C. Anode Catalysts in CO_2 Electrolysis: Challenges and Untapped Opportunities. *ACS Catal.* **2022**, *12*, 1037−1051.

(18) Endrődi, B.; Samu, A.; Kecsenovity, E.; Halmágyi, T.; Sebők, D.; Janáky, C. Operando Cathode Activation with Alkali Metal Cations for High Current Density Operation of Water-Fed Zero-Gap Carbon Dioxide Electrolysers. *Nat. Energy* **2021**, *6*, 439−448.

(19) Salvatore, D. A.; Gabardo, C. M.; Reyes, A.; O'Brien, C. P.; Holdcroft, S.; Pintauro, P.; Bahar, B.; Hickner, M.; Bae, C.; Sinton, D.; Sargent, E. H.; Berlinguette, C. P. Designing Anion Exchange Membranes for CO_2 Electrolysers. *Nat. Energy* **2021**, *6*, 339−348.

(20) Reyes, A.; Jansonius, R. P.; Mowbray, B. A. W.; Cao, Y.; Wheeler, D. G.; Chau, J.; Dvorak, D. J.; Berlinguette, C. P. Managing Hydration at the Cathode Enables Efficient CO_2 Electrolysis at Commercially Relevant Current Densities. *ACS Energy Lett.* **2020**, *5*, 1612−1618.

(21) Sarkar, S.; Sengupta, A. K.; Prakash, P. The Donnan Membrane Principle: Opportunities for Sustainable Engineered Processes and Materials. *Environ. Sci. Technol.* **2010**, *44*, 1161−1166.

(22) Ma, M.; Kim, S.; Chorkendorff, I.; Seger, B. Role of Ion-Selective Membranes in the Carbon Balance for CO_2 Electroreduction via Gas Diffusion Electrode Reactor Designs. *Chem. Sci.* **2020**, *11*, 8854−8861.

(23) Masel, R. I.; Liu, Z.; Yang, H.; Kaczur, J. J.; Carrillo, D.; Ren, S.; Salvatore, D.; Berlinguette, C. P. An Industrial Perspective on Catalysts for Low-Temperature CO_2 Electrolysis. *Nat. Nanotechnol.* **2021**, *16*, 118−128.

(24) Wakerley, D.; Lamaison, S.; Wicks, J.; Clemens, A.; Feaster, J.; Corral, D.; Jaffer, S. A.; Sarkar, A.; Fontecave, M.; Duoss, E. B.; Baker, S.; Sargent, E. H.; Jaramillo, T. F.; Hahn, C. Gas Diffusion Electrodes, Reactor Designs and Key Metrics of Low-Temperature CO_2 Electrolysers. *Nat. Energy* **2022**, *7*, 130−143.
(25) Deavin, O. I.; Murphy, S.; Ong, A. L.; Poynton, S. D.; Zeng, R.; Herman, H.; Varcoe, J. R. Anion-Exchange Membranes for Alkaline Polymer Electrolyte Fuel Cells: Comparison of Pendent Benzyltrimethylammonium- and Benzylmethylimidazolium-Head- Groups. *Energy Environ. Sci.* **2012**, *5*, 8584−8597.
(26) Biancolli, A. L. G.; Herranz, D.; Wang, L.; Stehlíková, G.; Bance-Soualhi, R.; Ponce-González, J.; Ocón, P.; Ticianelli, E. A.; Whelligan, D. K.; Varcoe, J. R.; Santiago, E. I. ETFE-Based Anion-Exchange Membrane Ionomer Powders for Alkaline Membrane Fuel Cells: A First Performance Comparison of Head-Group Chemistry. *J. Mater. Chem. A* **2018**, *6*, 24330−24341.
(27) Wang, L.; Peng, X.; Mustain, W. E.; Varcoe, J. R. Radiation-Grafted Anion-Exchange Membranes: The Switch from Low- to High-Density Polyethylene Leads to Remarkably Enhanced Fuel Cell Performance. *Energy Environ. Sci.* **2019**, *12*, 1575−1579.
(28) Luo, X.; Kushner, D. I.; Li, J.; Park, E. J.; Kim, Y. S.; Kusoglu, A. Anion Exchange Ionomers: Impact of Chemistry on Thin-Film Properties. *Adv. Funct. Mater.* **2021**, *31*, No. 2008778.
(29) Su, X.; Pan, Z.; An, L. Ion Transport Characteristics in Membranes for Direct Formate Fuel Cells. *Front. Chem.* **2020**, *8*, 765.
(30) Pan, J.; Han, J.; Zhu, L.; Hickner, M. A. Cationic Side-Chain Attachment to Poly(Phenylene Oxide) Backbones for Chemically Stable and Conductive Anion Exchange Membranes. *Chem. Mater.* **2017**, *29*, 5321−5330.
(31) Mason, T. J.; Millichamp, J.; Neville, T. P.; Shearing, P. R.; Simons, S.; Brett, D. J. L. A Study of the Effect of Water Management and Electrode Flooding on the Dimensional Change of Polymer Electrolyte Fuel Cells. *J. Power Sources* **2013**, *242*, 70−77.
(32) Shafaque, H. W.; Lee, C.; Fahy, K. F.; Lee, J. K.; Lamanna, J. M.; Baltic, E.; Hussey, D. S.; Jacobson, D. L.; Bazylak, A. Boosting Membrane Hydration for High Current Densities in Membrane Electrode Assembly CO_2 Electrolysis. *ACS Appl. Mater. Interfaces* **2020**, *12*, 54585−54595.
(33) Yassin, K.; Rasin, I. G.; Brandon, S.; Dekel, D. R. Quantifying the Critical Effect of Water Diffusivity in Anion Exchange Membranes for Fuel Cell Applications. *J. Membr. Sci.* **2020**, *608*, No. 118206.
(34) Peng, J.; Roy, A. L.; Greenbaum, S. G.; Zawodzinski, T. A. Effect of CO_2 Absorption on Ion and Water Mobility in an Anion Exchange Membrane. *J. Power Sources* **2018**, *380*, 64−75.
(35) Krödel, M.; Carter, B. M.; Rall, D.; Lohaus, J.; Wessling, M.; Miller, D. J. Rational Design of Ion Exchange Membrane Material Properties Limits the Crossover of CO_2 Reduction Products in Artificial Photosynthesis Devices. *ACS Appl. Mater. Interfaces* **2020**, *12*, 12030−12042.
(36) Carter, B. M.; Keller, L.; Wessling, M.; Miller, D. J. Preparation and Characterization of Crosslinked Poly(Vinylimidazolium) Anion Exchange Membranes for Artificial Photosynthesis. *J. Mater. Chem. A* **2019**, *7*, 23818−23829.
(37) Luque Di Salvo, J.; De Luca, G.; Cipollina, A.; Micale, G. Effect of Ion Exchange Capacity and Water Uptake on Hydroxide Transport in PSU-TMA Membranes: A DFT and Molecular Dynamics Study. *J. Membr. Sci.* **2020**, *599*, No. 117837.
(38) Noh, S.; Jeon, J. Y.; Adhikari, S.; Kim, Y. S.; Bae, C. Molecular Engineering of Hydroxide Conducting Polymers for Anion Exchange Membranes in Electrochemical Energy Conversion Technology. *Acc. Chem. Res.* **2019**, *52*, 2745−2755.
(39) Kutz, R. B.; Chen, Q.; Yang, H.; Sajjad, S. D.; Liu, Z.; Masel, I. R. Sustainion Imidazolium-Functionalized Polymers for Carbon Dioxide Electrolysis. *Energy Technol.* **2017**, *5*, 929−936.
(40) Peng, H.; Li, Q.; Hu, M.; Xiao, L.; Lu, J.; Zhuang, L. Alkaline Polymer Electrolyte Fuel Cells Stably Working at 80 °C. *J. Power Sources* **2018**, *390*, 165−167.
(41) Yin, Z.; Peng, H.; Wei, X.; Zhou, H.; Gong, J.; Huai, M.; Xiao, L.; Wang, G.; Lu, J.; Zhuang, L. An Alkaline Polymer Electrolyte CO_2 Electrolyzer Operated with Pure Water. *Energy Environ. Sci.* **2019**, *12*, 2455−2462.
(42) Ponce-González, J.; Whelligan, D. K.; Wang, L.; Bance-Soualhi, R.; Wang, Y.; Peng, Y.; Peng, H.; Apperley, D. C.; Sarode, H. N.; Pandey, T. P.; Divekar, A. G.; Seifert, S.; Herring, A. M.; Zhuang, L.; Varcoe, J. R. High Performance Aliphatic-Heterocyclic Benzyl-Quaternary Ammonium Radiation-Grafted Anion-Exchange Membranes. *Energy Environ. Sci.* **2016**, *9*, 3724−3735.
(43) Koronka, D.; Otsuji, K.; Matsumoto, A.; Miyatake, K.; Miyatake, K. Partially Fluorinated Copolymers Containing Pendant Piperidinium Head Groups as Anion Exchange Membranes for Alkaline Fuel Cells. *RSC Adv.* **2019**, *9*, 37391−37402.
(44) Zhou, T.; Shao, R.; Chen, S.; He, X.; Qiao, J.; Zhang, J. A Review of Radiation-Grafted Polymer Electrolyte Membranes for Alkaline Polymer Electrolyte Membrane Fuel Cells. *J. Power Sources* **2015**, *293*, 946−975.
(45) Kwasny, M. T.; Zhu, L.; Hickner, M. A.; Tew, G. N. Thermodynamics of Counterion Release Is Critical for Anion Exchange Membrane Conductivity. *J. Am. Chem. Soc.* **2018**, *140*, 7961−7969.
(46) Larrazábal, G. O.; Strøm-Hansen, P.; Heli, J. P.; Zeiter, K.; Therkildsen, K. T.; Chorkendorff, I.; Seger, B. Analysis of Mass Flows and Membrane Cross-over in CO_2 Reduction at High Current Densities in an MEA-Type Electrolyzer. *ACS Appl. Mater. Interfaces* **2019**, *11*, 41281−41288.
(47) Kim, C.; Bui, J. C.; Luo, X.; Cooper, J. K.; Kusoglu, A.; Weber, A. Z.; Bell, A. T. Tailored Catalyst Microenvironments for CO_2 Electroreduction to Multicarbon Products on Copper Using Bilayer Ionomer Coatings. *Nat. Energy* **2021**, *6*, 1026−1034.
(48) Leonard, M. E.; Clarke, L. E.; Forner-Cuenca, A.; Brown, S. M.; Brushett, F. R. Investigating Electrode Flooding in a Flowing Electrolyte Gas-Fed Carbon Dioxide Electrolyzer. *ChemSusChem* **2020**, *13*, 400−411.
(49) Weekes, D. M.; Salvatore, D. A.; Reyes, A.; Huang, A.; Berlinguette, C. P. Electrolytic CO_2 Reduction in a Flow Cell. *Acc. Chem. Res.* **2018**, *51*, 910−918.
(50) Wheeler, D. G.; Mowbray, B. A. W.; Reyes, A.; Habibzadeh, F.; He, J.; Berlinguette, C. P. Quantification of Water Transport in a CO_2 electrolyzer. *Energy Environ. Sci.* **2020**, *13*, 5126−5134.
(51) Weng, L. C.; Bell, A. T.; Weber, A. Z. Towards Membrane-Electrode Assembly Systems for CO_2 Reduction: A Modeling Study. *Energy Environ. Sci.* **2019**, *12*, 1950−1968.
(52) Kingsbury, R. S.; Bruning, K.; Zhu, S.; Flotron, S.; Miller, C. T.; Coronell, O. Influence of Water Uptake, Charge, Manning Parameter, and Contact Angle on Water and Salt Transport in Commercial Ion Exchange Membranes. *Ind. Eng. Chem. Res.* **2019**, *58*, 18663−18674.
(53) Li, Y. S.; Zhao, T. S.; Yang, W. W. Measurements of Water Uptake and Transport Properties in Anion-Exchange Membranes. *Int. J. Hydrogen Energy* **2010**, *35*, 5656−5665.
(54) Garg, S.; Giron Rodriguez, C. A.; Rufford, T. E.; Varcoe, J. R.; Seger, B. How Membrane Characteristics Influence the Performance of CO_2 and CO Electrolysis. *Energy Environ. Sci.* **2022**, *15*, 4400−4469.
(55) Jeng, E.; Jiao, F. Investigation of CO_2 Single-Pass Conversion in a Flow Electrolyzer. *React. Chem. Eng.* **2020**, *5*, 1768−1775.
(56) Endrődi, B.; Kecsenovity, E.; Samu, A.; Halmágyi, T.; Rojas-Carbonell, S.; Wang, L.; Yan, Y.; Janáky, C. High Carbonate Ion Conductance of a Robust PiperION Membrane Allows Industrial Current Density and Conversion in a Zero-Gap Carbon Dioxide Electrolyzer Cell. *Energy Environ. Sci.* **2020**, *13*, 4098−4105.
(57) He, Y.; Pan, J.; Wu, L.; Zhu, Y.; Ge, X.; Ran, J.; Yang, Z. J.; Xu, T. A Novel Methodology to Synthesize Highly Conductive Anion Exchange Membranes. *Sci. Rep.* **2015**, *5*, 13417.
(58) Dong, X.; Xue, B.; Qian, H.; Zheng, J.; Li, S.; Zhang, S. Novel Quaternary Ammonium Microblock Poly (p-Phenylene-Co-Aryl Ether Ketone)s as Anion Exchange Membranes for Alkaline Fuel Cells. *J. Power Sources* **2017**, *342*, 605−615.
(59) Amel, A.; Smedley, S. B.; Dekel, D. R.; Hickner, M. A.; Ein-Eli, Y. Characterization and Chemical Stability of Anion Exchange

https://doi.org/10.1021/acssuschemeng.2c06205
ACS Sustainable Chem. Eng. XXXX, XXX, XXX−XXX

Membranes Cross-Linked with Polar Electron-Donating Linkers. *J. Electrochem. Soc.* **2015**, *162*, 1047−1055.
(60) Ramdin, M.; De Mot, B.; Morrison, A. R. T.; Breugelmans, T.; Van Den Broeke, L. J. P.; Trusler, J. P. M.; Kortlever, R.; De Jong, W.; Moultos, O. A.; Xiao, P.; Webley, P. A.; Vlugt, T. J. H. Electroreduction of CO_2/CO to C_2 Products: Process Modeling, Downstream Separation, System Integration, and Economic Analysis. *Ind. Eng. Chem. Res.* **2021**, *60*, 17862−17880.
(61) Löwe, A.; Rieg, C.; Hierlemann, T.; Salas, N.; Kopljar, D.; Wagner, N.; Klemm, E. Influence of Temperature on the Performance of Gas Diffusion Electrodes in the CO_2 Reduction Reaction. *ChemElectroChem* **2019**, *6*, 4497−4506.
(62) Liu, Z.; Yang, H.; Kutz, R.; Masel, R. I. CO_2 Electrolysis to CO and O_2 at High Selectivity, Stability and Efficiency Using Sustainion Membranes. *J. Electrochem. Soc.* **2018**, *165*, 3371−3377.

https://doi.org/10.1021/acssuschemeng.2c06205
ACS Sustainable Chem. Eng. XXXX, XXX, XXX−XXX

- Supporting Information -

Influence of headgroups in ETFE-based radiation-grafted anion exchange membranes for CO_2 electrolysis

Carlos A. Giron Rodriguez,[a] Bjørt Óladottir Joensen,[a] Asger Barkholt Moss,[a] Gastón O. Larrazábal,[a] Daniel K. Whelligan,[b] Brian Seger,[a,*] John R. Varcoe,[b,*] and Terry R. Willson[b]

[a]*Surface Physics and Catalysis (SURFCAT) Section, Department of Physics, Technical University of Denmark, 2800 Kgs. Lyngby, Denmark*

[b]*Department of Chemistry, University of Surrey, Guildford GU2 7XH, United Kingdom*

**Correspondence to: Brian Seger, Email: brse@fysik.dtu.dk and Johm Varcoe, Email: varcoe@surrey.ac.uk*

SI document = 21 pages

Number of Figures = 14

Number of Tables = 6

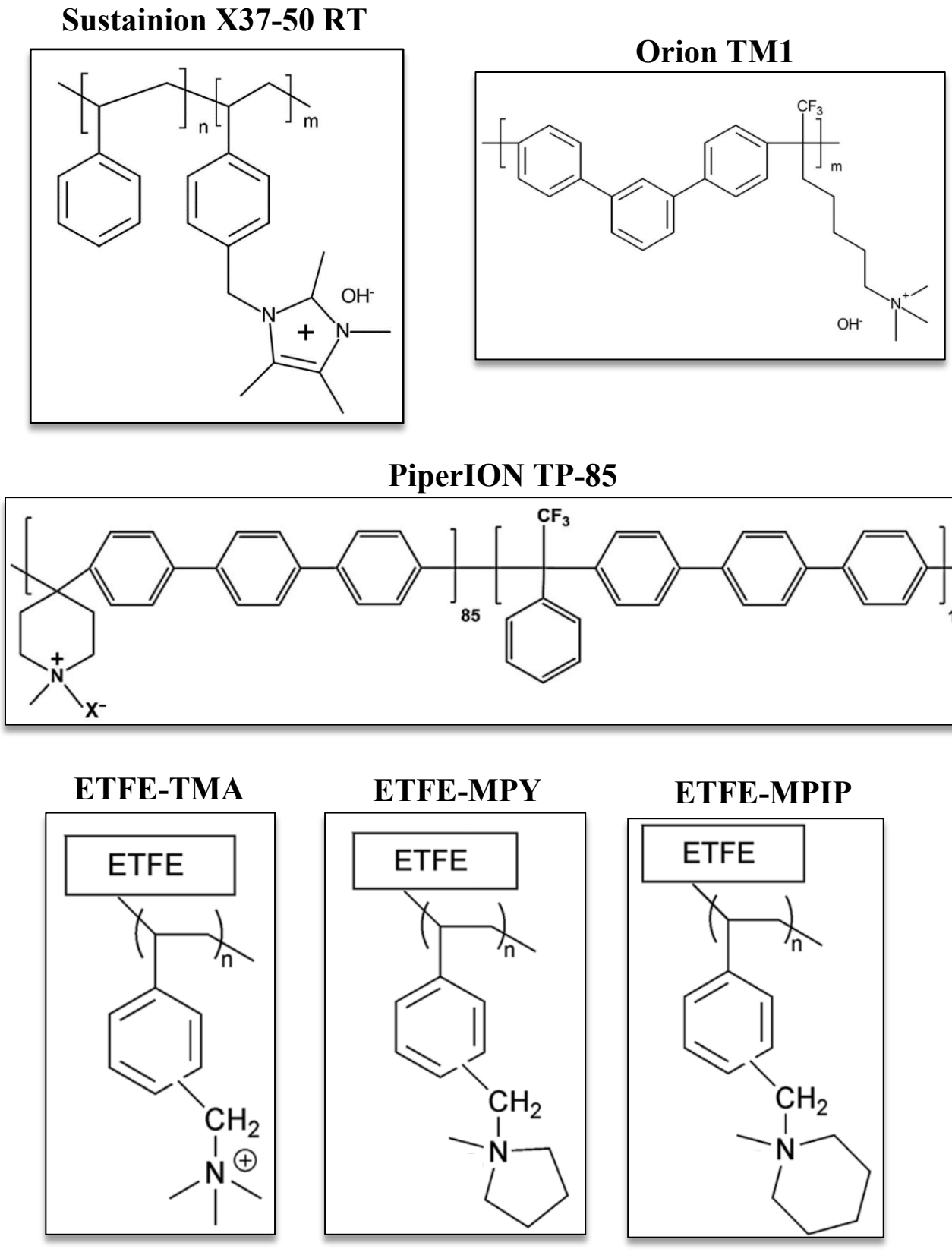

Figure S1 Chemical structures of different AEMs including the ETFE-based radiation-grafted AEMs that were the main subject of the paper.

Table S1 Main key properties of common AEMs for CO_2 electrolysis.

AEM	Counter Ion (anion)	Backbone	IEC (meq g^{-1})	λ	Tensile strength (MPa)	Thickness (µm)	WU (wt. %)	ASR (Ω cm^{-2})	σ (mS cm^{-1})
FAA-3-50[1]	Br^-	N.A	1.6-2.1	N.A	25-40	45-55	10-25	0.6-1.5 (Cl^- form)	3-8 (Cl^- form)
AMVN[2]	Cl^-	PVC	1.85 ± 0.04	N.A	0.3	100-150	15±2	2.5	3.8 (Cl^- form)
X37-50 RT[3]	HCO_3^-	Styrene	2.52	N.A	N.A.	50	>80	0.045 (1 M KOH)	80 (OH^- form)
PiperION	OH^-	Poly(aryl piperidinium)	2.35	N.A	>30	20	50	N.A	150 (OH^- form)
Orion TMI	OH^-	Poly (terphenylene)	2.19	N.A	30	30	33-37	N.A	54 (OH^- form)
m-TPN1[4]	OH^-	Terphenyl	2.1	18	29	15-25	25	0.18	54 (OH^- form)
A201	OH^-	PBI	1.8	25	96 (Cl^- form)	28	44±5	N.A	42
AFI-HNN8-50[5]	OH^-	HMT-PMBI	2.1-2.5	N.A	60 (I^- form)	50	39-50	0.13	>80

*Compiled data correspond to the reported properties from the data sheet of each manufacturer (missing data from the data sheet are found in the references). NA stands for the information not specified/available. Superscript numbers are literature references (see end of SI document).

Materials and chemicals

ETFE polymer films (25 and 50 µm thick) were supplied by Nowofol Kunststoffprodukte GmbH (Germany). VBC (97 % purity, a mixture of 3- and 4-ionomers, 700–1100 ppm nitromethane or 50–100 ppm tert-butylcatechol inhibitors) was purchased from Sigma Aldrich and used as supplied (no removal of inhibitor prior to use). Additionally, 1-octyl-2-pyrrolidone dispersant, *N*-methylpiperidine (99 % purity), aqueous trimethylamine (45 %vol), *N*-methylpyrrolidine (88 %), and acetone were purchased from Sigma-Aldrich (Merck). $AgNO_3$ titration standard analytical solutions (0.02000 ± 0.00006 M) were purchased from Honeywell-Fluka. The ultra-pure water (UPW) used throughout this study was generated using a Purite water purification system (resistivity = 18.2 MΩ cm).

Commercial AEMs Selemion® AMV, Fumasep® FAA-3-50, and PiperION) were purchased from FuelCellStore, while Sustainion® X37-50 RT was purchased from Dioxide Materials. A porous silver membrane with a pore size of 1.2 µm (99.9 % purity) was obtained from Sterterlich Inc. and used as the cathode. The commercial IrO_2-coated carbon paper anode was purchased from Dioxide Materials. $KHCO_3$ (Sigma-Aldrich 99.995 % trace metal basis) and KOH (Sigma-Aldrich 99.95 % trace metal basis) were used as an electrolyte for cell testing or membrane activation solutions.

Methodology for the RG-AEMs synthesis

The RG-AEMs were synthesized via the radiation-grafting peroxidation method. ETFE was selected as a substrate rather than LDPE and HDPE, as quick screening CO_2E cell tests showed that ETFE-based RG-AEMs led to the least parasitic H_2 generation. The VBC was grafted onto electron-beamed ETFE films (40 kGy total dose, 4.5 MeV electron beam) by immersing them in N_2 purged (O_2 free) aqueous dispersion of VBC (5 %vol) in 1-octyl-2-pyrrolidone (1 %vol) and heating at 70 °C for 24 h. After thorough washing in toluene/acetone and drying, batches of RG-membrane [designated ETFE-g-p(VBC)] were obtained with a degree of grafting (dog) = 79 % for the variant made from 25 µm thick ETFE and a dog = 68 % for the variant made

from 50 µm thick ETFE (see Equation S1 in the ESI† for the calculation of dog values). ETFE-g-p(VBC) samples were then aminated separately with either the aqueous trimethylamine (45 %mass, room temperature, 24 h), *N*-methylpyrrolidine (50 %vol, 60 °C, 18 h), or *N*-methylpiperidine (15 %vol, 60°C, 18 h), yielding the desired RG-AEMs.

After the amination, the RG-AEMs were washed multiple times in UPW and soaked in aqueous NaCl (1 M) solutions for 1 h (with at least three solution changes during this period) to ensure the pure Cl^- anion form. After thorough washing in UPW for at least 1 h (with multiple changes in UPW) to remove all excess co- and counter-ions, they were stored in UPW until use. The Cl^- form RG-AEMs can be converted into the predominant HCO_3^- form (with trace amounts of CO_3^{2-} anions) by immersion in aqueous $KHCO_3$ (1 M) for 1 h (multiple changes of solution during this time) followed by thorough washing with UPW (to remove excess co- and counter-ions).

Detailed descriptions for the different steps during RG-AEMs synthesis

Irradiation step: ETFE polymer films (ethylene-tetrafluoroethylene) were supplied by Nowofol Kunststoffprodukte GmbH (Germany) in both 25 and 50 µm thicknesses [designated E25 and E50]. The pre-cut ETFE films were subject to electron-beam irradiation in air to a total absorbed dose of 40kGy using a continuous vertical 4.5 MeV Electron Beam Accelerator, Synergy Health Sterilisation UK Limited, Daventry UK. Post-irradiation the films were immediately stored under solid CO_2 and transported to the University of Surrey where they were transferred to a - 40°C freezer for long-term storage (up to 12 months).

Grafting step: The electron-beamed ETFE films with approximate area of 12 × 12 cm^2 were submerged in an aqueous grafting solution containing 5% vol vinylbenzyl chloride (VBC, 97% purity, mixture of 3- and 4-iomers, 700–1100 ppm nitromethane or 50–100 ppm 4-*tert*-butylcatechol inhibitors, purchased from Sigma Aldrich) and 1 %vol 1-octyl-2-pyrrolidone in deionised water. The grafting solution was then purged with N_2 for 1 h before sealing the vessel and heating it to 70 °C for 24 h. Post-grafting the ETFE-g-poly(vinylbenzyl chloride) grafted films [designated ETFE-g-p(VBC) in the main paper] were thoroughly washed in acetone and toluene to remove any excess VBC as well as any non-grafted poly(VBC) homopolymer that may have formed during the graft reaction. The ETFE-g-p(VBC) membranes were then dried at 50 °C under reduced pressure (vacuum oven) for 3 h to remove all traces of solvent. The degree of grafting (dog, %) of the ETFE-g-p(VBC) intermediate membranes was calculated using the following equation:

$$\mathrm{dog} = \frac{m_g - m_i}{m_i} \times 100\ \% \qquad \textbf{(Eqn. S1)}$$

where m_g is the mass of the ETFE-g-p(VBC) membrane and m_i is the mass of the initial irradiated ETFE film. The dog for the ETFE-g-p(VBC) made from E25 and E50 were 80 % and 68 %, respectively. It was clear that when using the same grafting process (and radiation dose), the thicker ETFE grafted to a lower degree. However, we cannot use higher radiation doses with ETFE as this would lead to RG-AEMs that are too mechanically weak for use in electrochemical cells (especially at elevated temperatures),[6] as the electron-beam treatment process breaks a proportion of the C-C bonds in the ETFE chains (alongside the desired ability to graft monomers).

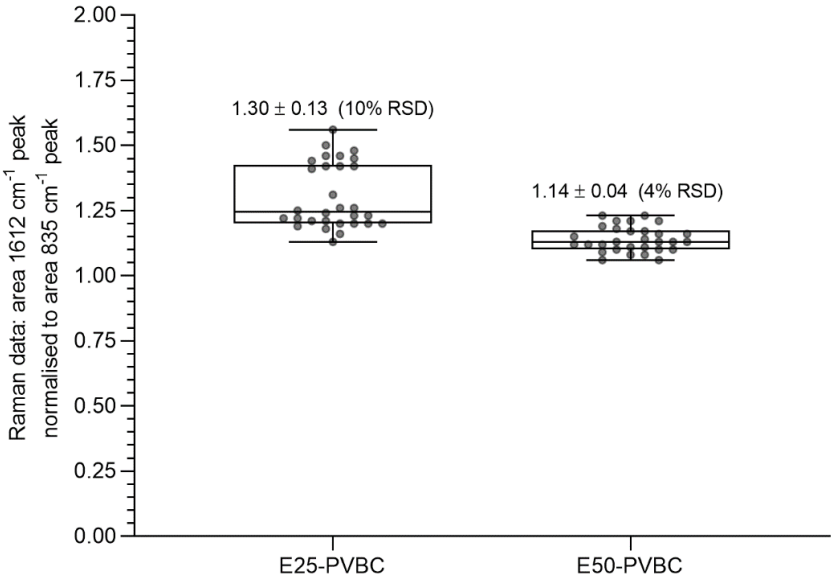

Figure S2 Box plots containing extracted integrated Raman peak area data for spectra recorded on 30 random spots (*ca.* 2 μm diameter laser spot sizes and depths, laser λ = 785 nm) recorded on both sides of the ETFE-*g*-p(VBC) made from both 25 and 50 μm thick ETFE substrate films (E25 and E50). The peak at 1612 cm^{-1} derives from the grafted poly(vinylbenzyl chloride) chains, while the peak at 835 cm^{-1} derives from the ETFE substrate films. Plots show max (top bar), interquartile range (box), median (middle bar), and minimum (bottom bar). The means and sample standard deviations (and relative standard deviations, RSD) are given above the boxes. This data is to evaluate grafting homogeneity (and levels – higher mean peak area ratios for a higher dog). An RSD of 10 % or lower is normal for such lab-fabricated RG-AEMs.

Table S2 The reaction conditions used to aminate the AEMs in this study (of both thicknesses).

	Amination reaction conditions used			
AEM	**Amine**	**Aqueous concentration (%vol)**	**Temp (°C)**	**Time (h)**
TMA	Trimethylamine	45	RT	24
MPY	*N*-Methylpyrrolidine	50	60	18
MPIP	*N*-Methylpiperidine	15	60	18

Amination step: The ETFE-*g*-p(VBC) intermediate films were subsequently converted to RG-AEMs: TMA-AEM, MPY-AEM and MPIP AEMs *via* submersion in aqueous solutions containing trimethylamine (TMA), *N*-methylpyrrolidine (MPY) and *N*-methylpiperidine (MPIP), respectively. Amination reactions were carried out under various conditions depending on the amine used, with the specific conditions summarised in Table S2. Post-amination all RG-AEMs were thoroughly washed in ultrapure water (UPW) before subsequent heating in fresh UPW at 60 °C for 18 h. This is to ensure that any unreacted amine is removed from the membrane.

Ion-Exchange process to ensure Cl^- forms for storage and initial experiments: To ensure complete conversion to the pristine Cl^- anion form RG-AEMs, the crude, as synthesised, RG-AEMs were submerged in aqueous NaCl solution (1 mol dm^{-3}) for 24 h with the NaCl solution being refreshed three times during this period. The resulting AEMs were then removed and

thoroughly washed with UPW to remove any excess free-ions: both co-ions (Na^+) and excess counter-ions (any Cl^- that are not charge balancing the quaternary ammonium positive charges). The pristine Cl^- anion form RG-AEMs were stored under UPW until use.

RG-AEM characterization

Raman Spectroscopy Raman spectra were recorded on dry samples of the ETFE-g-p(VBC) and final RG-AEMs using a Renishaw InVia Reflex Raman Microscope equipped with a 785 nm IR laser and a 20× (NA = 0.40) objective. All Raman data was collected and baseline corrected using Renishaw WiRE Software (Renishaw PLC, UK), with normalization and integration of band intensities conducted using Spectragryph (Spectroscopy Ninja, Germany).

Ion-exchange capacities (IEC) The ion exchange capacities (IEC) were determined using potentiometric AgCl precipitation titrations. For each RG-AEM in the Cl^- form, a dehydrated sample of known dry mass (m_{dry}) was immersed in 25 mL aqueous $NaNO_3$ solution (1.2 M) and continuously stirred for 16 h. Subsequently, the solution (still containing the RG-AEM sample) was acidified with aqueous 2 mL HNO_3 (2 M) and titrated against aqueous $AgNO_3$ standard solution (0.02000 ± 0.00006 M). A Metrohm 848 Titrino Plus autotitrator equipped with an Ag/AgCl Titrode was used for the dynamic equivalence point titrations (DET). The endpoint was calculated as the peak maxima in the first differential plot of potential *vs.* titrant volume data. IEC was calculated with Equation S2.

$$IEC\ (meq\ g^{-1}) = \frac{E_p \times C_{st}}{m_{dry}} \qquad \textbf{(Eqn. S2)}$$

where E_p represents the endpoint volume, C_{st} is the $AgNO_3$ standard concentration solution, and m_{dry} is the mass of the dry RG-AEM(Cl^-) sample under analysis. This procedure was undertaken on $n = 3$ samples of each RG-AEM.

Water uptake (WU) and through-plane swelling (TPS) A RG-AEM(Cl^-) sample was removed from UPW storage and the excess surface water was removed by blotting with a filter paper. The hydrated mass (m_{hy}) and thickness (T_{hyd}) were then recorded immediately. Masses were recorded on a 4 decimal place (0.1 mg) analytical balance, and thicknesses were recorded using an outside digital micrometer (precision of ± 2 μm). The RG-AEM(Cl^-) sample was dried under reduced pressure at 50 °C (vacuum oven) for 18 h before the dehydrated mass (m_{dry}) and thickness (T_{dry}) were recorded. All measurements were conducted on $n = 3$ samples of each RG-AEM(Cl^-). The gravimetric water uptake, through-plane swelling (TPS), and the hydration number (λ) for each sample were calculated using Equations S3 – S5.

$$\mathrm{WU}(\%) = \frac{\mathrm{m_{hyd} - m_{dry}}}{\mathrm{m_{dry}}} \times 100\ \% \qquad \textbf{(Eqn. S3)}$$

$$\mathrm{TPS}(\%) = \frac{\mathrm{T_{hyd} - T_{dry}}}{\mathrm{T_{dry}}} \times 100\ \% \qquad \textbf{(Eqn. S4)}$$

$$\lambda = \frac{\mathrm{WU}(\%)/100}{\mathrm{IEC} \times \mathrm{M_{water}}} \qquad \textbf{(Eqn. S5)}$$

where M_{water} corresponds to the molecular mass of water (18.015 g mol^{-1}). Area swelling values were calculated in the same way as TPS values but using the hydrated and dry areas measured at the same time as the thicknesses.

In-plane ion-conductivity The in-plane Cl^- and HCO_3^- anion conductivities of fully hydrated RG-AEM samples between room temperature and 80 °C were measured using a Solartron 1260/1287 combination controlled by ZPlot/ZView software (Scribner Associates, USA). Impedance spectra were collected over a frequency range of 1.0 – 10^6 Hz (10 mV a.c. amplitude) with the samples mounted in a 4-probe BekkTech BT-112 test cell (Alvatek, UK). Test cells containing samples of the Cl^- and HCO_3^- RG-AEM forms were then submerged in UPW. The ionic resistances values, taken as low-frequency *x-(real)*-axis intercepts in the collected Nyquist plots, were used to calculate the conductivities using Equation S6:

$$\sigma\ (\mathrm{S\ cm^{-1}}) = \frac{\mathrm{L}}{\mathrm{R\ w\ T}} \qquad \textbf{(Eqn. S6)}$$

where *L* corresponds to the working electrode distances (0.425 cm), and *w* and *T* are the width and thickness of the RG-AEM samples, respectively.

Table S3 Summary of the key properties of the E50-based AEMs (Cl^- forms). Errors are sample standard deviations on $n = 3$ repeat measurements (errors in λwater are calculated from the errors in IEC and WU using standard error propagation rules).

	E50-TMA-AEM	**E50-MPY-AEM**	**E50-MPIP-AEM**
Ion-exchange capacity IEC (mmol/g)	1.63 ± 0.09	1.56 ± 0.04	1.45 ± 0.04
Fully hydrated thickness (μm)	95 ± 2	106 ± 3	95 ± 2
Conductivity σ in Cl^- at room temperature (mS/cm)	15 ± 2	16 ± 1	12 ± 1
Thickness increase on hydration (%)	20 ± 1	23 ± 2	28 ± 1
Area swelling on hydration (%)	21 ± 1	49 ± 1	39 ± 9
Gravimetric water uptake (% wt.)	18 ± 4	27 ± 2	24 ± 5
λwater (H_2O molecules per exchange site)	6 ± 2	10 ± 1	9 ± 2

Table S4 A summary of key physical and electrochemical properties for Sustainion® X37-50 grade RT in this study.

Ion-exchange capacity IEC (mmol g^{-1})	1.4 ± 0.01
Fully hydrated thickness (μm)	81 ± 2
Conductivity σ in Cl^- at room temperature (mS cm^{-1})	13.5 ± 0.3
Area swelling on hydration (%)	15.1 ± 4.6
Gravimetric water uptake (% wt.)	90.7 ± 14.4
Ion-exchange capacity IEC (mmol g^{-1})	1.4 ± 0.01

Electrode Preparation

Preparation of Cu electrodes for CO_2E to C_{2+} products: Cu-based electrocatalysts were synthesized using physical-vapor deposition (PVD). Layers of 150 nm thick Cu (6N grade) were deposited onto commercial gas diffusion layers (Sigracet 39BB purchased from FuelCellStore) by magnetron sputtering (AJA International) in a vacuum environment (10^{-6} Torr) at a deposition rate of 1 Å s^{-1} under 10 sccm Ar with a sputtering pressure of 2 mTorr. Our Cu-electrodes don't require the addition of any ionomers as binder, so we can evaluate the effects of the membrane's chemistry in the AEM/cathode interface and the reaction, without the potential influence of the binder´s chemistry

Catalyst characterization: Scanning electron microscopy (SEM) of porous Ag and Cu-GDE catalysts was performed using FEI Quanta 200 FEG instrument with an accelerating voltage of 15 kV in secondary electron mode. In addition, X-ray photoelectron spectroscopy (XPS) measurements were carried out in a ThetaProbe instrument (Thermo Fisher Scientific) with monochromatic Al K_α radiation (1486.7 eV) equipped with a hemispherical analyzer. Scans were made in the binding energy range of 0−1400 eV with an analyzer pass energy of 100 eV.

Cell configuration and electrochemical tests: All electrochemical experiments were performed on a commercial electrolysis cell (Dioxide Materials) in a zero-gap MEA configuration. The assembly consisted of loading a fresh AEM (area = 7.4 cm^2) inserted between a cathode (area = 2.25 cm^2) and anode (area = 4 cm^2). PTFE gaskets further sandwiched the MEA device, which helped prevent electrolyte leakage and potential short-circuiting. The system was mechanically pressed, using cell bolts fastened with a torque of 3 N·m to guarantee an uniform and adequate compression. A Bio-Logic VSP 300 potentiostat with a booster channel was used for electrochemical measurements.

The CO_2 (AGA, purity 4.5) flow was set using a mass flow controller (MKS Instruments Inc.) and further humidified by sparging it into a container filled with UPW before being fed to the cathode (standard flow= 40 mL min^{-1}). A liquid trap was installed on the outlet line from the cathodic gas to prevent water from entering the gas chromatograph (GC). This also allowed for the collection of liquid effluent species. The anode was fed with aqueous 0.1 M $KHCO_3$ and continuously recirculated (40 ml min^{-1}) using a diaphragm pump (KNF Neuberger Inc.). The standard conditions for gas flow in this work are 293 K and 1 bar. An Ag/AgCl (3.5 M NaCl internal solution) was employed as the reference electrode. Current interrupt and impedance techniques measured the uncompensated and charge transfer resistances. An illustration of the electrochemical cell and the reaction setup used for these experiments can be found in Figure S3.

The molar outlet flow of the cathodic and anodic streams was measured using a volumetric flow meter (MesaLabs Defender 530) located downstream of the gas chromatograph (GC). The gas product's composition was quantified with a PerkinElmer Clarus 590 GC equipped with a Molecular Sieve 13x, and HayeSep Q packed column using Ar (10 ml min^{-1}) as the carrier gas, and a thermal conductivity detector (TCD). Liquid product analysis was carried out with Agilent Infinity 1260 high-performance liquid chromatography (HPLC), equipped with Aminex HPX-87H column, refractive index (RID), and diode-array (DAD) detectors.

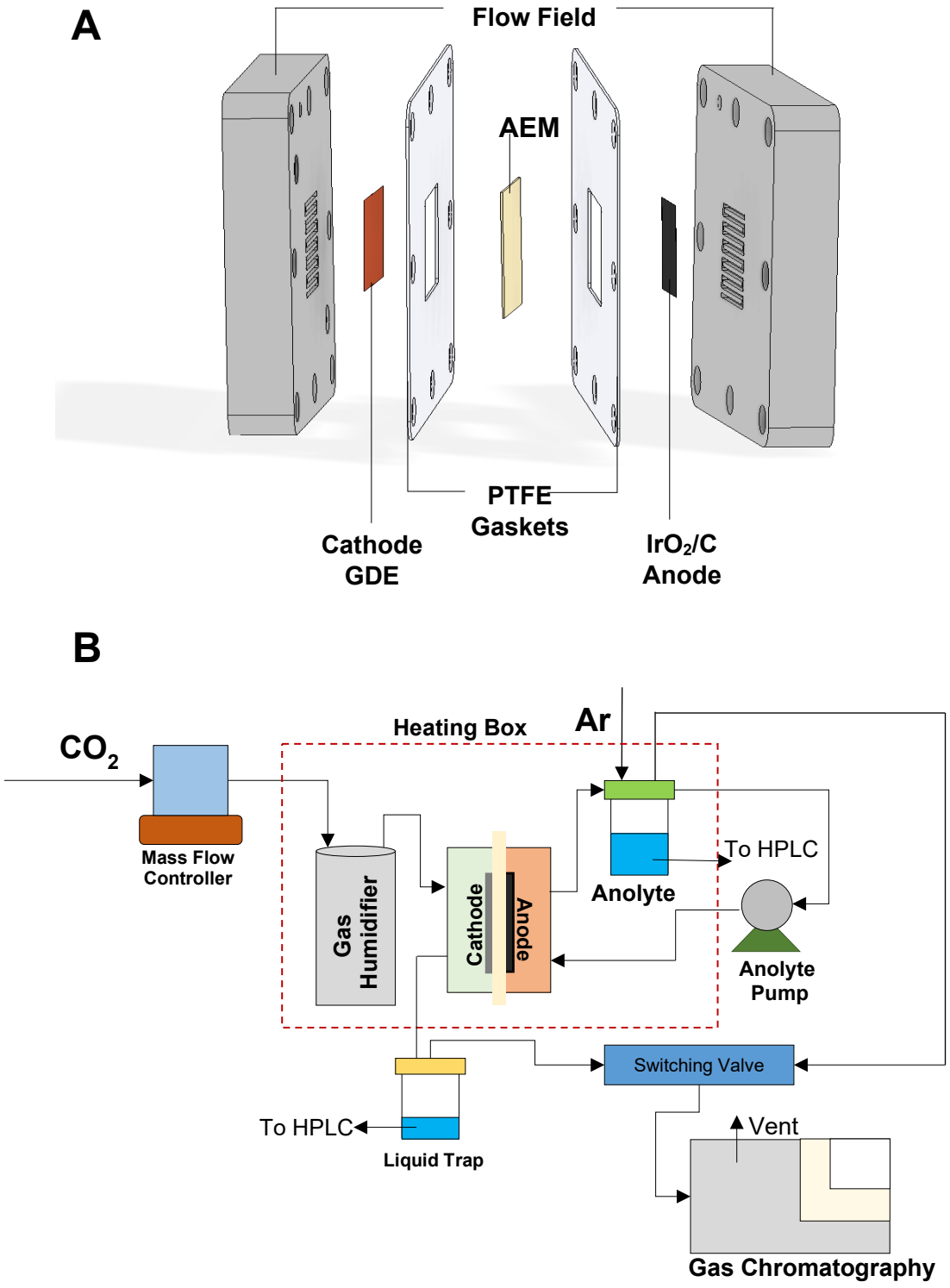

Figure S3 Scheme of **A)** the MEA-type electrolytic cell for electrochemical CO_2 reduction**,** and **B)** Electrolysis set up (use of backpressure regulators or MFM aren't shown in the figure but placed after the electrochemical cell and the gas chromatography).

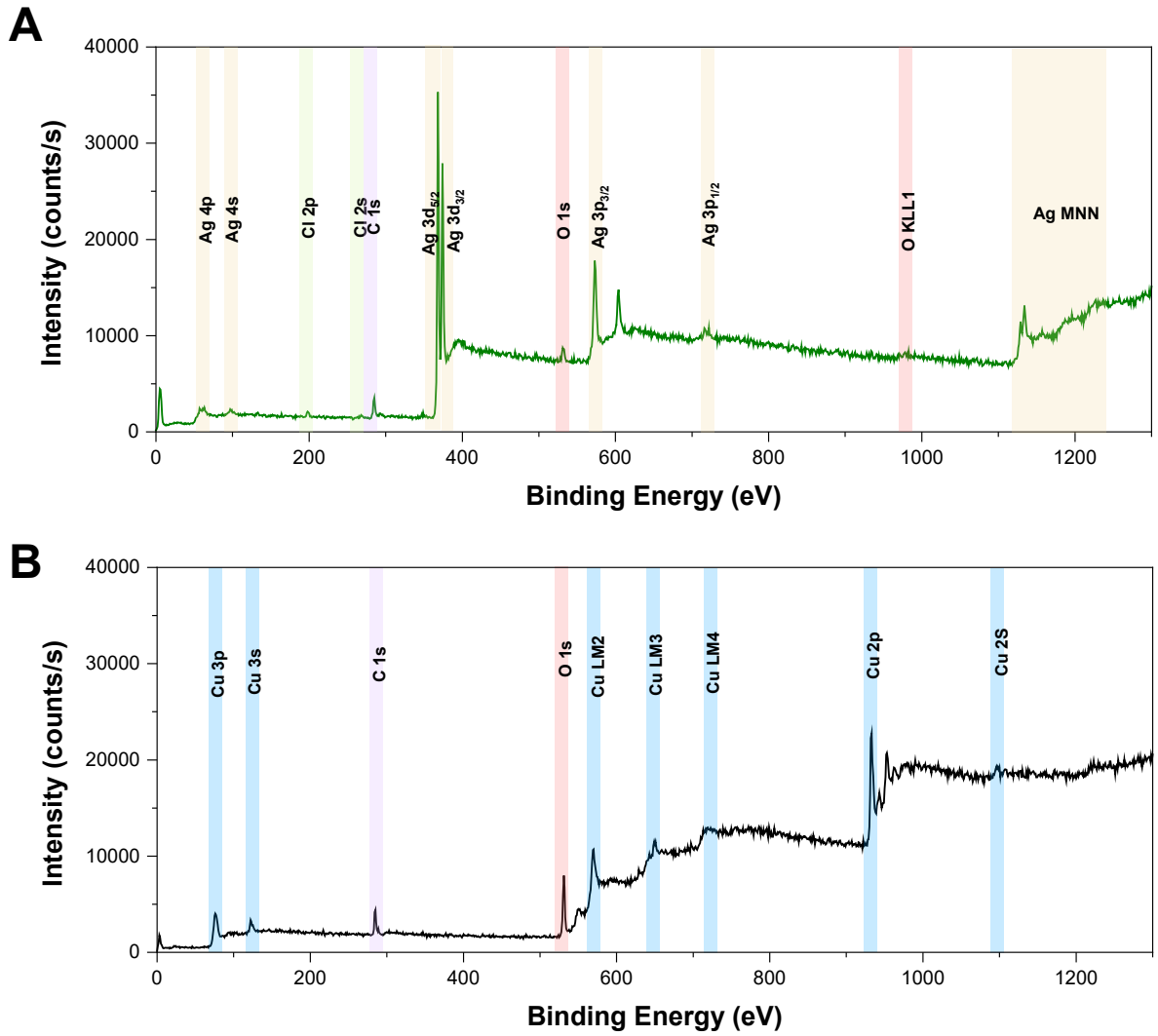

Figure S4 X-ray photoelectron spectroscopy of fresh **A)** Ag-porous based catalyst (Sterlich with a nominal pore size of 1.2 µm) and **B)** Fresh Sputtered Cu (150 nm) deposited in SG39BB. Chlorine and carbon features could be related to deposited traces while preparing the sample.

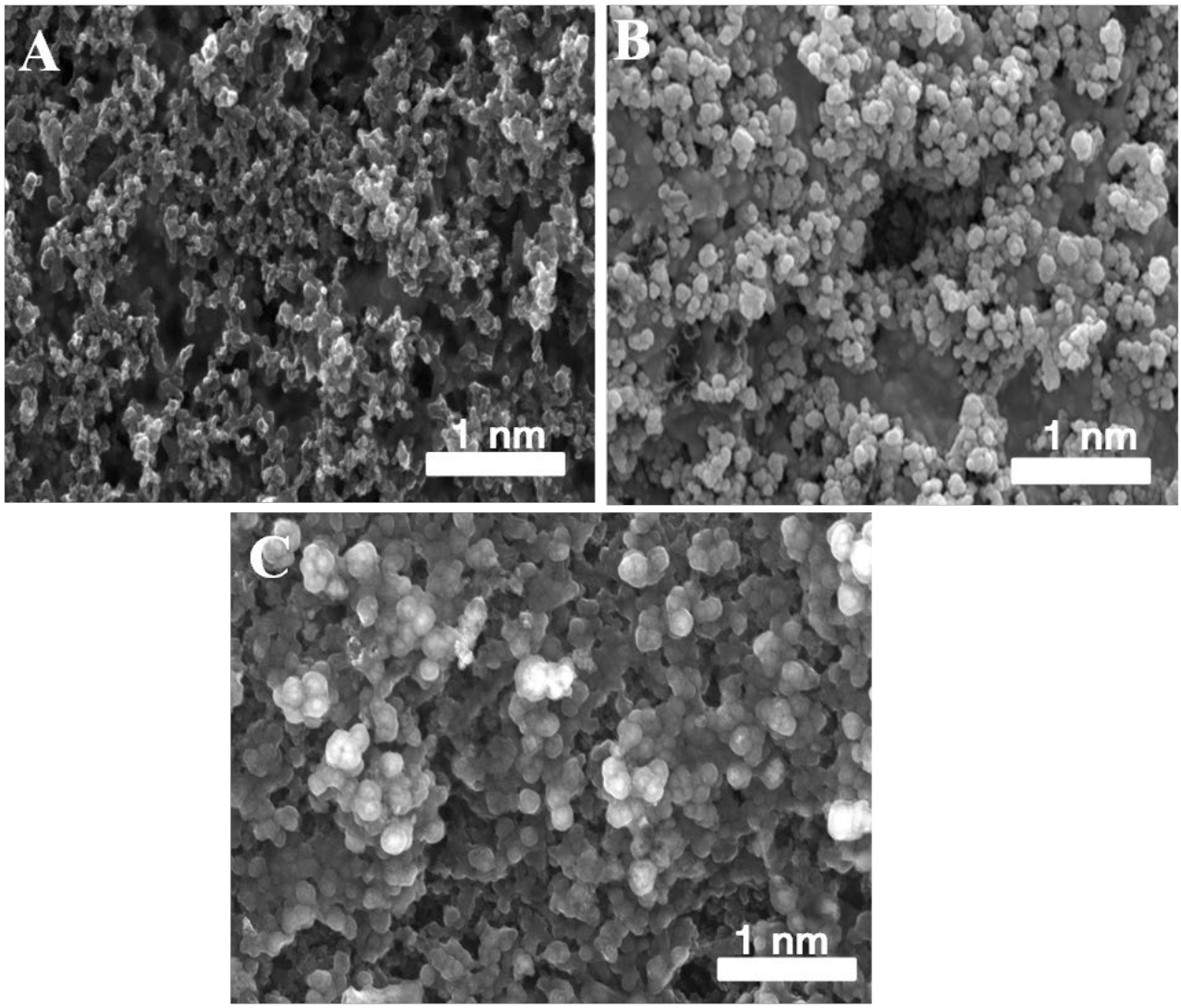

Figure S5 SEM images of the Cu-based catalyst **A)** gas-diffusion layer (GDL), **B)** Cu-GDE coated on microporous carbon layers of the commercial SG-39BB GDL before the electrochemical reaction and **C)** Post-reaction Cu-GDE

Calculation for partial current densities and Faradaic efficiencies

Gas and liquid products are quantified using GC, and HPLC analysis techniques. Partial current density and Faradaic efficiency are two of the methods used in this study to estimate the selectivity and electrochemical performance.

Faradaic efficiency can be defined as the amount of electric charge required to form a desired product over the total charge. It represents the selectivity towards a specific product and can be tuned to improve the conversion and reducing the energy consumption. The calculation of the parameter is expressed in Eqn. S7

$$FE_i = \frac{z \cdot n \cdot F}{Q} * 100\% \qquad (\mathbf{Eqn.\ S7})$$

where z corresponds to the number of electrons required per mol (z = 2 for CO and H_2), n is moles of the specific products, F is the Faraday´s constant, and Q is the total charge (current × time).

Furthermore, the current density can be defined as the ratio between the total current and the electrode area (geometric or ECSA). The partial current density is associated to the specific product and the product's reaction rate since the electrons transferred in a chemical reaction is proportional to the reaction's extent:

$$j_i = \frac{I}{A} \cdot FE_i \qquad (\mathbf{Eqn.\ S8})$$

Calculation of Faradaic efficiency, partial current density and crossover for $HCOO^-$

As mentioned in the main paper, the liquid products analysis was conducted using HPLC for the liquid trap at the cathode and the anolyte. The formate crossover across the membrane and further oxidation over the IrO_2 anode limited the quantification of the total Faradaic efficiency and the partial current density.

Initially, we measured the liquid products at the anolyte and the cathode (collected from the water trap) and correlated the generation of formate in terms of charge. To illustrate these calculations, we take as reference experiments done with the MPIP-AEM (25 μm) at 150 mA cm^{-2} (Figure 3C).

Table S5. Post reaction-liquid analysis and FE-charges for formate quantification

Sample	Volume (ml)	FE_{HCOO^-} (%)	$[HCOO^-]$ (mM)	n_{HCOO^-} (mmol)	q_{HCOO^-} (C)
Anolyte	60	3.64	3.41	0.205	39.5
Cathode	20	0.04	0.0944	$1.88x10^{-3}$	0.364
				Total	39.864

$$\text{Total passed charge (C)} = I * t = 1083.24\ C$$

$$\text{Ratio of corresponded charge (\%)} = \frac{q_{HCOO-}}{q_{total}} = 3.68\%$$

While the crossover and oxidation of the formate is presumed to happen fast (as evidenced in Table S5 and comparison between charge ratios), the quantification of the liquid in post-reaction techniques doesn't provide a good estimation of this product selectivity and reaction extent. Therefore, we assumed that over Ag-based catalysts, the "unaccounted product" is attributed to the CO_2E to $HCOO^-$ and therefore calculated using Eqn.S9 and S10

$$j_{formate} = j_{total} \cdot FE_{formate} \quad \textbf{(Eqn. S9)}$$

$$FE_{formate} = 100\% - FE_{H_2} - FE_{CO} \quad \textbf{(Eqn. S10)}$$

Larrazabal et al.[7] conducted previous experiments to estimate the FE of $HCOO^-$ oxidation over IrO_2/C at 200 mA cm^{-2}, showing that the decrease amount of $HCOO^-$ (in terms of concentration and remained charge) can be related to a FE for $HCOO^-$ ca. 20%.

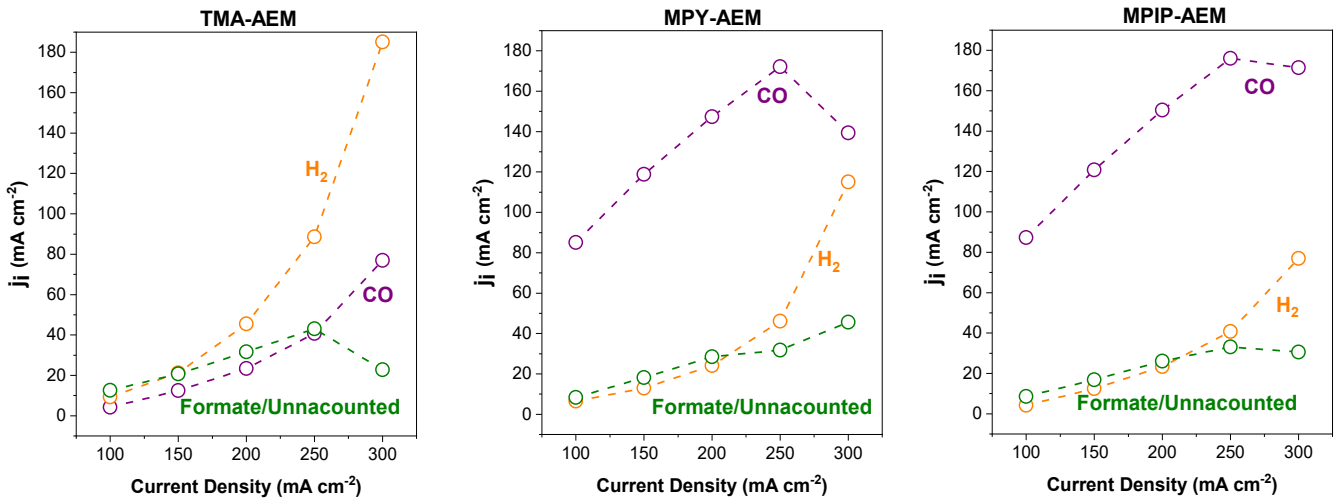

Figure S6 Partial current densities (j_i) for different products as a function of the total current density over Ag-electrocatalyst and 0.1 M $KHCO_3$ anolyte with our different RG-AEMs. Unaccounted products are assumed to be formate. The error bars in such represent the standard error of the mean of three independent measurements.

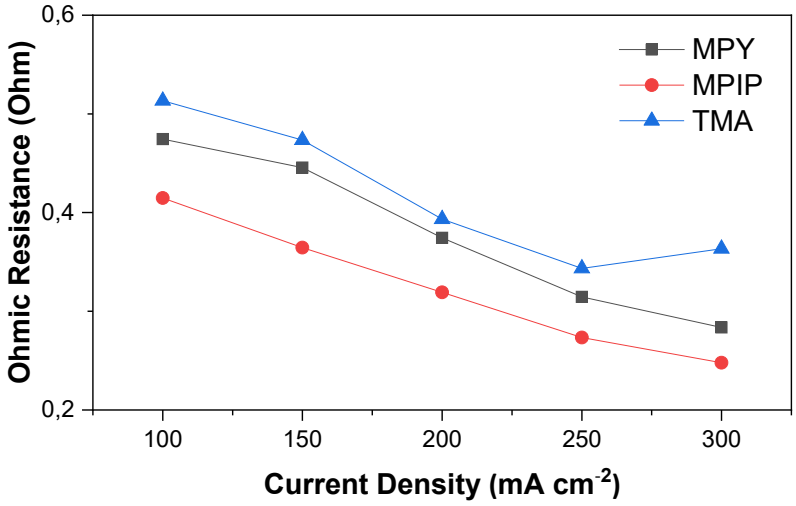

Figure S7 Measurement of ohmic resistances for experiments showed in Figure 3(C-E) for our different RG/AEM's using current interrupt technique (CI).

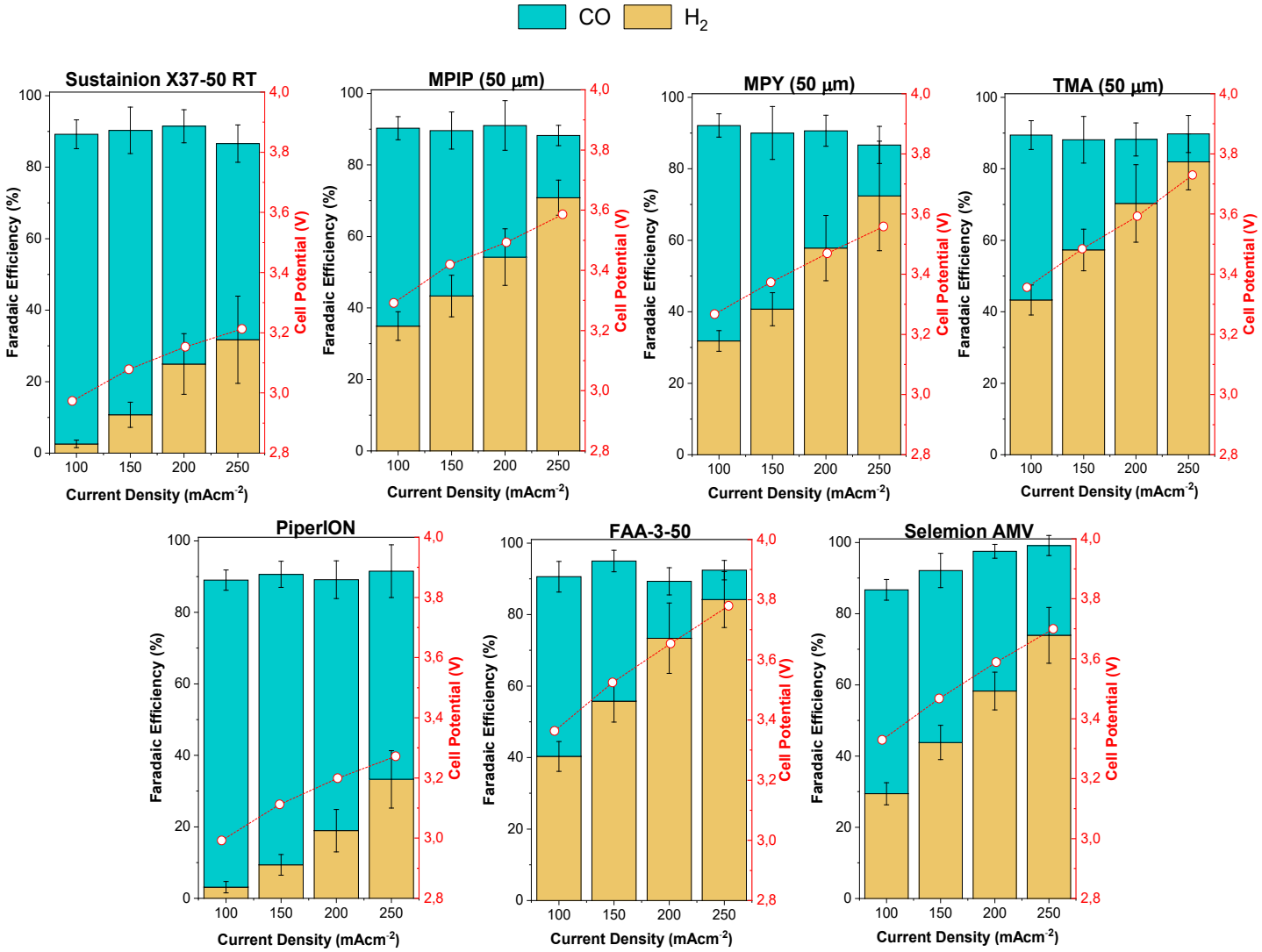

Figure S8 Product distribution and cell potentials at room temperature of different AEMs (including RG-AEM's with thicker 50 µm) as function of the total current density with 0.1 M $KHCO_3$ and Ag-electrocatalyst. The error bars in such represent the standard error of the mean of three independent measurements.

Neutralization reactions and gas evolution at the anode

Neutralization reactions:

$CO_2 + OH^- \rightarrow HCO_3^-$

$HCO_3^- + OH^- \rightarrow CO_3^{2-} + H_2O$

$OH^- + H^+ \rightarrow H_2O$

Gas evolution at the anode:

OER: $2H_2O \rightarrow O_2 + 4H^+ + 4e^-$

Combining the neutralization reaction with the gas evolution at the anode, we have:

$4HCO_3^- \rightarrow 4CO_2 + O_2 + 2H_2O + 4e^-$ **(CO_2/O_2 ratio = 4)**

$2CO_3^{2-} \rightarrow 2CO_2 + O_2 + 4e^-$ **(CO_2/O_2 ratio= 2)**

$4OH^- \rightarrow O_2 + 2H_2O + 4e^-$ **(CO_2/O_2 ratio = 0)**

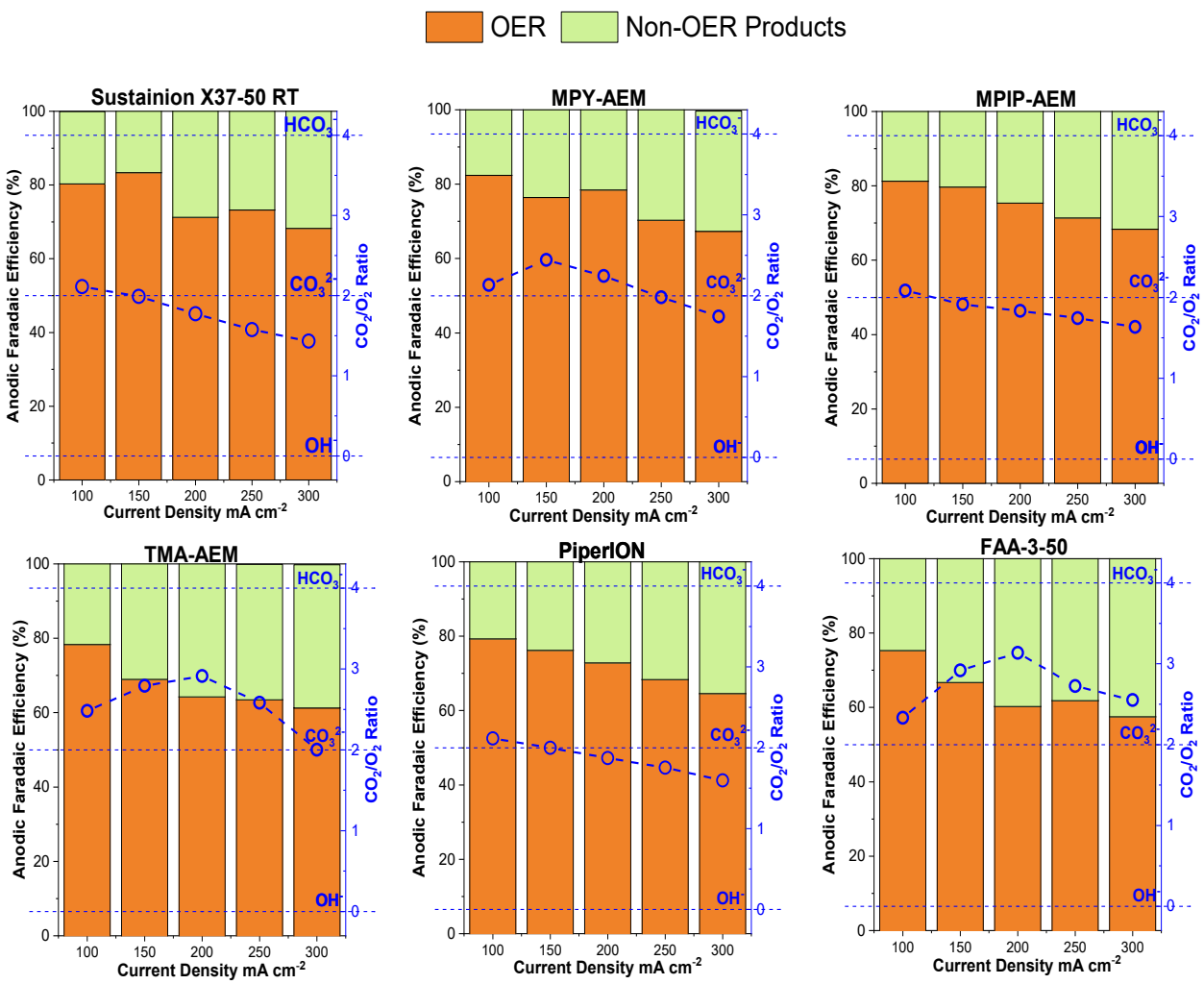

Figure S9 CO_2/O_2 ratio evolved over the anode as a function of total current density for different AEMs performing CO_2 electrolysis with Ag-electrocatalysts and 0.1 M $KHCO_3$

Water Transport across the AEM

Experimental set-up for these ex-situ measurements of the hydraulic water permeation were based on preliminary studies conducted by Duan et. al[8] and Luo et al.[9] for different ion-exchange membranes. By measuring the hydraulic water permeation flux (JHP) in terms of the pressure gradient in the cell, we can correlate the permeability using Equation S11.[10]

$$J_{HP} = \frac{k}{\mu\,\tau} \cdot \Delta P \cdot \frac{\rho_{H2O}}{M_{H2O}} \quad \textbf{(Eq. S11)}$$

where k is the permeability (cm^2), μ the water viscosity (mPa s), ΔP the pressure gradient (bar), τ the membrane thickness (μm).

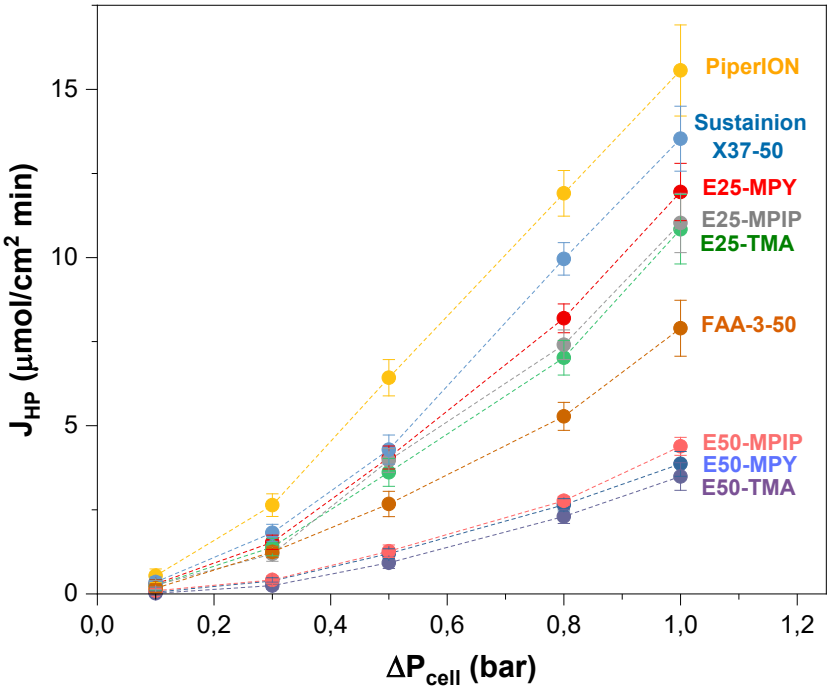

Figure S10 Hydraulic water permeation as function of pressure gradient for different AEMs. (E25 and E50 represents the thickness of the ETFE substrate in μm).

We estimate the permeability by calculating the slope of the curves from Figure S10, and such results are reported on Table S6.

Table S6 Permeability values for hydraulic permeation measurements

AEM	Permeability k (10^{16} cm^2)
MPY-25	2.85
MPY-50	1.38
PiperION	2.10
TMA-25	1.98
TMA-50	1.13
MPIP-25	2.52
MPIP-50	1.37
Sustainion X37-50	2.28
Fumasep FAA-3-50	1.16

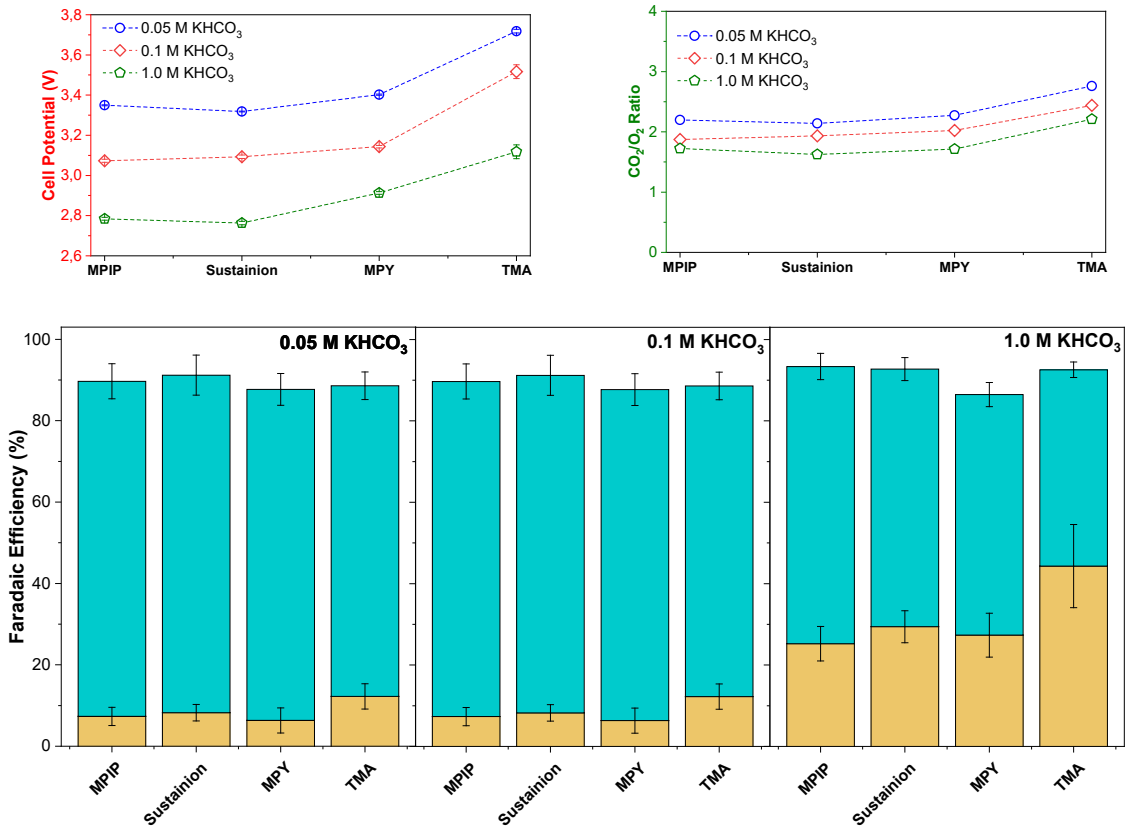

Figure S11 Product distribution, cell potential and CO_2/O_2 ratio using Ag-based electrocatalyst with different RG-AEM´s and commercial Sustainion X37-50 RT, varying the electrolyte concentrations (0.05-1 M $KHCO_3$) at total current density of 150 mA cm^{-2} The error bars in such represent the standard error of the mean of three independent measurements.

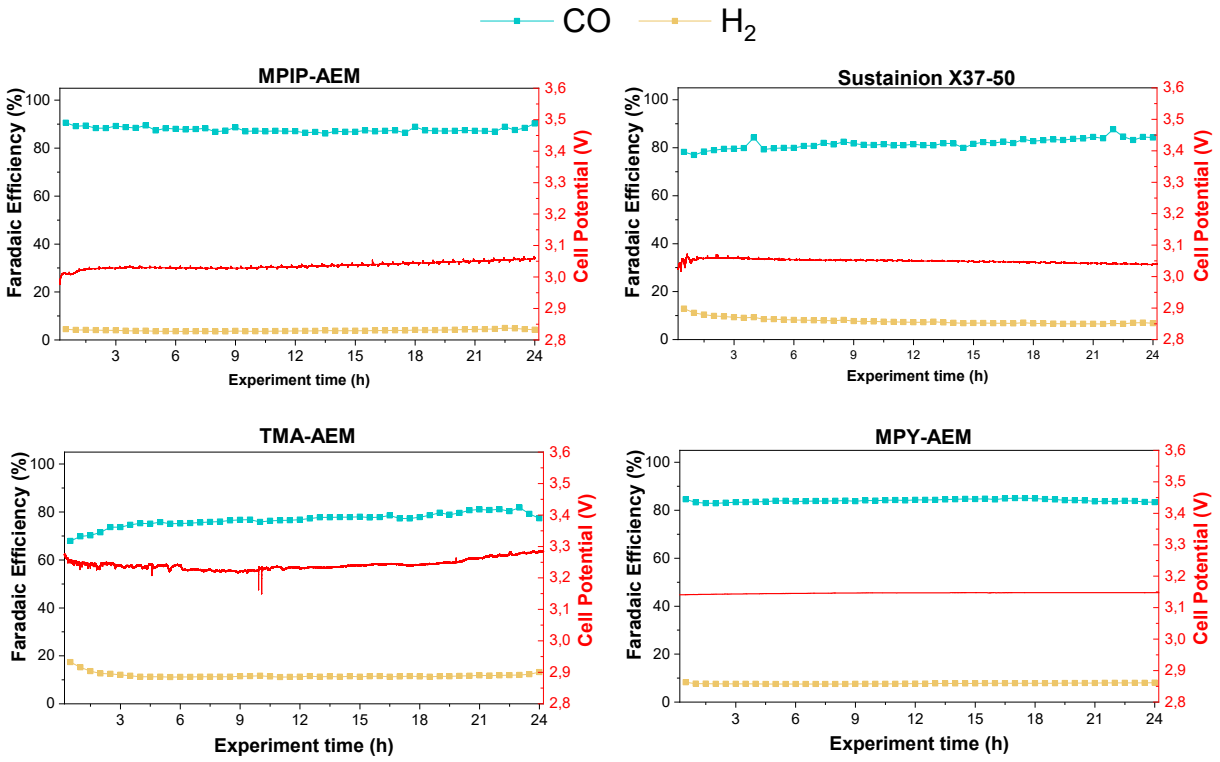

Figure S12 24h Stability-test for different AEMs at room temperature using 0.1 M $KHCO_3$ and Ag-based electrocatalyst. Experimental conditions used are described in the experiment section.

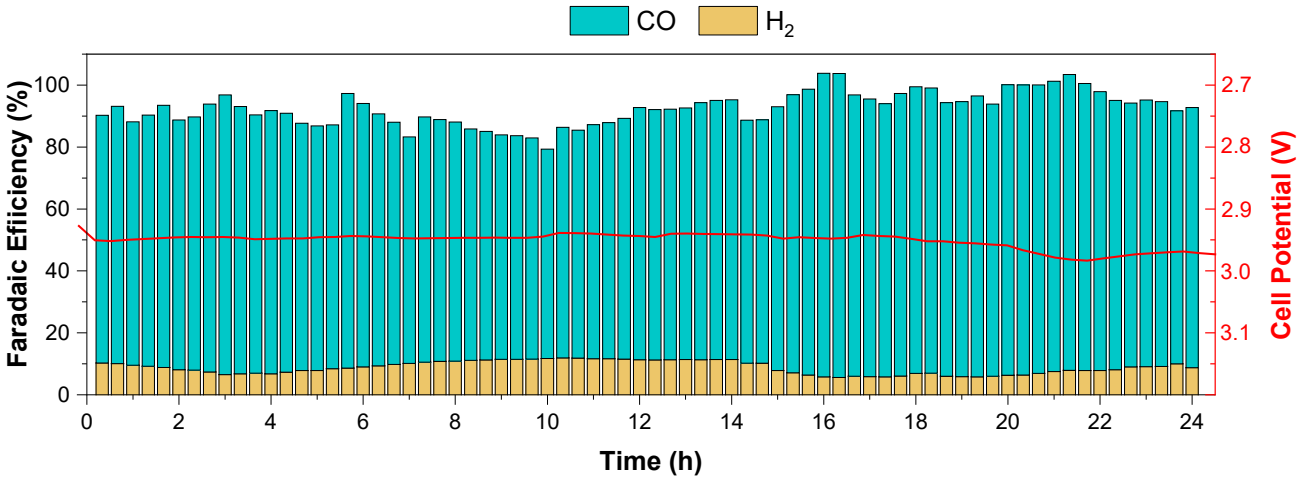

Figure S13 24h Stability-test of MPIP-AEM at 60°C using 0.1 M $KHCO_3$ and Ag-electrocatalyst at 150 mA cm^{-2}

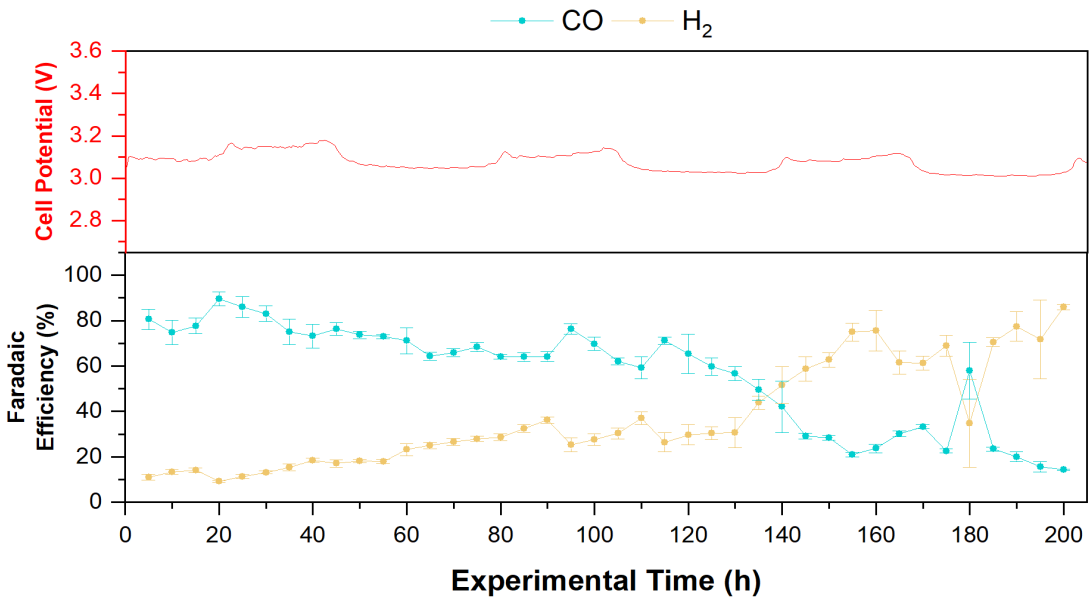

Figure S14 200 h stability test at room temperature using Sustainion X37-50 RT with 0.1 M $KHCO_3$ and Ag-based electrocatalyst.

References

(1) Henkensmeier, D.; Najibah, M.; Harms, C.; Žitka, J.; Hnát, J.; Bouzek, K. Overview: State-of-the Art Commercial Membranes for Anion Exchange Membrane Water Electrolysis. *Journal of Electrochemical Energy Conversion and Storage* **2021**, *18* (2). https://doi.org/10.1115/1.4047963.

(2) Ariono, D.; Khoiruddin; Subagjo; Wenten, I. G. Heterogeneous Structure and Its Effect on Properties and Electrochemical Behavior of Ion-Exchange Membrane. *Mater Res Express* **2017**, *4* (2). https://doi.org/10.1088/2053-1591/aa5cd4.

(3) Kutz, R. B.; Chen, Q.; Yang, H.; Sajjad, S. D.; Liu, Z.; Masel, I. R. Sustainion Imidazolium-Functionalized Polymers for Carbon Dioxide Electrolysis. *Energy Technology* **2017**, *5* (6), 929–936. https://doi.org/10.1002/ente.201600636.

(4) Lee, W. H.; Park, E. J.; Han, J.; Shin, D. W.; Kim, Y. S.; Bae, C. Poly(Terphenylene) Anion Exchange Membranes: The Effect of Backbone Structure on Morphology and Membrane Property. *ACS Macro Lett* **2017**, *6* (5), 566–570. https://doi.org/10.1021/acsmacrolett.7b00148.

(5) Gangrade, A. S.; Cassegrain, S.; Chandra Ghosh, P.; Holdcroft, S. Permselectivity of Ionene-Based, Aemion® Anion Exchange Membranes. *J Memb Sci* **2022**, *641* (August 2021), 119917. https://doi.org/10.1016/j.memsci.2021.119917.

(6) Wang, L.; Brink, J. J.; Liu, Y.; Herring, A. M.; Ponce-González, J.; Whelligan, D. K.; Varcoe, J. R. Non-Fluorinated Pre-Irradiation-Grafted (Peroxidated) LDPE-Based Anion-Exchange Membranes with High Performance and Stability. *Energy Environ Sci* **2017**, *10* (10), 2154–2167. https://doi.org/10.1039/c7ee02053h.

(7) Larrazábal, G. O.; Strøm-Hansen, P.; Heli, J. P.; Zeiter, K.; Therkildsen, K. T.; Chorkendorff, I.; Seger, B. Analysis of Mass Flows and Membrane Cross-over in CO_2 Reduction at High Current Densities in an MEA-Type Electrolyzer. *ACS Appl Mater Interfaces* **2019**, *11* (44), 41281–41288. https://doi.org/10.1021/acsami.9b13081.

(8) Duan, Q.; Wang, H.; Benziger, J. Transport of Liquid Water through Nafion Membranes. *J Memb Sci* **2012**, *392–393*, 88–94. https://doi.org/10.1016/j.memsci.2011.12.004.

(9) Luo, X.; Wright, A.; Weissbach, T.; Holdcroft, S. Water Permeation through Anion Exchange Membranes. *J Power Sources* **2018**, *375*, 442–451. https://doi.org/10.1016/j.jpowsour.2017.05.030.

(10) Garg, S.; Giron Rodriguez, C. A.; Rufford, T. E.; Varcoe, J. R.; Seger, B. How Membrane Characteristics Influence the Performance of CO_2 and CO Electrolysis. *Energy Environ Sc.* ***2022****, 15, 4400-4469*. https://doi.org/10.1039/d2ee01818g.

Appendix

Publications

Paper II
Insights into zero-gap CO_2 electrolyzer at elevated temperatures
Carlos A. Giron Rodriguez, Asger Barkholt Moss, Sahil Garg, Wanyu Deng, Ib Chorkendorff, and Brian Seger.
In preparation, 2023. *in appendix*

Insights into zero-gap CO_2 electrolyzers at elevated temperatures

Carlos A. Girón Rodriguez,[a] Asger Moss [a], Sahil Garg[a] , Wanyu Deng, [a] John.R Varcoe, Ib Chorkendorff[a] and Brian Seger[a]

[a]*Surface Physics and Catalysis (SURFCAT) Section, Department of Physics, Technical University of Denmark, 2800 Kgs. Lyngby, Denmark*

[b] *Department of Chemistry, University of Surrey, Guildford GU2 7XH, United Kingdom*

**Correspondence to: Brian Seger, Email: brse@fysik.dtu.dk*

Abstract

CO_2 electrolysis driven by renewable sources is a promising method for mitigating greenhouse gas emissions by converting CO2 into valuable feedstocks and storing renewable energy. Using gas diffusion electrodes (GDEs), membrane electrode assemblies (MEAs) can overcome the current limitations of aqueous-fed systems while bringing this technology to an economically competitive level. Many studies have been devoted to developing efficient catalyst materials and reactor designs in the last decade; however, operating conditions, such as temperature, have not been thoroughly examined. As temperature affects CO_2 electrolysis in a complex manner (simultaneous influences on CO_2 diffusivity, solubility, the ionic conductivity of the membrane, and the surface wettability of the GDE), a systematic investigation is necessary to determine temperature influences on product distribution.

In this study, we investigated the effects of temperature on CO_2 electrolysis of Cu-based GDEs in an MEA-based approach in a temperature range between room temperature and 80 C to enhance the selectivity of C_{2+} products and energy efficiency, while suppressing hydrogen evolution (HER) and AEM and GDE degradation. A robust temperature control and measurement system were developed for this investigation to establish guidelines for performing these electrocatalytic temperature measurements in a consistent and reproducible way. Results provide insight into how CO_2 diffusion, reaction kinetics, and enhanced CO_2 mass transport vary with temperature. Higher membrane ionic conductivity and better water management improved reaction rates and decreased cell voltages at higher temperatures. At temperatures above 60 °C, the experiments focused on selectivity and product crossover, setting up the optimal conditions for stable operation and higher faradaic efficiencies through carbon-based compounds.

Introduction

Electrochemical CO_2 reduction (CO_2R), powered by renewable energy sources, offers a sustainable alternative of converting CO_2 into chemicals and fuels.[1,2] Recently, it has been proven that CO_2 electrolysis using membrane electrode assemblies (MEAs) can achieve industrially relevant conditions with high C_{2+} selectivities, reducing mass-transfer resistances and ohmic losses inherent to liquid-fed CO_2R.[3–5] While most CO_2R research has been conducted under ambient conditions, commercial CO_2 electrolyzers should perform at elevated temperatures (>50 °C) due to the heat generated by overpotentials and resistive losses.[6] Additionally, studies on temperature dependence could provide insight into its role in the different electrochemical steps and identify optimal conditions for boosting the electrocatalytic performance.

Although the temperature rise improves the activity and lowers the cell potential, the intrinsic effect has not been fully understood. The lack of defined trends for CO_2R is caused by the complex interactions of numerous factors with temperature. Initially, temperature affects the CO_2 solubility, and diffusion coefficients, influencing mass transport.[7–9] Furthermore, it shifts the reaction environment, equilibrium potentials, and intermediate's adsorption equilibria, which can result in changes in the charge transfer and homogeneous reaction rates[9,10]. Moreover, it improves the ionic and membrane conductivity, reducing the ohmic and mass-transport overpotentials[11,12], and influences the water/liquid transport by increasing the electroosmotic flux and evaporation rates.[13] The effect of operating temperature on some reaction parameters and transport properties for CO_2R are shown in Figure 1a.

There have been few systematic investigations of the temperature impact on CO_2R, despite studies incorporating temperature-dependent experiments or computational models[12,14,15] (compiled data for different CO_2R studies at elevated temperatures is found in Figure 1b). The first fundamental study of temperature effects in CO_2R was conducted by Hori et al.[16], showing on Cu that CH_4 selectivity is favored at low temperatures (below ambient conditions), while CO, C_2H_4, and H_2 selectivities increase with temperature (up to 40 ^{O}C). Ahn et al. reported similar selectivity trends over Cu and -1.60 V vs. Ag/AgCl at the same operating temperatures, which they attributed to changes in CO_2 solubility and local pH caused by a higher buffer capacity at these conditions.[17] Recently, a study by Vos and Koper examined the effects of temperature, cation identity, and electrolyte on Au-electrocatalyst, finding that these coupled factors influence activity, product selectivity, and activation energy.[11]

Additionally, the influence of temperature on CO_2R has been evaluated using GDEs. For example, Lowe et al.[7] examined how the temperature impacts the formate formation over Sn-GDEs using a flow cell. They found an increase in formate selectivity (FE_{HCOO^-}= 80%) and current density (up to 1000 mA cm^{-2}) from

room temperature to 50 °C, while hydrogen evolution reaction (HER) dominated at 70 °C due to the interplay effects between the solubility and diffusion rates. On the other hand, Jeng and Jiao studied the temperature effect on CO_2 conversion over Ag-GDE.18, At 60 °C, they observed an increase in the CO_2 single-pass conversion due to an enhancement of the CO_2R and homogeneous reactions at elevated temperatures. Alternatively, Dufek et al. observed on Ag-electrocatalyst a decrease in cell potential by increasing the temperature, with enhanced CO selectivity at 35 °C but lowered at 70 °C due to limited CO_2 mass transport.[19] Other studies conducted by Endrodi et al.[15] over PiperION membranes or by Garcia de Arquer et al.[20], have evaluated the temperature effects using different ionomers, or membranes, on the catalyst stability.

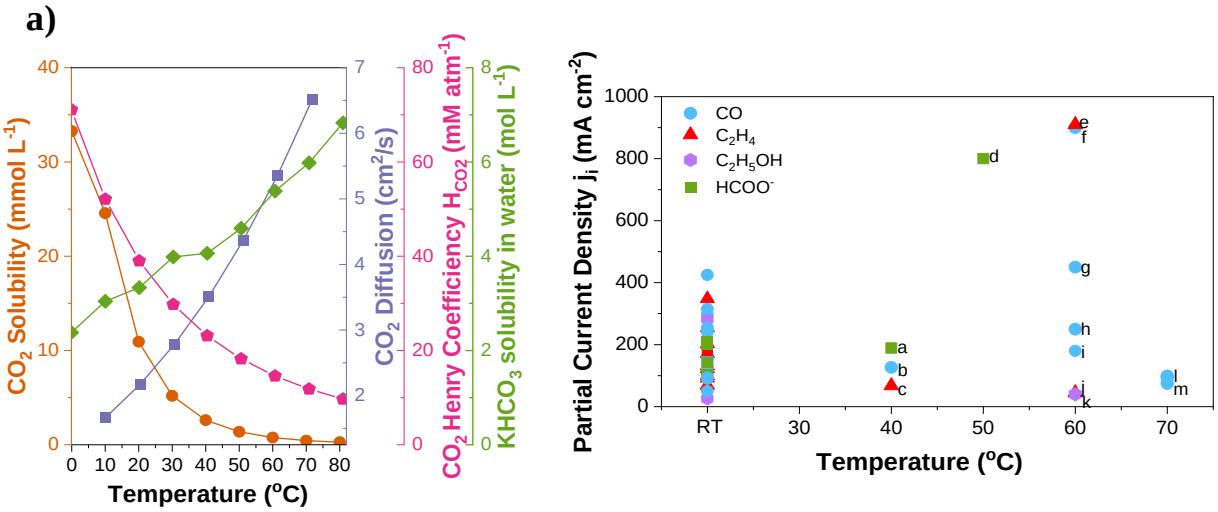

Figure 1. a) Transport and kinetics factor's temperature dependency on CO_2R (CO_2 solubility, CO_2 diffusion, salt solubility, and Henry's constant).[21] b) Summary of studies for CO_2R performed at elevated temperatures reported in the literature. (See Table S1 for the detailed information of the data)

When investigating temperature effects on CO_2 electrolysis, it is crucial to ensure uniform heating and temperature control to avoid inaccurate selectivity and water management trends. For example, a lack of uniform heating might change the temperature across the cell and reactor components, affecting the water supply and distribution (from humidified CO_2 or anolyte) into the system.[12] Such water imbalance can alter membrane hydration and conductivity, leading to changes in cathode overpotentials and ionic species diffusion or GDE water content, altering the water consumption or electrowetting.[12,22,23] Therefore, it is essential to measure and control the temperatures systematically to evaluate their actual effects on CO_2R.

Herein, we conducted systematic studies on temperature effects on CO_2 electrolysis of Cu-based GDEs using MEAs. We conducted electrochemical measurements, partial pressure experiments, and in-situ ATR-SEIRAS studies to evaluate how diffusion, solubility, kinetics, and mass transport vary with temperature

and influence performance. Our results showed an enhanced selectivity towards carbon-derived products, higher activity, and enhanced stability by increasing the temperature due to the convoluted effects of multiple transport properties and reaction conditions. Lastly, we assessed the effects of different heating methods and demonstrated the importance of proper heating on CO_2R.

Experimental Section

Materials

Ultra-pure water (UPW) used throughout this study was generated using a purity water purification system (resistivity = 18.2 MΩ cm). $KHCO_3$ (Sigma-Aldrich 99.995% Trace metal basis) and $CsHCO_3$ (Sigma-Aldrich 99.995% Trace metal basis) were used for the electrolyte preparation or membrane activation before the experimental tests. We purchased $HAuCl_4$ (98.0%), NH_4Cl (99.0%), Na_2SO_3 $Na_2S_2O_3{\cdot}5H_2O$, and NaOH from Alfa Aesar (China) Chemical Co., Ltd, AR to prepare the Au-films for ATR-SEIRAS.

Electrode preparation and electrolyzer configuration

Zero-gap MEA experiments

The cathode GDEs were prepared by sputtering a 150 nm layer of 6N Cu onto a commercial GDL (Sigracet 39BB from Fuel Cell store) in a vacuum environment (10^{-6} torr) at a deposition rate of ~ 1 Å s^{-1} under 10 sccm Ar, total pressure of 2 mTorr and room temperature. The anode-GDE corresponded to a commercial IrO_2-coated carbon paper (Dioxide Materials).

The electrochemical experiments were performed on a commercial electrolyzer (Dioxide Materials, grade 2 titanium serpentine flow field for the anode, and stainless steel for the cathode side). The assembly consisted of placing a fresh anion-exchange membrane (AEM, ETFE-MPIP from the University of Surrey with a total area of 7.4 cm^2) between the cathode-GDE (area: 2.25 cm^2) and anode (area: 4 cm^2). The AEMs were presoaked and activated in 1 M $KHCO_3$ for 24 hours and then washed with deionized water. PFA gaskets further sandwiched the MEA device, which helped prevent electrolyte leakage and potential short-circuiting. Finally, the system was mechanically pressed, using cell bolts fastened with a torque of 3 Nm to guarantee sufficient compression.

ATR-SEIRAS experiments

We prepared Cu-based electrodes over silicon wafers in a two-step process by chemically depositing an Au thin film and sputtering a 100 nm Cu layer, as reported before in the literature.[24] The Au film (60 nm) was used to increase the intensity of the infrared signals during measurements.

Au film electrodes were deposited directly on a Si prism used *in situ for* ATR-SEIRAS, following the proposed methodology by Miyake et al.[25] Initially, the Si substrate was polished using a polishing machine (YUZHOU PG-2B, 650 r/min) with 0.05 m Al_2O_3 polishing powder for 10 minutes and further immersed in Piranha solution (3:1 volume ratio H_2SO_4:H_2O_2) for 1 hour to clean the organic contaminants before deposition. Then, to improve the adhesion of Au film, we immersed the reflecting plane of the crystal in 40% NH_4F solution for approximately two minutes to remove the oxide layer and generate a hydrogen-terminated surface. The reflecting plane of Si crystal was then immersed in a mixture of 1 mL of 2% HF and 3 mL of Au plating solution containing 0.1050 g NaOH, 0.2276 g $HAuCl_4$, 0.1337 g NH_4Cl, 0.9845 g Na_2SO_3, and 0.6205 g $Na_2S_2O_3 \cdot 5H_2O$ at a constant volume of 100 mL for 4 minutes at 50 °C. Finally, the Si crystal was cleaned with pure water before the Cu deposition.

IrO_2/C GDE, an Ag/AgCl electrode, and Cu/Au films on the Si prism were used as the counter, reference, and working electrodes. In addition, a customized H-type electrochemical cell, separated with a bipolar membrane (Fumasep FBM from Fuel Cell Store), was used to accommodate the Si prism and avoid cross-contamination from the counter electrode.

Electrode Characterization

A scanning electron microscope (SEM) FEI Quanta 200 FEG instrument was used to characterize the electrode, operating at 15 kV in secondary electron mode. The catalyst's surface was further characterized by X-ray photoelectron spectroscopy (XPS) with a binding energy range of 0−1400 eV and an analyzer pass energy of 100 eV. For data analysis, we implemented the Probe instrument (Thermo FisherScientific), equipped with a hemispherical analyzer.

Electrochemical System

For the controlled-temperature experiments in MEA, CO_2 (AGA, purity 4.5) was supplied to the cathode flow fields with a flow rate of 40 sccm using a volumetric flow controller (Red-y from Voegtlin) and further humidified by sparging into a container filled with Millipore water. 0.1 M electrolyte reservoir was fed to the anode and recirculated continuously using a diaphragm pump (KNF) with a flow rate of around 10 mL/min. Gas products on the anolyte were measured by purging Ar (at 30 sccm) for carrying the gases for further analysis. A potentiostat (Bio-Logic VSP 300 with booster unit) operated in galvanostatic mode was the power source, and the cell potentials were reported without any *IR* corrections.

The cell and all the reaction components were placed in a heating oven with a PSU/box interfaced coupled to Raspberry Pi as a PID controller. A 230 heater (GPIO pin) was connected to thermocouples for temperature measurement, and a homemade Python program was developed to control and regulate the

reaction system's temperature. Thermocouples were placed in the electrochemical cell (cathode and anode flow fields), the humidifier, inlet and outlet streams, the heating plates, and the electrolyte reservoirs.

Experiments using different heating methods were achieved by preheating the anolyte with a heating plate coupled with a temperature controller or heating rods attached directly to the electrolyzer and controlled with a homemade temperature controller, simulating the effect of the commercial heating tape. Detailed Information on the heating system is described in the Supporting Information (SI).

For ATR-SEIRAS experiments, 0.1 M $KHCO_3$ aqueous solution was CO-saturated and preheated to the desired temperatures (20-80 °C) to be further filled in the catholyte and anolyte chambers. A mixture of CO/Ar (MKS flow controller) was fed to the cathode compartment at rates between 5-10 sccm depending on the operational temperature, varying the partial pressure to keep the CO concentration in the catholyte constant. The electrochemical cell was connected to a Bruker spectrometer equipped with an MCT detector, and a Pike Technologies VeeMAX III ATR accessory was employed for the electrochemical ATR-SEIRAS. All spectra were collected with a 4 cm^{-1} resolution and 16 scans. The reference spectrum was measured at -0.9 V vs. Ag/AgCl in Ar-saturated $KHCO_3$. In addition, experiments were conducted using chronoamperometry at potentials between -0.9 to -1.5 V vs. Ag/AgCl using potentiostat Bio-Logic VSP 200 at different temperatures, and the CO peak in the IR spectra was detected around 2050 cm^{-1}.

CO_2R product analysis

The outlet cathode stream was measured continuously using a volumetric flow meter (MesaLabs, Defender 530+). The products in the gas sample were determined with a gas chromatograph (PerkinElmer Clarus 590) coupled with a thermal conductivity detector (TCD), equipped with the Molecular Sieve 13x, and HayeSep Q packed column using Ar (10 mL/min) as the carrier gas. Liquid samples from the cathode were collected after the CO_2-outlet line using a condensation unit and cold trap to measure the vapor-phase liquid products. Detection of liquid products from the cathode and the anolyte were quantified using HPLC (Agilent 1260 Infinity II) with 5 mM H_2SO_4 as the mobile phase. Data analysis of the liquid products includes the cathode and the anode products. A description of the calculation methods for the Faradaic efficiency, partial current density, and calibration can be found in SI.

Results and Discussions

Electrochemical Tests

Temperature effect on the cathode activity

The influence of temperature on cathode activity was assessed by recording polarization curves via LSV (Figure 2a) and chronoamperometry measurements (Figure S3) using 0.1 M $KHCO_3$. Polarization curves show that the temperature has a pronounced effect on the total current density, increasing 3.0-fold at 80°C compared to ambient at the same cell potentials, similar to Lowe et al.[7] and Vos and Koper's observations[9]. The change in the cathode activity is most likely the result of improved CO_2R kinetics and mass transport at higher temperatures. While the increase in temperature decreases CO_2 solubility, it improves the diffusion coefficients and electrochemical/homogeneous reaction rates. It is possible that the reduced CO_2 solubility caused by the temperature rise might not offset the effects of the other factors, explaining why the cathode activity is enhanced (see further sections for a detailed analysis). Moreover, we calculated the thermodynamic equilibrium potential for multiple CO_2R products, which revealed a slight negative shift at higher temperatures (~20 mV for CO_2R to CO and ~40 mV for major C_{2+} from 20°C to 80°C). These findings indicate that significant effects are primarily determined by kinetics and mass transport rather than changes in thermodynamic potentials (see SI).

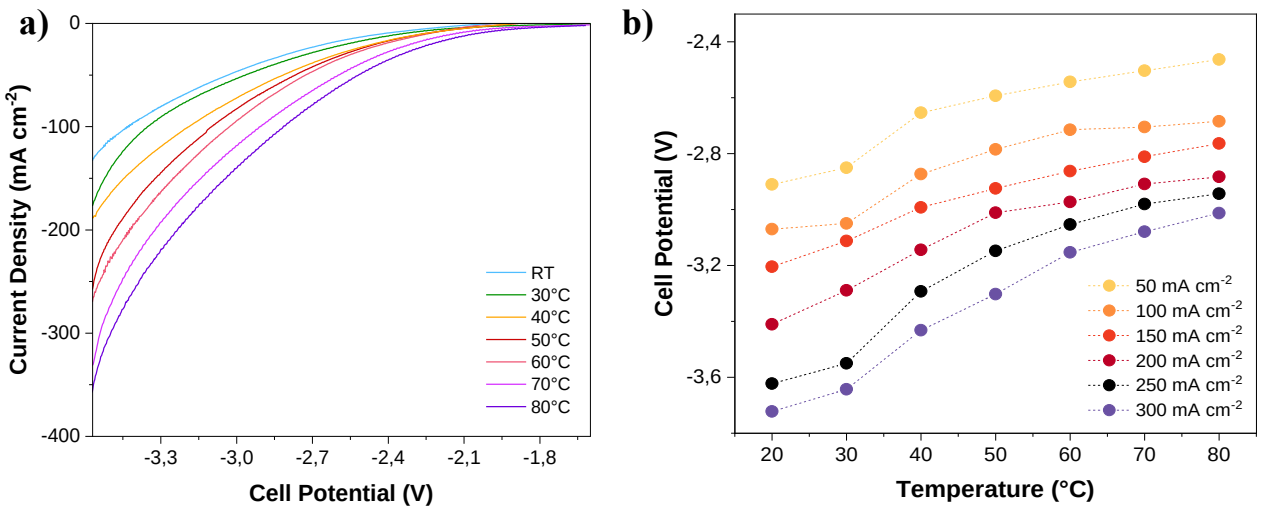

Figure 2. a) LSV Measurements for CO_2R at different potentials and temperatures b) Cell potential profiles as a function of the temperature and current density

In addition, Figure 2a shows that CO_2 mass transport is not a major factor at low cell potentials, even at elevated temperatures. This indicates that kinetic mechanisms play a greater role under such conditions.

Nonetheless, there is a difference in cathode activity towards carbon products at higher cell potentials independent of the operating temperature. At current densities above 300 mA cm^{-2}, we observed an increase in activity, which was not directly related to enhanced CO_2R activity, but rather an improved HER (Figure S4). Selectivity changes may be attributed to limited CO_2 transport to active sites (CO_2 depletion) or due to flooding caused by operating above the limiting current density regime. We expected no significant difference in the GDE electrowetting before our chronopotentiometry measurements (LSV back-scanning and capacitance measurements did not reveal any noticeable changes). However, we observed a significant increase in cathode activity following electrolysis (Figure S5), which can be attributed to the increase in catalyst surface area after flooding, resulting in a higher current density (at the same potential ranges) as more active catalyst sites are present.[26]

Overall, elevating the temperature lessened the cell potential (Figure 2B) and ohmic resistances (Figure S6). For all our tested current densities, the cell potential decreased as we increased the temperature (e.g., 500 mV reduction from ambient to 80°C at 200 mA cm^{-2}). The drop in voltage and ohmic resistance can be correlated with a higher cathode activity and ionic conductivity across the membrane (Figure S7)[27]. However, comparing our results of the current interrupt (Figure S6) and impedance spectrum (Figure S8), we determined that the high-frequency resistance (HFR) decreased by less than 0.6 Ω cm^2 when the temperature was elevated, resulting in only 60 mV voltage reduction. Thus, it can be deduced that the overall cell voltage change was primarily caused by reaction kinetics improvements rather than changes in ionic conductivity.

Temperature effect on the product distribution

We conducted chronopotentiometry (Figure 3) and chronoamperometry (Figure S9) measurements to determine how temperature affects product distribution. Our experiments at temperatures below 50°C showed no differences in product selectivity compared to those at room temperature. There were no significant changes in the faradaic efficiency of CO and C_{2+} while increasing temperature from ambient conditions to 40 °C (e.g., FE_{CO}=15% and C_{2+}=43% at room temperature compared to FE_{CO}=17% and C_{2+}=47% at 40°C for 200 mA cm^{-2}). However, when the temperature is raised from 20°C to 50°C, the CO selectivity increases considerably with faradaic efficiencies above 40% for all the measured current densities. The shift in selectivity towards CO may be attributed to temperature-dependent CO_2R kinetics and faster desorption from the surface (as shown in the ATR-SEIRAS experiments) over the CO coupling to C_{2+}. On the other hand, liquid products like ethanol also presented a higher selectivity at elevated temperatures, as the selectivity improved from 12% at 30°C to 21% operating at 80°C and 300 mA cm^{-2}. Surprisingly, the ethanol selectivity drops between 60°C and 70°C, which we attributed to enhanced water evaporation into the outlet stream.

Furthermore, some selectivity trends between C_1 and C_{2+} products are observed as a function of temperature. At current densities below 100 mA cm^{-2}, the faradaic efficiency ratios between C_{2+}/C_1 decrease with increasing temperature (Figure S10). However, at current densities above 100 mA cm^{-2}, a maximum C_{2+}/C_1 ratio is reached at 40°C, while at 60°C, the ratio reaches its lowest value (again, as a side effect of improved CO selectivity). The variations in product distribution prove the temperature dependence on the electrochemical reaction pathways, as temperature influences the thermodynamic potentials, the apparent activation energies (Arrhenius equation), and overpotentials (Butler-Volmer equation). Although increasing the temperature is known to enhance the selectivity of products with higher activation energies or transfer coefficients (e.g., ethanol or n-propanol), this conclusion is not always correct.[9,10,13] For example, HER's apparent activation energy is greater than those associated with CO_2R products over Cu.[10] If this were our case, we would have detected HER enhancement because of the temperature. However, we did not observe the such trend, as the HER mechanism has an unexpected dependency on mass transport and an influence on water transport, which may surpass its dependency on activation energy. [28,29]

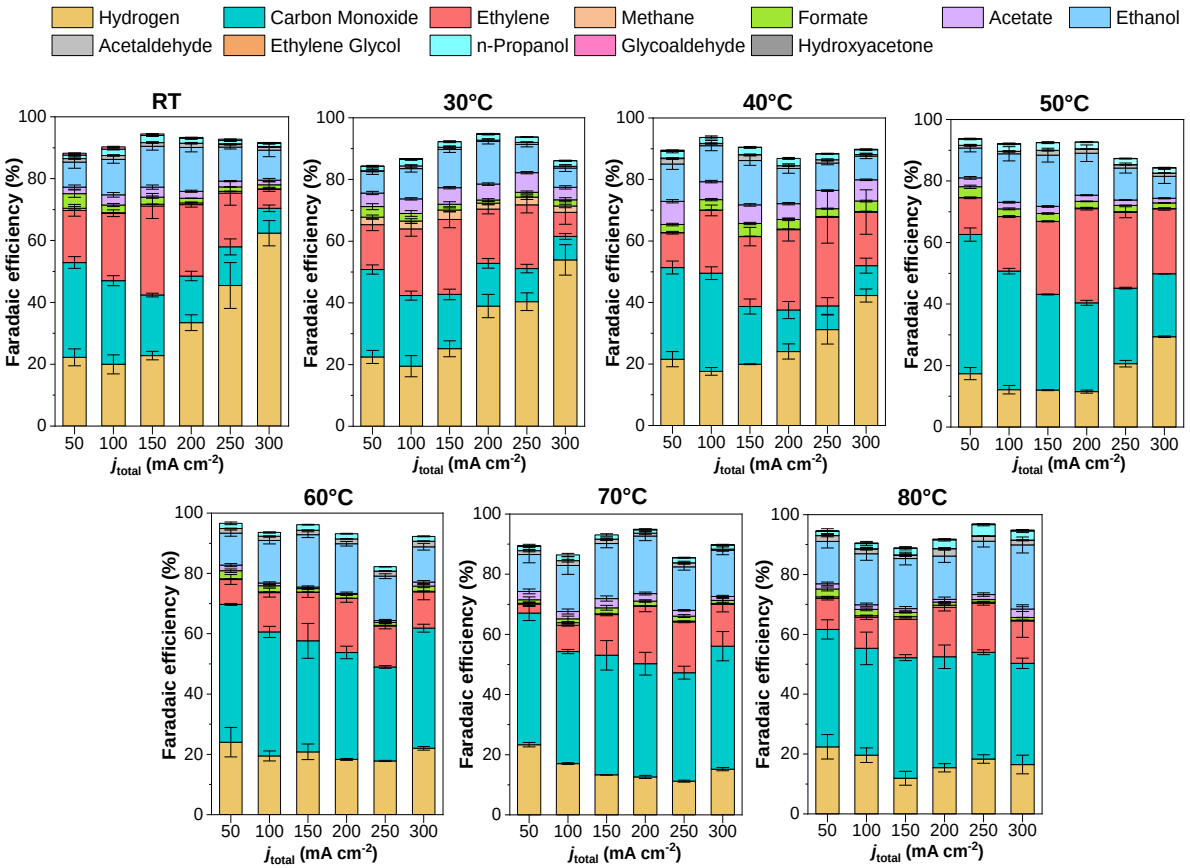

Figure 3. The product distribution of Cu-based electrocatalysis for CO_2R under different temperatures and current densities (Experimental Conditions: CO_2 flow rate 40 sccm, 0.1 M $KHCO_3$ as anolyte, Error bars represent the standard error of the mean for the measurements at each different conditions).

Accordingly, our hydrogen selectivity exhibits an exciting trend. As expected, performance at temperatures below 40°C was hampered by electrode flooding or lowered diffusion coefficients that did not compensate for CO_2 depletion. However, in our system, HER decreased beyond 50°C, indicating that HER is not primarily determined by CO_2 mass transport limitations but by ionomer conductivity or water management (see further section focused on temperature effect on the CO_2 mass transport).

In an MEA, the electroosmotic drag coefficients and AEM hydration increase with temperature, affecting the water uptake and the ionomer´s water content.[30,31] Therefore, a lower water activity at the cathode is anticipated due to increased water consumption from charge-transfer reactions and electroosmotic flux towards the anode.[13,30] This water drag to the anode might be beneficial, as it reduces the water penetration into the GDE and flooding. However, a water imbalance across the membrane could also be caused, as water at the anode is already in equilibrium with the liquid feed, favoring back-diffusion to the cathode. Considering the influence on the temperature in multiple transport properties and mechanisms, water management across the membrane may be difficult to predict in an MEA system due to its transient nature and dependence on the AEM properties and the cathode activity.[31–33]

In addition, the water content in the humidified stream may have an effect since temperature affects the water content and permeability of the humidified reactant gas (vapor vs. liquid feed). According to Garg et al., assuming 100% relative humidity (RH), 3% mol H_2O is present at 25 °C compared to 43% mol H_2O at 80°C.[32] Consequently, both water and CO_2 concentrations in humidified gases will be influenced by temperature. Nevertheless, our measurements varying the RH did not show any effect on the distribution of the product, indicating that the improved CO_2 diffusion at higher temperatures provides sufficient CO_2 concentration at the surface (Figure S11). RH effect is primarily detected through longer-term experiments by observing a decline in membrane conductivity as its hydration decreases (Figure S12).

Alternatively, a temperature rise can affect the homogeneous reaction rates (see SI Note 3), which can result in favoring the salt precipitation as CO_2 is starved in the electrolyzer. Therefore, carbonate anions cannot be formed, resulting in the predominance of OH^- and a decrease in the cell potential.[34] While the statement is true since membranes are most conducive in their OH^- forms, the analysis of the anodic CO_2/O_2 discharge did not show the switch to OH^- transfer as the majority ion carrier even at higher current densities (Figure S13). Ultimately, we believe this effect can be explained by an increased kinetics of the charge-transfer reactions that consume the OH^- before its transfer across the AEM. In addition, we observed that the salting-out effect was delayed while performing high-temperature experiments, serving as an indicator of enhanced stability (Figure S14).[35]

In terms of product crossover, a temperature rise leads to a lower crossover of volatile compounds through the AEM, resulting in higher concentrations at the cathode.[36] While those products (e.g., alcohols) are predicted to cross the GDE via condensation/evaporation mechanisms, most liquid products generated at the cathode tend to migrate to the anode, where they might be oxidized (Figure S14). Our results show a linear relationship between temperature rise and decrease in crossover ratio, as we favored ethanol transport through the GDE by enhancing evaporation over diffusion or electroosmotic drag (Figure S15). Negative charge compounds do not alter their crossover rate, as they are affected primarily by electromigration across AEM (Figure S14).[37] Additionally, operation at temperatures higher than 60 °C is likely to reduce the selectivity of compounds like formate and acetate since we may also increase the oxidation reaction rates at the anode. Control experiments adding potassium formate and acetate to the anode showed that oxidation towards CO_2 is favored at higher temperatures (Figure S16).

Temperature effect on CO_2 utilization and mass transport

Temperature directly impacts CO_2 mass transport since the concentration of CO_2 decreases at higher temperatures (Figure 1b). Therefore, we varied the partial pressures of CO_2 (p_{CO2}) using Ar at different current densities and temperatures, keeping constant the CO_2 concentration, to predict temperature's contribution to the CO_2 mass transport and utilization (Figure 4a). We adjusted the CO_2/Ar ratio for all experiments at the measured temperatures to match the same CO_2 concentration (at 1 bar and 80 °C) using Henry's law (Table S4 contains calculations of Henry's constant and CO_2 concentration).

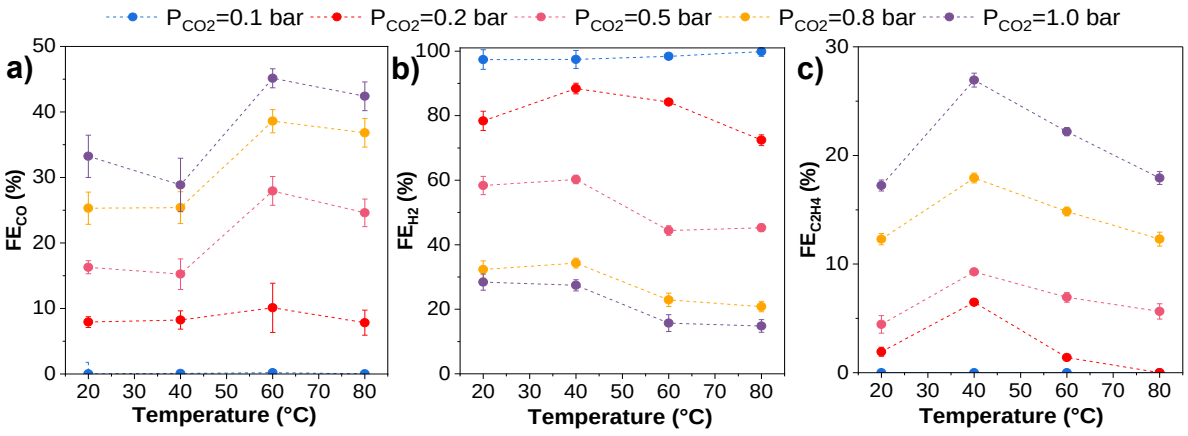

Figure 4. Effect of the CO_2 partial pressure on the faradaic efficiency of gas products. a) CO, b) H_2, and c) C_2H_4. Experiments were conducted at 200 mA cm^{-2}

While operating at p_{CO2} and temperatures above 0.5 bar and 60°C, we found higher selectivities toward carbon-derived products with lower HER. We observed that temperature effects on mass transport and

diffusion overrode its effects on CO_2 concentration, since we did not observe significant differences at lower CO_2 partial pressures (>0.5 bar), indicating that a decreased CO_2 concentration may not be a limiting factor for CO_2R at high temperatures. Additionally, we observed that HER selectivity was not significantly influenced by temperature when p_{CO2} was below 0.5 bar, as CO_2 was depleted on the catalyst surface. In terms of product selectivity, gas product selectivity (CO and C_2H_4) decreased with a reduction in p_{CO2}, as previously reported in the literature (FE_{C2H4}=26% at p_{CO2}=1bar vs. FE_{C2H4} =4% at p_{CO2}=0.2 bar).[38] FE_{C2H4} and FE_{CO} decrease linearly as sharply as HER increases, showing that both mechanisms are dependent.[39] Additional studies coupling the effects on partial pressure and temperature with variations in electrolyte concentration and the cation (K^+ vs. Cs^+) did not show any differences in the observed trend (Figure S17).

We also evaluated the temperature effects on CO_2 mass transport using a simplified version of the "thin film flooded agglomeration model" to calculate the limiting current density and correlate the observed selectivity trends assuming HER would be the dominant mechanism under CO_2-depleted conditions.[40–42] If the CO_2 drops to zero in the center of the agglomerate, we can correlate the partial current density (jH_2) and the c_{CO2} using first Fick's law and Faraday's law (Equation 1).

$$j_{H2} = \frac{D_{eff,CO2}(T)}{r} \cdot c_{CO2}(T) \cdot F \cdot z \qquad (1)$$

Where $D_{eff,CO2}$ corresponds to the effective diffusion, r the agglomerate radius, F the Faraday's constant, and z the number of electrons of the charge transfer reaction.

A detailed description of the model and the calculation of the CO_2 effective diffusion and dissolved concentrations are estimated from empirical equations according to Garcia de Arquer et al.[43] and Vos and Koper[9] and reported in the Supporting Information (Table S5). While this method is a rough estimation of the limiting current density (as assumptions on the agglomerate radius and simplified solutions of the ODE systems were made), it provides some correlation between the HER selectivity and activity. By varying the temperature from ambient conditions to 80°C, we observed a rise in the limiting current density from 240 mA cm^{-2} to 300 mA cm^{-2}. Thus, we observed that temperature enhances the CO_2 transport, as we predict that even at higher current densities, we would not operate at limiting current density regimes (e.g., the dominant HER (60%) at room temperature dropped dramatically to 15% at 80°C under 300 mA cm^2).

In addition, we correlated the CO_2 mass transport, electrowetting, and electrode flooding by the capacitance measurements via double-layer capacitance (DLC). Previous control experiments were done at room temperature after assuming the proper electrowetting, showing no significant variations in the capacitance measurements before the experiments (Figures S5 and S18). In GDE, the degree of wetting is an essential

parameter since it determines the amount of catalyst in contact with the electrolyte.[26] Therefore, we investigated the effect of temperature on the electrode flooding by measuring the DLC after electrolysis at each current density. The results in Figure 5 showed a plateau trend on the DLC at high temperatures, related to the inversely dropping of viscosity and surface tension of water as less water penetrated through the catalyst layer.[41] On the other hand, an increase in the DLC is observed for all the different measured current densities and lower temperatures, correlated with the increase in HER.

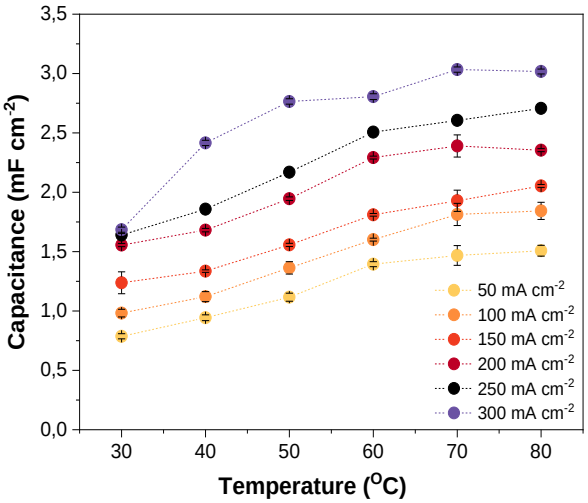

Figure 5. Tracking the electrode flooding by DLC measurements as a function of temperature and current density

Fundamental studies using the ATR-SEIRAS

To further understand the effect of temperature on the CO adsorption and binding strength on the Cu surface, we performed ATR-SEIRAS for COR instead of CO_2R, as CO is the primary product at high temperatures and a common intermediate for C_{2+} products. Figure 6 represents in-situ ATR-SEIRA spectra for CO signal (2050 cm^{-1}) at different potentials vs. RHE and temperatures in 0.1 M $KHCO_3$ (full SEIRAS spectra are found in Figure S19). Independent of the operational temperature, we observed a decrease in the CO peak intensity and position with more cathodic potentials, as previously reported in the literature.[44,45] These intensities and peak shift variations might be related to chemical effects due to bonding changes between the adsorbed CO and surface or the Stark effect due to the interaction between the dipoles with the electric field at the interface.[46] However, those effects appeared to be enhanced when the temperature was raised, as both the intensity area and stretching frequency of the CO peak decreased at all measured cathodic potentials.

While the CO coverage wasn't quantified, we estimated the relative concentration at the surface using the intensity and area of the CO peak (Table S6). Our ATR-SEIRAS spectra don't vary significantly between

ambient conditions and 40°C at low potentials, as peaks don't decrease their intensity, indicating a saturated CO concentration at the surface. However, experiments at 60°C showed a significant decrease in peak intensity because of the temperature effect on weakening the binding strength of CO with the surface, favoring the CO desorption, and decreasing the CO concentration at the surface for all potentials.[13] This pattern is consistent with our observation of increased CO selectivity at higher temperatures, as shown in Figure 3, but further studies are required to assess the temperature effect on the CO binding strength and coverage on Cu.

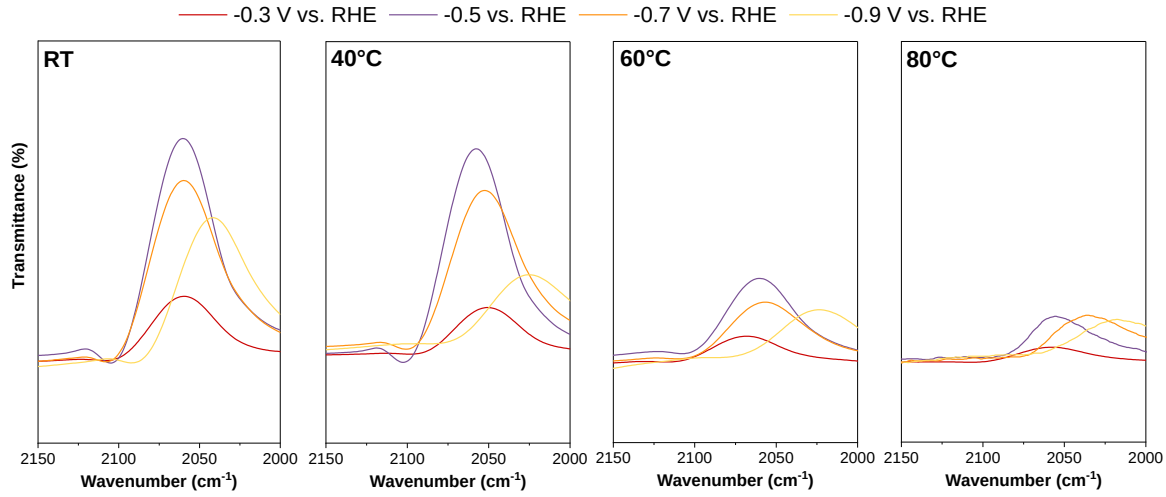

Figure 6. ATR-SEIRAS CO adsorption peak for COR at different potentials and temperatures

Effect of the heating method on the CO_2R performance

The lack of a standardized protocol and method for determining proper electrolyzer heating makes comparing studies performing measurements at high temperatures challenging. Therefore, we wanted to analyze the impact of the cell heating method on trends regarding product distribution. For these experiments, we implemented two additional methods for making the heating. With the first method, only the electrolyte reservoir was heated using a heating plate, and the temperature was controlled by measuring the temperature with a thermocouple (other elements of the reaction system are kept in the atmosphere). For the second method, we used hearing rods directly connected to the cathode and anode's flow field. The temperature was controlled with a simple RID control box by measuring the cell's temperature with a thermocouple. We tried to replicate a similar phenomenon obtained from a commercial heating plate for CO_2 electrolyzers. The results of these measurements are shown in Figure 7. We were interested in performing the experiments at elevated temperatures (>60°C) as the selectivity trends are more visible under those conditions.

Our results showed differences in the product distribution between our three heating methods. While slight differences can be appreciated between the direct cell heating method and the use of our heating box, significant variations are found while comparing those obtained from just heating the electrolyte. While it seemed that the C_{2+} selectivity improved by the effect of temperature, we found out that the actual temperature of the cell was far from the 60 °C initially expected (the actual values for the temperatures for the measured 60°C were around 28°C, 70°C was about 32°C and 80°C was about 35°C). Such discrepancies between the measured temperature in the electrolyte and the cell one caused an altogether product distribution trend, remarking the importance of how to heat the cell uniformly. On the other hand, differences in the Faradaic efficiency in HER and CO between the "cell heating" method and our heating box could be explained by the variations in the CO_2-humidified cell and the anolyte feed. The anolyte and the humidifier weren't heated in the cell heating scenario. We assumed that it might take some time for them to reach the cell temperature, generating temperature gradients that could influence the water management and, therefore, the selectivity.

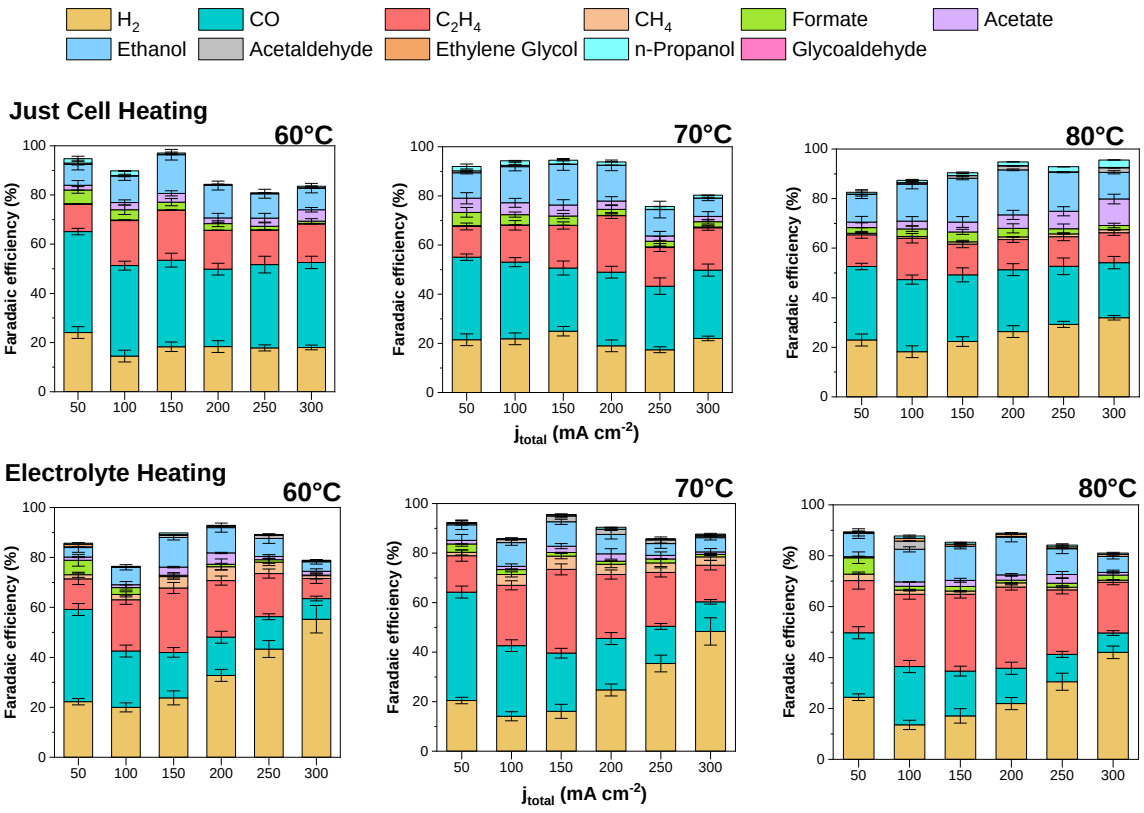

Figure 7. Effect of the cell heating in the product distribution using two different methods at elevated temperatures Experimental Conditions: CO_2 flow rate 40 mL sccm, 0.1 M $KHCO_3$ as anolyte)

On the other hand, we need to consider that CO_2 electrolyzers generate heat from the charge transfer and buffer or electrical resistances (resistive heating). Corral et al. described that temperature changes inside

the electrolyzer alter the CO_2 concentration at the gas-liquid interface, favoring the CO_2 mass transport limitations.[47] By measuring the temperature near the cathode surface, they observed a temperature increase of 7°C under 300 mA cm^{-2} and 24°C at 500 mA cm-^{2} for CO_2R, attributed these changes to the released heat by exothermic reactions at the surface.

Considering the possible effects of resistive heating on our performance, we used a customized MEA cell (Figure S19) that allows the placement of a thermocouple close to the GDE for a more precise measurement of temperature in the cell. Comparing results at 50 mA cm^{-2} vs. 300 mA cm^{-2}, we observed just a temperature rise of 3 °C inside the cathode (Figure S20) between experiments, matching the predicted increase estimated by modeling and showing a uniform temperature distribution in the cell. Therefore, temperature changes by resistive heating won't be significant in the system. Although our results differ from those of Corral et al. [47], we believe that such variations can be attributed to the different types of cells used in both studies and the higher thermal conductivity of aqueous catholyte later.

On the other hand, performance at 500 mA cm^{-2}, even at elevated temperatures, revealed limited CO_2R with selectivity switching to HER at a short experimental time and a temperature rise of around 7°C (Figure S21). In the context of industrial scale-up, this phenomenon remains relevant since resistive heating is dominant at elevated temperatures at larger-size electrolyzers, and electrodes must maintain stable operation under these operational conditions. Therefore, coupling some strategies with temperature, such as two-step CO_2 electrolysis, switching from K to Cs-based electrolytes, or adding ionomers, can improve performance and stability.

Long-term stability of CO_2R at elevated temperatures

We performed long-term experiments (50 hours) at high temperatures to track product distribution and stability. Figure 8 shows cell potential and product distribution of electrolysis at 60°C and 150 mA cm^{-2}. The FE of gas products is reported as the average of simultaneous GC injections, and the liquid products were achieved by periodically collecting anolyte and cathode samples. To avoid possible evaporation of the anolyte, we used a more extensive reservoir and maintained the operation without any intervention or technique to improve the GDE durability.

During the first 40-hour experiment, CO was the primary product with a constant cell potential (~-2.9 V). The FE_{CO} decreased by just 8% for 30 hours (from 39% at the beginning of the experiment to 31% at the end). In addition, neither the HER nor the ethylene showed significant changes in selectivity, with both showing changes of below 7% and 4%, respectively. As for the liquid product, the ethanol selectivity increased for the first few hours of testing (reaching 20% at 8 hours) but then decreased to 10%. The acetate

selectivity was lower at the beginning of the experiment, matching our trend presented in Figure 3, but it was slightly higher after 24 hours. We correlated this change to an enhancement of the oxidation mechanisms at the anode and the possible oxidation of ethanol to acetate or even CO_2.

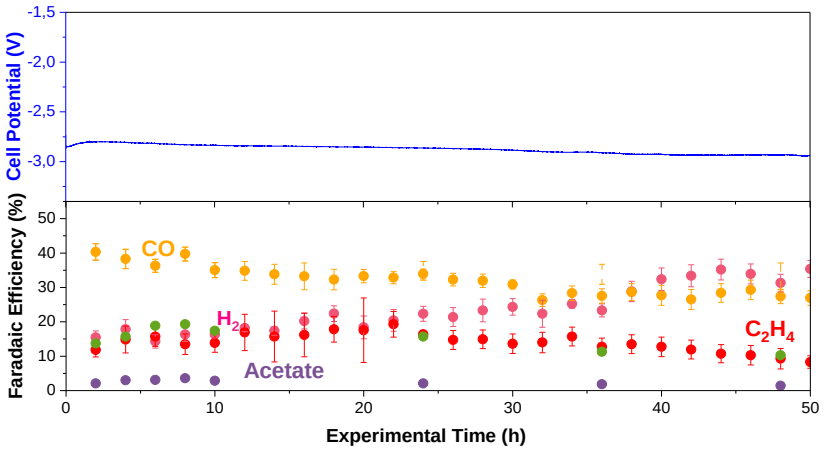

Figure 8. Long-term stability test operated at 60°C and 150 mA cm^{-2} using Cu-based electrode and MPIP- (with an 0.1 M $KHCO_3$ anolyte). Error bars represent the standard error of the mean for the measurements within 2 h intervals for gas products.

After 40 hours, we saw an enhancement of HER and a decrease in selectivity towards carbon products. The electrolyzer performed for 55 hours before we observed a jump in the potential and further cell short-circuited. We believed that we had reached a point where the membrane hydration was sufficiently low and began to suffer from chemical degradation (Figure S22), which affected its ability to operate longer-term. In our experiments, we demonstrated that temperature management might be an effective strategy to overcome limitations in CO_2 mass transport. However, it remains an issue for maintaining CO_2R at MEA for a more extended period.

Conclusions

We conducted a systematic study to investigate the effects of temperature on zero-gap CO_2 electrolysis to understand how this parameter influences selectivity, activity, and overall performance. We found that raising the temperature increased the current density towards CO_2R and lower cell potentials due to improved CO_2 mass transport, water management, and charge-transfer kinetics, overcoming the adverse effects of low solubility. Additionally, we observe a significant shift of selectivity toward CO at temperatures above 50°C (>40%), which is associated with a weakening of the binding strength of CO to the surface, favoring the desorption as observed by our ATR-SEIRAS measurements. By operating at elevated temperatures, we found the concomitant H_2 was suppressed (15.0% at 300 mA cm^{-2} at 80°C), and

GDE flooding was delayed, resulting in increased CO_2R durability. We heated our reaction system at 60°C and achieved stable CO_2 electrolysis over 40 hours without significant changes in derived CO_2R-products selectivity and cell potential (<3 V). As a final point, we presented the importance of proper heating when conducting such experiments, as differences in the heating methods might mislead the evaluation of the temperature effect and trends during the experiment. The insights obtained in this work noted the benefits of conducting CO_2R at elevated temperatures under industrially relevant conditions to decrease energy consumption and improve stability while providing strategies for combining these benefits with the design and optimization of selective electrocatalysts, GDEs, and AEMs to overcome current limitations in this field.

References

1 E. A. Quadrelli, G. Centi, J. L. Duplan and S. Perathoner, *ChemSusChem*, 2011, 4, 1194–1215.

2 P. de Luna, C. Hahn, D. Higgins, S. A. Jaffer, T. F. Jaramillo and E. H. Sargent, *Science (1979)*, 2019, 364.

3 T. Burdyny and W. A. Smith, *Energy Environ Sci*, 2019, **12**, 1442–1453.

4 C. M. Gabardo, C. P. O'Brien, J. P. Edwards, C. McCallum, Y. Xu, C. T. Dinh, J. Li, E. H. Sargent and D. Sinton, *Joule*, 2019, **3**, 2777–2791.

5 C. McCallum, C. M. Gabardo, C. P. O'Brien, J. P. Edwards, J. Wicks, Y. Xu, E. H. Sargent and D. Sinton, *Cell Rep Phys Sci*, , DOI:10.1016/j.xcrp.2021.100522.

6 R. Küngas, *J Electrochem Soc*, 2020, **167**, 044508.

7 A. Löwe, C. Rieg, T. Hierlemann, N. Salas, D. Kopljar, N. Wagner and E. Klemm, *ChemElectroChem*, 2019, **6**, 4497–4506.

8 H. W. Shafaque, J. K. Lee, K. Krause, C. H. Lee, K. F. Fahy, P. Shrestha, M. Balakrishnan and A. Bazylak, *Energy Convers Manag*, , DOI:10.1016/j.enconman.2021.114302.

9 R. E. Vos and M. T. M. Koper, *ChemElectroChem*, , DOI:10.1002/celc.202200239.

10 Y. Zong, P. Chakthranont and J. Suntivich, *Journal of Electrochemical Energy Conversion and Storage*, , DOI:10.1115/1.4046552.

11 E. Abouzari-Lotf, M. v. Jacob, H. Ghassemi, M. Zakeri, M. M. Nasef, Y. Abdolahi, A. Abbasi and A. Ahmad, *Sci Rep*, , DOI:10.1038/s41598-021-83161-9.

12 L. C. Weng, A. T. Bell and A. Z. Weber, *Energy Environ Sci*, 2020, **13**, 3592–3606.

13 L. C. Weng, A. T. Bell and A. Z. Weber, *Energy Environ Sci*, 2020, **13**, 3592–3606.

14 F. Pelayo García de Arquer, C.-T. Dinh, A. Ozden, J. Wicks, C. McCallum, A. R. Kirmani, D.-H. Nam, C. Gabardo, A. Seifitokaldani, X. Wang, Y. C. Li, F. Li, J. Edwards, L. J. Richter, S. J. Thorpe, D. Sinton and E. H. Sargent, *CO 2 electrolysis to multicarbon products at activities greater than 1 A cm −2*, .

15 B. Endrdi, E. Kecsenovity, A. Samu, T. Halmágyi, S. Rojas-Carbonell, L. Wang, Y. Yan and C. Janáky, *Energy Environ Sci*, 2020, **13**, 4098–4105.

16 Y. Hori, K. Kikuchi, A. Murata and S. Suzuki, *of Japan PRODUCTION OF METHANE AND ETHYLENE IN ELECTROCHEMICAL REDUCTION OF CARBON DIOXIDE AT COPPER ELECTRODE IN AQUEOUS HYDROGENCARBONATE SOLUTION*, 1986.

17 S. T. Ahn, I. Abu-Baker and G. T. R. Palmore, *Catal Today*, 2017, **288**, 24–29.

18 E. Jeng and F. Jiao, *React Chem Eng*, 2020, **5**, 1768–1775.

19 E. J. Dufek, T. E. Lister and M. E. McIlwain, *J Appl Electrochem*, 2011, **41**, 623–631.

20 F. Pelayo García de Arquer, C.-T. Dinh, A. Ozden, J. Wicks, C. McCallum, A. R. Kirmani, D.-H. Nam, C. Gabardo, A. Seifitokaldani, X. Wang, Y. C. Li, F. Li, J. Edwards, L. J. Richter, S. J. Thorpe, D. Sinton and E. H. Sargent, *CO 2 electrolysis to multicarbon products at activities greater than 1 A cm −2*, .

21 H. Zhong, K. Fujii and Y. Nakano, *Journal of Energy Chemistry*, 2016, **25**, 517–522.

22 D. G. Wheeler, B. A. W. Mowbray, A. Reyes, F. Habibzadeh, J. He and C. P. Berlinguette, *Energy Environ Sci*, 2020, **13**, 5126–5134.

23 M. E. Leonard, L. E. Clarke, A. Forner-Cuenca, S. M. Brown and F. R. Brushett, *ChemSusChem*, 2020, **13**, 400–411.

24 H. Miyake, S. Ye and M. Osawa, *Electroless deposition of gold thin films on silicon for surface-enhanced infrared spectroelectrochemistry*, .

25 W. Deng, T. Yuan, S. Chen, H. Li, C. Hu, H. Dong, B. Wu, T. Wang, J. Li, G. A. Ozin and J. Gong, *Fundamental Research*, 2021, **1**, 432–438.

26 M. Li, M. N. Idros, Y. Wu, T. Burdyny, S. Garg, X. S. Zhao, G. Wang and T. E. Rufford, *J Mater Chem A Mater*, 2021, 9, 19369–19409.

27 J. C. Douglin, R. K. Singh, S. Haj-Bsoul, S. Li, J. Biemolt, N. Yan, J. R. Varcoe, G. Rothenberg and D. R. Dekel, *Chemical Engineering Journal Advances*, , DOI:10.1016/j.ceja.2021.100153.

28 S. Chinnathambi, M. Ramdin and T. J. H. Vlugt, *Electrochem*, 2022, **3**, 549–569.

29 A. Goyal and M. T. M. Koper, *Angewandte Chemie - International Edition*, 2021, **60**, 13452–13462.

30 M. van Truong, N. B. Duong, C. L. Wang and H. Yang, *Materials*, , DOI:10.3390/ma12132048.

31 A. Reyes, R. P. Jansonius, B. A. W. Mowbray, Y. Cao, D. G. Wheeler, J. Chau, D. J. Dvorak and C. P. Berlinguette, *ACS Energy Lett*, 2020, **5**, 1612–1618.

32 S. Garg, C. A. Giron Rodriguez, T. E. Rufford, J. R. Varcoe and B. Seger, *Energy Environ Sci*, , DOI:10.1039/d2ee01818g.

33 D. G. Wheeler, B. A. W. Mowbray, A. Reyes, F. Habibzadeh, J. He and C. P. Berlinguette, *Energy Environ Sci*, 2020, **13**, 5126–5134.

34 M. Ma, E. L. Clark, K. T. Therkildsen, S. Dalsgaard, I. Chorkendorff and B. Seger, *Energy Environ Sci*, 2020, **13**, 977–985.

35 G. O. Larrazábal, P. Strøm-Hansen, J. P. Heli, K. Zeiter, K. T. Therkildsen, I. Chorkendorff and B. Seger, *ACS Appl Mater Interfaces*, 2019, **11**, 41281–41288.

36 R. K. Miao, Y. Xu, A. Ozden, A. Robb, C. P. O'Brien, C. M. Gabardo, G. Lee, J. P. Edwards, J. E. Huang, M. Fan, X. Wang, S. Liu, Y. Yan, E. H. Sargent and D. Sinton, *Joule*, 2021, **5**, 2742–2753.

37 J. Zhang, W. Luo and A. Züttel, *J Catal*, 2020, **385**, 140–145.

38 M. Moradzaman, C. S. Martínez and G. Mul, *Sustain Energy Fuels*, 2020, **4**, 5195–5202.

39 M. Moradzaman and G. Mul, *Journal of Physical Chemistry C*, 2021, **125**, 6546–6554.

40 J. Giner and C. Hunter, *The Mechanism of Operation of the Teflon-Bonded Gas Diffusion Electrode: A Mathematical Model*, .

41 M. E. Leonard, L. E. Clarke, A. Forner-Cuenca, S. M. Brown and F. R. Brushett, *ChemSusChem*, 2020, **13**, 400–411.

42 L. C. Weng, A. T. Bell and A. Z. Weber, *Physical Chemistry Chemical Physics*, 2018, **20**, 16973–16984.

43 F. Pelayo García de Arquer, C.-T. Dinh, A. Ozden, J. Wicks, C. McCallum, A. R. Kirmani, D.-H. Nam, C. Gabardo, A. Seifitokaldani, X. Wang, Y. C. Li, F. Li, J. Edwards, L. J. Richter, S. J. Thorpe, D. Sinton and E. H. Sargent, *CO 2 electrolysis to multicarbon products at activities greater than 1 A cm −2*, .

44 C. M. Gunathunge, J. Li, X. Li, J. J. Hong and M. M. Waegele, *ACS Catal*, 2020, **10**, 6908–6923.

45 D. P. Woodruff, B. E. Hayden, K. Prince and A. M. Bradshaw, *DIPOLE COUPLING AND CHEMICAL SHIFTS IN IRAS OF CO ADSORBED ON Cu(ll0)*, 1982, vol. 123.

46 C. M. Gunathunge, J. Li, X. Li and M. M. Waegele, *ACS Catal*, 2020, **10**, 11700–11711.

47 D. Corral, J. T. Feaster, S. Sobhani, J. R. Deotte, D. U. Lee, A. A. Wong, J. Hamilton, V. A. Beck, A. Sarkar, C. Hahn, T. F. Jaramillo, S. E. Baker and E. B. Duoss, *Energy Environ Sci*, 2021, **14**, 3064–3074.

- Supplementary Information -

Insights into zero-gap CO_2 electrolyzers at elevated temperatures

Carlos A. Girón Rodriguez, Asger Moss , Sahil Garg , Wanyu Deng, John R. Varcoe[b], Ib Chorkendorff and Brian Seger

[a]*Surface Physics and Catalysis (SURFCAT) Section, Department of Physics, Technical University of Denmark, 2800 Kgs. Lyngby, Denmark*

[b]*Department of Chemistry, University of Surrey, Guildford GU2 7XH, United Kingdom*

**Correspondence to: Brian Seger, Email: brse@fysik.dtu.dk*

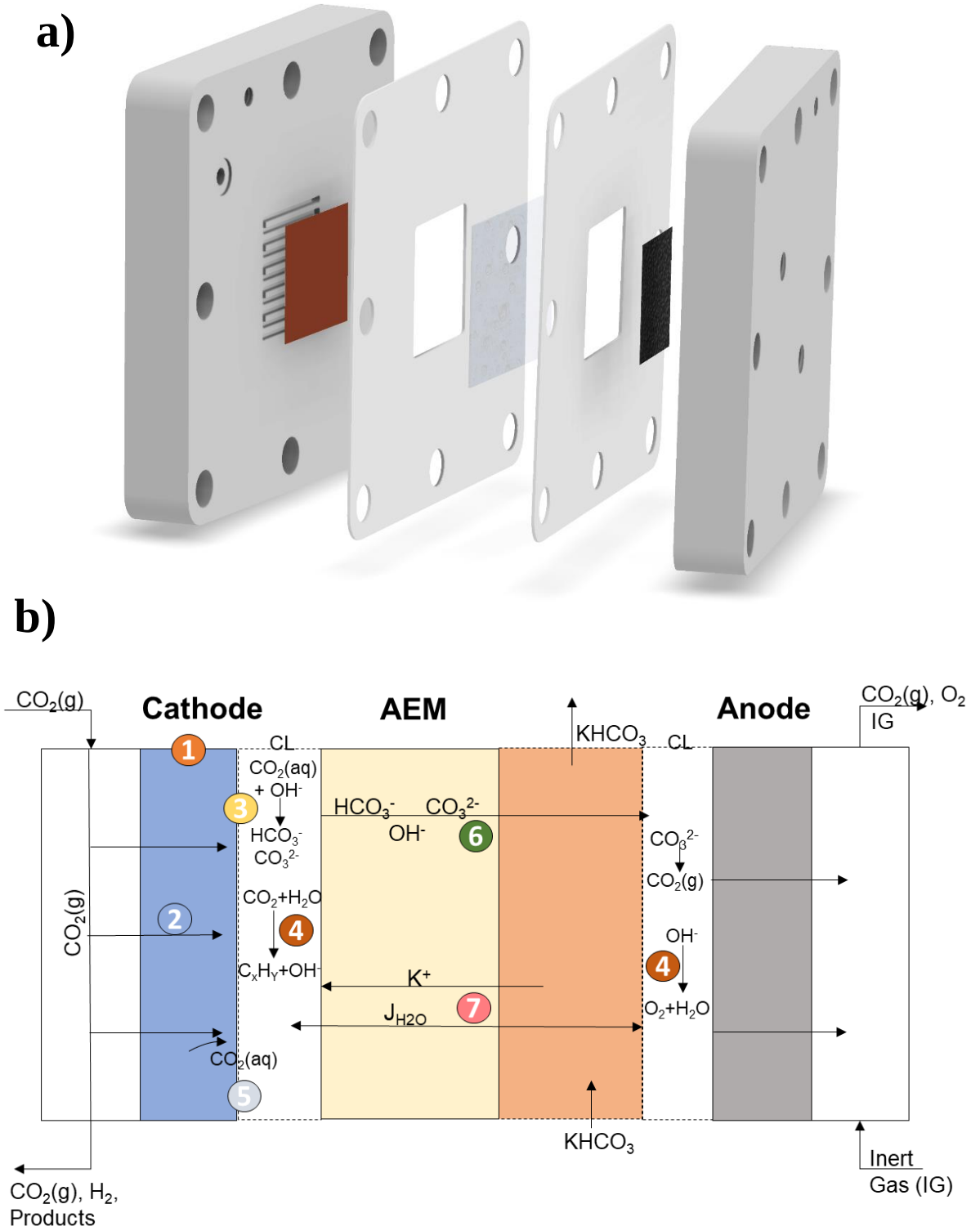

Figure S1. a) MEA cell drawing of CO_2 electrolyzer b). Schematic representation of the CO_2R in MEA configuration and main properties/parameters influenced by the temperature.

Influence of transport properties in CO_2 electrolysis as effect of temperature:

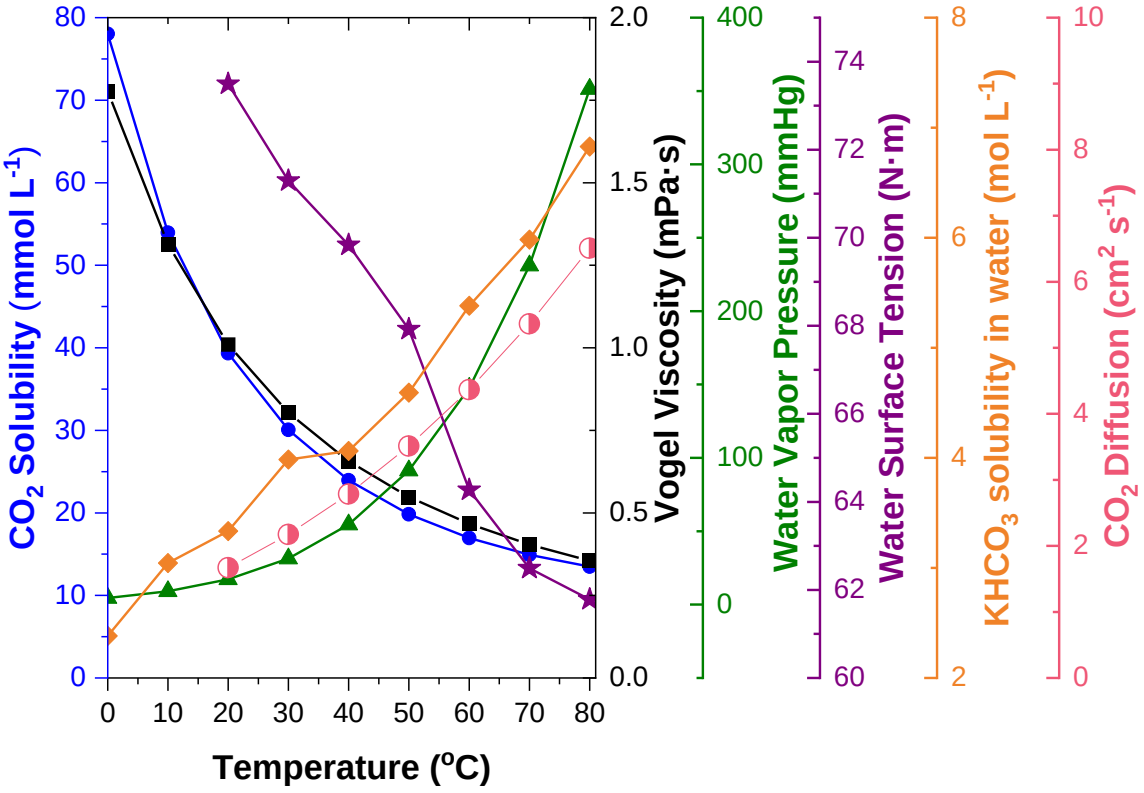

Figure S2. Transport and kinetics factor's temperature dependency on CO_2R (CO_2 solubility, CO_2 diffusion, water vapor pressure, surface tension, vogel viscosity, salt solubility, and Henry's constant).

CO_2 Solubility (in aqueous environment)[1]:

$$c_{CO2} = H_{CO2} * c_{CO2,gas} \quad \textbf{(Eq S. 1)}$$

$$H_{CO_2}\,(mM/atm) = 93{,}4517 \cdot \left(\frac{100}{\mathrm{T[K]}}\right) - 60{,}2409 + \left(23{,}3585 \cdot \log\left(\frac{T[K]}{100}\right)\right) \quad \textbf{(Eq S. 2)}$$

CO_2 Diffusion[2]:

$$D_{CO2}(cm^2/\mathrm{s}) = 2{,}17 \cdot 10^{-4} \cdot \mathrm{e}^{\left(-\frac{2345}{\frac{1}{\mathrm{T[K]}}+\frac{1}{\mathrm{T_{ref}}}}\right)} \quad \textbf{(Eq S. 3)}$$

Vogel Viscosity[3]:

$$\vartheta\ (mPa \cdot \mathrm{s}) = e^{-3{,}6413+542{,}\frac{05}{T[K]-144{,}15}} \quad \textbf{(Eq S. 4)}$$

Water vapor pressure[2,4]:

$$p_{H2O}(mmHg) = 10^{8{,}07-\left(\frac{1730{,}63}{T[K]-39{,}724}\right)} \quad \textbf{(Eq S. 5)}$$

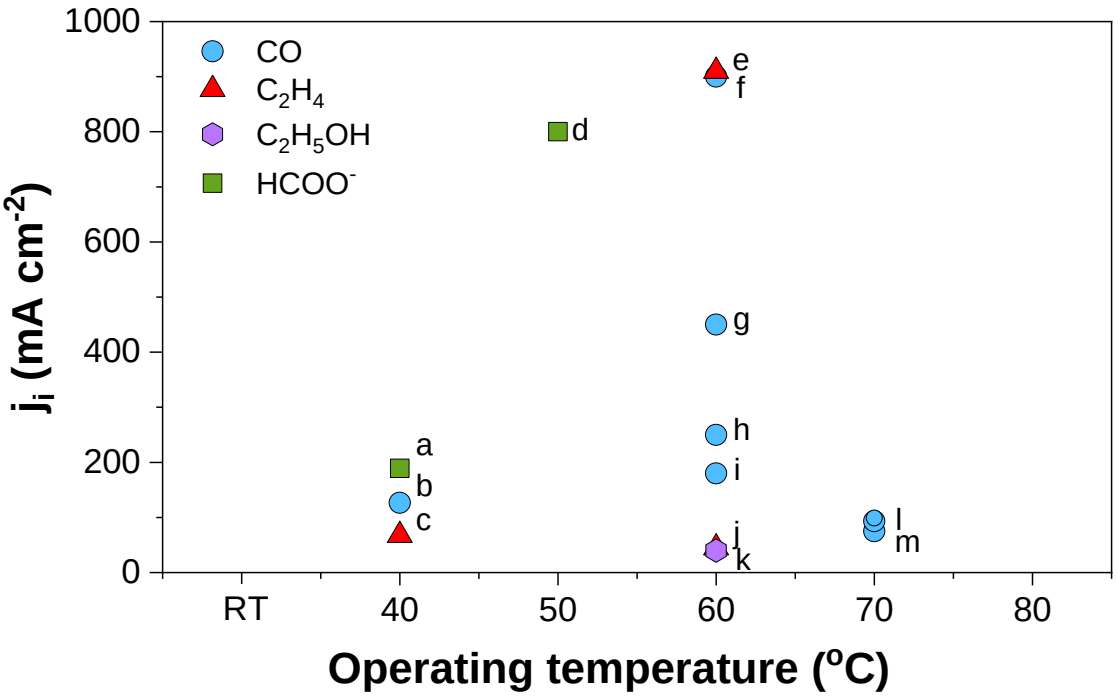

Figure S3. Summary of studies for CO_2R performed at elevated temperatures reported in the literature. (See Table S1 for the detailed information of the data). j_i corresponds to the partial current density of derived CO_2-product (CO, formate, ethanol and ethylene).

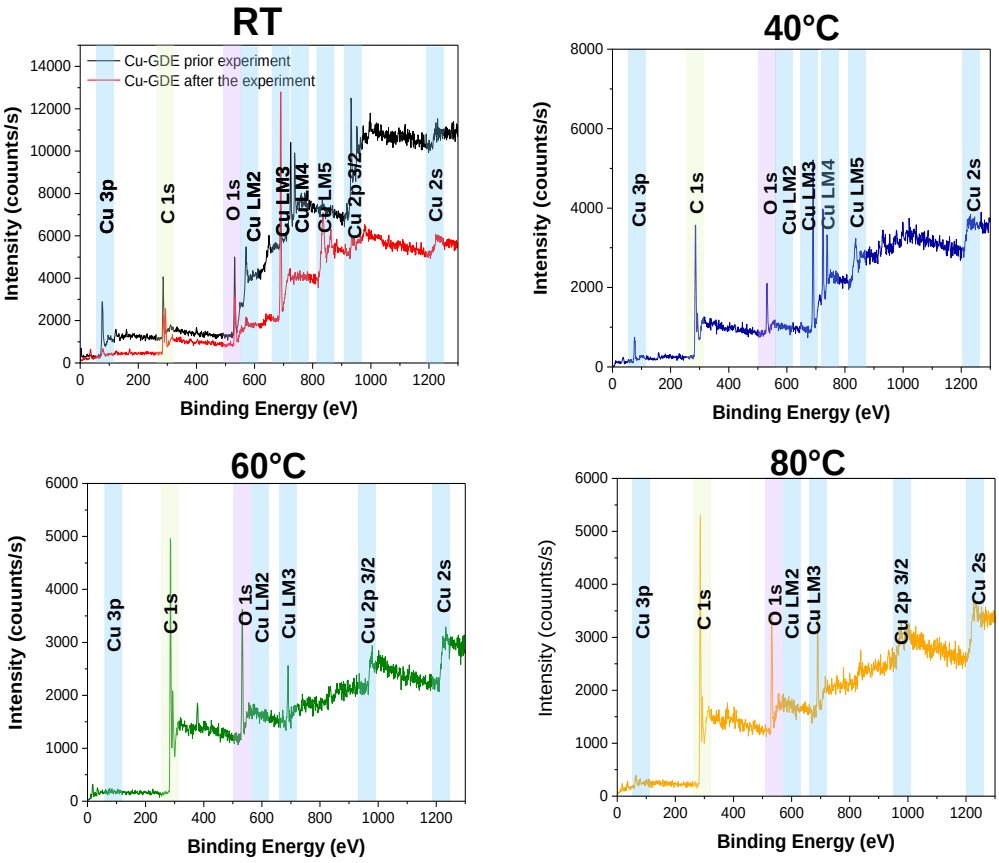

Figure S4. XPS pattern data of post-reaction Cu-GDE tested at different operating temperatures.

Table 1. Compiled data of different studies for CO_2 electrolysis performed at elevated temperatures and industrial relevant conditions

	Author	Year	Cathode	Anode	IEM	Type	Electrolyte	j_{total} (mA cm^{-2})	E_{cell} (V)	T (°C)	Cell Conf.	FE (%)
a	Endrodi et al.[5]	2020	Ag NPs on CP	IrOx-Ti	AEM	PiperION	0,1 CsOH	1000	2.6-3.4	60	MEA	90% CO
b	Dufek et al.[6]	2012	Ag GDE	RuOx	AEM	Excellion	2.5 M KOH	125	3.3	70	Flow Cell	60% CO
c	Yin et al.[7]	2019	Au	Ti-Sheet	AEM	QAPPT Membrane	Pure Water	500	3	60	MEA	90% CO
d	Yin et al.[7]	2019	CoPc	Ti-Sheet	AEM	QAPPT Membrane	Pure Water	200	2.8	60	MEA	90% CO
e	Pribyl-Kranewitter[8]	2021	Ag-GDE 29BC	$IrTiO_2$-Nafion	BPM	Fumasep BPM	DI Water	136	2.9	40	Flow Cell	93% CO
f	Gabardo et al.[9]	2019	Cu-GDE	IrO_2	AEM	Sustainion X37-50	0.1 M $KHCO_3$	150	4	40	MEA	45% C_2H_4
g	Gabardo et al.[9]	2019	Cu-GDE	IrO_2	AEM	Sustainion X37-50	0.1 M $KHCO_3$	100	3.7	60	MEA	30% C_2H_4
h	Kai Miao et al.[10]	2021	Cu-GDE in PTFE	IrO_2/Ti	AEM	Sustainion, PiperION	0.1 M $KHCO_3$	200	3.85	60	MEA	20% EtOH
i	Lee et al.[11]	2018	Sn-NPs on CP	Pt Black	CEM	Nafion 115	1 M $KHCO_3$ /1 M KOH	100	2.2	70	Flow Cell	93.3% $HCOO^-$
j	Li et al.[12]	2007	Sn NPs	Ti Mesh	CEM	Nafion 117	0,5 M $KHCO_3$+ 2 M KCl	310	3.9	40	Flow Cell	61% $HCOO^-$
k	Dufek et al.[13]	2014	Ag GDE	Ir-Ni mesh	CEM	Nafion 115	0,5 M K_2SO_4	275	3.4-3.6	60	Flow Cell	90% CO
l	Dufek et al.[6]	2011	Ag-GDE	Ru- DSA	CEM	Nafion 424	0,8 M K_2SO_4	110	1.57	70	Flow Cell	90% CO
m	Jeng and Jiao[14]	2020	Ag-GDE	IrO_2	AEM	Sustainion	0.05 M $KHCO_3$	200	3.1	60	MEA	90% CO
n	Garcia de Arquer et al.[1]	2020	Cu-CIBH	Ni Foam	AEM	Fumasep FA-PK 130	7 M KOH	1400	5.5	60	Flow Cell	65% C_2H_4
o	Lowe et al.[15]	2019	Sn-GDE	Ni Gauze	CEM	Nafion 117	2 M $KHCO_3$	1000	1.72 V SHE	50	Flow Cell	80% HCOO-

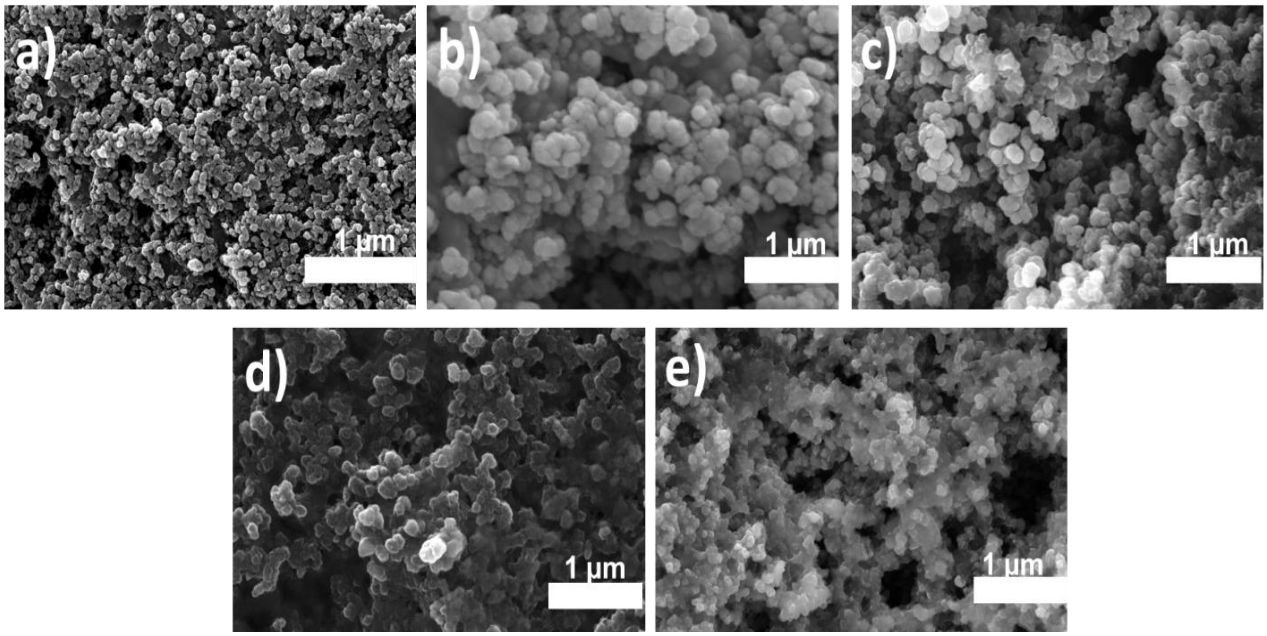

Figure S5. SEM images of the Cu-based catalyst a) gas-diffusion layer, Cu-GDEcoated on microporous carbon layers of the SG-39BB GDL at b) RT before electrolysis, c) RT after electrolysis, d) 60 °C before electrolysis and e) 60 °C after electrolysis

Supplementary Note I

Estimation of the standard equilibrium potentials

We can estimate the standard cell potentials by correlating the change in free energy.

$$\Delta G^0 = -z\,F\,E^0_{cell} \quad (\textbf{Eq S. 6})$$

In Equation (Eq S.6), z corresponds to the moles of electrons, F the Faraday's constant, ΔG^0 the Gibbs free energy related to the electrical work and E^0_{cell} is the standard cell potential. The thermochemistry data for carbon products from CO_2R can bee found from literature[16]

Table S3. Effect of operating temperature in the standard potentials for different CO_2R products

Temperature (°C)	E° CO (V)	E° C_2H_4 (V)	E° EtOH (V)	E° PrOH (V)	E° CH_4 (V)
20	-0.104	0.081	0.080	0.096	0.171
30	-0.108	0.075	0.074	0.090	0.165
40	-0.112	0.069	0.068	0.083	0.160
50	-0.116	0.062	0.062	0.077	0.155
60	-0.120	0.056	0.056	0.070	0.150
70	-0.123	0.050	0.049	0.063	0.144
80	-0.127	0.044	0.043	0.057	0.139

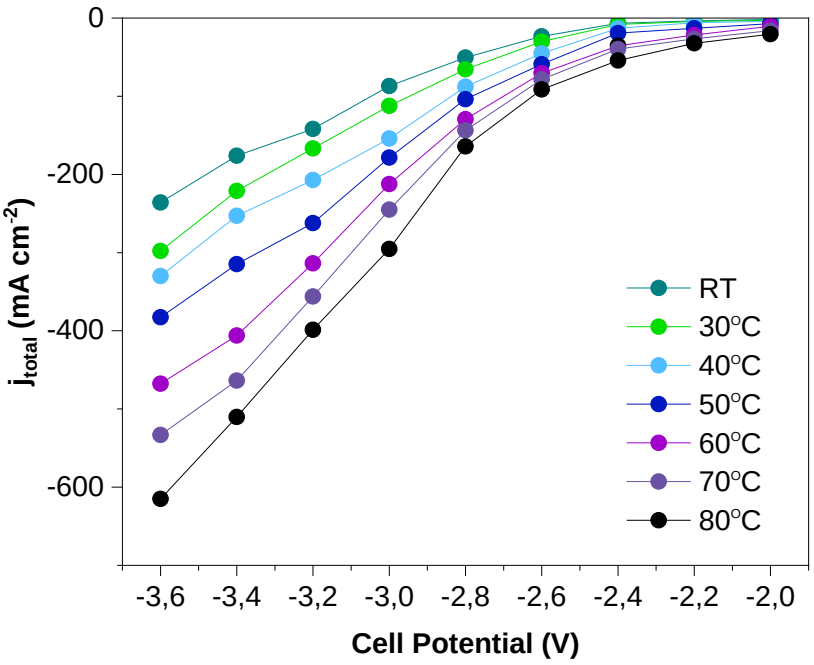

Figure S6. Chronoamperiometry measurements of CO_2 electrolysis at different cell potentials and temperatures in prior experiments.

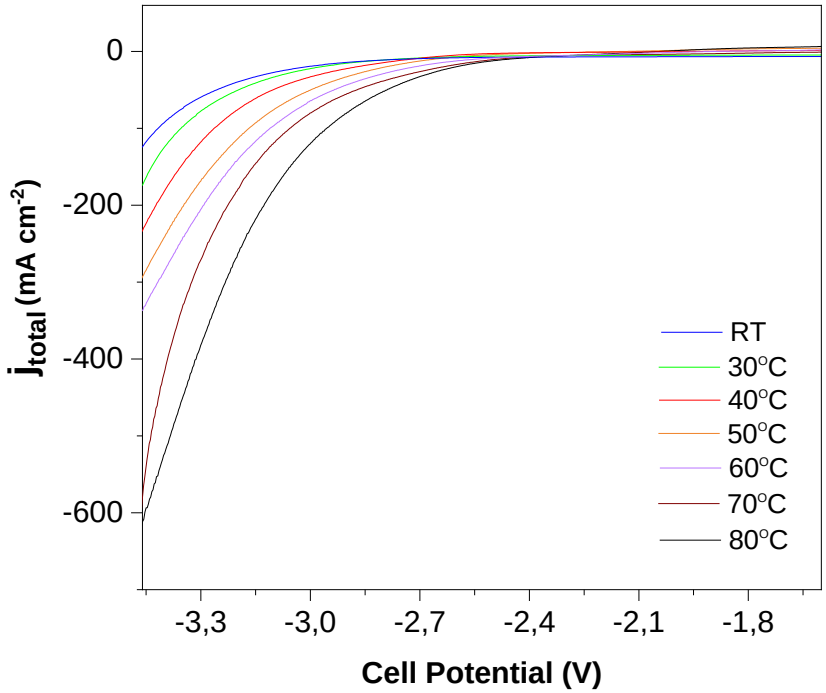

Figure S7. Post-electrolysis LSV of CO_2 reduction at different temperatures and cell potentials (scan rate: 20 mV s^{-1}). Experimental conditions: Cu-GDE (Cathode), MPIP-AEM, IO_2 (Anode), CO_2 feeding rate 40 sccm, 0.1 M $KHCO_3$.

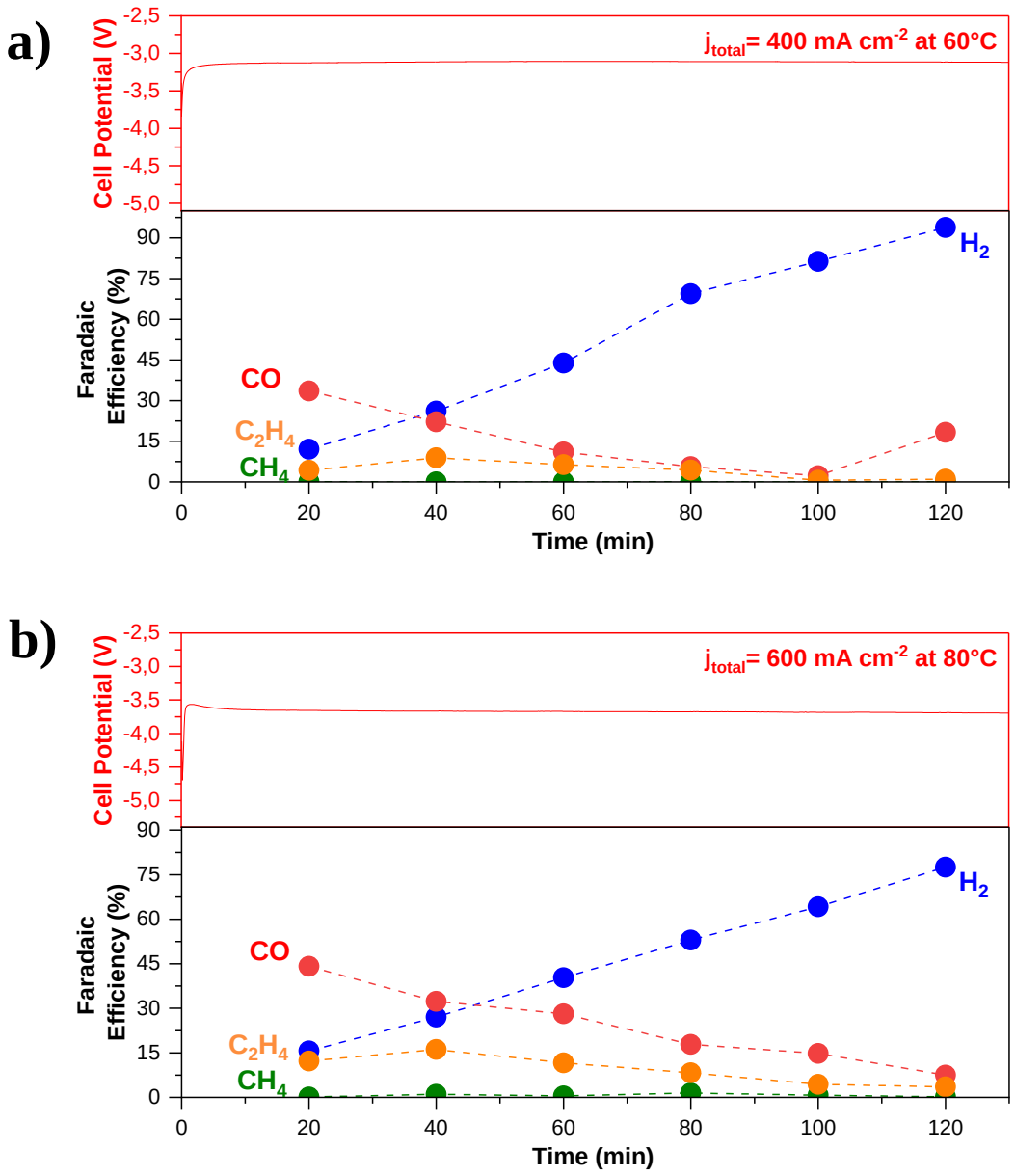

Figure S8. Product distribution and CO_2 electrolysis experiments at high current densities beyond the limiting current densities a) Performance at 400 mA cm^2 at 60°c and b) 600 mA cm^{-2} at 80°C. (Experimental conditions: Cu-GDE (Cathode), MPIP-AEM, IO_2 (Anode), CO_2 feeding rate 40 sccm, 0.1 M $KHCO_3$) .

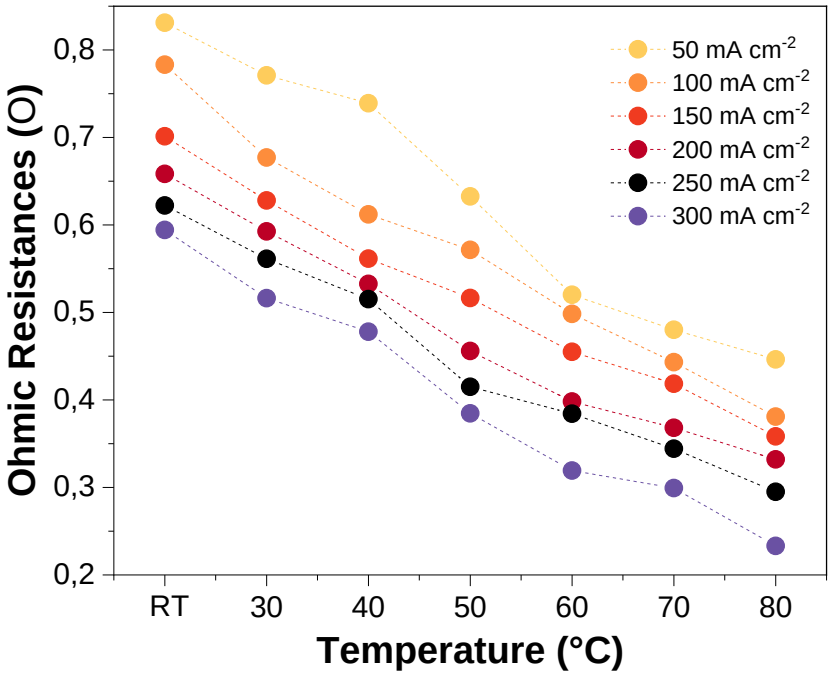

Figure S9. Measurements of ohmic resistances at different current densities and temperatures. USING current interrupt technique. This parameter was measured after the galvanostatic experiments.

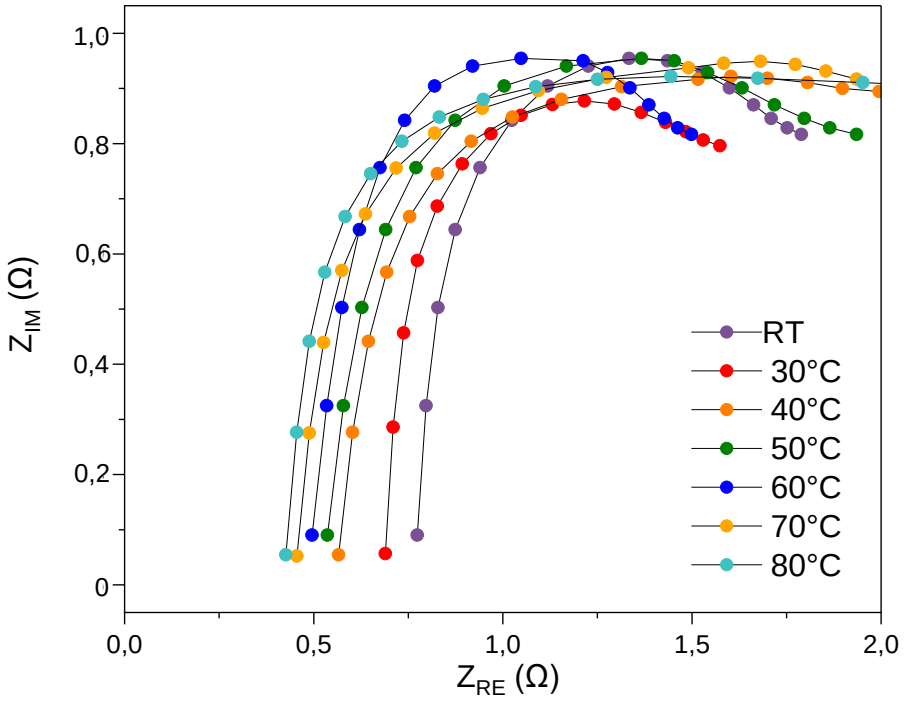

Figure S10. Galvano-electro impedance spectroscopy (GEIS) for CO_2 electrolysis at different temperatures. (High-frequency region indicates potential variations of the ionic conductivity).

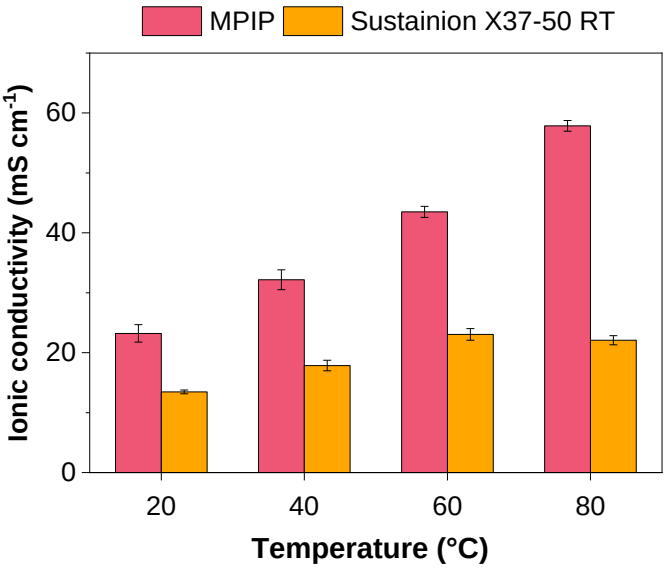

Figure S11. Measurement of the Ionic Conductivity in the HCO_3- for different AEMs

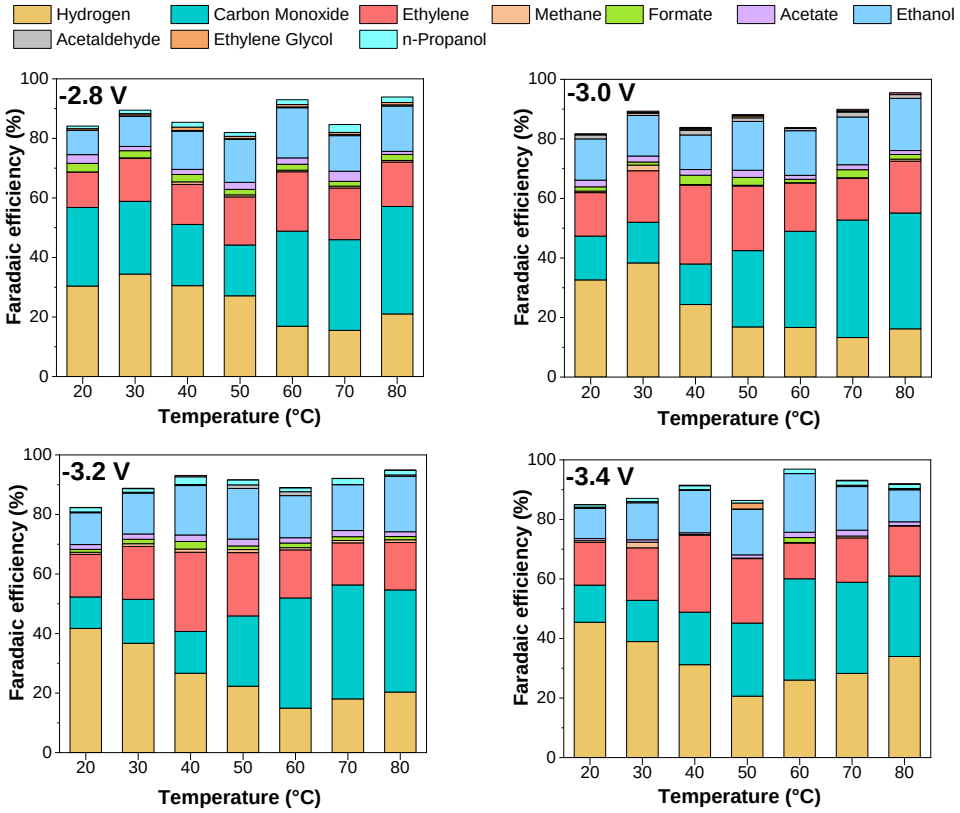

Figure S12. Product distribution as an effect of the temperature and cell potential for CO_2 electrolysis.

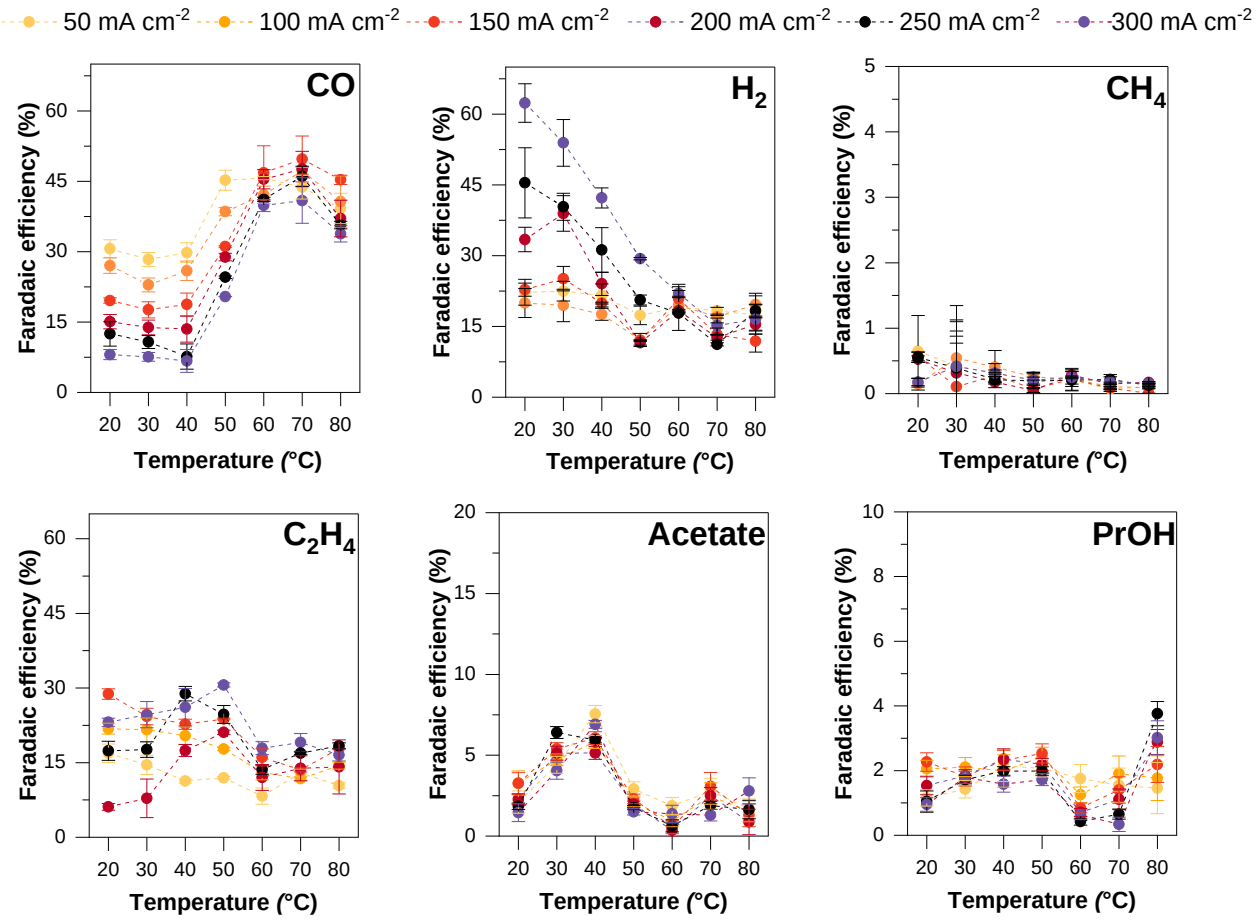

Figure S13. Trends of major electrochemical CO_2-derived products (CO, acetate, n-propanol, ethylene, methane) and HER as a function of the total current density and temperature (results linked to Figure 3 of the main manuscript**).**

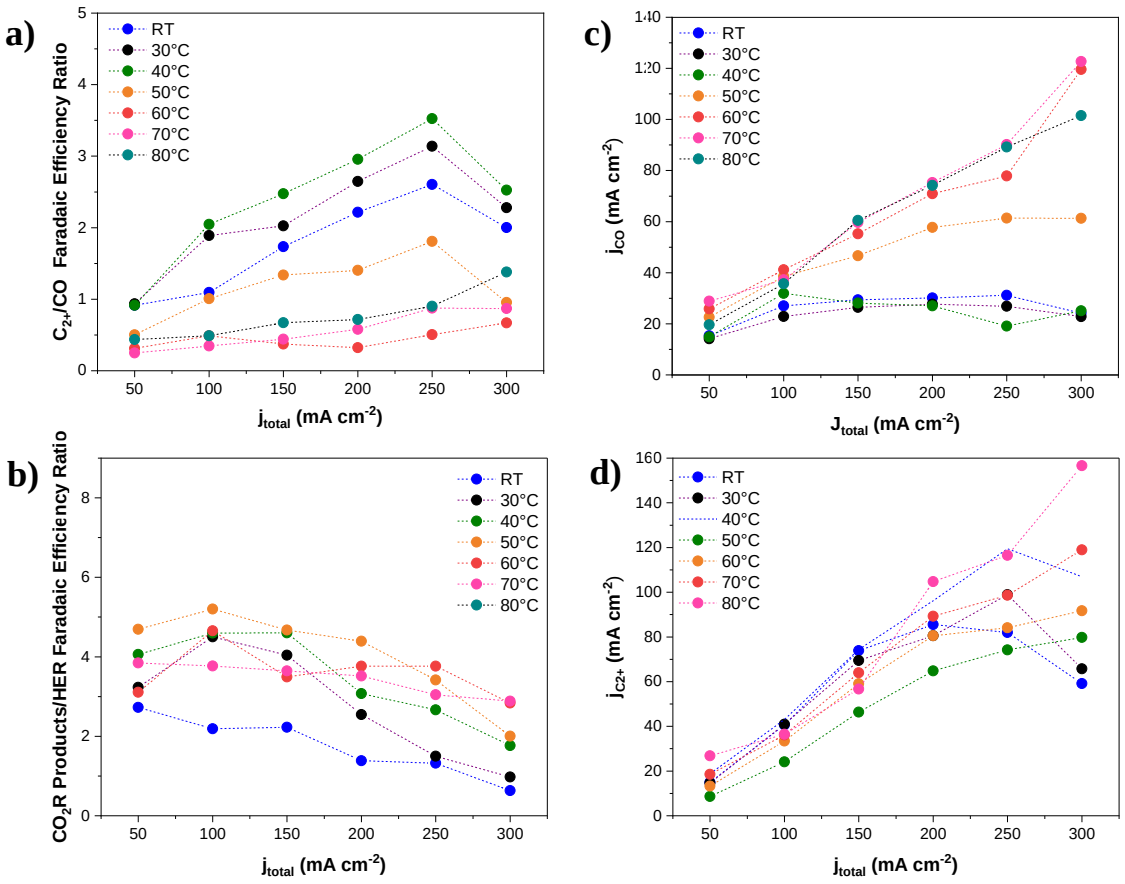

Figure S14. a) C_{2+}/CO Faradaic efficiency ratio, b) CO_2-derived products/H_2 faradaic efficiency ratio, c) CO partial current density (j_{CO}), and d) C_{2+} products partial current density (j_{C2+}) as a function of the temperature and total current densities. (Experimental conditions: Cu-GDE (Cathode), MPIP-AEM, IO_2 (Anode), CO_2 feeding rate 40 sccm, 0.1 M $KHCO_3$) .

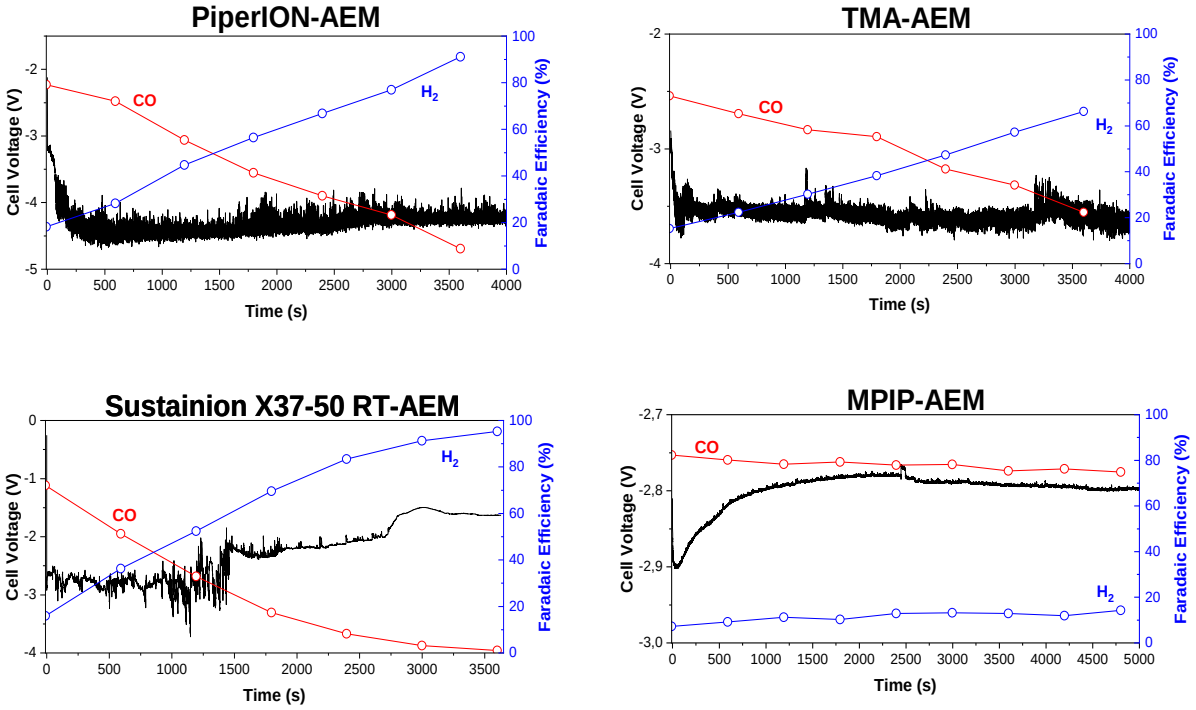

Figure S15. Effect of high-temperature CO_2-electrolysis performance for different AEMs in the chemical stability over Ag-GDE. (Experimental conditions: Cu-GDE (Cathode), MPIP-AEM, IO_2 (Anode), CO_2 feeding rate 40 sccm, 0.1 M $KHCO_3$, temperature: 90°C) .

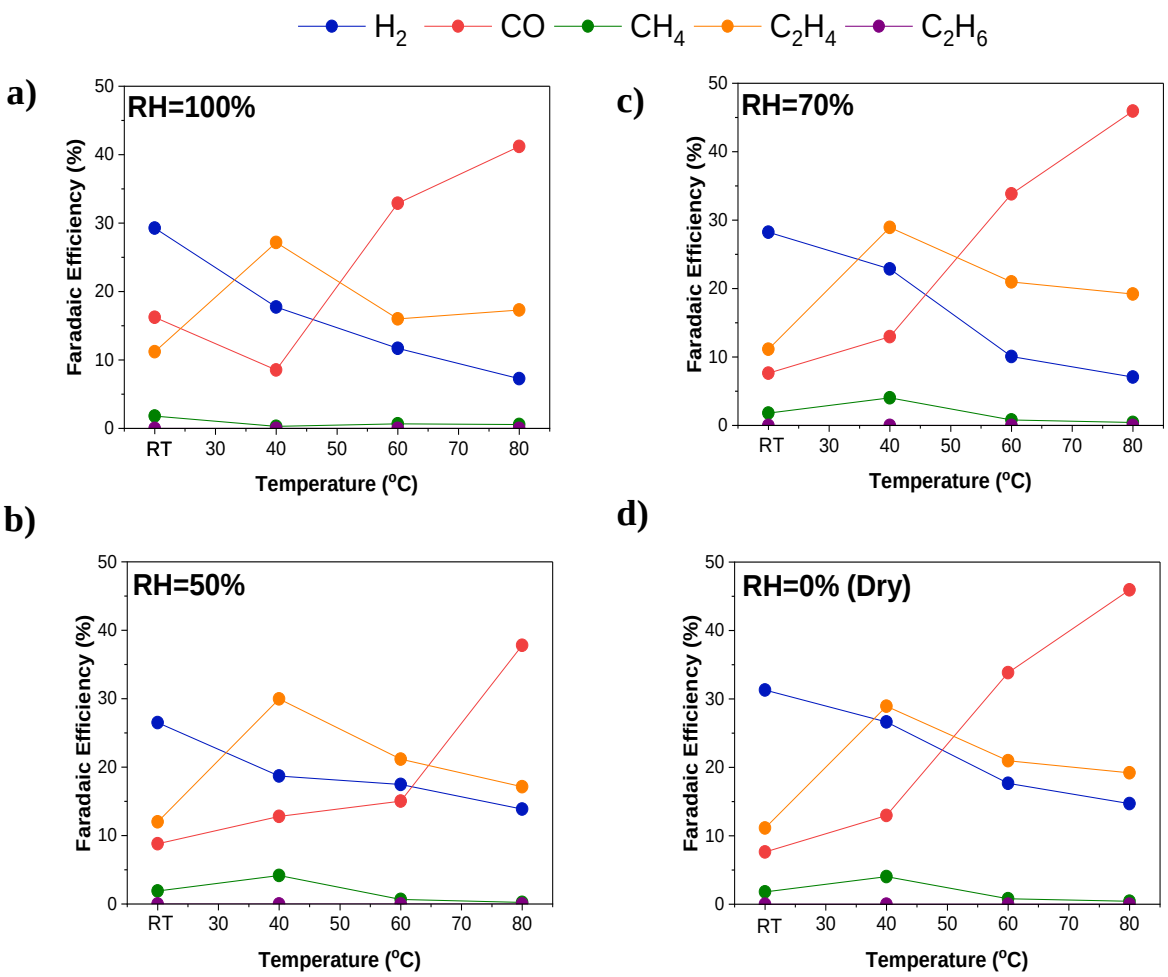

Figure S16. Effect of the relative humidity (different humidity in CO_2-inlet feed) in the product distribution of gas-products for CO_2 electrolysis as a function of the temperature. A) 100%, b) 50%, c) 70%, and d) Dry CO_2. Experimental conditions: Cu-GDE (Cathode), MPIP-AEM, IO_2 (Anode), CO_2 feeding rate 40 sccm, 0.1 M $KHCO_3$. Operating time: 90 min for each measurement).

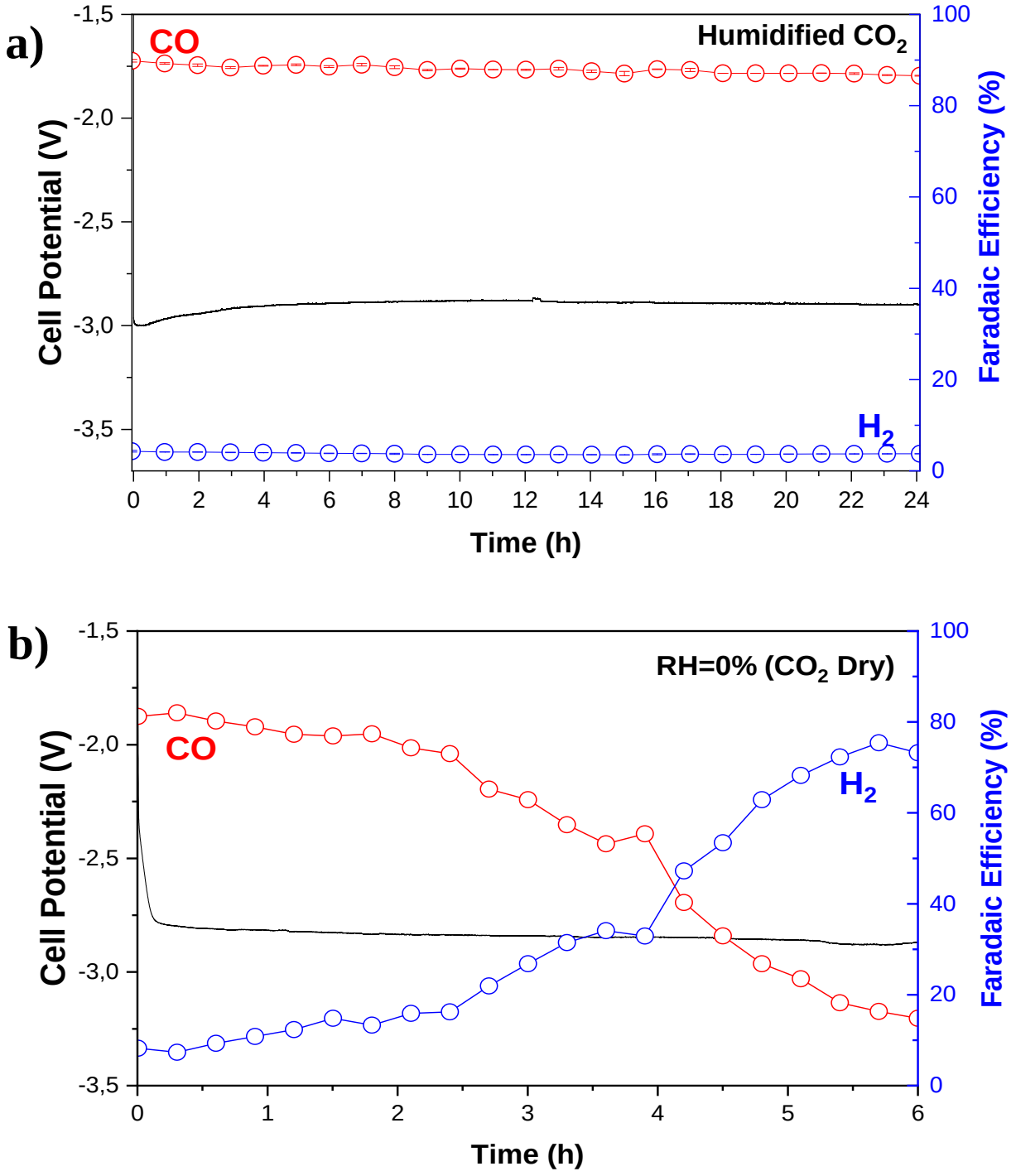

Figure S17. Coupled effect of temperature and water content by evaluating the effect of humidified CO_2 inlet vs. dry CO_2 in long-term CO_2 electrolysis at 80 °C. a). Humidified CO_2, and b). Dry CO_2

Homogeneous reactions

$CO_2 + OH^- \rightarrow HCO_3^-$

$HCO_3^- + OH^- \rightarrow CO_3^{2-} + H_2O$

$OH^- + H^+ \rightarrow H_2O$

Main anodic reaction

OER: $2H_2O \rightarrow O_2 + 4H^+ + 4e^-$

(CO_2/O_2 ratio = 0) $4OH^- \rightarrow O_2 + 2H_2O + 4e^-$

(CO_2/O_2 ratio= 2) $2CO_3^{2-} \rightarrow 2CO_2 + O_2 + 4e^-$

(CO_2/O_2 ratio = 4) $4HCO_3^- \rightarrow 4CO_2 + O_2 + 2H_2O + 4e^-$

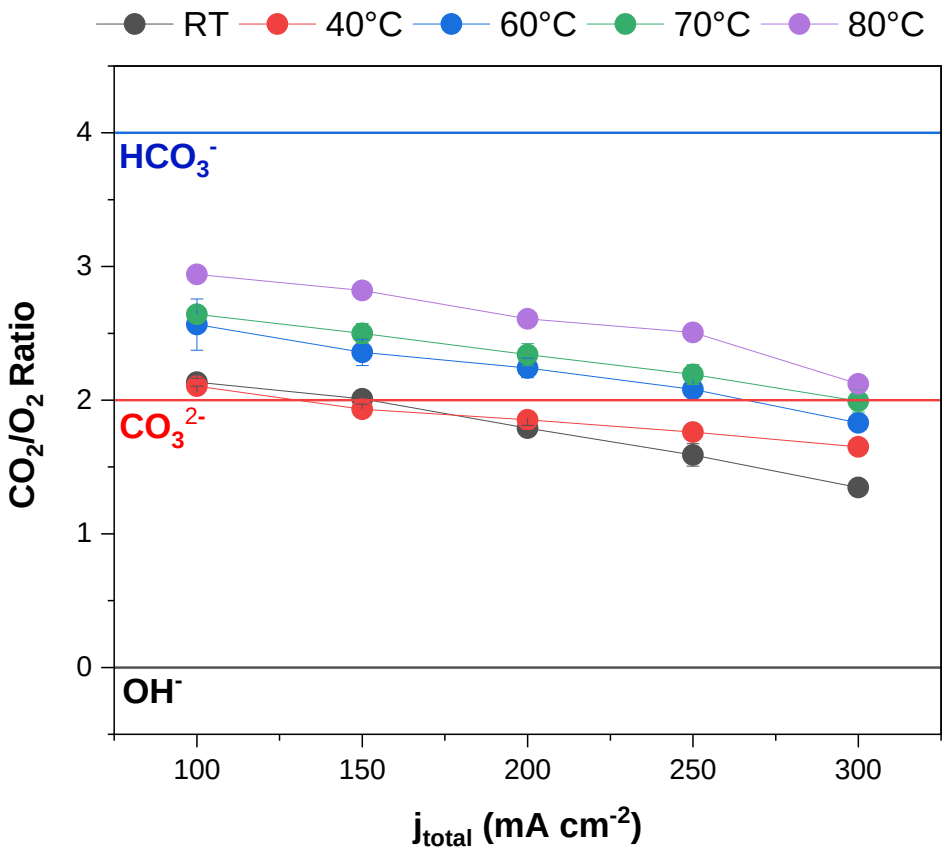

Figure S18. CO_2/O_2 ratio at the anode as a function of total current density for different temperatures CO_2 electrolysis.

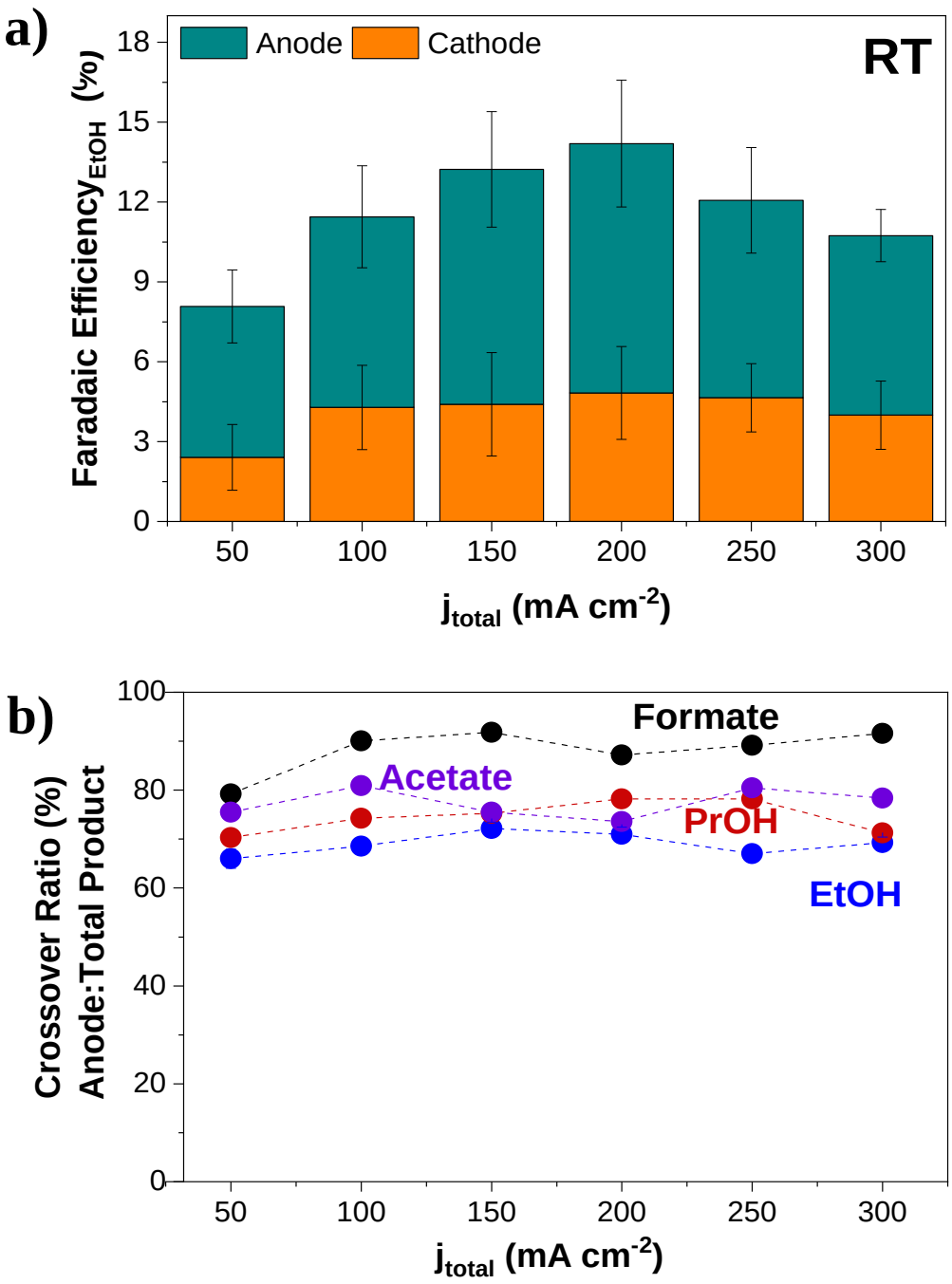

Figure S19. A crossover study of ethanol at room temperature in MEA-based CO_2 electrolysis a) Ethanol faradaic efficiencies at different current densities and quantification of the product in the cathode and anode compartments. B). Crossover ratio of product detected at the anode vs. total products for main CO2-liquid products (ethanol, n-propanol, acetate, and formate).

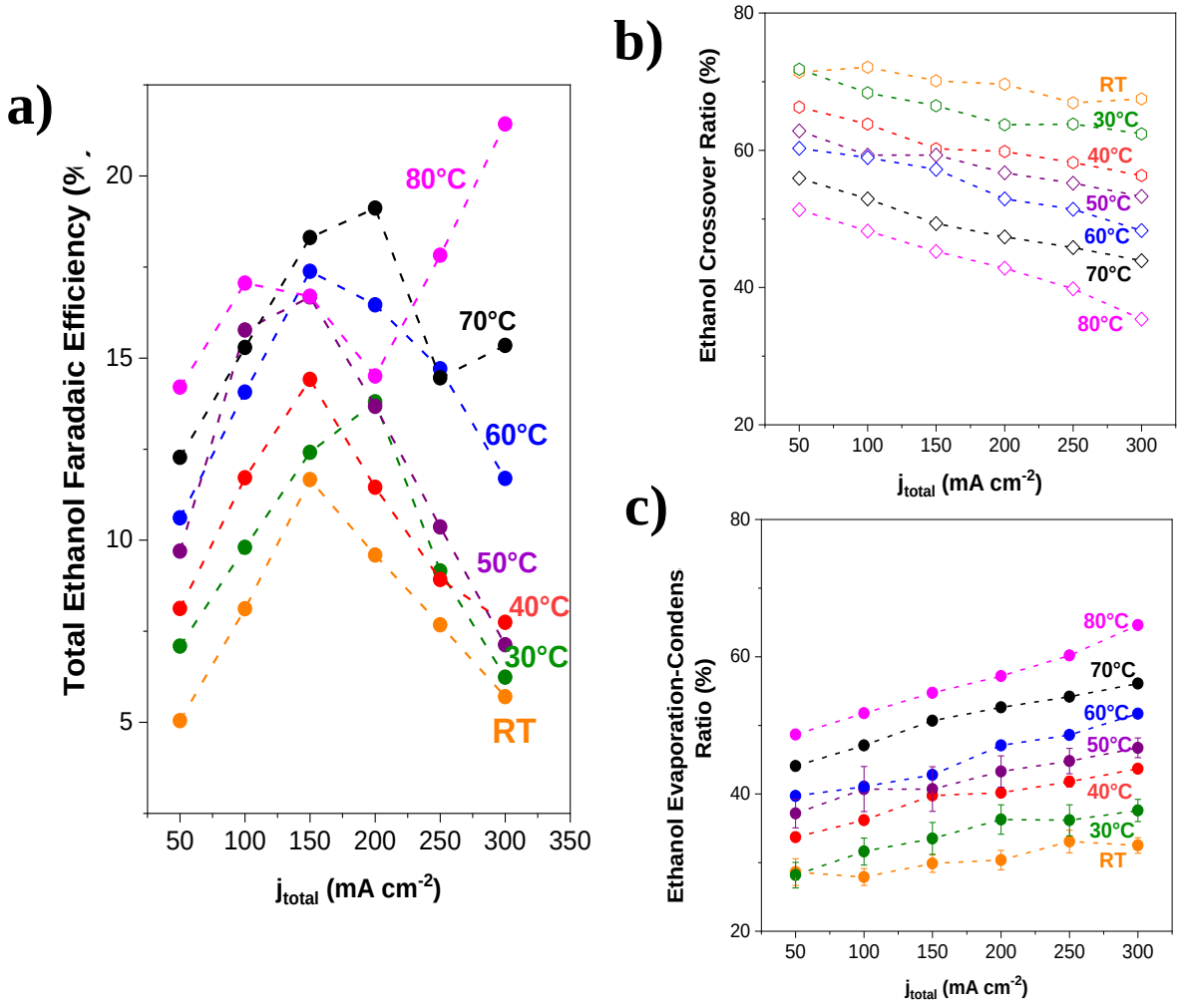

Figure S20. a). Effect of temperature in the ethanol selectivity at different total current densities b). Ethanol crossover ratio as a function of the operating temperature and the current density, and c). The evaporation rate of ethanol across the cathode-GDE is a function of the temperature. Experimental conditions: Cu-GDE (Cathode), MPIP-AEM, IO_2 (Anode), CO_2 feeding rate 40 sccm, 0.1 M $KHCO_3$. Operating time: 90 min for each measurement).

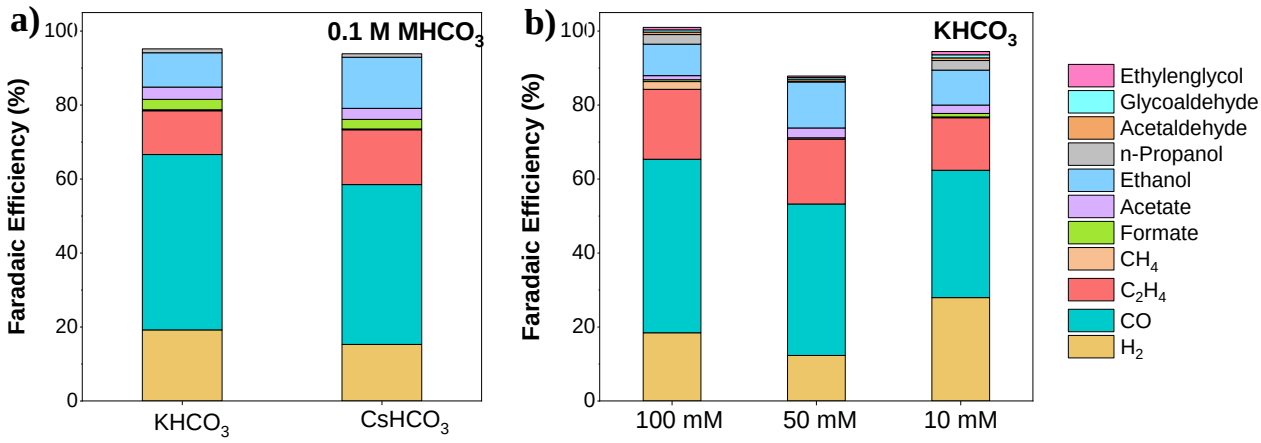

Figure S21. Study of the effect of the electrolyte at elevated temperatures (60ºC). a). Effect of the cation in the anolyte at 0.1 M. b). Effect of the electrolyte concentration for KHCO3-electrolyte solutions. Experimental conditions: Cu-GDE (Cathode), MPIP-AEM, IO_2 (Anode), CO_2 feeding rate 40 sccm).

Supplementary Note II

Flooded-agglomeration model for limiting current density estimation.

To correlate the temperature influence on the CO_2-mass transport, we will implement the "flooded-agglomeration model" coupled with the thin-film model proposed by and implemented for Løwe et al.[15] to correlate the CO_2 depletion and further HER increase.[17–19] When the CO_2 drops to zero in the center of the agglomerate, we can correlate the partial current density (j_{H2}) and the c_{CO2} using first Fick's law and Faraday's law.

Diffusion limited mechanism into the porous:

$$J_i = -D\,\frac{dc}{dx} \quad \textbf{(Eq S. 9)}$$

$$J_{CO2,dif} = -D_{CO2}\,\frac{c_{CO2,surface}}{r_p} \quad \textbf{(Eq S. 10)}$$

With 1st Faraday's law: $J_{CO2,dif} = \frac{j_{CO2,max}}{zF}$

$$j_{CO2\_max} = \frac{D_{CO2}(T)}{r} \cdot c_{CO2}(T) \cdot F \cdot z \quad \textbf{(Eq S. 11)}$$

Where Ji is the mass flux, c_{co2} surface the concentration at the surface, $D_{eff,CO2}$ corresponds to the effective diffusion (m^2 s), r the agglomerate radius, F the Faraday's constant, and z the number of electrons of the

charge transfer reaction. The CO_2 solubility and diffusion calculation are taken from Eq S.1 and S.2. The porosity and tortuosity of the agglomerate were considered. The values were setting it up following Weng et al.[20] as diffusion and charge transfer reactions happen simultaneously, the estimation of the limiting current density is only an approximation by using this model.

Table S4. Estimation of the limiting current density as a function of the temperature

Temperature (ºC)	**$j_{CO2,max}$ (mA cm^2)**
20	240
30	239
40	243
50	25
60	270
70	292
80	320

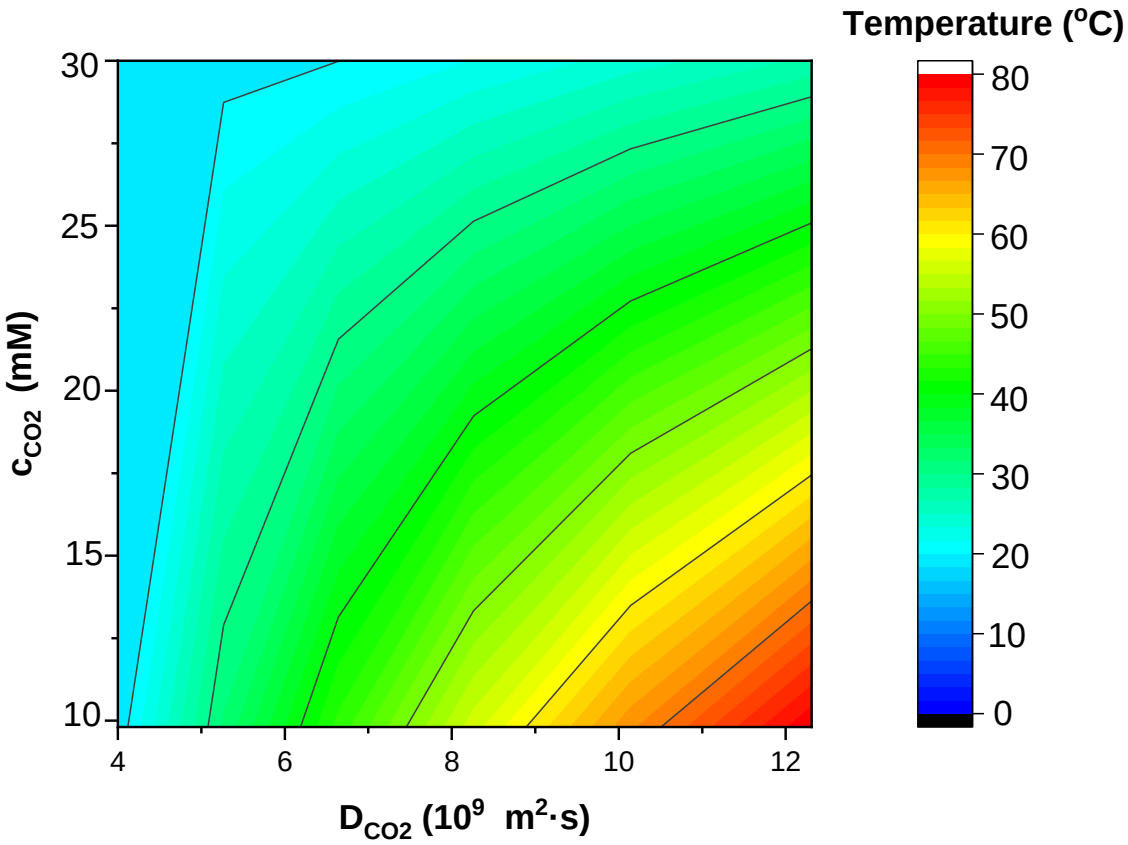

Figure S22. Contour plot of the effect of temperature on the CO_2 solubility (c_{CO2}) and diffusion (D_{CO2}). Data obtained from equations (S.1 and S.2)

Table S5. CO_2 concentration in aqueous solution and diffusion as a function of operating temperature

Temperature (K)	c_{CO2} (mM)	D_{CO2} (10^9 m^2 s^{-1})
283	53.9	2.38
293	39.3	3.16
303	30.1	4.11
313	24.0	5.27
323	19.8	6.64
333	16.9	8.26
343	14.9	10.14
353	13.5	12.31

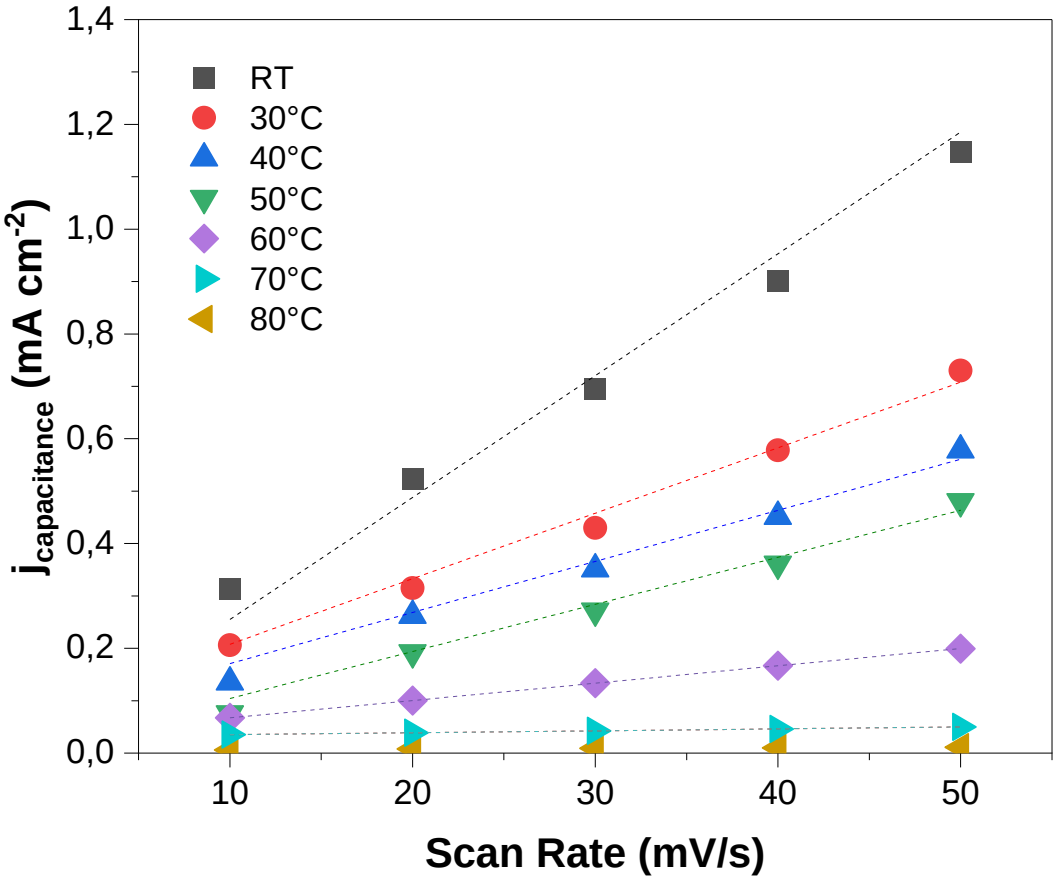

Figure S23. Electrochemical capacitance measurements after CO_2 electrolysis at different temperatures. The potential was cycled in between 0.1 and 0.35 V VS RHE at different scan rates

Table S6. Measurements of the double-layer capacitance after CO_2 electrolysis at 200 mA cm^{-2}

Temperature (°C)	**DLC (mF cm^{-2})**
20	2,05
30	1,31
40	1,08
50	0,98
60	0,64
70	0,56
80	0,53

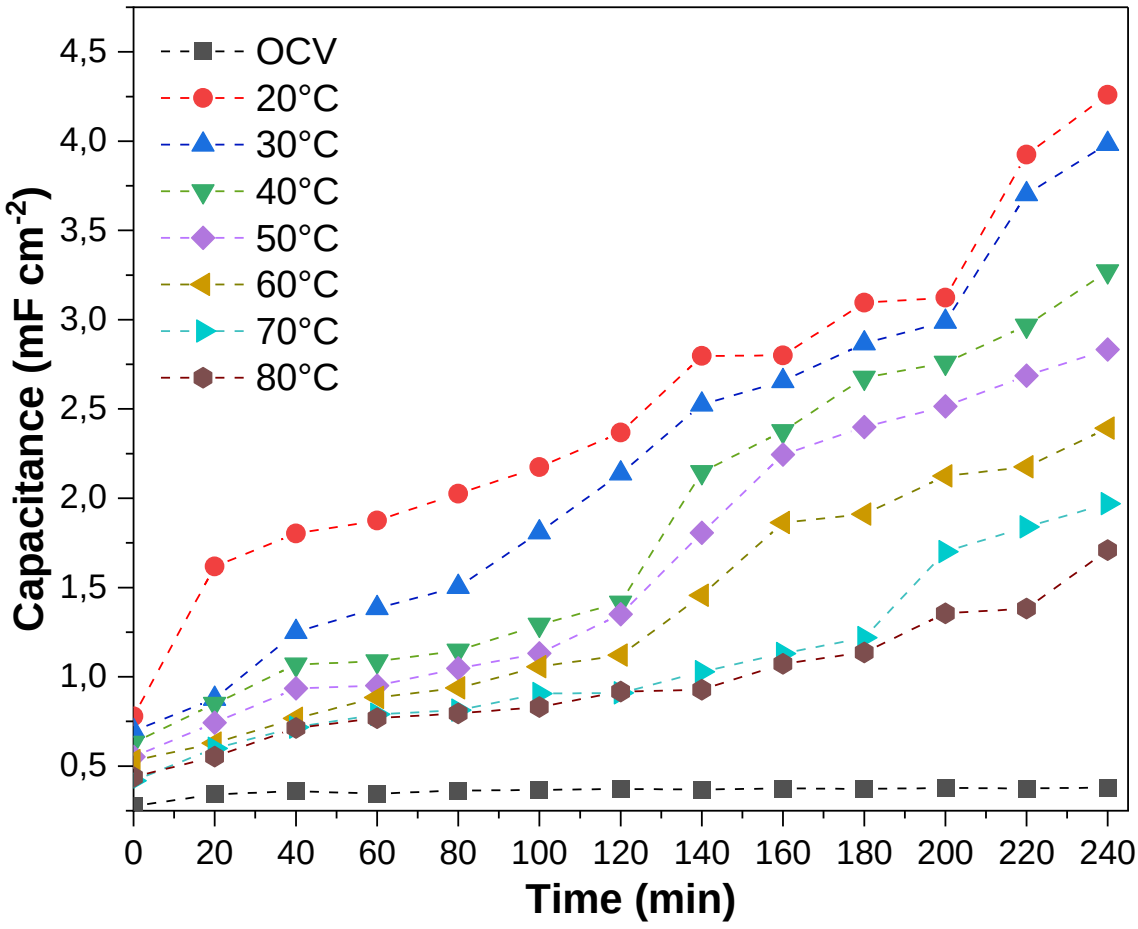

Figure S24. Tracking the electrode flooding by measuring the electrochemical capacitance at 200 mA cm^{-2} as a function of the operating temperature. (Experimental conditions: Cu-GDE (Cathode), MPIP-AEM, IO_2 (Anode), CO_2 feeding rate 40 sccm, 0.1 M $KHCO_3$) .

Effect of the reflux ratio in product distribution for CO2R to CO at 150 mA cm-2

Effect of temperature on CO solubility

Empirical expression for CO concentration in aqueous solutions as the effect of the temperature.[21]

$$c_{co}\left(\frac{mol}{kg\ bar}\right) = 9.9\ \cdot 10^{-4}\ \cdot \exp\left(1300 \cdot \frac{1}{T[K]} - \frac{1}{298}\right) \quad \textbf{(Eq S. 12)}$$

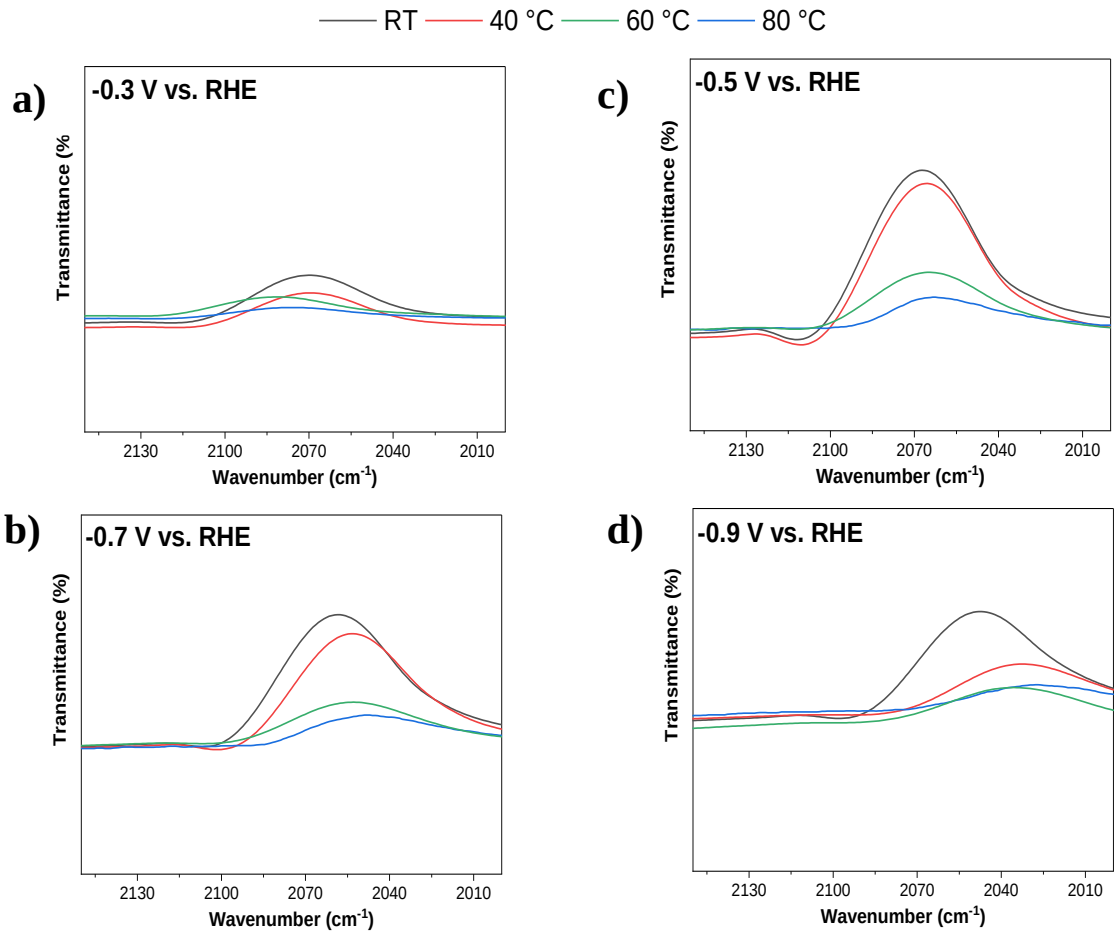

Figure S25. CO features from ATR-SEIRAS spectra at different temperatures as a function of the cathodic potentials a). -0.3 V b). -0.5 V c) -0.7 V and d). -0.9 V vs. RHE

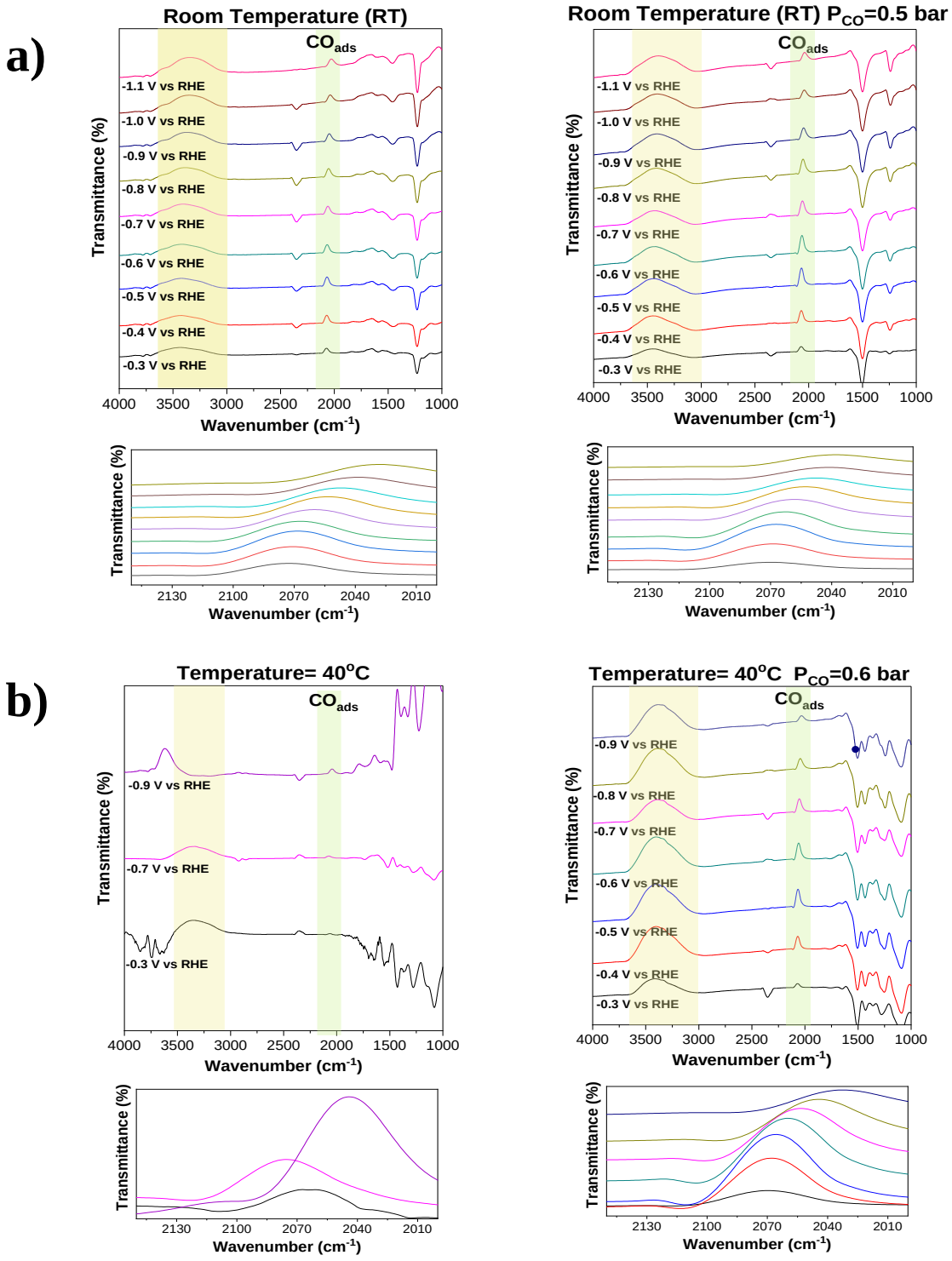

Figure S26. Full ATR-SEIRAS for CO electrolysis at different cathodic potentials at different temperatures and partial pressures a). room temperature b). room temperature and P_{CO}=0.5 bar c). 40 °C and d). 40 °C and P_{CO}=0.6 bar

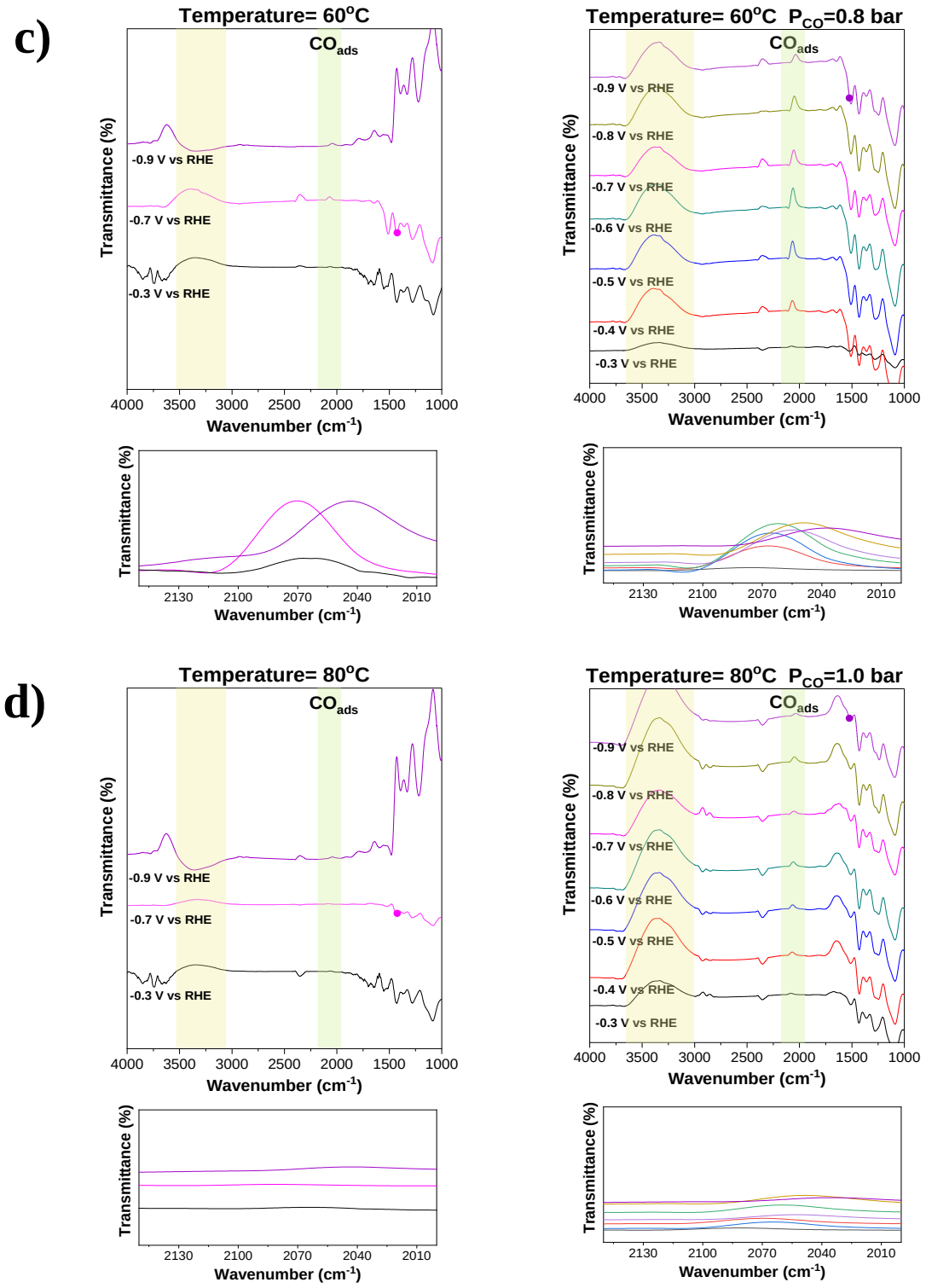

Figure S27. Full ATR-SEIRAS for CO electrolysis at different cathodic potentials at different temperatures and partial pressures a). 60 °C b). 60 °C and P_{CO}=0.8 bar c). 80 °C, and d). 80 °C and P_{CO}=1.0 bar

Scheme of configurations to evaluate the effect of the heating method

a). Use of heating rods connected to the flow field on both compartments

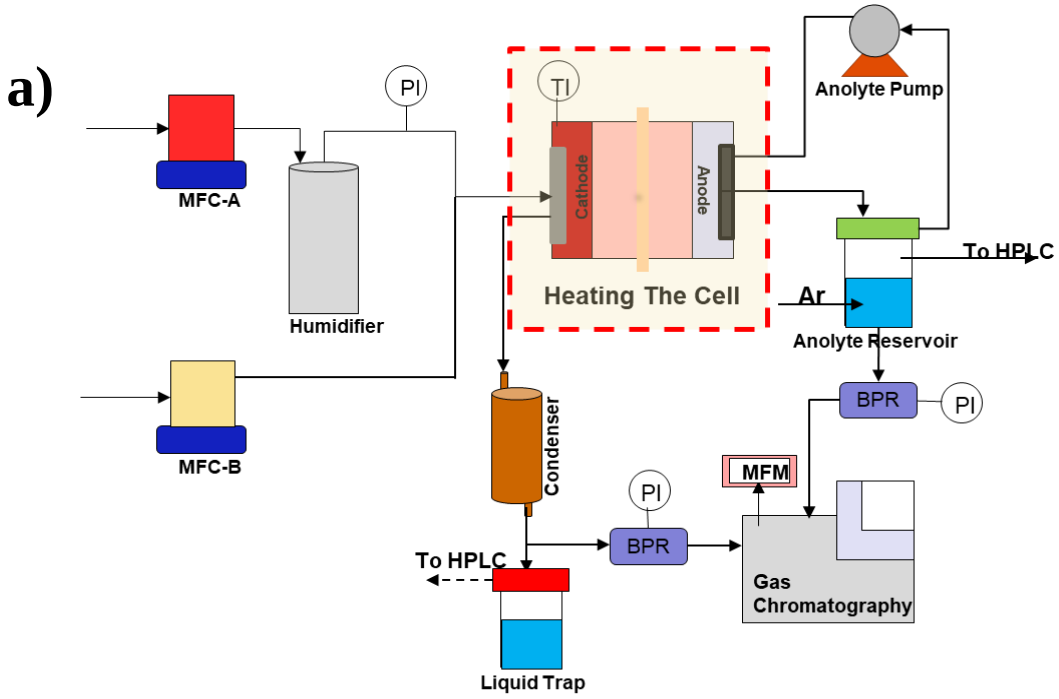

a). Use of a heating plate for the electrolyte reservoir heating

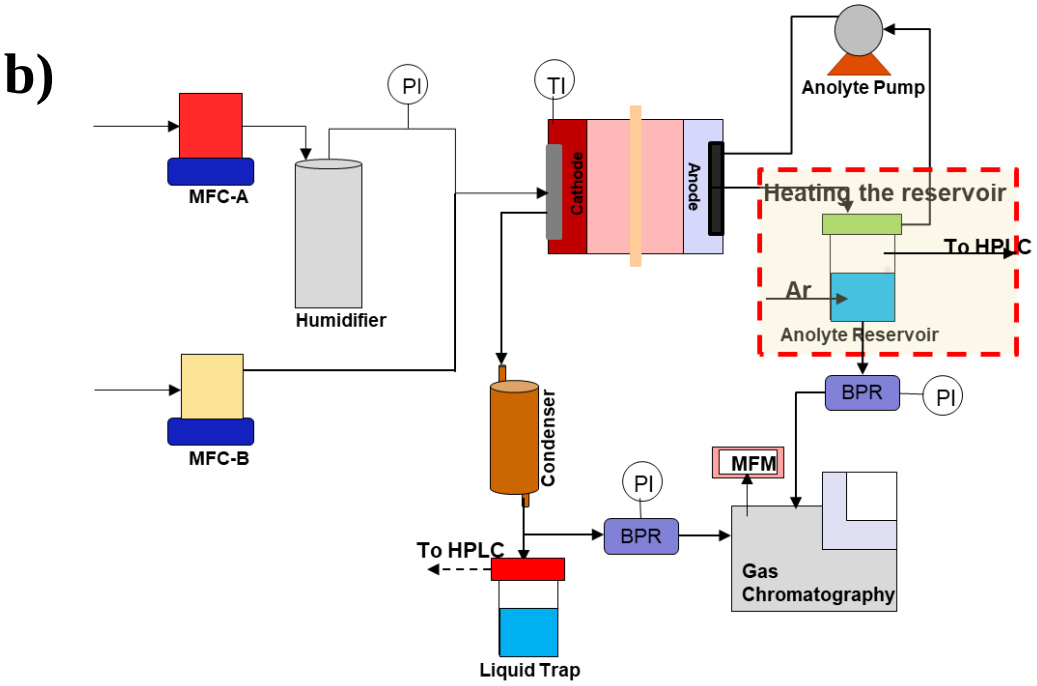

Figure S28. Schematic representation of heating methods a), Heating the EC and b) Anolyte

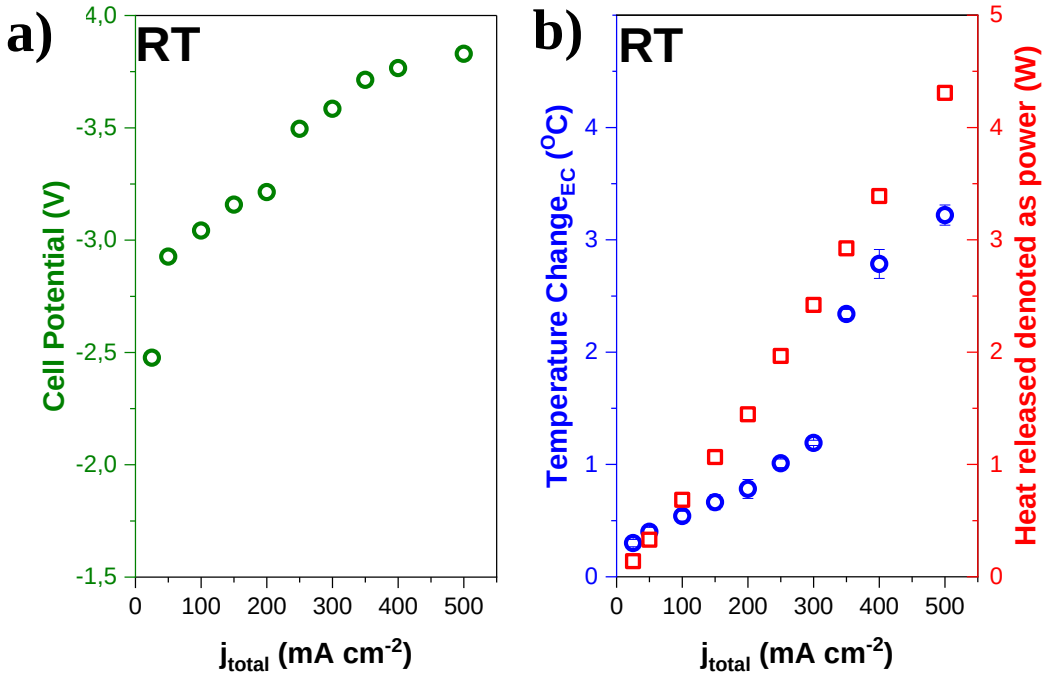

Figure S29. a). Cell potential as a function of total current density for CO_2 electrolysis b). measurements of the temperature changes due to the resistive heating at room temperature at different current densities.

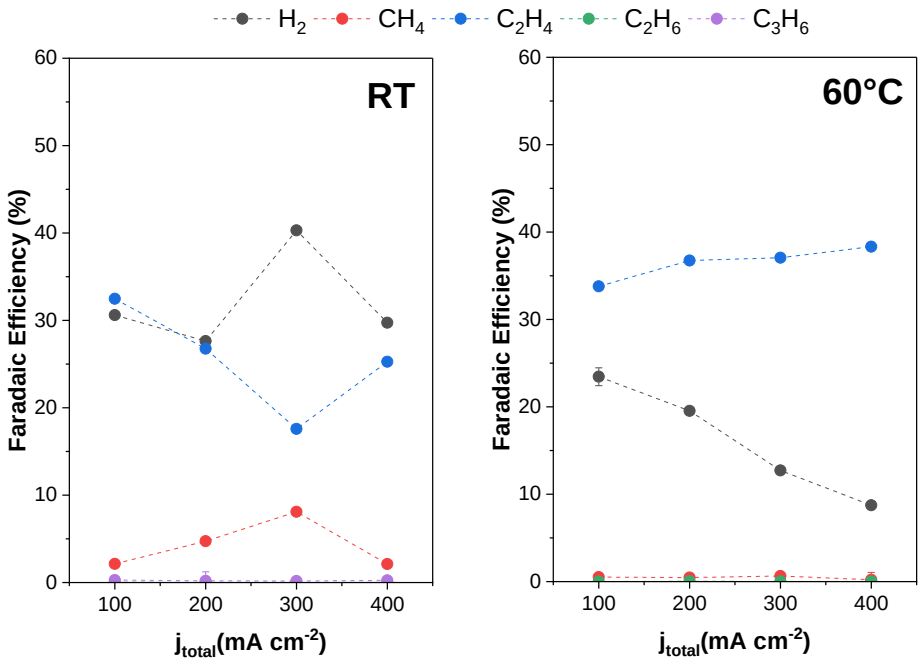

Figure S30. The product distribution of gas-products at different current densities for CO electrolysis at different temperatures a). Room temperature, and b). 60°C.

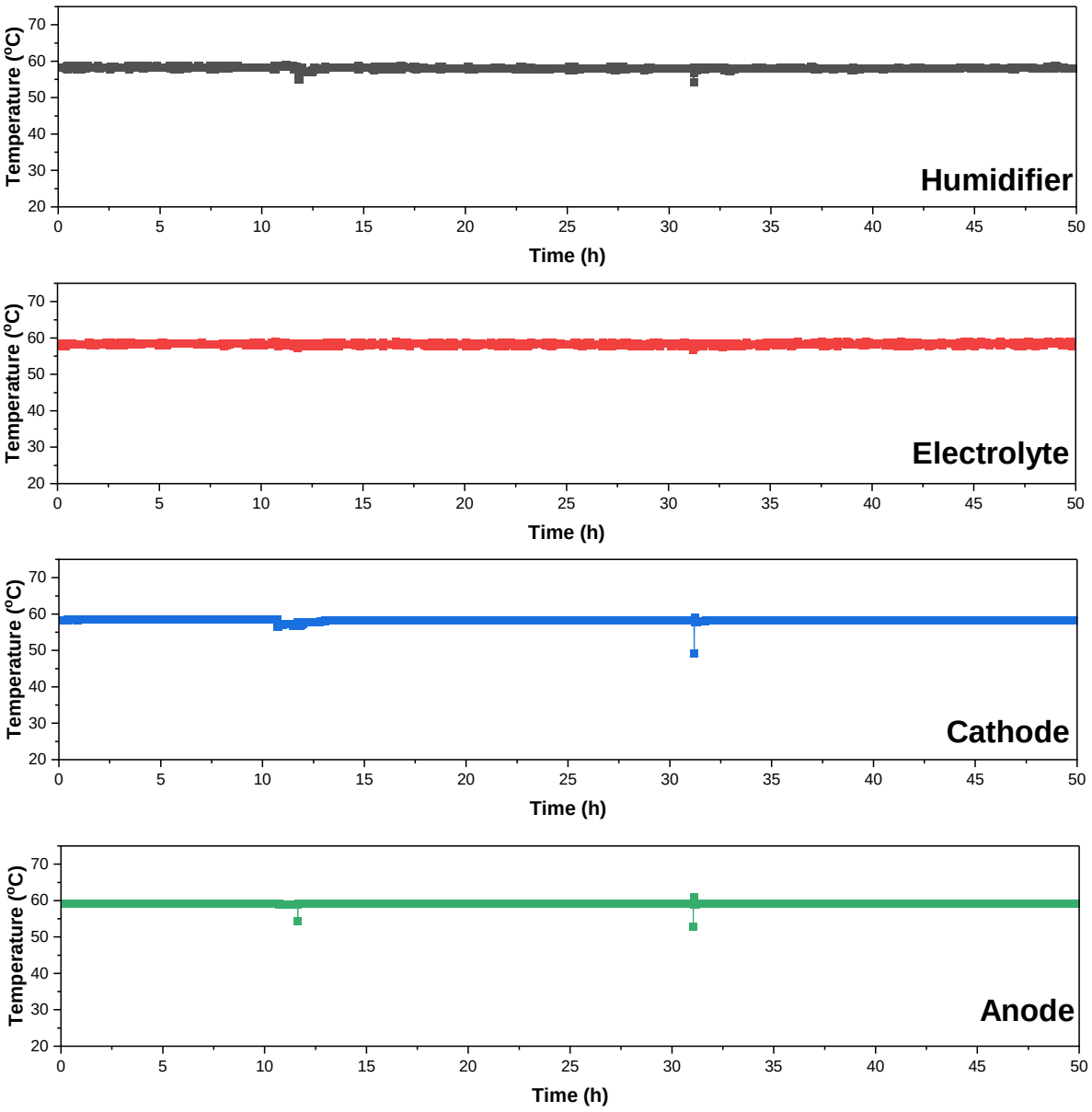

Figure S31. Temperature profile for the long-term experiment (Figure 8 of the main manuscript) for different reaction components (humidifier, electrolyte, and electrochemical cell).

Supplementary Note III

Overall balance and influence of temperature in CO_2 electrolysis using MEA approach.[22] *We highlighted the direct parameters, mechanisms or equations that involves temperature on it.*

Cathode Gas Channel

Overall Mass Balance: $\nabla(\rho u) = 0$

Component Mass Balance (Flux per species): $\nabla n_i = 0 \qquad i = CO_2, H_2, C_2H_4, H_2, H_2O$

Multicomponent Flux: $n_i = -\rho w_i \sum_{j=i}^{n} D_{ij}(T) \left[\frac{M_g}{M_j}\left(\nabla w_i + w_j \frac{\nabla M_g}{M_g}\right) + \left(x_j - w_j\right)\frac{\nabla p}{p}\right] + \rho u w_i$

Molas mass of gas mixture: $M_g = x_{CO2}M_{CO2} + x_{CO}M_{CO} + x_{C2H4}M_{C2H4} + x_{H2O}M_{H2O} + x_{H2}M_{H2}$

Fuller Diffusion Coefficient: $\boldsymbol{D_{ij} = \frac{0.0101325 \cdot T^{1.75}\left(\frac{1}{M_i}+\frac{1}{M_j}\right)^{0.5}}{p\left(v_i^{\frac{1}{3}}+v_j^{\frac{1}{3}}\right)}}$

Mass Fraction: $w_{CO2} + w_{CO} + w_{C2H4} + w_{H2} + w_{H2O} = 1$

Gas and liquid-water transport in the GDL and CL (Porous Media)

Overall Mass Balance: $\nabla(\rho u) = Q$

Mass Source Term (Q): $Q = R_{CO2} + R_{CO} + R_{H2} + R_{H2O}$

The mass-average velocity field of phase (Darcy's Law): $u_p = -\frac{k}{\mu}\nabla p$

Permeability (On the GDL using Tomadakis-Sotirchos model): $k = \frac{\varepsilon}{8\,(\ln \varepsilon)^2}\,\frac{(\varepsilon-\varepsilon_p)^{\alpha+2}\, r_f^2}{\varepsilon(1-\varepsilon_p)^{\alpha}[(\alpha+1)(\varepsilon-\varepsilon_p)]^2}$

Component Mass Balance: $\nabla n_i = R_i = R_{CT,i} + R_{B,i} + R_{PT,i} \qquad i = CO_2, H_2, C_2H_4, H_2, H_2O$

Molar Flux (from the mass flux): $n_i = -\rho w_i \sum_{j=1}^{N} D_{ij}^{eff}\left[\frac{M_g}{M_j}\left(\nabla w_j + w_j \frac{\nabla M_g}{M_g}\right) + \left(x_i - w_j\right)\frac{\nabla p}{p}\right] + \rho u w_i$

Effective gas diffusivity (Bruggeman correction): $D_{ij}^{eff} = \varepsilon^{1.5} D_{ij}$

Mole Fraction: $\sum x_i = 1 \qquad x_i = \frac{w_i M_g}{M_i}$

<u>Charge transfer reaction in CL (R_{CT})</u>

Charge conservation: $\nabla i = 0$

Current Density (Ohm's law): $i = -\sigma_{GDL}\nabla\phi_s$

Overpotential: $\eta_k = (\phi_S - \phi_L) - \left(U_k^0 - \frac{2.303RT}{F}\right) pH$

Reaction Rate Charge transfer: $R_{CT.I} = -M_i \sum_k \frac{s_i k a_v i_k}{zF}$

Charge transfer reactions per species: $\boldsymbol{i_k = -i_{0,k}\left(\frac{c_j}{c_j^{ref}}\right)^{\gamma_k} \exp\left(\frac{-\alpha_{c,k}F}{RT}\eta_k\right)}$

Exchange current density: $\boldsymbol{i_{0,k} = A_K \exp\left(-\frac{E_{a,k}}{RT}\right)}$

Current Source Terms associated with solid phase: $S_s = \left(-\sigma_{CL,s}\nabla\phi_s\right) = -a_i i_i$

Current Source Terms associated with the liquid phase: $S_l = \left(-\sigma_{CL,l}\nabla\phi_l\right) = a_i i_i$

<u>Electrolyte</u>

Current Density (Ohm's law): $i = -\sigma_{electrolyte}\nabla\phi_l$

Ionomer/membrane

Water flux: $n_w = -\alpha_w^{eff}\nabla\mu_w + \sum_j \epsilon_j^{eff} n_j$

Electro-osmotic coefficient: $\sum_j \epsilon_j^{eff} n_j = \epsilon_j^{eff}\frac{i_L}{F}$

Water activity: $a_w = \frac{p_v}{p_w^{vap}}$

Water mole fraction in the Ionomer: $x_w = \frac{\lambda}{1+\lambda}$

Water volume fraction in the Ionomer: $\beta_L = \frac{\lambda V_W}{\lambda V_W + \left(\frac{1}{IEC\,\rho_M}\right)}$

Chemical Potential Water: $\boldsymbol{\mu_w = RT\ln(a_w) + \beta_L * (p_{L,M} - p^{ref})}$

Concentration CO_2 at the CL/ionomer interface: $\boldsymbol{c^G_{CO2} = H_{CO2}(T) p_G y_{CO2}}$

Equilibrium water Liquid/vapor CL/ionomer interface: $c^G_w = c_M \lambda \qquad w_w = \frac{p_{sat} M_w}{p M_g}$

Donnan Potential (potential difference membrane/electrolyte) interface: $\Delta\phi_D = \phi_l^M - \phi_l^E$

Equilibrium species between Ionomer and electrolyte: $c_i^M = c_i^E \left(-\frac{z_i F}{RT}\Delta\phi_D\right)$

Molar flux other liquid species: $n_{j\neq w} = -D_j^{eff}\nabla c_j - \frac{z_j F}{RT} D_j^{eff} c_j \nabla\phi_L$

Electroneutrality: $\sum_j z_j c_j = 0$

Bulk reactions (homogeneous reactions $R_{B,i}$)

Reaction rate due homogeneous reactions: $R_{B,i} = M_i \sum s_{i,n} \left(k_n \prod_{s_i,n} c_i^{-s_{i,n}} - \frac{k_n}{K_n}\prod_{s_{i,n}} c_i^{s_i,n}\right)$

Equilibrium constants (Van't Hoff equations): $\boldsymbol{K_n = \exp\left(\frac{\Delta S_n}{R}\right)\exp\left(-\frac{\Delta H_n}{RT}\right)}$

Phase transfer (rate of mass transfer between phases of CO_2, water and liquid products) $R_{PT,i}$

Phase transfer of CO_2 and liquid products: $R_{PT,i,I}\ (CL) = a_s k_{MT,i}(c_i^{eq} - c_i)$

Phase transfer of water into the Ionomer: $\boldsymbol{R_{PT,w,ionomer} = a_s K_{MT}\left(\frac{RH}{100} - a_w\right) + \frac{a_s k_{MT,L}}{RT}(p_L - p_{L,M})}$

Relative humidity of the Gas phase: $R_H = \frac{p_G y_0}{p_o^{sat}}$

Phase transfer of water in the gas phase: $R_{PT,w,G} = -a_s K_{MT}\left(\frac{RH}{100} - a_w\right) - K_{MT}(RH - 100\%)\left[H_0\left(\frac{p_L}{p^{ref}} + H_0(RH - 100\%)\right]\right.$

Phase transfer of water in the gas phase: $\boldsymbol{R_{PT,w,L} = -\frac{a_s K_{MT}}{RT}(p_L - p_{L,M}) + K_{MT}(RH - 100\%)\left[H_0\left(\frac{p_L}{p^{ref}} + H_0(RH - 100\%)\right]\right.}$

Overall Mass Balance associated to phase transfer

Gas phase: $Q_G = -M_{CO2} R_{PR,CO2} + M_W R_{PT,W,G} + \sum M_i R_{CT,i}$

Liquid phase: $Q_L = M_W R_{PT,W,L}$

Anode CL

Overpotential: $\eta_k = (\phi_S - \phi_L) - \left(U_k^0 - \frac{2.303RT}{F}\right) pH$

Mass balance in the anode: $Q = R_{CT} = R_{O2} + R_{H2O}$

Charge transfer reactions per species: $\boldsymbol{i_k = -i_{0,k}\left(\frac{c_j}{c_j^{ref}}\right)^{\gamma_k}\exp\left(\frac{-\alpha_{c,k}F}{RT}\eta_k\right)}$

Exchange current density: $\boldsymbol{i_{0,k} = A_K \exp\left(-\frac{E_{a,k}}{RT}\right)}$

Overall Cell Potential: $E_{cell} = E_{cat} - E_{an}$

Reaction Rate OER: $R_{O2} = \frac{a_{O2} i_{O2}}{4F} M_{O2}$

Reaction Rate water: $R_{H2O} = \frac{a_{O2} i_{O2}}{2F} M_{H2O}$

Heat balance

Overall heat balance: $Q_H = Q_{CT} + Q_B + Q_J$

Heat generated from charge transfer reactions: $Q_{CT} = \sum_K (i_k \eta_k + i_k \cup_k)$

Peltier coefficient for HER: $\cup_K = \boldsymbol{240\ \frac{T[K]}{298}}$

Peltier coefficient for OER: $\cup_K = \boldsymbol{13\ \frac{T[K]}{298}}$

Peltier coefficient for COER: $\cup_K = \boldsymbol{240\ \frac{T[K]}{298}}$

Heat generated from homogeneous bulk bicarbonate: $Q_B = \sum_n \Delta H_n \left(k_n \prod_{s_i,n} c_i^{-s_{i,n}} - \frac{k_n}{K_n}\prod_{s_{i,n}} c_i^{s_i,n}\right)$

Joule heating (due to electrical resistance): $Q_j = i_s^2/\sigma_m$